Systematic Control Design and Stability Analysis Approaches for Microgrid Inverters to Enhance Overall Performance and Efficiency

by

Nima Amouzegar Ashtiani

A thesis submitted in partial fulfillment of the requirements for the degree of

Doctor of Philosophy
in
Energy Systems

Department of Electrical and Computer Engineering
University of Alberta

Abstract

This thesis addresses a systematic design and implementation of control systems of power converters in microgrids to guarantee system level stability and improve performance and efficiency. Due to the high penetration of power converters in power systems, proper operation of converters in different situations is crucial to maintain the entire system stable. Therefore, depending on the role of the power converter in the system, the control system should be designed properly to address control objectives. With respect to the control objectives and converter configurations, design of the control system faces various challenges. For a single-converter system, uncertainties and practical issues may affect the system performance and its stability. For a multiple-converter system, the interaction among power converters along with its impact on the system stability, and also the overall efficiency optimization introduce other challenges for the control system. In this research, the proposed systematic control system design for a single- and multiple-converter systems are investigated, simulated and experimentally verified as summarized below.

First, a robust control system for a single-phase photovoltaic (PV) converter with an LCL-filter under weak grid operation is proposed. The control system guarantees system robustness against weak grid uncertainties such as grid impedance variations and voltage harmonics. Moreover, the controller compensates the system delays. The control system minimizes the bus voltage fluctuations caused by variations of PV system power generation. Furthermore, power decoupling is achieved by the control system without any auxiliary circuit.

For converter control systems, a systematic and optimal control design approach is proposed for control structures which involve multiple cascade, or nested, loops. The proposed approach relaxes the limiting condition that the internal loops must be much faster than the external loops. Therefore, faster yet smoother responses can be achieved using the proposed design approach. As an example, the method is also used to systematically design a cascade control system, including voltage and current control loops, for a single-phase standalone inverter.

To further investigate the performance of the individual inverters in a microgrid, an approach is proposed for modeling and stability analysis of a single-phase standalone microgrid containing parallel inverters. Using the approach, interactions among parallel inverters and the impact of each parameter variations on the system are studied in details. Based on this approach, a nonlinear microgrid can be linearized, and the microgrid behaviors can be assessed using several tools available for linear systems. As an example, the model and stability of a single-phase microgrid with two parallel inverters are provided. It is shown that the proposed model predicts the system responses more accurately than the existing modeling approaches, especially, for systems with a small stability margin.

Finally, to improve the overall efficiency of the investigated microgrid at light loads, a communicationless modified droop strategy is introduced. The main idea is to revise the power sharing among parallel inverters such that the output power of each inverter is maintained within a proper range with respect to the inverter efficiency curve and the load demand instead of the proportional power sharing, realized through the conventional droop control strategy. Moreover, to evaluate the performance of the proposed method, a system with parallel inverters is simulated and experimentally tested. It is observed that the proposed strategy can improve the overall system efficiency by up to 14% at light loads.

Acknowledgements

Firstly, I would like to express my deeepset gratitude to my supervisors, Prof. S. Ali Khajehoddin, for his immense knowledge and valuable suggestions that helped me over the course of my Ph.D. studies. His gentle personality, enthusisiasm, and rigorous attitude toward research have made the past couple of years the most constructive and gratifying experience.

My appreciation is extended to Prof. Gregory Kish, Prof. Alan Lynch, and other members of my committee for their constructive comments and feedbacks.

I would like to aknowledge Dr. Masoud Karimi-Ghartemani, Dr. S. Mohsen Azizi, and Dr. Ahmadreza Tabesh for all of the insightful and productive discussions. I am deeply indebted to Mohammad Ebrahimi and Mohammad Daryaei for sharing their experiences and providing intellectual inputs. My greatest appreciation is extended to Ali Sheykhi. Our collaboration significantly facilitates accomplishing our mutual research objectives.

I would like to offer my thanks to my fellow graduate students in the uAPEL lab, especially, Rouzbeh Reza Ahrabi, Atrin Tavakoli, Mohammad Shahabbasi, Amin Khakparvar, Navid Shabanikia, Morteza Mahdavifard, and Manouchehr Fathi for their constructive comments and friendship during the last few years.

The last but certainly not the least, my warmest gratitude goes to my lovely wife, my parents, and my sister for all their invaluable emotional support, encouragement, and devotion. Without their support, none of this would have been possible.

Dedicated to my lovely family

Contents

List of Figures

List of Tables

Abbreviations

2DOF	Two-degree-of-freedom
APF	All-pass Filter
CCM	Current-controlled Mode
DG	Distributed Generator
DSP	Digital Signal Processor
FAE	Fictive Axis Emulation
FF	Feedforward
GFL	Grid-following
GFM	Grid-forming
IAE	Integral of Absolute Error
LFT	Linear Fractional Transformation
LHP	Left Hand Plane
LPF	Low-pass Filter
LQG	Linear Quadratic Gaussian
LQR	Linear Quadratic Regulator
LQT	Linear Quadratic Tracking
LTI	Linear Time-invariant
LVRT	Low Voltage Ride Through
MIMO	Multiple-input Multiple-output
MPP	Maximum Power Point
MPPT	Maximum Power Point Tracking
OID	Online-inverter Detection
OSG	Orthogonal Signal Generation
P	Proportional
PCC	Point of Common Coupling
PI	Proportional-integral

PLL	Phase-locked Loop
PR	Proportional-resonant
PV	Photovoltaic
PWM	Pulse-width Modulation
RBOSG	Reference-based Orthogonal Signal Generation
SCR	Short Circuit Ratio
SOGI	Second-order Generalized Integrator
THD	Total Harmonic Distortion
UPS	Uninterruptible Power Supply
VSC	Voltage Source Converter
WT	Wind Turbine

Chapter 1

Introduction

Usage of power converters has been growing up considerably in power systems and renewable energy applications such as photovoltaic (PV) and wind turbine (WT) systems [1–6]. A power converter is a piece of equipment with different applications and dynamics. In each application, the control system of the power converter plays a crucial role in proper operation of the entire system. Therefore, the control system should be designed properly to address control objectives. Depending on the control objectives and converter configurations and its applications, the design of the control system faces various challenges.

For one converter, power system uncertainties such as grid impedance variations, load changes, etc. may affect the converter stability and performance. Also, practical issues such as nonlinear behavior of system elements and delays, which are due to the micro-processor calculation, measurement, and pulse-width modulation (PWM), are other challenges of the control system, which should be compensated, in the one-converter level.

Owing to the high penetration of power converters in power systems, interactions among power converters lead to other challenges such as power system instability and system performance degradation in the multi-converter level. Furthermore, in some cases, integrating multiple power converters with different dynamics into a power system makes the entire system nonlinear. As there are only few tools to study nonlinear systems, a linear model of the entire system is required to study the system dynamics, stability, and etc. by using several tools available for linear systems.

Another control challenge in the multi-converter level is to determine an efficient power-sharing strategy that optimizes the overall efficiency of the system with

respect to the load profile. For this purpose, a reliable model of the system is also required to guarantee the stable operation of the system for the efficiency optimization strategy. In this thesis, some of the aforementioned issues are discussed in detail for single-phase systems, and the control challenges are addressed by using proposed methods.

1.1 Robust Control of Single-phase Converters in Weak Grids

Integration of remote renewable energy systems like WT and PV systems into a grid via long transmission lines may result in a weak grid operation [7]. According to the IEEE Transmission and Distribution Committee, the short circuit ratio (SCR) is used to describe the grid strength. A grid is defined as a weak grid if SCR$<$ 3 [8]. As mentioned, weak grid situations happen in remote areas due to the impedance of transmission and distribution lines. Fig. 1.1 represents a configuration of a single-phase converter connected to a grid. If the grid is stiff, typically, a dual-loop control system is used for the system shown in Fig. 1.1. However, in a weak grid situation, system dynamics become more complicated, and the control system faces various challenges due to the grid impedance uncertainties. It is desired to use the same control system for both stiff and weak grids.

As shown in Fig. 1.1, the outer loop is a dc link control loop, designed to regulate the dc link voltage. The inner loop is a current control loop which should follow the current reference determined by the dc link controller. This configuration is normally used as the second converter in two-stage PV systems [1]. Depending on the application of the power converter and weak grid features, the control system of the aforementioned system faces several challenges such as grid impedance uncertainties, grid harmonics rejection, practical issues like delays, damping resonant oscillations, and power decoupling. Each control loop is responsible to address some of the aforementioned challenges which are discussed in the following.

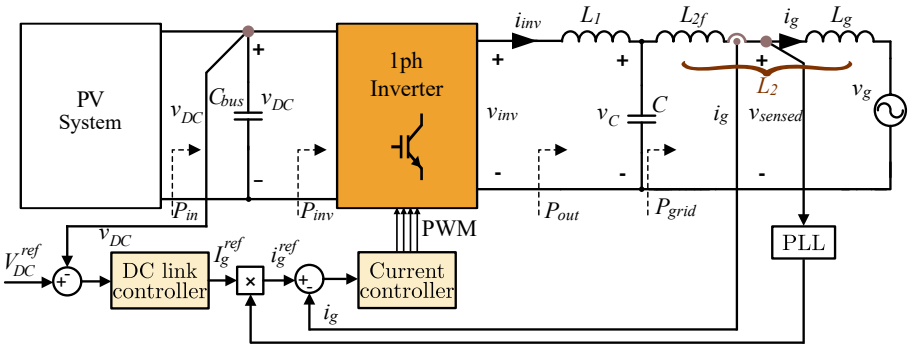

Fig. 1.1: Configuration of a single-phase converter connected to a weak grid.

1.1.1 Current Controller

The current control loop is commonly much faster than the dc link control loop. Thus, the current control loop tackles to control objectives with faster dynamics. The current control loop is normally responsible to track the current reference signal, damping resonant oscillations of high-order filters, compensate grid voltage deviations, keep the system stability against system uncertainties, and compensate delays in practical implementations.

Diverse current control strategies have been introduced for grid-connected voltage source converters (VSCs) to mitigate issues with grid voltage harmonics, which are common in weak grids, and resonant oscillations. Predictive control [9] and linear quadratic gaussian (LQG) control [10] methods are used to design a current controller for inverter with high-order filter. In [11], a repetitive controller is used to deal with undesirable harmonics and grid frequency variations. However, delay uncertainties are not compensated, and the range of inductance variation is not explicitly indicated. The admittance compensation method is utilized in[12, 13] where extra capacitor voltage or current feedbacks are used to improve the system stability and to attenuate resonant oscillations. Whereas, such methods cannot ensure the system robustness in the presence of system parameter uncertainties.

Using the H_∞ method, a robust current controller is designed for grid-connected VSCs in [14–16]. However, in proposed control methods, an additional damping

loop must be used to damp the resonant oscillations, so it needs multiple state measurements. Other robust controllers against system uncertainties are proposed in [17–22]. However, either the range of grid impedance variation is not wide enough to be suitable for weak grid applications, or delay impacts are not compensated. Adaptive control is used to design current controller in [23]. However, performance and robustness analysis techniques used for adaptive systems are not as straightforward and standard as those of the linear systems, e.g. root locus, bode plot, phase/gain margins, system norms, μ-synthesis, H_∞, etc. Moreover, in [23], delay uncertainties are not compensated.

As mentioned earlier, in practical implementation of each control system, there are some delays owing to the micro-processor calculation, measurement, and PWM. Also, there are some delay uncertainties caused by aliasing and quantization effects [24]. The aforementioned issues may lead to steady-state errors or even system instability [25, 26]. Therefore, the current controller is responsible to compensate practical delays to avoid impacts of delays on the system. There are several studies conducted on this issue in the literature [25–32]. Although they have compensated the effect of delay on the control system performance by using predictive control, area equalization concept, etc., either they do not compensate the effect of delay uncertainties, or they are not robust against grid impedance variations which are expected in a weak grid application.

1.1.2 Voltage Controller

As shown in Fig. 1.1, the dc link controller regulates the dc link voltage by determining the reference signal for the inner loop. Because dynamics of the dc link control loop are conventionally much slower than the inner loop, the dc link control loop addresses control objectives with slower dynamics.

As stated before, control objectives may vary based on the system applications and specifications. In two-stage PV systems, the dc link reference is usually kept constant for the second converter. Therefore, for this specification, the dc link

control of a single-phase grid-connected converter faces two challenges: 1) power coupling between dc link and ac grid, which leads to double-frequency oscillations on the dc link [1, 33, 34]; and 2) PV input power variations leading to dc link voltage fluctuations [34].

Power decoupling is usually achieved by using a large electrolytic capacitor. However, this solution is not desirable because it makes the system bulky and expensive, and also reduces the system lifetime. Using auxiliary circuits is another solution proposed in the literature to supply the double frequency component of the power. By using auxiliary circuits, the ripple power is supplied by another energy storage components which can tolerate higher ripples of the current or voltage. Thus, the dc link capacitance can be reduced [35–39]. However, using auxiliary circuits needs extra switches and energy storage components, which decrease the total system efficiency and increase costs.

The aforementioned approaches suffer from either short lifetime and huge system volume, or low efficiency and high costs. Another approach to address power decoupling and double frequency mitigation is based on the control systems. For this purpose, [1, 33] use a proportional-integral (PI) controller with a modified PWM to remove double frequency ripples from the injected current into the grid. However, the robustness of the proposed method is not studied.

Other challenge of the dc link control loop of a single-phase grid-connected converter is to suppress dc link fluctuations caused by input power variations. If the dc link voltage deviates considerably from its nominal value, such fluctuations may damage the dc link capacitor and/or the inverter switches or at minimum will activate the protection system leading to frequent shutdowns and system efficiency drop [33, 40, 41]. To suppress the effects of disturbances on the dc link, a nonlinear control method is proposed in [42] for three-phase systems. However, this method is not applicable for single-phase systems as the control system should address power decoupling as well. Typically, simple controllers such as proportional (P) and PI are

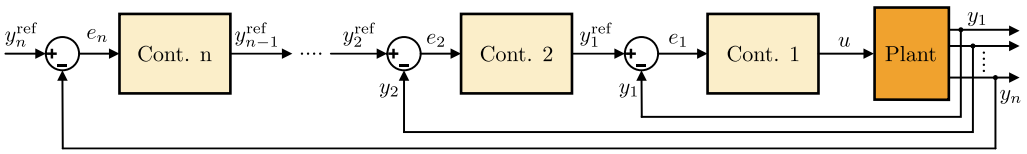

Fig. 1.2: General configuration of a cascade control system.

used as the dc link controller [43, 44]. Different methods for the design of conventional controllers exist such as pole placement, pole-zero cancellation, and criteria optimization methods [1, 33, 34, 45]. However, these methods cannot guarantees system robustness against input power variations.

1.2 Cascade Control Systems

Control system approaches to achieve a desired performance and output control in a power converter include classic transfer function methods, state-feedback, or other alternative control techniques. Methods such as state-feedback and pole-placement cannot directly shape and control individual modes of the system. Cascade, or nested-loop, control systems, however, can control individual variables and have been widely used in various power electronic applications such as renewable energy converters, motor drives, battery chargers, etc [46–50].

Fig. 1.2 depicts a general structure of a cascade control system. Respecting the consecutive impacts of system variables on each other, multiple control loops are placed into one another where each loop provides the reference for its internal loop. For example, this approach is used in a grid-connected inverter [51–56], where the inner loop controls and limits the current and maintains its quality, e.g. low harmonics, while the outer loop controls the dc link voltage.

Considering Fig. 1.2, an advantage of the cascade control approach is to provide the intermediary variables (y_1^{ref}, y_2^{ref}, ... , y_{n-1}^{ref}) that serve as the references for the corresponding variables. This allows to closely keep those variables under control and shape their dynamics. For example, by inserting a limiter function after

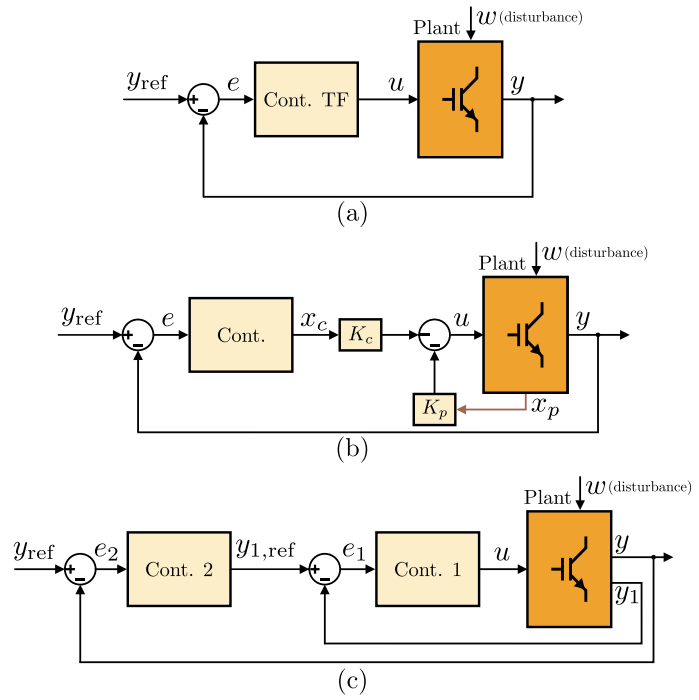

Fig. 1.3: Control system structures: (a) single-loop transfer function, (b) state feedback, and (c) conventional cascade structure.

each reference variable, the control system limits those variables in response to unexpected and/or severe disturbances such as short-circuit grid faults in an inverter. This advantage cannot be directly achieved using a regular single-loop control or a state-feedback approach.

1.2.1 Existing Control System Structures

Fig. 1.3 illustrates three common approaches to control the same plant: single-loop, state-feedback, and cascade control systems. Contrary to the first two, the cascade control structure, whose only two loops are shown for simplicity, provides the opportunity to have a direct control on internal variable y_1 in addition to controlling the system output y. This approach also breaks down the controller into simpler ones, i.e. Cont. 1 and Cont. 2 have simpler structures than Cont. TF in general.

1.2.2 Conventional Design of Cascade Control Systems

Besides shaping both the individual modes and the system output, another advantage of cascade control structure is to simplify the control system design by breaking it down to multiple stages. In this case, the most internal loop is designed first while all external loops are ignored; then, the other loops are consecutively designed until the entire system is designed. Each external loop is conventionally designed to be sufficiently, e.g. 10-20 times, slower than its internal loop. Therefore, the internal loop dynamics is either ignored or approximated by a low-pass filter with the cut-off frequency equal to the internal loop bandwidth, while designing the external loop. This is a widely-used procedure to design the control system in either the stationary or synchronous rotating frame [7, 48, 57–65]. Despite the clear advantage of this approach in facilitating the control system design, the required timescale difference between the loops poses a limitation that can lead to an overall sluggish performance.

On the other hand, if it is desired to have a fast outer loop at a timescale close or comparable to that of the internal loop, the internal loop dynamics should be considered in the design procedure of the external loop controller. In this case, the design procedure and structure of the external controller would be complicated because the external controller should handle a high-order system that contains the internal control loop plus the original plant without having access to its full-state variables.

To improve the dynamic performance of a cascade control system, reference feedforward [66–68] and disturbance feedforward techniques [48, 69, 70] have been proposed. However, the feedforward techniques reportedly are not usually as effective as a cascade control system with a fast external loop [71]. Moreover, depending on the application, the disturbance feedforward technique may require more sensors for the disturbance measurement, and the technique may make the reference noisy in practice [72].

The backstepping control techniques have also been used to design nonlinear-feedback control systems [73–76]. Also, the system stability is verified using the Lyapunov analysis [77]. However, it needs heavy computational efforts, its implementation could be complicated in practice, and the load of extra control loops may negatively affect the dynamic performance of the entire system [78].

1.3 Modeling and Stability Analysis of Single-phase Microgrid

Parallel power converters are commonly used in power systems to achieve advantages such as modularity, flexibility, reliability, and power rating enhancement [47, 79–84]. Parallel system configurations are implemented in different applications like PV and WT systems, standalone and grid-connected microgrids, and hybrid microgrids as interlinking converters [81, 83, 85, 86].

As mentioned earlier, depending on the role of each converter in a microgrid and microgrid configuration, proper control strategy should be selected. A general categorization of control strategies for converters can be grid-following (GFL) and grid-forming (GFM) strategies. The GFL strategy is used in grid-connected microgrids. In this strategy, the frequency and voltage are forced by the grid at the point of common coupling (PCC). Therefore, converters inject/consume active and/or reactive powers with respect to their control objectives [48, 87]. On the other hand, the GFM strategy is commonly utilized in standalone microgrids. In this strategy, a converter is responsible to regulate the frequency and voltage of the microgrid at the PCC. Also, the converter participates in the load sharing to supply microgrid loads [48, 87].

Due to the aforementioned features of the GFM converters, they are increasingly used in single-phase microgrids such as shown in Fig. 1.4, mostly for remote areas where there is no access to the main grid or for sensitive applications such as

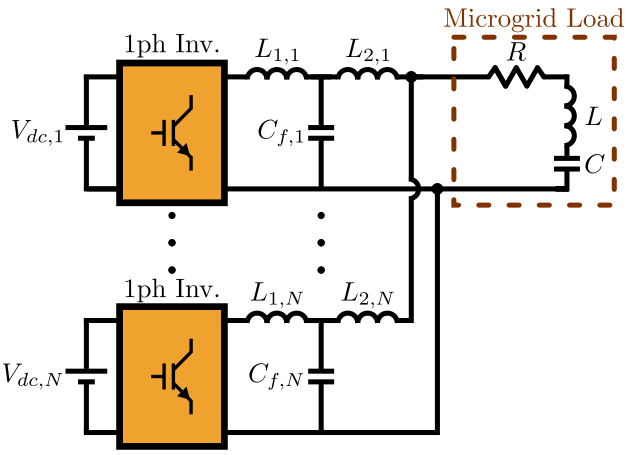

Fig. 1.4: Single-phase microgrid with parallel inverters.

hospitals [47, 88, 89]. As their level of penetration increases, single-phase GFM converters can significantly affect the voltage, frequency, and stability of single-phase microgrid.

1.3.1 Implementation of Single-phase Control Systems

A single-phase control system can be implemented in the stationary frame or the rotating frame. In both frames, output-feedback, such as the proportional-resonant (PR) in the stationary frame or the PI in the rotating frame, state-feedback, or more complicated compensators can be used. However, an orthogonal signal generation (OSG) unit to enable Park's ($\alpha\beta \rightarrow dq$) transformation [90] is required in rotating frame.

Orthogonal signals are generated by phase-shift methods such as time-domain delay [91], Hilbert transform [92], or second-order generalized integrator (SOGI) [93]. While the steady-state performance of the phase-shift approaches is acceptable, these OSG methods add undesirable dynamics leading to slower and oscillatory responses. Fictive axis emulation (FAE) method [94] generates orthogonal signals by emulating β-axis circuit in the processor. However, its accuracy depends on system parameters, and a parameter mismatch may lead to steady-state errors in the orthogonal signals, which makes the system responses more oscillatory. In

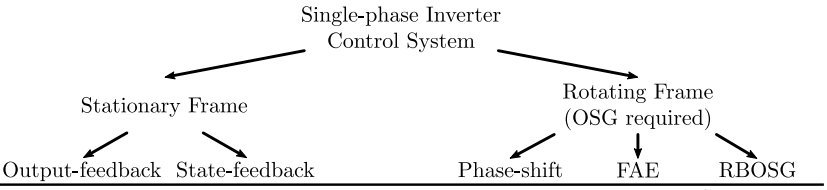

Drawbacks of Added OSG	Not applicable		Slower dynamics and oscillatory responses	Sensitive to parameter variations	Complexity in derivation of state variable orthogonal ref.
Standalone Inverter Stability Analysis (droop controlled)	✗ Nonlinear system, mixed dc and ac state variables, the system is not suitable for linearization and small-signal analysis		✓ Nonlinear system, constant operating point, the system is suitable for linearization and small-signal analysis		

Fig. 1.5: Comparison of single-phase control systems in stationary and rotating frames.

reference-based OSG (RBOSG) method [95], the orthogonal signal is generated based on the reference values in the rotating frame. In this method, the reference value of $\beta - axis$ is considered as the orthogonal signal of the measured signal, $\alpha - axis$ component, and used in Park's transformation. However, this method is useful only when the reference values are available in the rotating frame.

As the literature indicates, the stability analysis and design of the control system in the rotating frame are simple, but the OSG units compromise the performance and limit the stability margins. Contrarily, the implementation of the control system in the stationary frame provides more robust performances with improved stability margins, but the stability analysis and design become challenging due to mixed ac/dc variables and nonlinear dynamics [96]. Fig. 1.5 briefly compares advantages and disadvantages of the control systems implemented in the stationary frame and rotating frame.

1.3.2 Existing Stability Analysis Approaches of Single-phase Systems

Fig. 1.4 illustrates a single-phase standalone microgrid consisting of parallel droop-controlled inverters and loads. To achieve a stable operation of parallel inverters in a microgrid, not only must each inverter be stable, but also the stability of the entire system should be investigated because interactions among converters

may lead to the system instability. The stability analysis of the aforementioned system is challenging as the entire system that includes cascade control loops (droop, voltage, and current control loops), filters, and loads becomes nonlinear. To study the stability of the system shown in Fig. 1.4, some approaches are proposed in the literature which are explained in the following.

In [97], the stability analysis is addressed for two uninterruptible power supply (UPS) systems. However, the nonlinearity caused by the droop terms is not considered. In [64], load sharing strategies are proposed for droop-controlled inverters in microgrids. However, the interaction among inverters is not discussed. A small-signal stability analysis is carried out by using the common rotating frame analysis for three-phase systems in [6, 98]. However, this analysis and similar three-phase analysis approaches are not applicable to single-phase systems controlled in the stationary frame due to the lack of orthogonal ac variables to transform the system to the rotating frame. In [99], the Nyquist stability criterion is used. However, it cannot predict how a parameter variation may change the system pole locations.

1.3.3 Existing Modeling Approaches of Single-phase Systems

Conventionally, the control implementation and modeling are both done either in the stationary or in the rotating frame. Fig. 1.6 illustrates these two different perspectives in the implementation and mathematical modeling of a single-phase droop-controlled standalone inverter. Fig. 1.6(a) shows the approach in the rotating frame. From the control system perspective, it requires the implementation of OSGs to generate the quadrature signals and to convert the system to the rotating frame. From the modeling point of view, OSG dynamics are not (and probably cannot be) modeled because OSG dynamics is arisen from its state; to convert the OSG state to the rotating frame, another OSG is needed to generate the required quadrature state for the Park's transformation. This makes the system modeling inaccurate for the control system design. Also, the system stability study based on analyzing

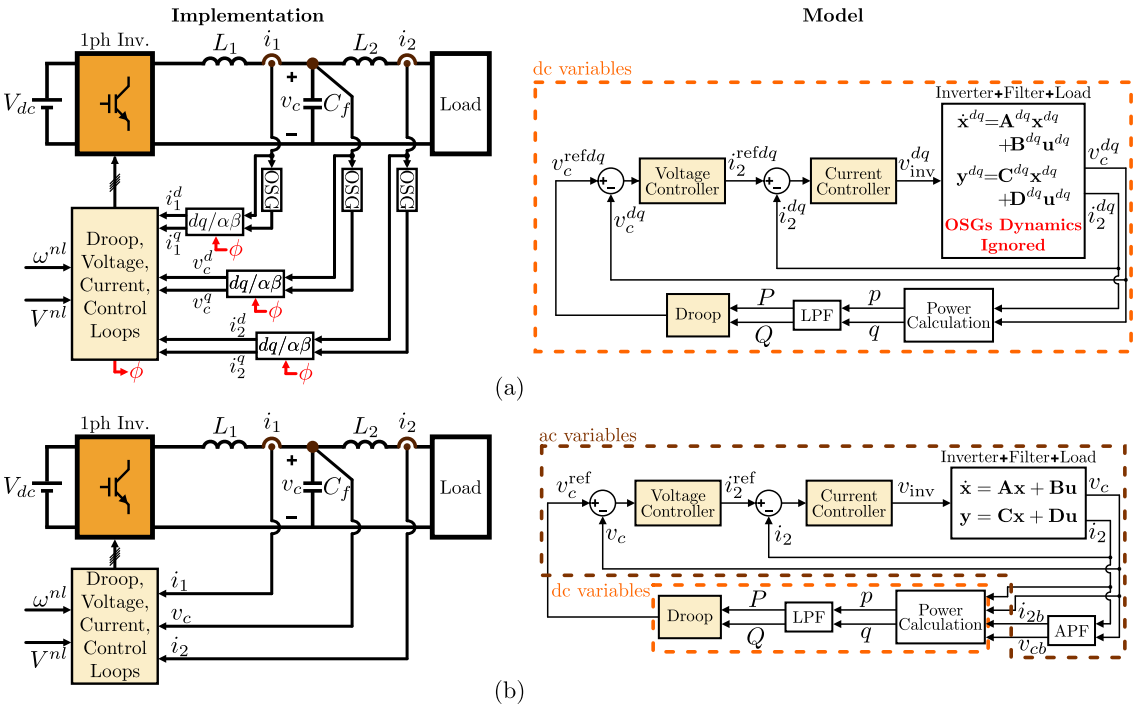

Fig. 1.6: Control system implementation and existing modeling approaches for a single-phase droop-controlled inverter: (a) controlled and modeled in the rotating frame, and (b) controlled and modeled in the stationary frame.

the eigenvalues of the mathematical model, shown in Fig. 1.6(a), would not be fully reliable, especially, when the system operates close to its stability margins.

The alternative approach is to implement the control system and model it in the stationary frame as depicted in Fig. 1.6(b). In this approach, no OSGs are used in the control system. However, as shown in this figure, the system contains mixed dc and ac state variables. Moreover, due to the power calculation block and droop characteristics, the system is nonlinear. For the small-signal stability analysis, the system should be linearized around an operating point. However, due to the sinusoidal nature of the ac variables, no operating point can be found for the system. Therefore, the mathematical model, shown in Fig. 1.6(b), is not directly usable for the stability analysis using common eigenvalue analysis.

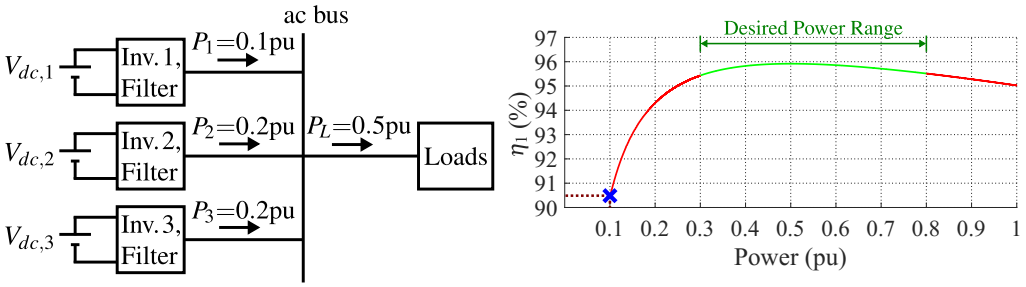

Fig. 1.7: Power sharing among three parallel inverter using the conventional droop strategy $P_L = \sum_{k=1}^{3} P_k = 0.5$ and the efficiency curve of inverters.

1.4 Parallel-inverter System Efficiency Improvement

As stated before, parallel GFM inverters are widely utilized in power systems. In some applications, the system may operate at light loads for a period of time such as portable battery-powered energy storage systems, PV systems, and remote microgrids where the load profile is below half of the peak value for the majority of the day [100]. In such light-load applications, the efficiency of the inverter is normally low. Hence, improving the system efficiency of parallel inverters in the low-power operating ranges plays a key role in energy savings of such systems.

The droop control method has been conventionally used to share the required power by the loads among parallel inverters proportional to their power capacity. However, this method does not guarantee efficient power sharing, especially at light-load conditions, where the inverters only process a portion of the low output power forcing them to operate at their low efficiency curve region as shown in Fig. 1.7. Hence, the power sharing among inverters needs to be revised to reduce the losses and increase the system efficiency. Control strategies proposed in the literature to improve the inverter system efficiency can be classified into three categories.

The first category includes optimization algorithms used to minimize the losses and enhance the system efficiency. An adaptive control method based on an exhaustive optimization algorithm is presented in [101] to enhance the reliability and

efficiency of parallel wind power converters by optimizing the power sharing. A hybrid control structure to optimize the system efficiency is proposed in [100], where an average power control method is utilized to determine the power-sharing ratio that enhances the efficiency of blocks of interconnected inverters. The loss minimization problem of parallel inverters is solved in [102] by particle swarm optimization algorithm to achieve optimal power sharing among the units. A similar method is proposed in [103], where the current reference of each inverter is determined by particle swarm optimization with the purpose of optimizing the overall system efficiency.

The second category involves efficiency-improvement methods through hierarchical control strategies. A forward-backward sweep method based on the tertiary level of hierarchical control strategy is developed in [104] to determine the optimal power sharing of parallel inverters. Such tertiary-level control can also stabilize the voltage using the hierarchical control framework[105]. The efficiency and reliability[106] improvements can also be achieved by the secondary control level of hierarchical control schemes, where finite state machine model is utilized in [107] to find the optimal number of inverters to share the load power. Although the mentioned methods in the first and second categories are beneficial for the efficiency optimization, their main drawback is the need for communication links among the units, which could lead to expensive infrastructure especially in remote areas, system instability in case of communication disconnection, and reliability mitigation due to time delays and data dropouts that may cause oscillations and even collapse of the system [108–111].

The third category is based on the droop control strategy, which has not been fully investigated in the literature. Optimal conditions to obtain the maximum system efficiency are derived using Lagrange multiplier method in [112], where the droop parameters of the inverters are retuned to adjust the power sharing among the inverters and increase the overall efficiency. A similar adaptive droop strategy is proposed in [113], where the authors improve the method of [112] by incorporating

both active and reactive powers and achieving optimal reactive power sharing, using a dynamic impedance compensation loop. Despite the benefits of the aforementioned methods, the methods have several drawbacks, such as the optimal system efficiency dependency on the system component variations, efficiency improvement for nonidentical converter cases only, and the lack of a clear strategy to optimally turn on and off the inverters at light loads.

1.5 Thesis Objectives

The main objective of this thesis is to propose robust, optimal, and systematic control design methods and structures for power converters in microgrids. Moreover, a systematic approach is proposed to model a single-phase microgrid including several GFM inverters and to analyze its stability. Eventually, a communicationless unequal power-sharing strategy is proposed to improve the overall efficiency of a microgrid containing multiple GFM inverters. For each proposed method, an appropriate model, systematic approach, and detailed stability analysis are developed. Briefly, the thesis's objectives are:

1. To design a robust dual-loop control system for a single-phase inverter in weak grid operation while addressing grid impedance variations, delay compensation, grid harmonic rejection, and power decoupling.

2. To propose and develop a systematic and optimal approach to design a cascade control system for power converters.

3. To derive an accurate large- and small-signal models for a single-phase microgrid including parallel GFM inverters with nonlinear control system in order to study the stability of the microgrid.

4. To propose and develop a communicationless modified droop strategy, based on the unequal power sharing, to enhance the overall efficiency of a parallel inverter system.

5. To verify the system design and analysis using simulation and experimental results.

1.6 Thesis Outlines

In Chapter 2, the design procedure of a robust control system for a single-phase grid-connected inverter under a weak grid operation is proposed. For the current control loop, the μ-synthesis method is used to design the current controller, which only relies on the output current feedback. Also, the μ-synthesis current controller compensates delays arising due to PWM, etc. Furthermore, the current controller rejects the impacts of the grid voltage harmonics on the injected current to the grid to meet the IEEE 1547 standard. In addition, the active damping is achieved without using partial or full state-feedback systems. Then, an H_∞ dc link controller is proposed for the external loop, which guarantees the system robustness against input power variations. Also, the power decoupling between ac and dc systems is achieved by the control system without using any auxiliary circuits.

In Chapter 3, an optimal and systematic design method for cascade control systems is proposed based on the linear quadratic tracker (LQT) method. The proposed method considers interactions among cascade loops using intra-loop state feedback, which results in relaxing the limiting condition that the inner loops must be much faster than the outer loops in conventional approaches. After that, the proposed approach is used to design a cascade control system, containing current and voltage control loops, for a single-phase standalone inverter.

In Chapter 4, an approach is proposed to systematically model and perform stability analysis for a single-phase microgrid consisting of multiple GFM inverters with stationary-frame controllers. The approach is based on defining a complementary system that allows transformation to the rotating frame without using OSG units, introducing time-varying (double-frequency) terms, and altering the stability properties. The proposed model considers the control system nonlinearities and is proper for the small-signal stability analysis because it contains only dc variables.

Also, the stability analysis clearly represents how the closed-loop poles of the entire system are affected due to the variations of each system parameter.

In Chapter 5, a communicationless modified droop strategy is proposed to improve the overall efficiency of a single-phase standalone microgrid with parallel inverters. The main idea is to revise the power sharing among parallel inverters such that the output power of each inverter is maintained within a proper range with respect to the inverter efficiency curve. As a result, according to the load demand, an optimal number of inverters supply the load, and the unnecessary inverters do not share any power. It is observed that the proposed power-sharing strategy can enhance the overall system efficiency as much as 14% at light loads compared with the conventional droop strategy.

Finally, Chapter 6 summarizes the contributions of the thesis and represents the future work.

Chapter 2

Investigation of Robust Controllers for Inverter Applications

In systems with several uncertainties, robust controllers seem a viable option as disturbances, uncertainties, and stability of the system are considered in the design procedure. As the ultimate objective of this research is the design and stability analysis of microgrid systems that include single-phase inverters, this chapter investigates the robust control approach for this application.

In this chapter, first, robust current and dc link voltage controllers are proposed based on μ-synthesis and H_∞ methods, respectively, for a single-phase PV inverter with an LCL filter under weak grid operation as shown in Fig. 2.1. The μ-synthesis current controller guarantees system robustness against weak grid uncertainties such as grid impedance variations and voltage harmonics. Moreover, the controller compensates the system delays arising from calculation and PWM as well as delay uncertainties. The current controller only uses the grid current feedback which eliminates the requirement for additional loops or state measurements utilized in partial or full state-feedback systems.

Additionally, the H_∞ dc link voltage controller minimizes the bus voltage fluctuations caused by variations of PV system power generation. The controller ensures system robustness against such power variations, which conventional controllers fail to perform. In the proposed system, power decoupling is achieved by the control system without any auxiliary circuit. The stability and robust performance of the phase-locked loop (PLL) in a weak grid with major impedance changes are also verified.

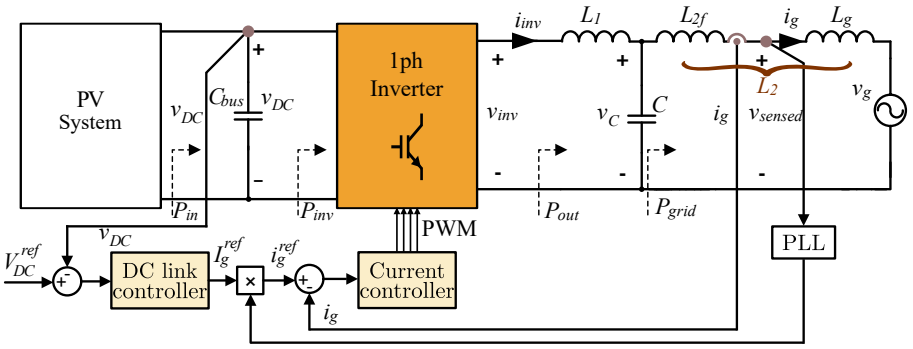

Fig. 2.1: Conventional double-stage inverter structure with control loops for PV application.

Finally, the feasibility of using robust control systems for single-phase standalone inverters operating in the microgrid is briefly reviewed and compared with grid-connected inverters.

2.1 Current Controller Design

In this section, a robust current controller is proposed to address the following control objectives:

- tracking the reference signal,
- ensuring system robustness against weak grid uncertainties such as grid impedance variations and voltage harmonics, and delay uncertainties,
- suppressing undesirable resonant oscillations.

According to Fig. 2.1, the following equations represent the current control loop dynamics

$$\begin{aligned} i_{inv} &= G_{i_{inv}}(v_{inv} - v_c),\ G_{i_{inv}} \triangleq \frac{1}{L_1 s}, \\ v_c &= G_{v_c}(i_{inv} - i_g),\ G_{v_c} \triangleq \frac{1}{Cs}, \\ i_g &= G_{i_g}(v_c - v_g),\ G_{i_g} \triangleq \frac{1}{L_2 s + R_2}, \end{aligned} \tag{2.1}$$

where L_2 and R_2 represent the lumped values of filter and grid inductance and resistance, respectively, i.e. $L_2 = L_{2f} + L_g$ and $R_2 = R_{2f} + R_g$.

The objective is to design a robust controller with respect to the grid impedance variations and delay uncertainties by applying the μ-synthesis method. It is worth mentioning that, in this section, the current controller will be designed for every part of Fig. 2.2 except for the feedforward (FF) and PLL loops, which are demonstrated in "red" color. The robustness analysis of the FF and PLL loops will be performed later in Section 2.3.3.

2.1.1 Current Loop Uncertainty Models and Performance Constraints

2.1.1.1 Current Loop Parameter Uncertainties

The grid-side inductance and resistance are the uncertain parameters of the system shown in Fig. 2.1. Therefore, they can be written as follows

$$\begin{aligned} L_2 &= \bar{L}_2(1+\delta_{L_2}\mathscr{E}_{L_2}), \\ R_2 &= \bar{R}_2(1+\delta_{R_2}\mathscr{E}_{R_2}), \end{aligned} \tag{2.2}$$

where "$^-$", "δ", and "$\mathscr{E}$" indicate a parameter nominal value, the "normalized uncertainty variable" such that $|\delta| \leq 1$, and the "maximum percentage deviation", respectively.

If a transfer function matrix G is defined as bellow

$$G = \begin{bmatrix} G_{11} & G_{12} \\ G_{21} & G_{22} \end{bmatrix}, \tag{2.3}$$

the upper linear fractional transformation (LFT) operator for the transfer function G and variable δ is defined as

$$\mathscr{F}_U(G,\delta) = G_{22} + G_{21}\delta(I - G_{11}\delta)^{-1}G_{12}, \tag{2.4}$$

where I is the identity matrix. Substituting the values provided for L_2 and R_2 from

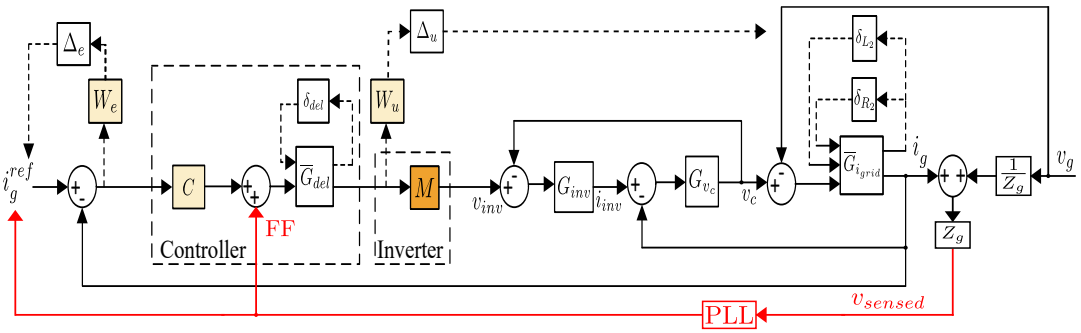

Fig. 2.2: Extended model of the system including system parameters uncertainties (2.5) and delay uncertainties (2.10).

(2.2) into (2.1) and using the LFT definition (2.4), the following equations can be derived (detailed derivation is provided in Appendix A)

$$
\begin{aligned}
G_{i_g}(s) &= \mathscr{F}_U\left(\bar{G}_{i_g}(s), \begin{bmatrix} \delta_{L_2} \\ \delta_{R_2} \end{bmatrix}\right), \\
\bar{G}_{i_g}(s) &\triangleq \frac{1}{\bar{L}_2 s + \bar{R}_2} \begin{bmatrix} -\bar{L}_2\mathscr{E}_{L_2}s & -\bar{R}_2\mathscr{E}_{R_2} & 1 \\ -\bar{L}_2\mathscr{E}_{L_2}s & -\bar{R}_2\mathscr{E}_{R_2} & 1 \end{bmatrix}.
\end{aligned}
\tag{2.5}
$$

Using equations (2.1), (2.2), and (2.5), the extended system control diagram which contains the system parameters uncertainties is derived as depicted in Fig. 2.2. In this figure, the block M is used to model the inverter gain, and the block Z_g denotes the grid impedance where $Z_g = R_g + sL_g$.

Moreover, in Fig. 2.1, it is depicted where the voltage is measured and sensed v_{sensed} for the FF as well as the PLL loops. Thus, in case of a stiff grid connection, i.e. $L_g = 0\ mH$ and $R_g = 0\ \Omega$, the input voltage of PLL and FF signal is equal to the grid voltage $v_{sensed} = v_g$. Otherwise, for a weak grid connection, the sensed voltage is different from the grid voltage, i.e. $v_{sensed} = v_g + R_g i_g + L_g \frac{di_g}{dt}$, which is used instead of the grid voltage by the FF and PLL loops [114]. The case of a weak grid connection will be studied in Section 2.3.3.

2.1.1.2 Time Delay Uncertainties

In practical applications, there are some delays due to the micro-processor calculation, measurement, and PWM. Also, there are some delay uncertainties caused by the aliasing and quantization effects [24]. If the effects of these delays are not compensated by the controller, they may result in undesirable controller performance and system instability. The magnitude of these delays depends on the sampling frequency, carrier waveform such as sawtooth waveform or triangular waveform, and updating rate of the PWM mode, i.e. single updating or multiple updating. Fig. 2.3 shows the formation of such delays [24]. In this figure, the signals $m_s(t)$, $c(t)$, and $V_{MO}(t)$ are the modulating signal, the carrier waveform, and the PWM waveform, respectively. As indicated in this figure, in the worst case scenario, the calculation delay is equal to the sampling time T_s [24]. Also, the amount of the PWM delay is equal to a half of the sampling time. Thus, the total delay is equal to $T_d = 1.5T_s$ [24]. The controller should not only compensate the effect of this delay, but also should guarantee the system robustness with respect to delay uncertainties caused by aliasing and quantization effects. For this purpose, the system and delay uncertainties should be modeled and considered in the controller design process.

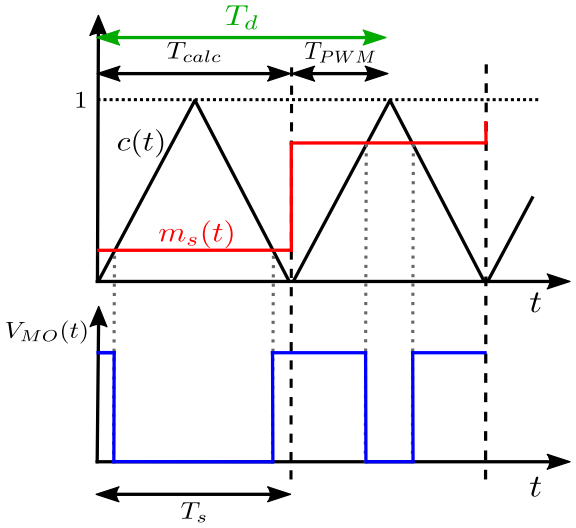

Fig. 2.3: Single update mode PWM, calculation delay, and PWM delay in the presence of triangular carrier.

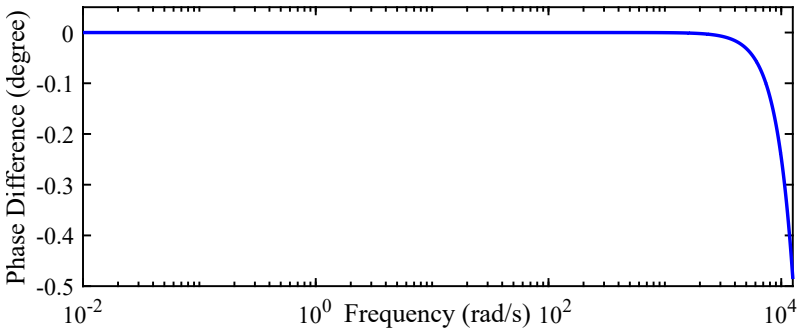

Fig. 2.4: Phase difference between the original delay function $e^{-T_d s}$ and the approximated function.

A time delay of T_d in the time domain can be modeled by the transfer function $e^{-T_d s}$ in the frequency domain, where $s = j\omega$. Since this transfer function is not rational, it cannot be used for designing the controller. Thus, $e^{-T_d s}$ is approximated by a rational transfer function as follows

$$G_{del}(s) = \frac{\frac{-T_d}{2}s + 1}{\frac{T_d}{2}s + 1}. \tag{2.6}$$

As shown in Fig. 2.4, for the desired frequency range, which is about 10% of the switching frequency, the phase difference between the original delay function $e^{-T_d s}$ and the approximated function (2.6) is less than 0.5°. Thus, the approximated transfer function (2.6) can be used to design the current controller.

As discussed, the time delay T_d is uncertain, so it can be rewritten similar to other uncertain parameters in (2.2)

$$T_d = \bar{T}_d(1 + \delta_{T_d}\mathscr{E}_{T_d}). \tag{2.7}$$

The nominal value of $G_{del}(s)$ is defined at $T_d = \bar{T}_d$ as follows

$$G_{del,n}(s) = \frac{\frac{-\bar{T}_d}{2}s + 1}{\frac{\bar{T}_d}{2}s + 1}. \tag{2.8}$$

If the weight transfer function $W_{del}(s)$ is defined as the upper envelope on the amplitudes of all the transfer functions $\frac{G_{del}(s) - G_{del,n}(s)}{G_{del,n}(s)}$ in the frequency domain, the

transfer function $G_{del}(s)$ can be rewritten as

$$|G_{del}(s)| = |G_{del,n}(s)|(1 + \delta_{del}|W_{del}(s)|). \tag{2.9}$$

Using the upper LFT definition provided by (2.4), the transfer function $G_{del}(s)$ can be reformulated as

$$\begin{aligned} G_{del}(s) &= \mathscr{F}_U\left(\bar{G}_{del}(s), \delta_{del}\right), \\ \bar{G}_{del}(s) &\triangleq \begin{bmatrix} 0 & G_{del,n}W_{del} \\ 1 & G_{del,n} \end{bmatrix}. \end{aligned} \tag{2.10}$$

Now, the delay uncertainties are modeled by (2.10) as shown in the extended system control diagram Fig. 2.2.

2.1.1.3 Performance Constraints

The μ-synthesis method ensures the system performance if appropriate performance constraints are defined [115]. For this purpose, as shown in Fig. 2.2, $G_e(s)$ and $G_u(s)$ are defined as the transfer functions from i_g^{ref} to the current error e ($e \triangleq i_g^{ref} - i_g$), and from the disturbance v_g to the input u, respectively. Based on these definitions, the performance constraints are presented as bellow

$$\begin{aligned} G_e(s)W_e(s) &< \frac{1}{\Delta_e}, \\ G_u(s)W_u(s) &< \frac{1}{\Delta_u}, \end{aligned} \tag{2.11}$$

where $W_e(s)$ and $W_u(s)$ are the weight transfer functions chosen based on the control objective. Furthermore, the parameters Δ_e and Δ_u specify the constraints tightness. The two criteria in (2.11) are shown in Fig. 2.2 by using the parameters Δ_e and Δ_u. These weight transfer functions will be designed next.

2.1.2 Weight Function Selection

In order to achieve the control objectives, the weight transfer functions $W_e(s)$ and $W_u(s)$ should be defined properly. In the following, the choice of $W_e(s)$ which amplifies the error between the reference and output signals is discussed.

2.1.2.1 Reference Tracking

$W_e(s)$ should have a pole at $s = 0$ to provide a high gain for low frequencies in addition to preventing steady-state dc error. Moreover, according to the *Internal Model Principle*, $W_e(s)$ must include two poles at $s = \pm j\omega_g$ where $\omega_g = 2\pi 60\ \frac{\text{rad}}{s}$. Furthermore, in order to compensate grid voltage harmonics, the control system bandwidth must be wide enough to comprise the harmonics. Thus, $W_e(s)$ should include two zeros at $s = \pm j\omega_g$ with different damping ratios to limit the effects of the added poles around $s = \pm j\omega_g$ as follows

$$\frac{s^2 + 600s + \omega_g^2}{s^2 + 0.1s + \omega_g^2}. \tag{2.12}$$

The effect of (2.12) is concentrated around ω_g frequency and has a negligible effect on other frequency ranges.

2.1.2.2 Harmonic Compensation

In this section, it is assumed that the grid voltage may contain the $3^{rd}, 5^{th}$, and 7^{th} harmonic voltages. Therefore, the controller should have the ability to reject these harmonics. Thus, similar to the fundamental frequency, $W_e(s)$ should include transfer functions similar to (2.12) to compensate each undesirable harmonic. $W_e(s)$ should contain the following transfer function

$$\prod_{k=1,3,5,7} \frac{s^2 + 600s + (k\omega_g)^2}{s^2 + 0.1s + (k\omega_g)^2}. \tag{2.13}$$

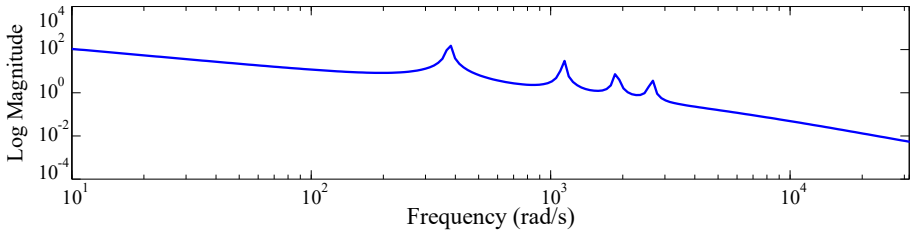

Fig. 2.5: Bode plot of the weight transfer function $W_e(s)$.

Additionally, since the bandwidth of the control system should be much smaller than the switching frequency, a pole at $s = -5000$ is added to (2.13) to limit the bandwidth of the closed-loop system.

2.1.2.3 Active Damping Resonant Oscillations

One major issue which must be considered in choosing $W_e(s)$ is how to damp the resonant oscillations due to the existence of an LCL filter. One of the control objectives is to damp the resonant oscillations without using any additional measurement or inner loop. On the one hand, if the closed-loop control system has enough gain at the resonant frequency $\omega_r = 1/\sqrt{(L_1||L_2)C}$, the controller can actively damp the resonant oscillations without using any additional measurements or passive elements. On the other hand, since L_2 is an uncertain element and subject to variations, ω_r may vary in a frequency range. Hence, the closed-loop control system should have enough gain in this frequency range to damp resonant oscillations. Finally, to satisfy all of the aforementioned considerations, $W_e(s)$ is selected as follows

$$W_e(s) = \frac{592}{s(0.0002s+1)} \prod_{k=1,3,5,7} \frac{s^2 + 600s + (k\omega_g)^2}{s^2 + 0.1s + (k\omega_g)^2}. \tag{2.14}$$

The Bode plot of $W_e(s)$ is indicated in Fig. 2.5.

The function W_u is the weight of the controller, and its value is set to 10^{-5}. It is worth mentioning that the weight selections are accomplished after a few iterations of a trial-and-error process, which is a standard common practice in robust control design techniques.

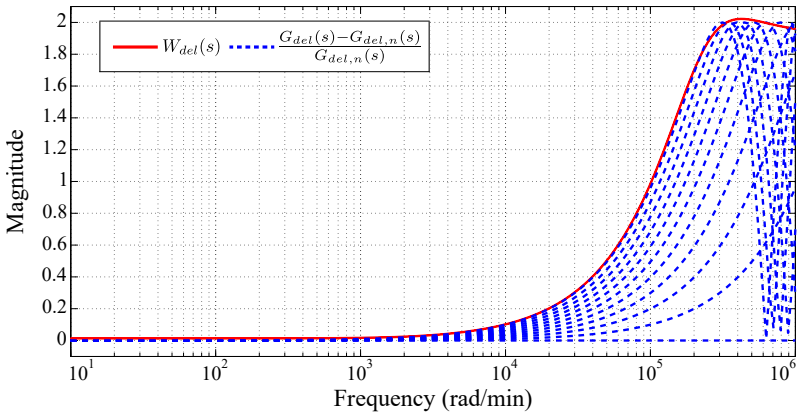

Fig. 2.6: Transfer function $W_{del}(s)$ of equation (2.15) in bold line, and the transfer functions $\frac{G_{del}(s)-G_{del,n}(s)}{G_{del,n}(s)}$ in dashed lines.

2.1.2.4 Time Delay

To model delay uncertainties, the weight transfer function $W_{del}(s)$ is defined as the upper envelope on the amplitudes of all the transfer functions $\frac{G_{del}(s)-G_{del,n}(s)}{G_{del,n}(s)}$, in the frequency domain. For the case of $T_d = 1.5T_s = 37.5\mu s$ [24] and $\mathscr{E}_T = 40\%$, as shown in Fig. 2.6, the weight transfer function $W_{del}(s)$ is attained by using the `fitmag` command in Matlab as below

$$W_{del}(s) = K\frac{b_2 s^2 + b_1 s + b_0}{a_2 s^2 + a_1 s + a_0}, \tag{2.15}$$

where $K = 0.01$, $b_2 = 1.967 \times 10^{-8}$, $b_1 = 4.138 \times 10^{-3}$, $b_0 = 7.079$, $a_2 = 10^{-10}$, $a_1 = 2.755 \times 10^{-5}$, and $a_0 = 2.429$.

2.1.3 Robust Current Controller Design

In order to design a robust controller based on the μ-synthesis method for the system, the extended model of the system in Fig. 2.2 is converted into the $\Delta/G/C$ structure. The vector Δ is defined as the normalized uncertainty matrix which contains all the system uncertainties and performance constraints in (2.2), (2.5),

(2.7), (2.9), (2.10), and (2.11) as

$$\Delta = \text{diag}([\delta_{L_2} \quad \delta_{R_2}]^T, \delta_{del}, \Delta_e, \Delta_u), \tag{2.16}$$

where C is defined as the system controller, and G is defined to include the dynamics of all transfer functions in Fig. 2.2.

To achieve a robust controller, the controller $C(s)$ should be designed such that it can satisfy the following μ-synthesis condition [115]

$$\mu_\Delta(\mathscr{F}(G(s), C(s))) < 1. \tag{2.17}$$

To design the controller in μ-synthesis framework, the extended control system depicted in Fig. 2.2 is first formulated. Then, the robust controller is designed by using the `dkit` command in Matlab.

2.2 DC Link Voltage Controller Design

In this section, a robust dc link controller is proposed to address the following control objectives:

- tracking the dc link reference,
- rejecting harmonics from the reference of the gird current,
- ensuring bus voltage robustness against system disturbances.

As shown in Fig. 2.1, the dc link voltage controller determines the amplitude of the reference current for the current controller. In the following, the process of designing a robust dc link voltage controller based on H_∞ is presented.

2.2.1 Dynamics of the Voltage Control Loop

According to Fig. 2.1, assuming that the input power is denoted by P_{in} and the power injected into the grid is denoted by P_{grid}, and if any losses are ignored,

the power balance equation can be written as

$$P_{in} = P_{dc} + P_{LCL} + P_{grid}, \tag{2.18}$$

where P_{dc} and P_{LCL} represent the instantaneous power of dc link and LCL filter, respectively. Also, the instantaneous power of the dc link is equal to $P_{dc} = \frac{1}{2}C_{bus}\frac{d(v_{dc}^2)}{dt}$. The control loop is closed on v_{dc} and the system is linearized using the following approximation for the capacitor energy E_{dc} [33]

$$\begin{aligned} E_{dc} &= \frac{1}{2}C_{bus}\left(V_{dc}^{ref} + v_{dc} - V_{dc}^{ref}\right)^2, \\ E_{dc} &\simeq -\frac{1}{2}C_{bus}(V_{dc}^{ref})^2 + C_{bus}V_{dc}^{ref}v_{dc}, \end{aligned} \tag{2.19}$$

where V_{dc}^{ref} denotes the reference value for the dc link voltage. According to equation (2.19), v_{dc} is linearized as $v_{dc} \simeq \frac{E_{dc}}{C_{bus}V_{dc}^{ref}} + \frac{1}{2}V_{dc}^{ref}$. Therefore, Fig. 2.7 depicts the detailed model of the dc link voltage control loop comprising the linearized model, where CC refers to the inner current control loop.

2.2.2 System Disturbances

As shown in Fig. 2.7, the extracted power P_{in} from the first stage is considered as a disturbance signal for the dc link controller because its value always changes, and it depends on different parameters such as cell temperature and irradiation level. The P_{in} variations cause dc link voltage fluctuations. Thus, the dc link controller should appropriately reject P_{in} disturbances. Furthermore, the double-frequency ripples are generated due to the single-phase operation of inverter. These ripples are injected into the dc link control loop where the output signal of CC block is multiplied to v_g signal shown in Fig. 2.7. Therefore, the instantaneous power injected to the grid P_{grid} contains a dc component and a double-frequency component as represented in the following

$$P_{grid} = v_g i_g = V_g I_g cos^2(\omega_g t) = \frac{V_g I_g}{2} + \frac{V_g I_g}{2} cos(2\omega_g t). \tag{2.20}$$

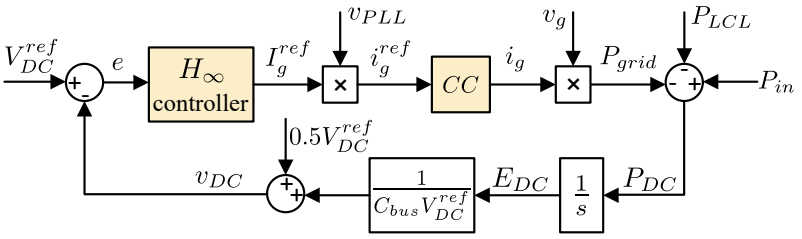

Fig. 2.7: DC link voltage control loop.

Moreover, the LCL filter consumes instantaneous power, which introduces another source of nonlinearity to the loop. Using equation (2.1) and ignoring the grid-side resistance R_2, P_{LCL} is calculated as follows

$$P_{LCL} = \frac{1}{2}L_1\frac{d(i_{inv}^2)}{dt} + \frac{1}{2}C\frac{d(v_C^2)}{dt} + \frac{1}{2}L_2\frac{d(i_g^2)}{dt} \tag{2.21}$$

It is assumed that the CC block is fast enough to make the grid current in phase with the grid voltage. In this case, the transients of CC block are ignored as compared with the dc link control loop, and the grid voltage and current are considered as $v_g = V_g cos(\omega_g t)$ and $i_g = I_g cos(\omega_g t)$. Thus, using equations (2.1) and (2.21), P_{LCL} at steady-state condition is reformulated as follows

$$P_{LCL} = \frac{1}{2}L_1\omega_g I_{inv}^2 sin(2\omega_g t + 2\phi_{i_{inv}}) + \frac{1}{2}C\omega_g V_C^2 sin(2\omega_g t + 2\phi_{v_C}) + \frac{1}{2}L_2\omega_g I_g^2 sin(2\omega_g t), \tag{2.22}$$

where I_{inv}, ϕ_{inv}, V_C, and ϕ_{v_C} are defined below

$$\begin{aligned} I_{inv} = \sqrt{V_g^2\omega_g^2C^2 + I_g^2(1 - L_2\omega_g^2C)^2},\ \phi_{i_{inv}} = \arctan\left(\frac{V_g\omega_g C}{I_g(1 - L_2\omega_g^2 C)}\right), \\ V_C = \sqrt{I_g^2\omega_g^2L_2^2 + V_g^2},\ \phi_{v_C} = \arctan\left(\frac{I_g\omega_g L_2}{V_g}\right). \end{aligned} \tag{2.23}$$

As equations (2.20), (2.22), and (2.23) show, the double-frequency ripples are injected into the dc control loop due to the single-phase operation of inverter and instantaneous power consumption of the LCL filter. Furthermore, all of the double-frequency ripples are functions of the magnitude of the grid current determined by the dc link controller. According to equations (2.20), (2.22), and (2.23), the system

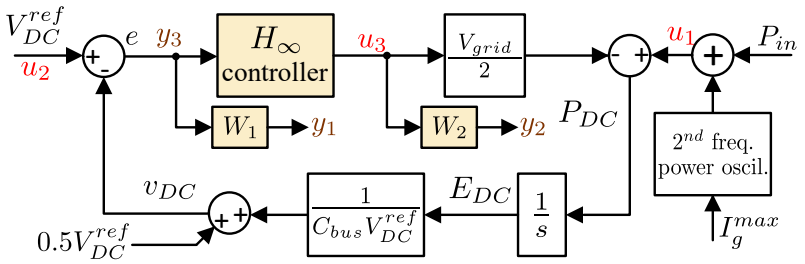

Fig. 2.8: Augmented model of the dc link voltage control loop.

is nonlinear and time-varying.

To achieve a linear time-invariant (LTI) system, the aforementioned double-frequency ripples are considered as a disturbance to the system. As they are functions of I_g, to consider the worst case scenario, the maximum magnitude of the grid current I_g^{max} is selected to generate the maximum double-frequency ripples as a disturbance. Therefore, Fig. 2.7 is simplified as shown in Fig. 2.8. Now, the system shown in Fig. 2.8 is LTI, and a robust controller based on H_∞ method can be designed for it.

2.2.3 Formulating MIMO System for H_∞ Controller Design

As mentioned earlier, since P_{in} depends on unpredictable parameters such as environmental temperature and irradiation level, the H_∞ method is used to attain a robust controller for the dc link voltage.

To design the H_∞ controller, firstly, a multi-input multi-output (MIMO) system should be defined based on H_∞ performance requirements. Fig. 2.8 demonstrates the augmented model of the dc link control loop where W_1 and W_2 are the output weight transfer functions. Two types of inputs are defined for the system. One input type is the disturbances, denoted by u_1 and u_2, that consist of P_{in}, double-frequency ripples, and V_{ref}^{dc}. The other input type is the signal determined by the H_∞ controller, denoted by u_3.

Similarly, two types of outputs are considered for the system. One output type is denoted by y_1 and y_2, which are the output signals of the transfer functions W_1 and W_2. These weight transfer functions should be selected properly to minimize

y_1 and y_2 in the required frequency ranges and to obviate the effect of the double-frequency ripples on the magnitude of the grid current. The other output type is the error signal, denoted by y_3.

After defining the inputs and outputs as shown in Fig. 2.8, the MIMO system can be written as follows

$$\begin{bmatrix} y_1 \\ y_2 \\ y_3 \end{bmatrix} = G_{dc}(s) \begin{bmatrix} u_1 \\ u_2 \\ u_3 \end{bmatrix}, \; G_{dc}(s) = \begin{bmatrix} G_{11} & G_{12} & G_{13} \\ G_{21} & G_{22} & G_{23} \\ G_{31} & G_{32} & G_{33} \end{bmatrix}, \tag{2.24}$$

where the transfer function $G_{dc}(s)$ is defined based on Fig. 2.8 as follows

$$G_{dc}(s) = \begin{bmatrix} \dfrac{-W_1(s)}{C_{bus}V_{ref}^{dc}s} & 0.5W_1(s) & \dfrac{V_g W_1(s)}{2C_{bus}V_{ref}^{dc}s} \\ 0 & 0 & W_2(s) \\ \dfrac{-1}{C_{bus}V_{ref}^{dc}s} & 0.5 & \dfrac{V_g}{2C_{bus}V_{ref}^{dc}s} \end{bmatrix} \tag{2.25}$$

Thus, the system transfer function is determined based on the defined inputs and outputs.

2.2.4 Robust Controller Design Based on H_∞ Method

According to Fig. 2.8, the weight functions W_1 and W_2 are applied to the error signal y_3 and the output signal of the H_∞ controller u_3, respectively. To properly design the H_∞ controller, W_1 should be small within the desired control bandwidth ($500 \; \frac{\text{rad}}{s}$) to achieve an acceptable rejection capability for disturbances, i.e. P_{in} variations. Moreover, W_2 should be small outside the control bandwidth to ensure system robustness and stability margin. However, to mitigate the impact of the double frequency ripples on the controller performance, W_2 should provide a high gain at the double frequency point.

Therefore, by tuning W_1, the following control loop characteristics are addressed: 1) high dc gain to minimize steady-state error, and 2) high control bandwidth to suppress effects of P_{in} variations on v_{dc}. For this purpose, W_1 is selected as $W_1(s) = \frac{k_1 s}{(\frac{s}{\omega_0})^2+2\frac{\xi}{\omega_0}s+1}$. According to this equation, W_1 has a zero at $s = 0$ in order that the H_∞ controller has high gain in low frequencies. Also, by appropriately tuning k_1 and ω_0, the acceptable control bandwidth is achieved. Moreover, ξ denotes the damping ratio. The values of k_1, ω_0, and ξ are set to $k_1 = 550$, $\omega_0 = 0.05\ \frac{rad}{s}$, and $\xi = 0.707$.

The dc link control bandwidth should not contain the second harmonic frequency. On the other hand, the bandwidth should be wide enough to achieve fast dynamic response. Thus, W_2 is tuned in a way that it eliminates the undesirable effects of double-frequency ripples on I_g. Therefore, the W_2 transfer function is selected as $W_2(s) = k_2\frac{(\frac{s}{2\omega_g})^2+\frac{\xi}{\omega_g}s+1}{(\frac{s}{2\omega_g})^2+\frac{\xi}{\omega_g k_3}s+1}$. W_2 has small magnitude in all frequency ranges except at $s = 2\omega_g$ where it has a peak. Thus, the H_∞ controller has a very small gain at this frequency to eliminate the impact of double-frequency oscillations on I_g. This peak is regulated by coefficients k_2 and k_3 whose values are set to $k_2 = 0.01$ and $k_3 = 15000$. It is worth mentioning that the weight designs are accomplished after a few iterations of a trial-and-error process, which is a standard common practice in robust control design techniques.

The H_∞ controller can be designed by using the `hinfsyn` command in Matlab. Also, the following criteria must be satisfied to guarantee the system robustness

$$||\mathscr{F}(G_{dc}(s), C_{dc}(s))||_\infty < 1, \tag{2.26}$$

where $C_{dc}(s)$ denotes the H_∞ dc link voltage controller.

Table 2.1: System nominal parameter and maximum deviation values.

Parameter	Value	Parameter	Value
L_1	$3\,mH$	C_{bus}	$44\,\mu F$
C	$2\,\mu F$	V_{dc}	$200\,V$
L_2	$4\,mH$	V_g	$120\,V$
R_2	$10\,m\Omega$	P_{nom}	$200\,W$
T_d	$37.5\,\mu s$	I_g^{max}	$3\,A$

Parameter	Value
$\mathscr{E}_{L_2}$	70 %
$\mathscr{E}_{R_2}$	70 %
$\mathscr{E}_T$	40 %

2.3 Robustness Analysis and Simulation Results

In this section, the μ-synthesis current controller and the H_∞ dc link voltage controller are designed, analyzed, and simulated for the system whose nominal values and maximum percentage of deviations are represented in Table 2.1. Moreover, the effects of PLL dynamics and FF signal on the system stability and robustness are investigated analytically and by simulation.

2.3.1 Current Controller Robustness Analysis and Simulation

The designed current controller must satisfy the robustness criteria mentioned in equation (2.17). Fig. 2.9 shows that the criteria is satisfied, which implies that the proposed current controller can stabilize the system, ensure the system robustness, and satisfy all of the aforementioned current control objectives in the presence of the system parameter uncertainties δ_{L_2}, δ_{R_2}, and the delay uncertainties δ_{del}. Furthermore, since the order of the designed controller is 42, the `reduce` command is used in Matlab to decrease the order of the controller down to 15. The reduced order controller also satisfies the μ-synthesis condition (2.17) as shown in Fig. 2.9. In the following subsections, the performance of the proposed current controller is evaluated and also compared with the H_∞ method proposed in [14].

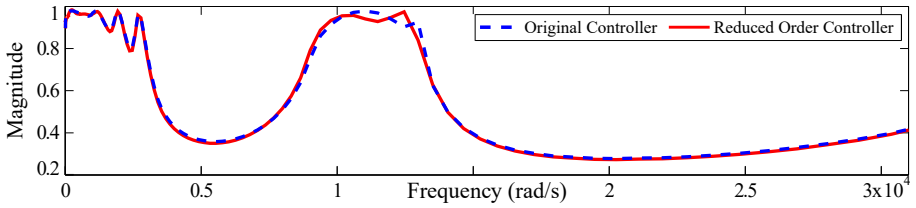

Fig. 2.9: μ-synthesis condition (2.17) for the original controller (42 order) and the reduced-order controller (15 order).

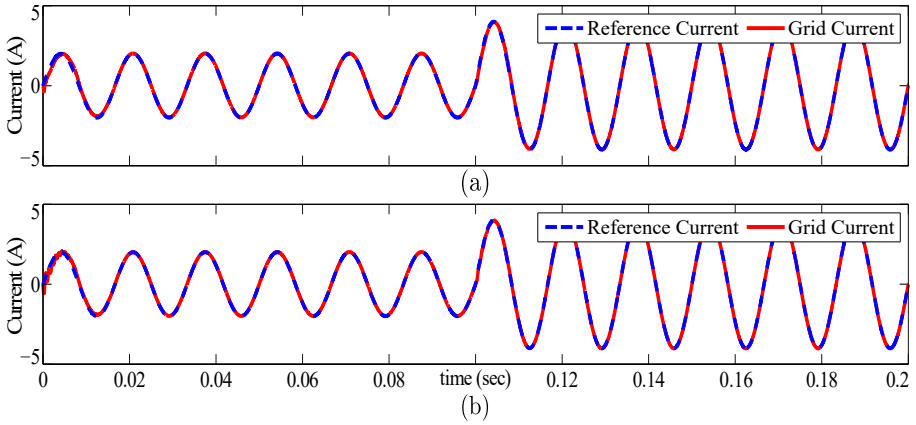

Fig. 2.10: Tracking performance of the proposed controller: (a) nominal system, and (b) deviated system with $\Delta_{L_2} = +70\%$, $\Delta_{R_2} = +70\%$, $\Delta_T = +40\%$.

2.3.1.1 Proposed Robust Current Controller Performance

Fig. 2.10 illustrates the tracking performance of the μ-synthesis controller for the case of nominal system and deviated system including 70% increase in L_2 and R_2, and 40% increase in time delay T_d. Moreover, as shown in this figure, the resonant oscillations are damped.

In addition, the proposed current controller can compensate the grid voltage harmonics to inject a high-power-quality current to the grid. As indicated in Fig. 2.11(b), the system injects a pure sinusoidal current to the grid in the presence of the 3^{rd}, 5^{th}, and 7^{th} grid voltage harmonics depicted in Fig. 2.11 (a).

2.3.1.2 Performance Comparison with H_∞ Method

As an alternative to μ-synthesis, the H_∞ method can be used to design a robust current controller for a grid-connected VSC with an LCL filter, shown in

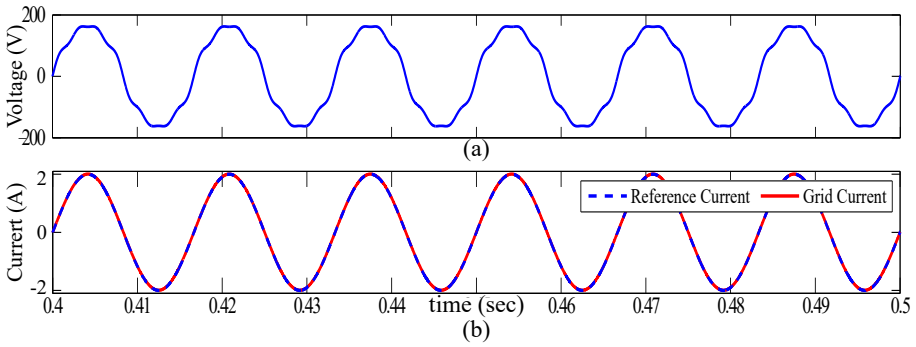

Fig. 2.11: Disturbance rejection capability: (a) grid voltage, and (b) injected current.

Fig. 2.1. In [14], the H_∞ method was used to design a robust controller to ensure the system robustness against the grid-side inductance variations. However, the proposed method has some deficiencies. In the following, to have a fair comparison, the proposed μ-synthesis current controller is designed for the system parameters used in [14].

Firstly, the PWM delay is not considered in designing the H_∞ current controller in [14]. Although the H_∞ controller maintains the closed-loop stability in the presence of the delays, the reference signal is tracked with a considerable steady-state error. Fig. 2.12 depicts the steady-state error of the H_∞ current controller and our proposed μ-synthesis current controller for the system with nominal parameters. Although no parameter uncertainty is present, for the H_∞ controller, the error amplitude is about 15.43% of the reference signal. However, for our proposed μ-synthesis controller, this ratio is about 0.11%. Moreover, both controllers are robust to the L_2 with a value of 30 times bigger than the nominal value. In another scenario, the time delay is increased by 40%. In this case, the ratio is about 23.04% and 0.66% for the H_∞ controller and our proposed μ-synthesis controller, respectively.

Thus, by using the H_∞ controller [14], the injected current into the grid follows the reference signal with a steady-state error. Moreover, the H_∞ controller in [14] does not have the ability to compensate the grid voltage harmonics. In addition to the aforementioned defects, the H_∞ control system in [14] requires an additional

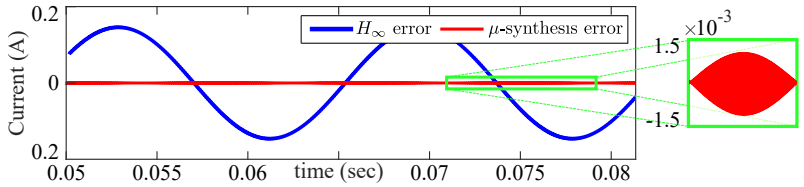

Fig. 2.12: Steady-state error signal of the H_∞ controller and μ-synthesis controller for the system with nominal parameters.

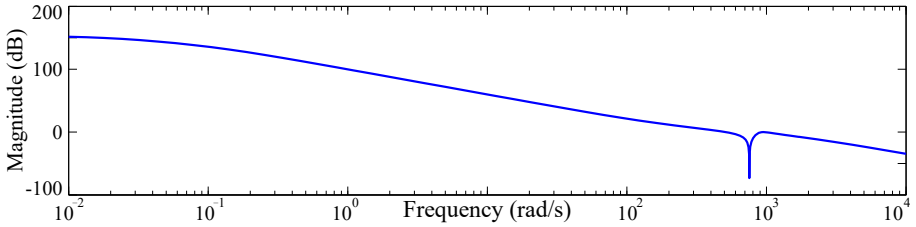

Fig. 2.13: Bode plot of the dc link control loop.

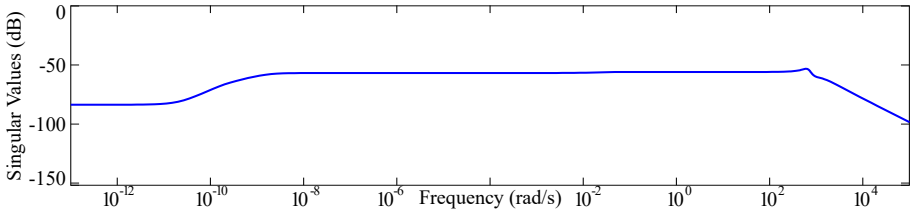

Fig. 2.14: H_∞ robustness criteria in equation (2.26).

current feedback i_{inv}, and hence an additional current sensor, which is not required by the proposed μ-synthesis controller.

2.3.2 DC Link Controller Robustness Analysis and Simulation

The H_∞ dc link controller is designed for the system, whose nominal parameters are represented by Table 2.1. The order of the proposed controller is 5, and Fig. 2.13 demonstrates the magnitude of Bode plot of the open-loop dc link control system. The open-loop control system has high gain in low frequencies and extremely attenuates the second harmonic frequency. Also, the proposed dc link controller satisfies the robustness criteria mentioned in equation (2.26) as shown in Fig. 2.14.

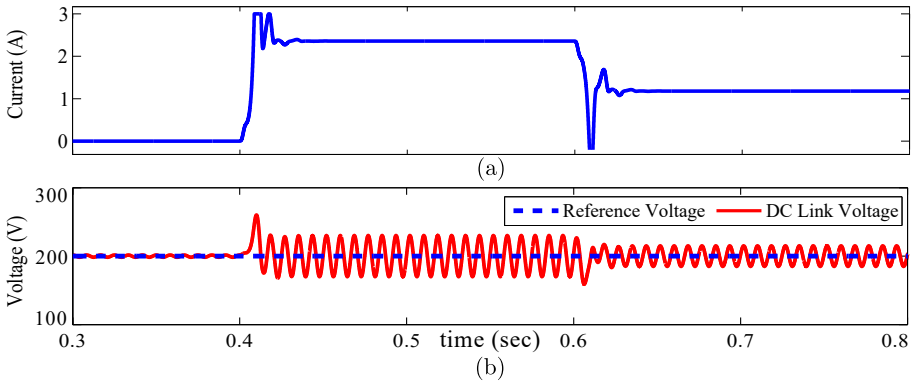

Fig. 2.15: H_∞ dc link voltage controller performance: (a) magnitude of the grid reference current I_g^{ref} determined by H_∞ controller, and (b) dc link voltage.

As mentioned before, P_{in} varies randomly due to the variations of unpredictable factors such as temperature and irradiation level. In this scenario, P_{in} changes from zero to its nominal value at $t = 0.4\ s$ with the slope of 20 W/ms. Then, it decreases to half of the nominal value at $t = 0.6\ s$ with the slope of $-20\ W/ms$. Fig. 2.15 illustrates the simulation results for this scenario. Although P_{in} variations are significant, the H_∞ dc link controller successfully suppresses the effect of the P_{in} disturbance on the dc link voltage. Moreover, Fig. 2.15 shows that although the dc link control loop contains double frequency ripples, the magnitude of the grid current I_g does not contain any second harmonic oscillations. Therefore, the proposed dc link controller ensures system robustness against system disturbances and obviates the second harmonic oscillation from the magnitude of the grid current.

2.3.3 Feedforward and PLL Loops Robustness Analysis and Simulation in a Weak Grid

The current controller designed so far is for the case of a stiff grid in which the grid voltage is directly measured for the FF loop and used as a feedback for the PLL loop. However, in the case of a weak grid, the grid voltage cannot be directly measured, and instead the voltage at the point of contact between the LCL filter and the grid impedance Z_g is measured and used for the FF and PLL loops. This

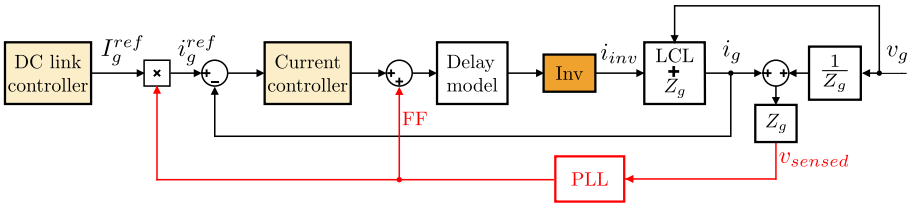

Fig. 2.16: Closed-loop block diagram of the system in a weak grid situation.

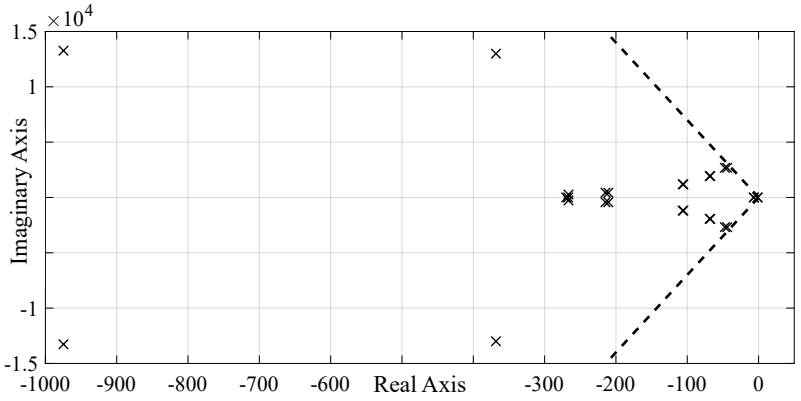

Fig. 2.17: Dominant closed-loop poles with $L_g = 0\ mH$ (stiff grid).

measured voltage is different from the grid voltage due to a non-zero grid impedance, which may lead to system instability and poor performance [17]. Therefore, some performance analysis and simulation results are required in order to guarantee the robustness of the designed controller in the presence of a weak grid. To this end, the closed-loop system block diagram including the inverter and LCL filter model, current controller, delay model, PLL, and grid impedance ($Z_g = R_g + sL_g$) is depicted in Fig. 2.16 where $F_{PLL}(s) = \frac{\mu s}{s^2+\mu s+\omega_n^2}$, $\mu = \sqrt{2}\omega_n$, and $\omega_n = 2\pi 60\ \frac{rad}{s}$ [116]. Using the closed-loop block diagram of the system in this figure, the robustness analysis can now be performed by using the root locus technique for different values of L_g.

The dominant closed-loop poles with the stiff grid, $L_g = 0$, are depicted in Fig. 2.17. This figure indicates that the poles are confined to the two dashed lines which intersect at the origin. In order to maintain the damping behavior and hence the performance of the closed-loop system in a weak grid situation, $L_g \neq 0$, all poles should stay to the left of these two intersecting dashed lines.

The root locus analysis in Fig. 2.18 shows that the closed-loop poles of the system for $L_g = 10.87\ mH$ are all confined to the left of the two intersecting dashed

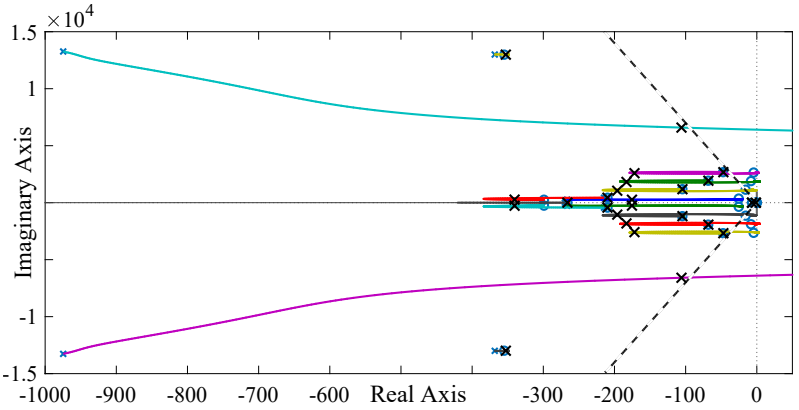

Fig. 2.18: Root locus analysis of the dominant closed-loop poles with $L_g = 10.87\ mH$.

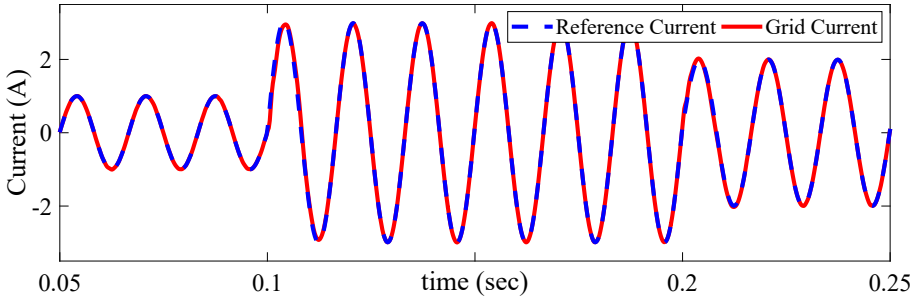

Fig. 2.19: Injected current into the weak grid with $L_g = 10.87\ mH$.

lines, and for any L_g values greater than 10.87 mH the closed-loop poles will pass through the two intersecting lines. Therefore, the root locus analysis guarantees that the performance of our designed controller is robust to the maximum impedance value $L_g = 10\ mH$ of a weak grid. This result is also tested by simulations, in which $L_g = 10\ mH$ is used for the weak grid. The simulation result depicted in Fig. 2.19 confirms the satisfactory performance of our proposed controller in the presence of a weak grid, in which the grid voltage is not measurable and instead the voltage of PCC is measured and used for the FF and PLL loops.

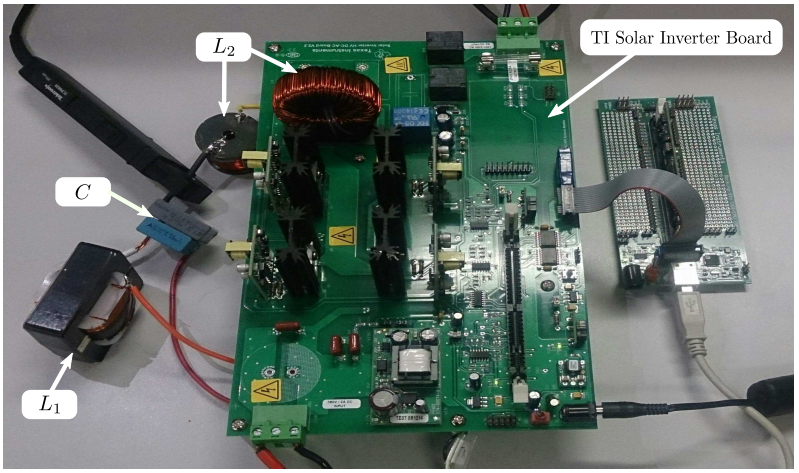

Fig. 2.20: Experimental setup configuration.

2.4 Experimental Results

An experimental verification of the proposed controllers for the configuration shown in Fig. 2.1 is carried out by using Texas Instrument Solar Inverter HV DC-AC Board, Chroma PV Simulator 62050H-600S, Chroma Programmable AC Source 61502, and Texas Instrument TMS320F28335 DSP. The calculation time of the proposed control system is 14 μs, while it is 9 μs for a traditional control system. Also, in this experiment, switching frequency and digital signal processor (DSP) speed are 40 kHz and 150 MHz, respectively.

Fig. 2.20 presents the experimental setup configuration. Also, the system parameters are presented in Table 2.1. Fig. 2.21 displays the experimental results for the system with nominal parameters. As shown in this figure, the proposed μ-synthesis current controller provides a satisfactory reference tracking and steady-state performance. Also, the controller actively damps the resonant oscillations.

Moreover, Fig. 2.22 illustrates two cases in which the grid-side impedance deviates with $\Delta_{L_2} = \pm 70\%$ and $\Delta_{R_2} = \pm 70\%$ from its nominal values. This figure shows the performance of the proposed current controller in the presence of grid-side impedance uncertainties and delay uncertainties. In this case, the total harmonic distortion (THD) of the injected current is 2.38% and 3.11% for $\Delta_{L_2} = \Delta_{R_2} = 70\%$

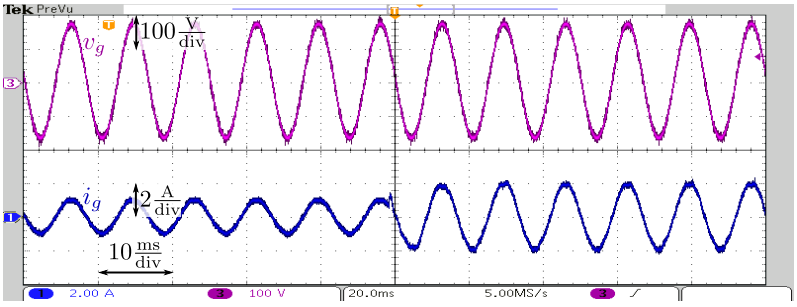

Fig. 2.21: Performance of the proposed controller for the system with the nominal parameters.

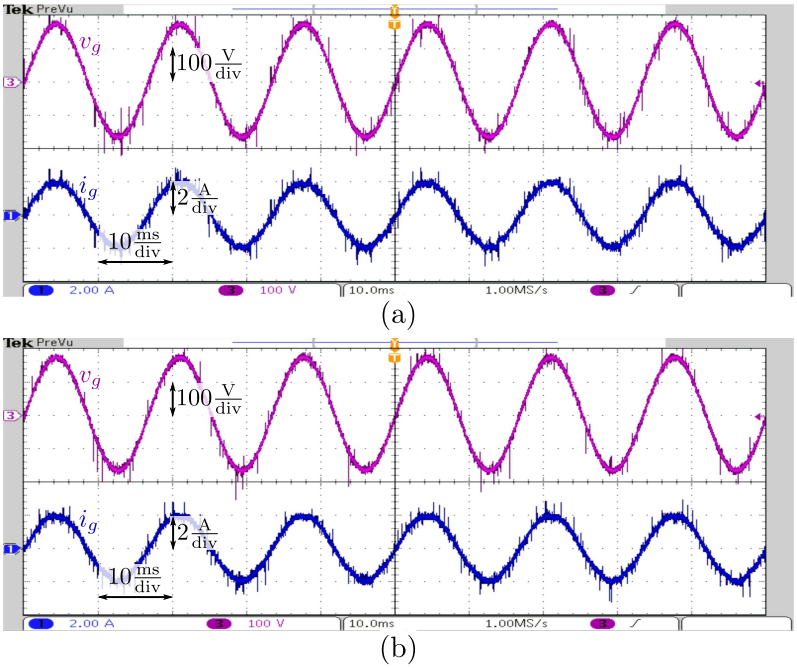

Fig. 2.22: Performance of the proposed controller for the system with deviated parameters: (a) $\Delta_{L_2} = +70\%$ and $\Delta_{R_2} = +70\%$ (weak grid situation), and (b) $\Delta_{L_2} = -70\%$ and $\Delta_{R_2} = -70\%$.

(weak grid situation) and $\Delta_{L_2} = \Delta_{R_2} = -70\%$, respectively. Hence, in these situations, the injected current satisfies the IEEE 1547 standard [117], which requires the THD to be less than 5%.

Furthermore, in another test, the disturbance rejection capability of the proposed controller in a distorted grid voltage condition is evaluated. In this test, the grid voltage is polluted by 5% of the 3^{rd}, 5^{th}, and 7^{th} grid harmonics. The harmonic contents of the injected current for the distorted grid voltage are demonstrated in

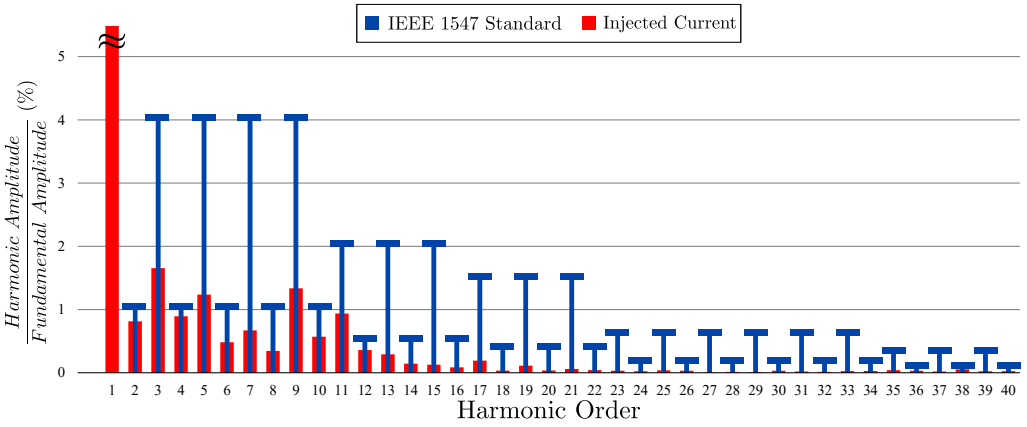

Fig. 2.23: Harmonic contents of the injected current for the case of distorted grid voltage containing 5% of the 3^{rd}, 5^{th}, and 7^{th} voltage harmonics.

Fig. 2.23. As shown in this figure, the harmonic contents of the injected currents meet the IEEE 1547 standard. The injected current THD and grid voltage THD for sinusoidal voltage are 2.54% and 0.438%, respectively. Moreover, the current THD and grid voltage THD for polluted voltage are 3.14% and 8.4%, respectively. It is worth mentioning that the application of the proposed controller is for micro and mini inverters, where several modular low-power inverters are connected in parallel, and the whole system is connected to the grid. In this kind of application, a higher THD is acceptable for each inverter as compared with high-power rating inverters. Also, because the power density is an important factor for this application, system components are physically smaller. As a result, ripples and distortions become bigger in comparison with the fundamental harmonic.

2.5 Robust Control System for Standalone Inverters to Form a Microgrid

Fig. 2.24 depicts the configuration of a droop-controlled standalone inverter and its control block diagram. As shown in this figure, the cascade control system contains robust current, voltage, and droop control loops. The current control loop is responsible to track the current reference i_2^{ref} determined by the voltage control

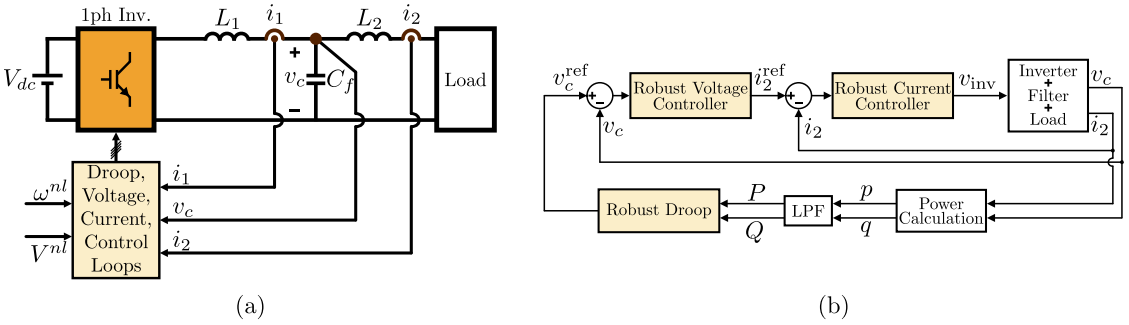

Fig. 2.24: Single-phase droop-controlled standalone inverter: (a) system configuration, and (b) control system.

loop. Also, the voltage controller adjusts the capacitor voltage of the output filter v_c with respect to the reference determined by the droop controller v_c^{ref}. Eventually, the droop specifies the angular frequency ω and voltage amplitude $\hat{V}_c$ for the system based on the active and reactive powers demanded by the load.

Unlike the grid-connected operation mode where the sinusoidal current should be injected into the grid to comply with standards, in the standalone operation mode, the voltage quality is important, and the inverter is required to generate a sinusoidal voltage. Therefore, in addition to tracking the reference voltage v_c^{ref}, the voltage controller is responsible for harmonic rejection as well. Moreover, compared to the grid-connected system investigated earlier in this chapter, the droop loop is nonlinear. Also, as the frequency is not forced by the grid in the standalone mode, the system frequency may change due to the load variations.

A robust control system can be designed for the standalone system shown in Fig. 2.24 using μ-synthesis and H_∞ methods as discussed in this chapter. However, considering the aforementioned differences between a standalone and grid-connected systems, especially, system nonlinearities due to the droop loop and frequency variations, the design procedure would be more complicated than the grid-connected system, and, more importantly, the resulting controller will be more complicated. Also, the complexity of selecting proper weight transfer functions for robust controllers makes the design procedure even more challenging. Moreover, as mentioned

in Section 2.3, robust control techniques adopted to design current and voltage controllers for a grid-connected system leads to high-order controllers, i.e. the current controller is of order 15, and the voltage controller is of order 5. Consequently, since the standalone system is more complicated and has more control loops than the grid-connected one, it is expected that using robust control design approach to address control objectives in the standalone operation mode yields a very high-order system. As one of the thesis objective is to study a single-phase microgrid that contains multiple standalone inverters and how inverters interact with each other, using such a high-order control system for each standalone inverter makes the microgrid analysis too complicated. Accordingly, robust controllers are not used in the rest of this thesis. In the next chapter, a systematic approach is introduced to design cascade control systems based on the intra-loop state feedback technique where the order of the proposed control system is the same as the conventional control system.

2.6 Summary

This chapter investigates the usage of robust controllers for inverters operating in grid-connected or standalone mode. Robust current and dc link voltage controllers are proposed based on μ-synthesis and H_∞ methods, respectively, for a single-phase PV inverter with an LCL filter that operates in a weak grid situation. It is demonstrated that the current controller ensures system robustness against weak grid impedance variations and also compensates time delay arising from calculation and PWM as well as delay uncertainties. The controller provides active damping of undesirable resonant oscillations as well. On the other hand, the proposed dc link voltage controller ensures system stability and robustness against input power variations. The dc link controller quickly suppresses voltage fluctuation caused by input power variations thanks to its wide control bandwidth. Furthermore, the proposed controller satisfies power decoupling and double-frequency mitigation to inject high-power-quality current into the grid and prevent power factor deviation and third harmonic injection. In addition, the stability and robust performance of

the PLL loop in a weak grid with major impedance changes is proven. Moreover, the viability of using robust control systems for single-phase standalone inverters operating in a microgrid is briefly reviewed. It is explained that using robust control design approach in the standalone operation mode yields a very high-order control system, which makes the microgrid analysis too complicated. Consequently, robust controllers are not used in the rest of this thesis.

Chapter 3

Cascade Control Design Based on Intra-loop State Feedbacks

The approach of using cascade control loops to construct and design a control system has been widely used in various power electronic applications such as renewable energy converters, motor drives, battery chargers, etc [46–50]. Cascade control structures are inspired from the successive impacts of system variables on each other, where multiple control loops are placed into one another, and each loop provides the reference for its immediate internal loop.

As discussed in Chapter 1, it is normally assumed that each inner loop is sufficiently faster than its immediate outer loop. Thus, the inner loop dynamics are practically invisible to the outer loop and can be ignored when designing the outer loop [7, 48, 57–64]. Such assumption has been essential to simplify the design procedure of the cascade control system. However, the distinct timescale assignment between the loops limits the design flexibility and may lead to excessively slow dynamic responses at outer loops.

On the other hand, if a fast outer loop at a timescale close or comparable to that of the internal loop is required, the internal loop dynamics should be considered in the design of the outer loop controller. Consequently, the design procedure and structure of the external controller would be complicated because the external controller should handle a high-order system that contains the internal control loop plus the original plant.

The proposed method in this chapter removes the aforementioned limitation on the timescales of the cascade loops while retaining the cascade control structure and its advantages. The proposed idea is to include the inner loop dynamics in the

design of the outer loops using intra-loop state feedbacks. Therefore, a systematic design approach is introduced to maintain the design simplicity advantage of cascade control systems. In fact, similar to the conventional approach, the proposed design procedure starts from the most inner loop and successively proceeds outwardly to design all loops so that the design simplicity is maintained.

In the following, first, the LQT method proposed in [118] to optimally design a state-feedback controller is briefly reviewed. Next, drawbacks and constraints of conventional design approaches for cascade control systems are stated. Then, inspired by the LQT method, the proposed cascade control system is structured based on the intra-loop state feedbacks, and the corresponding design approach is presented, which resolves the shortcomings of the conventional design approaches. Finally, the proposed approach is used to design a cascade control system, containing current and voltage control loops, for a single-phase standalone inverter, and it is shown that the distinct timescale constraint is relaxed using the proposed method.

3.1 Linear Quadratic Tracking Method

The linear quadratic regulator (LQR) method is a well-known approach that can be used to optimally design gains of a state feedback controller. The application of this control design approach to power converter systems has some challenges, which have been discussed in the literature. In [119], a controller is designed based on the conventional LQR method to control a three-phase inverter in the synchronous rotating frame. In [120], an LQR-based controller is used for a three-phase inverter where its cost function is arranged such that it contains errors of the state variables. Therefore, the approach relies on the availability of the reference values of system state variables to achieve zero steady-state tracking error [118]. The aforementioned approaches have the following drawbacks. First, the reference and disturbance signals are not considered in the controller design procedure, which is an important issue for applications where the tracking feature is required. In addition, there is no meaningful correlation between weight factors in the cost function

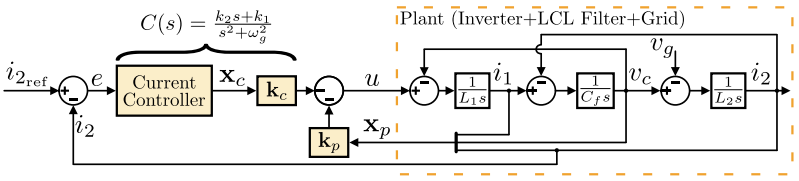

Fig. 3.1: Block diagram of the current control loop for the single-phase grid-connected inverter.

and the state variables of the tracking problem, which does not provide insight in the design procedure.

To resolve the above mentioned drawbacks, an approach is introduced in [118] to transform the state-space model of the system to a new state-space model with a well-defined cost function for the sinusoidal tracking problem. Additionally, using this approach, the tracking error explicitly appears in the cost function; therefore, minimizing the cost function results in the error minimization as well.

The approach is used to optimally design a state feedback current controller for a single-phase grid-connected inverter with an LCL filter, whose block diagram is depicted in Fig. 3.1. For this purpose, first, the state-space equations of the controller and plant, including the inverter and LCL filter, should be derived.

To track a sinusoidal reference with zero steady-state error, its dynamics must be included in the transfer function of the controller based on the internal model principle. Thus, a resonant controller with the following transfer function is used

$$C(s) = \frac{N(s)}{\Delta(s)} = \frac{k_2 s + k_1}{s^2 + \omega_g^2}, \tag{3.1}$$

where ω_g refers to the grid angular frequency. Therefore, the state-space equation of the resonant controller is

$$\dot{\mathbf{x}}_c = \mathbf{A}_c \mathbf{x}_c + \mathbf{B}_c e \tag{3.2}$$

where $\mathbf{x}_c = [x_{c1}\ x_{c2}]^T$ and $e = i_{2_{\text{ref}}} - i_2$ is the tracking error. Also, matrices $\mathbf{A}_c$ and $\mathbf{B}_c$ are derived in the controllable canonical form as

$$\mathbf{A}_c = \begin{bmatrix} 0 & 1 \\ -\omega_g^2 & 0 \end{bmatrix},\ \mathbf{B}_c = \begin{bmatrix} 0 \\ 1 \end{bmatrix}. \tag{3.3}$$

According to Fig. 3.1, the state-space equations of the plant are

$$\dot{\mathbf{x}}_p = \mathbf{A}_p\mathbf{x}_p + \mathbf{B}_p u + \mathbf{B}_g v_g,\ y_p = \mathbf{C}_p\mathbf{x}_p, \tag{3.4}$$

where $\mathbf{x}_p = [i_1\ v_c\ i_2]^T$, $y_p = i_2$, and u refers to the control signal. Thus, the state-space matrices $\mathbf{A}_p$, $\mathbf{B}_p$, $\mathbf{B}_g$, and $\mathbf{C}_p$ are

$$\mathbf{A}_p = \begin{bmatrix} 0 & -\frac{1}{L_1} & 0 \\ \frac{1}{C_f} & 0 & -\frac{1}{C_f} \\ 0 & \frac{1}{L_2} & 0 \end{bmatrix},\ \mathbf{B}_p = \begin{bmatrix} \frac{1}{L_1} \\ 0 \\ 0 \end{bmatrix},\ \mathbf{B}_g = \begin{bmatrix} 0 \\ 0 \\ -\frac{1}{L_2} \end{bmatrix},\ \mathbf{C}_p = \begin{bmatrix} 0 & 0 & 1 \end{bmatrix}. \tag{3.5}$$

Augmenting (3.2) and (3.4) yields

$$\dot{\mathbf{x}} = \mathbf{A}\mathbf{x} + \mathbf{B}_u u + \mathbf{B}_{\text{ref}} i_{2_{\text{ref}}} + \mathbf{B}_w v_g, \tag{3.6}$$

where $\mathbf{x} = [\mathbf{x}_c\ \mathbf{x}_p]^T$, and $\mathbf{A}$, $\mathbf{B}_u$, $\mathbf{B}_{\text{ref}}$, $\mathbf{B}_w$, and $\mathbf{C}$ are given by (3.7)

$$\mathbf{A} = \begin{bmatrix} \mathbf{A}_c & -\mathbf{B}_c\mathbf{C}_p \\ \mathbf{0} & \mathbf{A}_p \end{bmatrix}, \mathbf{B}_u = \begin{bmatrix} \mathbf{0} \\ \mathbf{B}_p \end{bmatrix}, \mathbf{B}_{\text{ref}} = \begin{bmatrix} \mathbf{B}_c \\ \mathbf{0} \end{bmatrix}, \mathbf{B}_w = \begin{bmatrix} \mathbf{0} \\ \mathbf{B}_g \end{bmatrix}, \mathbf{C} = \begin{bmatrix} \mathbf{0} & \mathbf{C}_p \end{bmatrix}. \tag{3.7}$$

In addition, the control signal is defined as $u = -\mathbf{k}\mathbf{x}$ where $\mathbf{k} = [\mathbf{k}_c\ \mathbf{k}_p]$, $\mathbf{k}_c = [k_1\ k_2]$, and $\mathbf{k}_p = [k_3\ k_4\ k_5]$.

Define the operator $D(p)$ according to $\Delta(s)$ in (3.1) as $D(p) = p^2 + \omega_g^2$ in the time domain, where $p = (d/dt)$ is the time-derivative operator. It is also assumed that the grid voltage is a sinusoidal waveform as $v_g = V\sin(\omega_g t)$. Thus, multiplying $D(p)$ to v_g results in $D(p)v_g = (d^2/dt^2)\,(V\sin(\omega_g t)) + \omega_g^2\,(V\sin(\omega_g t)) = 0$. By the same

token, it is concluded that $D(p)i_{2_{\text{ref}}}=0$. Consequently, applying the transformation $D(p)$ to both sides of (3.6) yields

$$\dot{\mathbf{z}} = \mathbf{A}\mathbf{z} + \mathbf{B}_u v, \tag{3.8}$$

where $\mathbf{z}$ and v are the transformed state vector and control signal, respectively, and they are defined as $\mathbf{z}=D(p)\mathbf{x}=\ \ddot{\mathbf{x}}+\omega_g^2\mathbf{x}$ and $v=D(p)u=\ddot{u}+\omega_g^2 u$. Furthermore, according to (3.2) and (3.3), it can be seen that

$$z_1 = \ddot{x}_{c1} + \omega_g^2 x_{c1} = e,\ \ z_2 = \ddot{x}_{c2} + \omega_g^2 x_{c2} = \dot{e}. \tag{3.9}$$

Now, the LQR method can be used to optimally design the controller gains for the system represented by (3.8). In this case, the following cost function would be minimized by the LQR method

$$J = \int_0^\infty \left(\mathbf{z}^T\mathbf{Q}\mathbf{z} + rv^2\right) dt = \int_0^\infty \left(q_1 e^2 + q_2\dot{e}^2 + \mathbf{z}_p^T\mathbf{Q}_p\mathbf{z}_p + rv^2\right) dt, \tag{3.10}$$

where $v=-\mathbf{k}\mathbf{z}$, and $\mathbf{Q}=\text{diag}\,(q_1, q_2, \mathbf{Q}_p)$ and $\mathbf{Q}_p=\text{diag}\,(q_3, q_4, q_5)$ are positive semi-definite weight matrices. Also, r ($r>0$) refers to the weight factor of the transformed control signal v. Generally, by modifying the value of r, the penalization dedicated to the control signal in (3.10) is adjusted accordingly. Thus, the weight factor r can be used to limit the control effort. Moreover, according to (3.10), the tracking error e and its derivative $\dot{e}$ explicitly appear in the cost function, which indicates the cost function is well-defined as its minimization leads to the error minimization. Therefore, regarding to the definition of $\mathbf{Q}$ and (3.10), the weight factors q_1 and q_2 directly affect the tracking error and its derivative.

To sum up, the LQT approach converts the tracking and disturbance rejection problems to a regulation problem. In this approach, the transformation $D(p) = \det(p\mathbf{I}-\mathbf{A}_c)$ is used to map $\mathbf{x}$ to $\mathbf{z}=D(p)\mathbf{x}$ and u to $v=D(p)u$. The transformed state-space equation in the new coordinate is $\dot{\mathbf{z}} = \mathbf{A}\mathbf{z} + \mathbf{B}_u v$, where the definitions

of the state-space matrices $\mathbf{A}$ and $\mathbf{B}_u$ are provided in (3.7). It is worth mentioning that the transformation $D(p)$ nullifies both the disturbance and the reference signals as they are all sinusoidal, i.e. $D(p)v_g = 0$ and $D(p)i_{2_{\text{ref}}} = 0$, because the dynamics of v_g and $i_{2_{\text{ref}}}$ are included in the controller's dynamics denoted by $\Delta(s)$. Finally, by applying the LQR method to the transformed state-space equation (3.8), the optimal values of the controller gains $\mathbf{k}$ can be calculated in Matlab software using the `lqr` command.

As explained in this section, the proposed LQT method is used to design a current controller for a single-phase grid-connected inverter. In Section 3.3, the application of the LQT method is extended to propose a systematic design approach for a general cascade control system which has intra-loop state feedbacks. Then, the proposed approach is used to design a cascade control system, consisting of the voltage and current control loops, for a single-phase standalone inverter.

3.2 Problem Statement

As mentioned earlier, cascade control systems can be used in several power electronic applications. Fig. 3.2 shows an example of cascade control system used for the integration of a single-stage PV system to the grid. The system configuration is shown in Fig. 3.2(a). Also, Fig. 3.2(b) illustrates the block diagram of the cascade control system of the inverter. In this figure, the internal controller is responsible for the current quality indices such as harmonics and also current limiting to ensure the current does not cross the limits during fast transients. The external controller regulates the dc link voltage by determining the current reference i^c_{ref}. Also, the limiter block is used for protection to ensure that the current reference lies within the acceptable range during harsh transients

$$i_{\text{ref}} = \begin{cases} i^c_{\text{ref}} & |i^c_{\text{ref}}| \leqslant I_{\max} \\ \text{sgn}(i^c_{\text{ref}}) I_{\max} & |i^c_{\text{ref}}| > I_{\max} \end{cases} \tag{3.11}$$

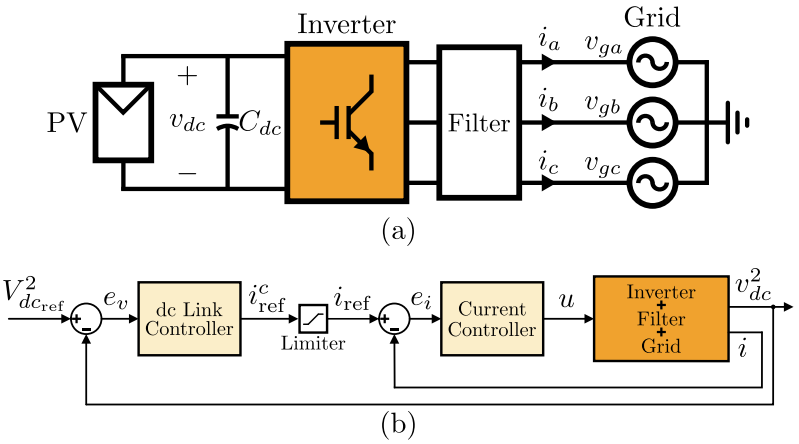

Fig. 3.2: An example of the cascade control system utilization for the integration of the PV system to the grid: (a) system configuration, and (b) control block diagram.

where i_{ref} and $I_{\max}$ refer to the output of the limiter block and the maximum acceptable current, respectively.

Regarding Fig. 3.2(b), the current controller can be designed using the LQT method as explained in Section 3.1. For the conventional design of the voltage controller, two different approaches can be chosen which are explained in the following.

Approach 1, which is more common, is to consider the external loop sufficiently slower (10-20 times) than the internal loop to avoid the interaction between cascade loops. In this case, as the internal loop dynamics are invisible to the external loop, the internal loop dynamics can be ignored for the design of the external controller, which simplifies the design procedure. However, this approach sacrifices the fast and swift responses of the external controller that could have been achieved by a faster controller.

In *Approach 2*, the internal loop dynamics are considered in the design procedure of the external controller. Therefore, as the cascade loop interactions are included in the design procedure, a faster external loop can be designed at a timescale close or comparable to that of the internal loop. In this case, the design procedure of the external controller becomes more complicated compared with the first approach because the external controller should consider a high-order plant, including the internal control loop and the original plant. Moreover, due to the limiter block placed

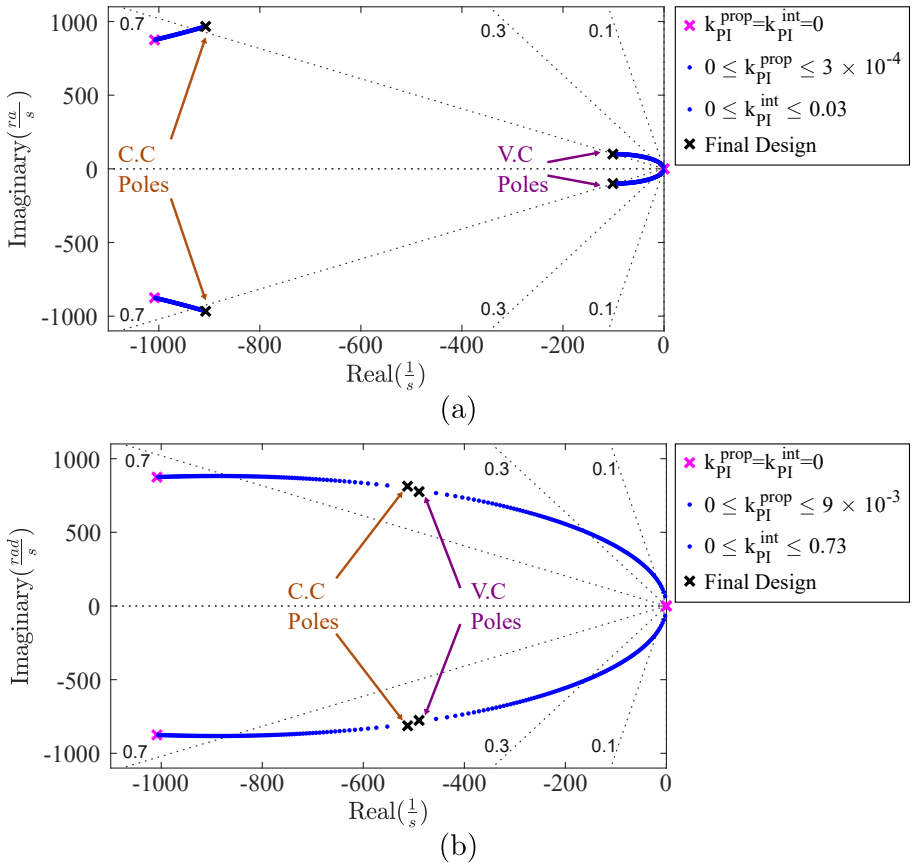

Fig. 3.3: Closed-loop poles of conventional cascade control systems designed based on: (a) *Approach 1* (slow external loop), and (b) *Approach 2* (fast external loop).

between the external controller and internal loop, the output of the fast external controller may be saturated easily during transients because of the large control effort applied by the external controller, which may degrade the overall performance of the system or can enter the system to limit cycles if not unstable.

Fig. 3.3 displays the closed-loop poles of the conventional cascade control systems which are designed based on *Approach 1* (slow external loop) and *Approach 2* (fast external loop), where an LQT-based controller is used as the current controller and a PI controller with the transfer function $C_{PI}(s) = k_{PI}^{\text{prop}} + \frac{k_{PI}^{\text{int}}}{s}$ is used to regulate the dc link voltage. According to Fig. 3.3(a), the dominant poles of the voltage controller are placed far from the dominant poles of the current controller in *Approach 1*, which leads to slower dynamic responses at the external loop. On the

other hand, in *Approach 2*, the poles of the voltage controller are placed close to the current controller poles as depicted in Fig. 3.3(b) to enhance the dynamic performance of the external controller. However, the external loop dynamic improvement is achieved at the price of slowing down the internal loop dynamics. In fact, as the poles of the conventional voltage controller move to left side by changing the gains of the PI controller, the poles of the current controller are pushed to the right side, which leads to slower dynamics for the internal loop.

Fig. 3.4 displays the simulation results for the single-stage PV system of Fig. 3.2, whose cascade control system is designed using either *Approach 1* or *Approach 2*. The extracted power from the PV panel p_{ext} jumps from 0 to 10 kW at $t=0.1$ s. According to Fig. 3.4(a), it is observed that the dc link of the control system designed based on *Approach 2* experiences smaller fluctuations thanks to the faster external controller. Then, p_{ext} decreases to from 10 kW to 9 kW at $t = 0.21$ s, and $V_{dc_{\text{ref}}}$ changes from 600 V to 500 V at the same time. Fig. 3.4(b) shows that the output of the dc link controller in *Approach 2* is excessively saturated due to the harsh transient. Fig. 3.4(a) also illustrates the dc link tolerates more extreme deviations than the system with slower external controller (*Approach 1*), which indicates that the controller's saturation degrades the performance of *Approach 2*. Moreover, as displayed in Fig. 3.4(c), the control system designed using *Approach 2* fails to limit the injected current within the acceptable range during the transient, which may damage the inverter or activate the protection system.

To sum up, as highlighted by this example, it is concluded that using *Approach 2* can lead to the external controller's saturation and/or design complexity in general. Therefore, *Approach 1* is commonly used to design such systems, where the cascade control loops must have distinct timescales. However, this translates into an overall sluggish performance at the outer loop. In the next section, the proposed method is presented to resolve the aforementioned drawbacks of the conventional design approaches.

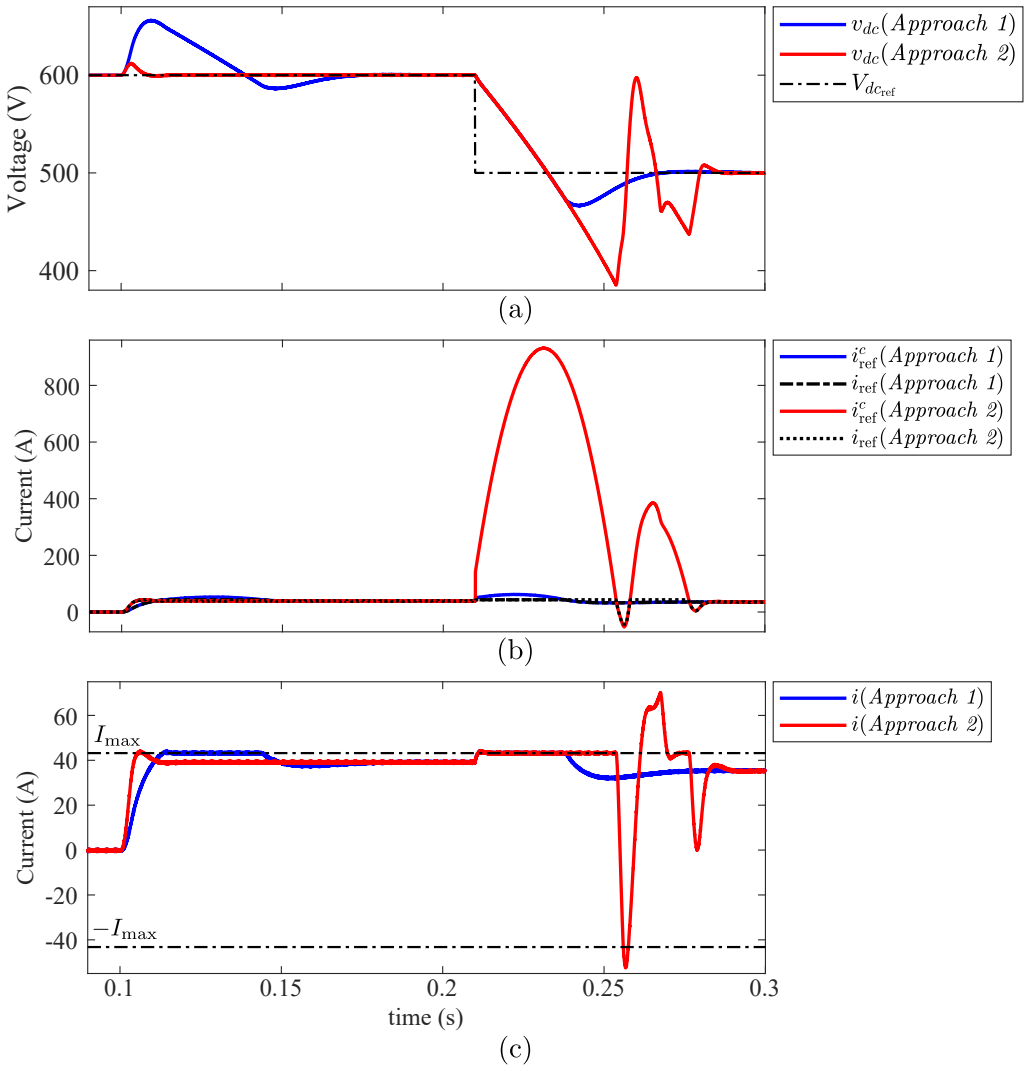

Fig. 3.4: Performance comparison of conventional cascade control systems designed using *Approach 1* and *Approach 2*: (a) dc link voltage, (b) current reference determined by the external controller i^c_{ref} and its limited value i_{ref}, and (c) injected current to the grid.

3.3 Cascade Control Design Using Proposed Intra-Loop State Feedbacks

This section describes the proposed cascade control structure, containing intra-loop state feedback, and the corresponding proposed design approach based on the LQT method.

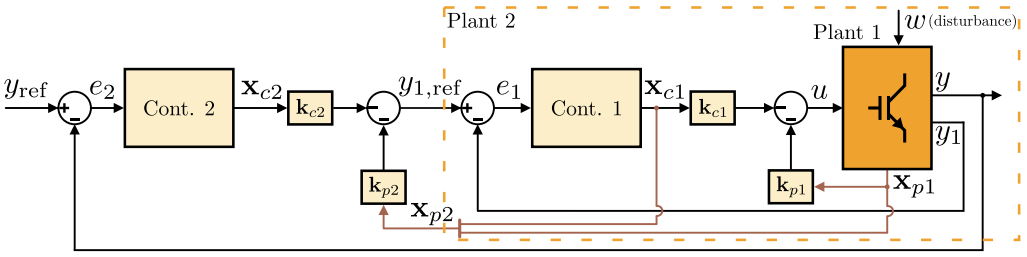

Fig. 3.5: Proposed cascade control structure based on intra-loop state-feedback systems.

3.3.1 Proposed Control structure

Fig. 3.5 shows the proposed cascade control structure, where two loops are depicted in a simple block diagram. The proposed structure maintains the cascade structure property and allows tight control and limiting of the internal variable, e.g. y_1. As depicted in Fig. 3.5, state variables of the internal loop are feedbacked to the external loop through $\mathbf{k}_{p2}\mathbf{x}_{p2}$ to generate the external loop control signal $y_{1,\text{ref}}$ that is the reference signal for the internal loop. The proposed method takes account of the interaction among loops, and the distinct-timescales constraint is alleviated.

Assuming the cascade control contains several loops, the design procedure of the proposed system illustrated in Fig. 3.5 is as follows. Firstly, the most internal loop is designed using the LQT approach. Then, the dynamics of the internal loop are feedbacked to the design of the external level. At this level, again a full-state feedback, including all the state variables at both levels, is optimally designed. The plant and controller of each internal loop together form a new plant for the next external loop as shown in Fig. 3.5. This process is continued until all loops are designed. This way, it is not required to assume that the internal loops are much faster than the outer loops because the full-state feedback design ensures the stability and smooth responses.

It is worth mentioning that the proposed approach not only guarantees stability but also the optimality of controllers using the LQR method. Moreover, the order of the proposed control system is the same as the conventional control system. This procedure is formulated and illustrated below.

3.3.2 Proposed Design Procedure Based on LQT Method

In this section, the proposed design approach for the cascade control system, depicted in Fig. 3.5, is presented in general. For this purpose, the internal loop is first considered. As discussed in Section 3.1, it is assumed that the dynamics of the internal loop reference signal $y_{1,\text{ref}}$ and disturbance signal w are included in the internal controller's dynamics to achieve zero steady-state tracking error. In other words, the denominator of the internal controller $\Delta_1(s)$ is selected based on the internal model principle. According to Fig. 3.5, the state-space equation of the internal controller is

$$\dot{\mathbf{x}}_{c1} = \mathbf{A}_{c1}\mathbf{x}_{c1} + \mathbf{B}_{c1}e_1, \tag{3.12}$$

where $\mathbf{x}_{c1}$ refers to the state vector of the internal loop controller and $e_1 = y_{1,\text{ref}} - y_1$ is the error of the internal loop. Also, matrices $\mathbf{A}_{c1}$ and $\mathbf{B}_{c1}$ are in the controllable canonical form.

The state-space equations of the internal loop plant (*Plant 1*) are

$$\dot{\mathbf{x}}_{p1} = \mathbf{A}_{p1}\mathbf{x}_{p1} + \mathbf{B}_{p1}u + \mathbf{B}_w w, \tag{3.13}$$

$$y_1 = \mathbf{C}_{p1}\mathbf{x}_{p1} + \mathbf{D}_{p1}u + \mathbf{D}_w w, \tag{3.14}$$

where $\mathbf{x}_{p1}$ and y_1 stand for the state vector and output of the internal loop plant, respectively. Now, (3.12)-(3.14) are augmented to form the state-space equations of the internal loop as

$$\dot{\mathbf{x}}_1 = \mathbf{A}_1\mathbf{x}_1 + \mathbf{B}_1^u u + \mathbf{B}_1^{1,\text{ref}} y_{1,\text{ref}} + \mathbf{B}_1^w w, \tag{3.15}$$

$$y_1 = \mathbf{C}_1 x_1 + \mathbf{D}_{p1}u + \mathbf{D}_w w, \tag{3.16}$$

where $\mathbf{x}_1 = [\mathbf{x}_{c1}\ \mathbf{x}_{p1}]^T$, and matrices $\mathbf{A}_1$, $\mathbf{B}_1^u$, $\mathbf{B}_1^{1,\text{ref}}$, $\mathbf{B}_1^w$, and $\mathbf{C}_1$ are defined as follows

$$\begin{aligned} \mathbf{A}_1 &= \begin{bmatrix} \mathbf{A}_{c1} & -\mathbf{B}_{c1}\mathbf{C}_{p1} \\ \mathbf{0} & \mathbf{A}_{p1} \end{bmatrix},\ \mathbf{B}_1^u = \begin{bmatrix} \mathbf{0} \\ \mathbf{B}_{p1} \end{bmatrix}, \\ \mathbf{B}_1^{1,\text{ref}} &= \begin{bmatrix} \mathbf{B}_{c1} \\ \mathbf{0} \end{bmatrix},\ \mathbf{B}_1^w = \begin{bmatrix} \mathbf{0} \\ \mathbf{B}_w \end{bmatrix}, \mathbf{C}_1 = \begin{bmatrix} \mathbf{0} & \mathbf{C}_{p1} \end{bmatrix}. \end{aligned} \tag{3.17}$$

Also, u is the internal control signal and defined as

$$u = -\mathbf{k}_{c1}\mathbf{x}_{c1} - \mathbf{k}_{p1}\mathbf{x}_{p1} = -\mathbf{k}_1\mathbf{x}_1, \tag{3.18}$$

where $\mathbf{k}_1 = [\mathbf{k}_{c1}\ \mathbf{k}_{p1}]$, and $\mathbf{k}_{c1}$ and $\mathbf{k}_{p1}$ are the gain vectors of the internal controller.

Similar to Section 3.1, to convert the tracking problem to a regulation problem, the transformation $D_1(p)$ is defined as follows

$$D_1(p) = \det(p\mathbf{I} - \mathbf{A}_{c1}) = p^m + a_{m-1}p^{m-1} + ... + a_0, \tag{3.19}$$

where $p = (d/dt)$ is the time-derivative operator and m refers to the order of the internal controller. Since the dynamics of the internal reference signal $y_{1,\text{ref}}$ and disturbance signal w are included in the internal controller, the transformation nullifies both the internal reference and disturbance signals, i.e. $D_1(p)y_{1,\text{ref}} = 0$ and $D_1(p)w = 0$. Consequently, applying $D_1(p)$ to both sides of (3.15) yields

$$\dot{\mathbf{z}}_1 = \mathbf{A}_1\mathbf{z}_1 + \mathbf{B}_1^u v_1, \tag{3.20}$$

where $\mathbf{z}_1 = D_1(p)\mathbf{x}_1$ and $v_1 = D_1(p)u$ are the transformed internal loop state vector and control signal, respectively. Now, as indicated in Section 3.1, if the matrices $\mathbf{A}_{c1}$ and $\mathbf{B}_{c1}$ are in the controllable canonical form, the transformed state variables of the internal controller $\mathbf{z}_{c1} = D_1(p)\mathbf{x}_{c1} = [z_{11}\ \cdots\ z_{1m}]^T$ are related to the internal

loop error e_1 and its derivatives as, [118],

$$z_{11} = e_1, \quad z_{12} = \frac{de_1}{dt}, \quad \cdots, \quad z_{1m} = \frac{d^{m-1}e_1}{dt^{m-1}}. \tag{3.21}$$

Then, applying the LQR method, $\mathbf{k}_1$ can be optimally calculated in Matlab software using the `lqr` command to minimize the following cost function

$$J_1 = \int_0^\infty \left(\mathbf{z}_1^T \mathbf{Q_1} \mathbf{z_1} + r_1 v_1^2\right) dt = \int_0^\infty \left(q_{11} z_{11}^2 + \cdots + q_{1m} z_{1m}^2 + \mathbf{z}_{p1}^T \mathbf{Q}_{p1} \mathbf{z}_{p1} + r_1 v_1^2\right) dt, \tag{3.22}$$

where $\mathbf{Q_1} = \text{diag}\,(q_{11}, \cdots, q_{1m}, \mathbf{Q}_{p1})$ is the weight matrix for the transformed internal loop state variables $\mathbf{z}_1$, and r_1 is the weight factor related to the transformed internal loop control signal v_1. According to (3.21) and (3.22), the internal loop tracking error and its derivatives explicitly appear in the cost function of the internal loop, which means the cost function is well-defined as its minimization results in the error minimization for the internal loop.

To design the external loop controller, the whole internal loop is considered as a new plant (*Plant 2*), i.e. $\mathbf{x}_{p2} = \mathbf{x}_1 = [\mathbf{x}_{c1}\ \mathbf{x}_{p1}]^T$. Similar to the internal loop, it is assumed that the dynamics of the external loop reference signal y_{ref} is included in the external controller's dynamics $\Delta_2(s)$. According to Fig. 3.5, the state-space equation of the external loop controller is

$$\dot{\mathbf{x}}_{c2} = \mathbf{A}_{c2}\mathbf{x}_{c2} + \mathbf{B}_{c2} e_2, \tag{3.23}$$

where $\mathbf{x}_{c2}$ stands for the state vector of the external controller, and $e_2 = y_{\text{ref}} - y$ is the error of the external loop. Also, $\mathbf{A}_{c2}$ and $\mathbf{B}_{c2}$ are in the controllable canonical form.

For the external loop plant (*Plant 2*), as the disturbance impact w is compensated in the internal loop, the state-space equations are

$$\dot{\mathbf{x}}_{p2} = \mathbf{A}_{p2}\mathbf{x}_{p2} + \mathbf{B}_{p2} y_{1,\text{ref}}, \tag{3.24}$$

$$y = \mathbf{C}_{p2}\mathbf{x}_{p2} + \mathbf{D}_{p2}y_{1,\text{ref}}, \tag{3.25}$$

where $\mathbf{x}_{p2}$ and y refer to the state vector and output of the external loop plant, respectively. Since the internal loop is considered as the external loop plant, substituting (3.18) into (3.15) results in $\mathbf{A}_{p2} = \mathbf{A}_1 - \mathbf{B}_1^u\mathbf{k}_1$ and $\mathbf{B}_{p2} = \mathbf{B}_1^{1,\text{ref}}$. Assuming $\mathbf{x}_2 = [\mathbf{x}_{c2}\ \mathbf{x}_{p2}]^T$, the state-space equations of the external loop are derived by augmenting (3.23)-(3.25) as

$$\dot{\mathbf{x}}_2 = \mathbf{A}_2\mathbf{x}_2 + \mathbf{B}_2^{1,\text{ref}}y_{1,\text{ref}} + \mathbf{B}_2^{\text{ref}}y_{\text{ref}}. \tag{3.26}$$

$$y = \mathbf{C}_2\mathbf{x}_2 + \mathbf{D}_{p2}y_{1,\text{ref}}, \tag{3.27}$$

where matrices $\mathbf{A}_2$, $\mathbf{B}_2^{1,\text{ref}}$, $\mathbf{B}_2^{\text{ref}}$, and $\mathbf{C}_2$ are

$$\begin{aligned} \mathbf{A}_2 &= \begin{bmatrix} \mathbf{A}_{c2} & -\mathbf{B}_{c2}\mathbf{C}_{p2} \\ \mathbf{0} & \mathbf{A}_{p2} \end{bmatrix}, \quad \mathbf{B}_2^{1,\text{ref}} = \begin{bmatrix} \mathbf{0} \\ \mathbf{B}_{p2} \end{bmatrix}, \\ \mathbf{B}_2^{\text{ref}} &= \begin{bmatrix} \mathbf{B}_{c2} \\ \mathbf{0} \end{bmatrix}, \ \mathbf{C}_2 = \begin{bmatrix} \mathbf{0} & \mathbf{C}_{p2} \end{bmatrix}. \end{aligned} \tag{3.28}$$

Also, the external loop control signal $y_{1,\text{ref}}$ is defined as

$$y_{1,\text{ref}} = -\mathbf{k}_{c2}\mathbf{x}_{c2} - \mathbf{k}_{p2}\mathbf{x}_{p2} = -\mathbf{k}_2\mathbf{x}_2, \tag{3.29}$$

where $\mathbf{k}_2 = [\mathbf{k}_{c2}\ \mathbf{k}_{p2}]$, and $\mathbf{k}_{c2}$ and $\mathbf{k}_{p2}$ are the gain vectors of the external loop controller.

Similar to the internal loop, to convert the tracking problem to a regulation one, the transformation $D_2(p)$ is defined as $D_2(p) = \det(p\mathbf{I} - \mathbf{A}_{c2})$ to map $\mathbf{x}_2$ to $\mathbf{z}_2 = D_2(p)\mathbf{x}_2$ and $y_{1,\text{ref}}$ to $v_2 = D_2(p)y_{1,\text{ref}}$. Note that $D_2(p)y_{\text{ref}} = 0$ because the dynamics of the external loop reference signal y_{ref} is included in the external controller. Therefore, by applying $D_2(p)$ to both sides of (3.26), the transformed state-space

equation of the external loop in the new coordinate is

$$\dot{\mathbf{z}}_2 = \mathbf{A}_2\mathbf{z}_2 + \mathbf{B}_2^{1,\text{ref}}\mathbf{v}_2. \tag{3.30}$$

As stated earlier, this transformation correlates the transformed state variables of the external controller $\mathbf{z}_{c2} = D_2(p)\mathbf{x}_{c2} = [z_{21} \ \cdots \ z_{2n}]^T$ to the external loop error e_2 and its derivatives as follows

$$z_{21} = e_2, \quad z_{22} = \frac{de_2}{dt}, \quad \cdots, \quad z_{2n} = \frac{d^{n-1}e_2}{dt^{n-1}}, \tag{3.31}$$

where n denotes the order of the external controller.

Next, the optimum value of $\mathbf{k}_2$ can be calculated in Matlab using the `lqr` command to minimize the following cost function

$$J_2 = \int_0^\infty \left(\mathbf{z}_2^T\mathbf{Q}_2\mathbf{z_2} + r_2v_2^2\right) dt = \int_0^\infty \left(q_{21}z_{21}^2 + \cdots + q_{2n}z_{2n}^2 + \mathbf{z}_{p2}^T\mathbf{Q}_{p2}\mathbf{z}_{p2} + r_2v_2^2\right) dt, \tag{3.32}$$

where $\mathbf{Q_2} = \text{diag}\,(q_{21}, \cdots, q_{2n}, \mathbf{Q}_{p2})$ is the weight matrix for the transformed external loop state variables and r_2 denotes the weight factor of the transformed control signal. According to (3.31) and (3.32), it is observed that the cost function contains the external loop error and its derivative terms, which indicates the cost function minimization leads to the external loop error minimization as well. It is worth noting that, by modifying r_2, the external loop control effort $y_{1,\text{ref}}$ will be adjusted and saturation can be avoided.

As discussed in this section, the proposed approach based on the LQT method considers cascade loop interactions in the design procedure. Hence, the distinct-timescale constraint among cascade loops is relaxed here. Moreover, the proposed design approach explicitly engages the internal and external loop errors and their derivatives in the corresponding LQR cost functions. Therefore, there is a transparent correlation between weight factors and error minimization in this approach. The proposed design algorithm, including the weight factor selection, for the cascade

control system shown in Fig. 3.5 is summarized below.

3.3.3 Step-by-step Design Algorithm

3.3.3.1 Internal Loop Design

Step 1 : Form the denominator of the inner loop controller $\Delta_1(s)$ based on the internal model principle to ensure the reference tracking and disturbance rejection.

Step 2 : Find $\mathbf{A}_{c1}$ and $\mathbf{B}_{c1}$ in the controllable canonical form.

Step 3 : Derive state-space matrices of *Plant 1*, $\mathbf{A}_{p1}$, $\mathbf{B}_{p1}$, $\mathbf{C}_{p1}$, and $\mathbf{D}_{p1}$.

Step 4 : Augment the inner loop controller and *Plant 1* equations to derive (3.15) and (3.17).

Step 5 : Select $r_1 = 1$ and $\mathbf{Q_1} = \text{diag}\,(q_{11}, \cdots, q_{1m}, \mathbf{Q}_{p1})$, and solve the LQR problem for (3.20) to minimize (3.22) and to find the optimum values of $\mathbf{k}_{c1}$ and $\mathbf{k}_{p1}$. For this purpose, firstly, a weight value q_{11_0} is assigned for q_{11}, which is applied to the internal loop error e_1 (3.22), and other weight factors are set to zero $\mathbf{Q}_1 = \text{diag}\,(q_{11_0}, 0, \cdots, 0)$. Observe how the closed-loop poles vary due to the assigned value for the weight factor q_{11}. Repeat the same procedure for other weight factors q_{1i} $(i \geqslant 2)$ until all the poles of the internal loop system are mapped to appropriate places. It is worth mentioning that it is not necessary to assign values for all weight factors, and some of them can be set to zero. Finally, the value of r_1 can be tuned to adjust the internal loop control effort as well.

3.3.3.2 External Loop Design

Step 6 : Similar to *Step 1*, form the denominator of the outer loop controller $\Delta_2(s)$ using the internal model principle.

Step 7 : Similar to *Step 2*, derive $\mathbf{A}_{c2}$ and $\mathbf{B}_{c2}$ in the controllable canonical form.

Step 8 : Form state-space matrices of *Plant 2* as $\mathbf{A}_{p2} = \mathbf{A}_1 - \mathbf{B}_1^u \mathbf{k}_1$ and $\mathbf{B}_{p2} = \mathbf{B}_1^{1,\text{ref}}$ by using $\mathbf{k}_1 = [\mathbf{k}_{c1}\ \mathbf{k}_{p1}]$ of *Step 5*.

Step 9 : Augment the outer loop controller and *Plant 2* equations to derive (3.26) and (3.28).

Step 10 : Select $r_2 = 1$ and $\mathbf{Q_2} = \text{diag}\,(q_{21}, \cdots, q_{2n}, \mathbf{Q}_{p2})$, and solve the LQR for (3.30) to minimize (3.32) and to find the optimum values of $\mathbf{k}_{c2}$ and $\mathbf{k}_{p2}$. Similar to *Step 5*, the value of r_2 can be modified to avoid the control effort saturation.

3.4 Design Cascade Control System for Single-phase Standalone Inverter

In this section, the voltage and current control loops of a single-phase standalone inverter are structured and designed based on the proposed method. Fig. 3.6 shows the system configuration and the proposed cascade control system based on the intra-loop state feedback. System parameters are listed in Table 3.1.

To design the cascade control system, the internal loop is first considered. As discussed earlier, to track the sinusoidal reference of the internal loop $i_{2_{\text{ref}}}$, a resonant controller with the following transfer function is used as the internal controller

$$C_1(s) = \frac{k_{c12}s + k_{c11}}{s^2 + \omega^2}, \tag{3.33}$$

Table 3.1: Parameters of the single-phase standalone inverter

Parameter	Value
P_{nom}	1 kW
L_1	2 mH
C_f	2.2 μF
L_2	2 mH

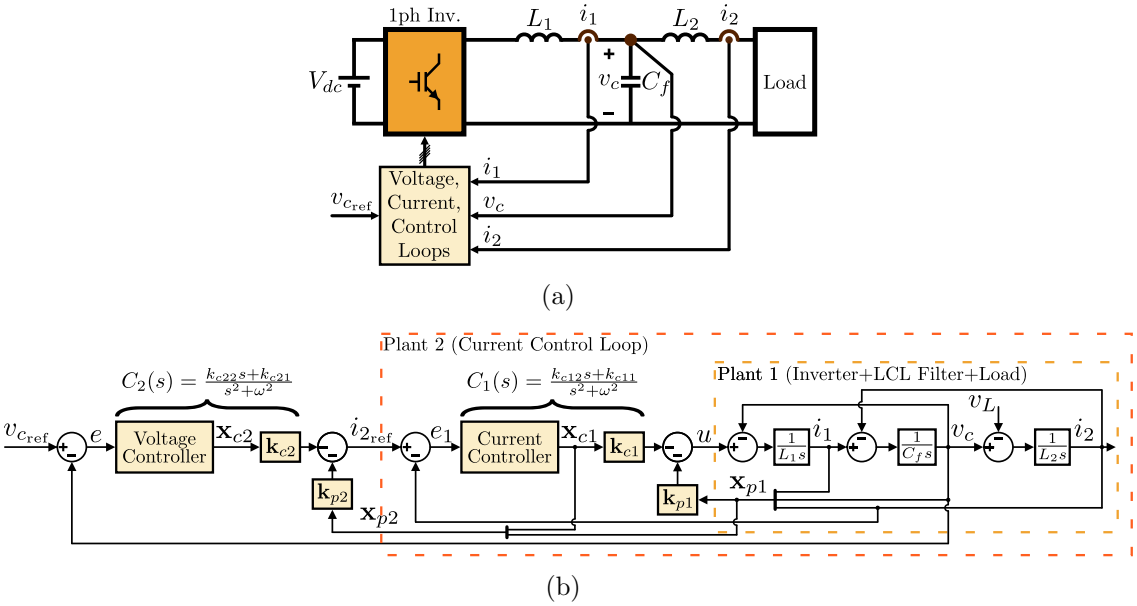

Fig. 3.6: Single-phase standalone inverter: (a) system configuration, and (b) proposed cascade control system.

where $\mathbf{k}_{c1} = [k_{c11}\ k_{c12}]$ and ω refers to the angular frequency. According to (3.33), the denominator of the internal controller is selected as $\Delta_1(s) = s^2 + \omega^2$ (*Step 1*). The State-space equation of the current controller is

$$\dot{\mathbf{x}}_{c1} = \mathbf{A}_{c1}\mathbf{x}_{c1} + \mathbf{B}_{c1}e_1, \tag{3.34}$$

where $e_1 = i_{2_{\text{ref}}} - i_2$ is the error of the current loop. Also, matrices $\mathbf{A}_{c1}$ and $\mathbf{B}_{c1}$ are formed in the controllable canonical form (*Step 2*) as

$$\mathbf{A}_{c1} = \begin{bmatrix} 0 & 1 \\ -\omega^2 & 0 \end{bmatrix},\ \mathbf{B}_{c1} = \begin{bmatrix} 0 \\ 1 \end{bmatrix}. \tag{3.35}$$

According to Fig. 3.6(b), the state-space equations of *Plant 1*, containing the inverter and its filter, are

$$\dot{\mathbf{x}}_{p1} = \mathbf{A}_{p1}\mathbf{x}_{p1} + \mathbf{B}_{p1}u + \mathbf{B}_L v_L,\ \mathbf{y}_{p1} = \mathbf{C}_{p1}\mathbf{x}_{p1}, \tag{3.36}$$

where $\mathbf{x}_{p1} = [i_1\ v_c\ i_2]^T$ and $\mathbf{y}_{p1} = [i_2\ v_c]^T$. Also, i_1, v_c, i_2, u, and v_L refer to the

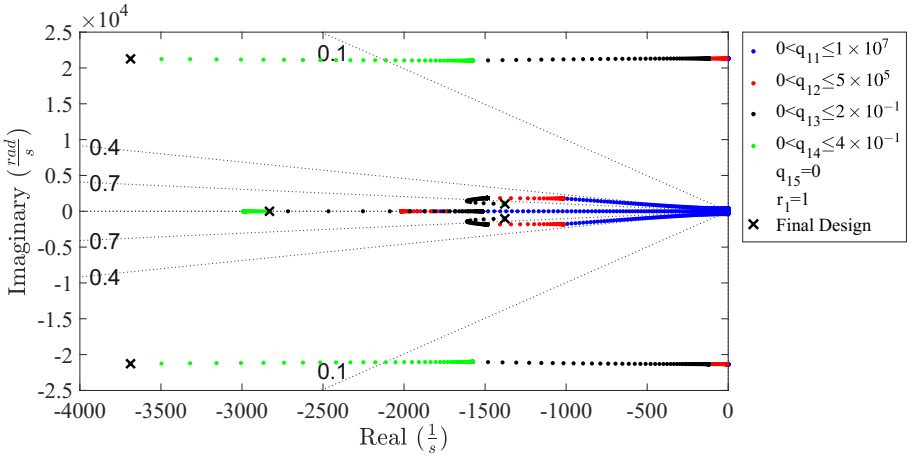

Fig. 3.7: Closed-loop poles of the current loop.

current of the inverter-side inductor L_1, the capacitor voltage C_f, the current of the load-side inductor L_2, the internal loop control signal, and the load voltage, respectively. Moreover, $\mathbf{A}_{p1}$, $\mathbf{B}_{p1}$, $\mathbf{B}_L$, and $\mathbf{C}_{p1}$ are defined as follows (*Step 3*)

$$\mathbf{A}_{p1}=\begin{bmatrix} 0 & \frac{-1}{L_1} & 0 \\ \frac{1}{C_f} & 0 & \frac{-1}{C_f} \\ 0 & \frac{1}{L_2} & 0 \end{bmatrix}, \mathbf{B}_{p1}=\begin{bmatrix} \frac{1}{L_1} \\ 0 \\ 0 \end{bmatrix}, \mathbf{B}_L=\begin{bmatrix} 0 \\ 0 \\ \frac{-1}{L_2} \end{bmatrix}, \tag{3.37}$$
$$\mathbf{C}_{p1}=\begin{bmatrix} \mathbf{C}_{p1_i} & \mathbf{C}_{p1_v} \end{bmatrix}^T, \mathbf{C}_{p1_i}=\begin{bmatrix} 0 & 0 & 1 \end{bmatrix}, \mathbf{C}_{p1_v}=\begin{bmatrix} 0 & 1 & 0 \end{bmatrix}.$$

Now, (3.34) and (3.36) are augmented to form the state-space equation of the entire internal loop (*Step 4*)

$$\dot{\mathbf{x}}_1 = \mathbf{A}_1\mathbf{x}_1 + \mathbf{B}_1^u u + \mathbf{B}_1^{1,\text{ref}} i_{2_{\text{ref}}} + \mathbf{B}_1^w v_L, \tag{3.38}$$

where the definitions of $\mathbf{A}_1$, $\mathbf{B}_1^u$, $\mathbf{B}_1^{1,\text{ref}}$, and $\mathbf{B}_1^w$ are provided by (3.17).

Eventually, $r_1=1$ and $\mathbf{Q}_1=\text{diag}\,(q_{11}, q_{12}, ..., q_{15})$ are selected as weight factors of the LQR cost function for the internal loop (3.22). Now, by solving the LQR problem, the poles of the current control loop can be mapped to appropriate places and the optimum values of $\mathbf{k}_{c1}$ and $\mathbf{k}_{p1}$ are found (*Step 5*). Fig. 3.7 shows the displacement and final locations of the current control loop poles while varying the weight factors.

To track the sinusoidal reference of the external loop $v_{c_{\text{ref}}}$, the following resonant controller is used

$$C_2(s) = \frac{k_{c22}s + k_{c21}}{s^2 + \omega^2}, \tag{3.39}$$

where $\mathbf{k}_{c2} = [k_{c21}\ k_{c22}]$ and ω. According to (3.39), the denominator of the voltage controller is $\Delta_2(s) = s^2 + \omega^2$ (*Step 6*). Also, the State-space equation of the voltage controller is

$$\dot{\mathbf{x}}_{c2} = \mathbf{A}_{c2}\mathbf{x}_{c2} + \mathbf{B}_{c2}e_2, \tag{3.40}$$

where $e_2 = v_{c_{\text{ref}}} - v_c$ is the voltage error. Also, matrices $\mathbf{A}_{c2}$ and $\mathbf{B}_{c2}$ are the same as $\mathbf{A}_{c1}$ and $\mathbf{B}_{c1}$ in (3.34), respectively (*Step 7*).

As mentioned earlier, to include the internal loop dynamics in the design procedure of the external controller, the entire internal loop is considered as a new plant for the controller (*Plant 2*). Therefore, the state-space equation of *Plant 2* is

$$\dot{\mathbf{x}}_2 = \mathbf{A}_2\mathbf{x}_2 + \mathbf{B}_2^{1,\text{ref}} i_{2_{\text{ref}}} + \mathbf{B}_2^{\text{ref}} v_{c_{\text{ref}}}. \tag{3.41}$$

where $\mathbf{A}_{p2} = \mathbf{A}_1 - \mathbf{B}_1^u\mathbf{k}_1$ and $\mathbf{B}_{p2} = \mathbf{B}_1^{1,\text{ref}}$ (*Step 8*).

After that, (3.40) and (3.41) are augmented to form the state-space equation of the external loop (*Step 9*)

$$\dot{\mathbf{x}}_2 = \mathbf{A}_2\mathbf{x}_2 + \mathbf{B}_2^{1,\text{ref}} i_{2_{\text{ref}}} + \mathbf{B}_2^{\text{ref}} v_{c_{\text{ref}}}. \tag{3.42}$$

where the definitions of $\mathbf{A}_2$, $\mathbf{B}_2^{1,\text{ref}}$, and $\mathbf{B}_2^{\text{ref}}$ are given by (3.28).

Finally, the weight factors of the LQR cost function for the external loop (3.32) are chosen as $r_2 = 1$ and $\mathbf{Q}_2 = \text{diag}\,(q_{21}, q_{22}, ..., q_{27})$. By solving the LQR problem, the closed-loop poles of the voltage control loop can be placed properly and the optimum values of $\mathbf{k}_{c2}$ and $\mathbf{k}_{p2}$ are calculated accordingly (*Step 10*). Fig. 3.8 depicts the displacement and final locations of the voltage control loop poles with respect to variations in the weight factors. Table 3.2 represents parameters of the current and voltage controllers designed based on the proposed design approach. Simulation

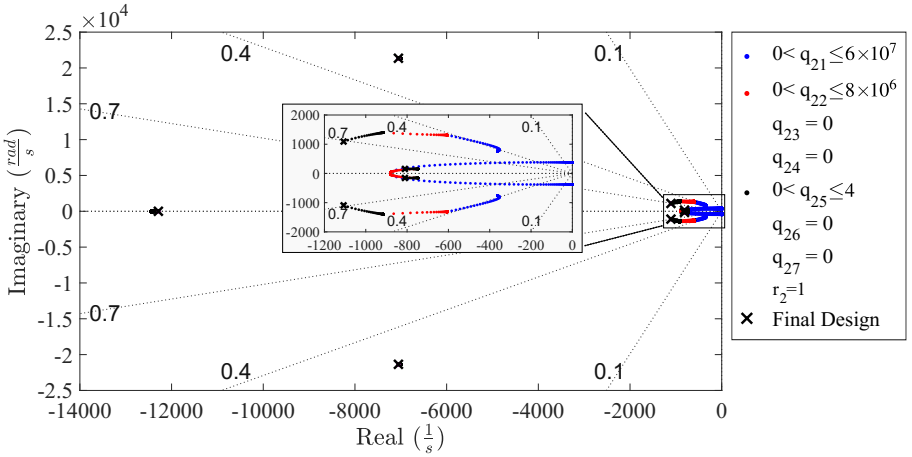

Fig. 3.8: Closed-loop poles of the voltage loop.

and experimental results of the proposed cascade control system within different scenarios are presented in Chapter 4 and Chapter 5.

It is worth mentioning that the proposed approach can be used to design a cascade control system for three-phase systems as well. However, to maintain the thesis's consistency, the example is provided in Appendix C.

Table 3.2: Parameters of the proposed current and voltage controllers

Parameter		Value
Current Controller	k_{c11}	-3.08×10^7
	k_{c12}	-3.89×10^4
	k_{p11}	20.58
	k_{p12}	0.13
	k_{p13}	-0.82
Voltage Controller	k_{c21}	-6.6×10^4
	k_{c22}	-162
	k_{p21}	-4.36×10^3
	k_{p22}	2.75×10^3
	k_{p23}	0.09
	k_{p24}	6.9×10^{-3}
	k_{p25}	-0.22
Closed-loop poles	$\lambda_{1,2}$	$-8.11 \times 10^2 \pm j1.55 \times 10^2$
	$\lambda_{3,4}$	$-1.09 \times 10^3 \pm j1.09 \times 10^3$
	$\lambda_{5,6}$	$-7.05 \times 10^3 \pm j2.14 \times 10^4$
	λ_7	-1.23×10^4

3.5 Summary

A method to restructure and design cascade control loops is proposed based on the linear quadratic theory in this chapter. By considering the interactions among cascade control loops, the proposed method alleviates the limitation on the timescales of the loops. Therefore, using the proposed method, the external loops can be designed much faster than the conventional approach. Consequently, the proposed control system can exhibit swifter and smoother responses. The proposed method is also used to design a cascade control system, including voltage and current control loops, for a single-phase standalone inverter. Moreover, in Chapter 4 and Chapter 5, where interactions among parallel inverters and the efficiency improvement in a single-phase microgrid are studied, the proposed method is used to structure and design voltage and current control loops of inverters operating in the microgrid.

Chapter 4

Modeling and Stability Analysis of Single-phase Microgrids Controlled in Stationary Frame

Modern microgrids are transitioning toward having an increasing portion of GFM converters to support nontraditional sources such as renewable energy and energy storage systems while aiming to improve system stability, reliability, power rating, and flexibility. Understanding the interaction among parallel GFM converters to guarantee the microgrid stability within various operating conditions is necessary.

As discussed in Chapter 1, for single-phase systems, when the controllers are implemented in the rotating frame to facilitate the stability analysis and design, the required OSG units degrade the system stability. In fact, in the rotating frame, because the dynamics originated from OSG units is not modeled, the accuracy of the entire model and the stability analysis are questionable. On the other hand, when the controllers are implemented in the stationary frame to avoid OSG-related problems, the stability analysis becomes particularly challenging due to nonlinearities and mixed dc and ac state variables.

In this chapter, a new approach is proposed to systematically model and perform the stability analysis of a single-phase GFM inverter controlled in stationary frame. The proposed approach is based on defining a complementary imaginary system that allows transformation to the synchronous rotating frame without introducing time-varying (double-frequency) terms and without altering the stability properties. Therefore, this study uses the preferred way of implementation of the

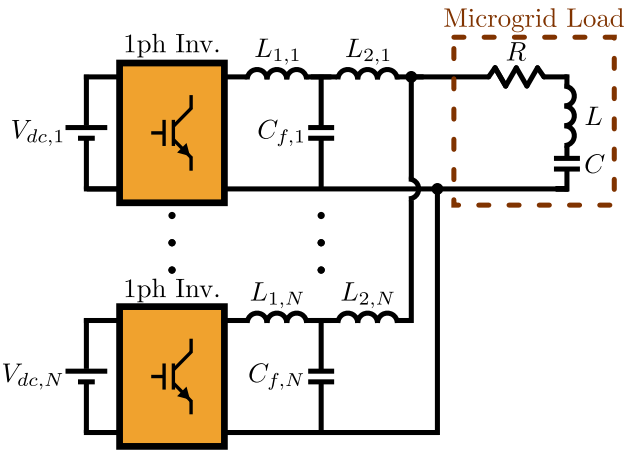

Fig. 4.1: Single-phase microgrid with parallel inverters.

controller that is in the stationary frame without OSGs, while modeling it in the preferred frame that is the rotating frame to achieve dc quantities.

The proposed model can be used for small-signal stability analysis, tuning system parameters, and studying the system sensitivity against parameter variations. Moreover, the proposed model is able to represent behaviors of the fast dynamic variables of the internal loops such as currents and voltages. Also, the proposed imaginary system does not affect the actual system dynamics because the imaginary dynamics does not interact with the system variables directly. In fact, there is no feedback from the imaginary system to the original system, and the imaginary system is only augmented with the system to allow the transformation to the rotating frame. Eventually, the proposed approach is used for modeling and stability analysis of the system containing parallel GFM inverters controlled in the stationary frame such as shown in Fig. 4.1. It is worth mentioning that, to address variable frequency tracking in this study, a standalone microgrid is studied where the frequency is not fixed, and adaptive resonant controllers are successfully implemented in simulations and practice.

4.1 Proposed Modeling Approach

As discussed in Chapter 1, in the conventional approaches, both controller implementation and modeling are done in the same frame. However, each approach has some drawbacks that make the mathematical modeling either unusable or not fully accurate for the stability analysis. The proposed approach to resolve the aforementioned problems is displayed in Fig. 4.2. As shown in Fig. 4.2(a), the control system is designed and implemented in the stationary frame. Since the mathematical model in the stationary frame consists of dc and ac state variables, the stationary frame model is not proper for small-signal stability analysis. Therefore, the mathematical model should be derived in the rotating frame to contain only dc variables. For this purpose, an imaginary system is defined such that it is the same as the ac subsystem of the original system, and its input comes from the droop $v_c^{\mathrm{ref}\beta}$ as shown in Fig. 4.2(b). In this case, because the inputs of the ac subsystem of the original system $v_c^{\mathrm{ref}\alpha}$ and the imaginary system $v_c^{\mathrm{ref}\beta}$ are orthogonal, the imaginary system generates orthogonal variables of the ac subsystem of the original system. Therefore, the augmented system, which is the combination of the original and imaginary systems, is ready for the conversion to the rotating frame. Fig. 4.2(c) illustrates the transformed system that is the accurate mathematical model of the single-phase droop-controlled standalone inverter in the rotating frame. This model is also suitable for the small-signal stability analysis.

In general, consider state-space equations of the original ac subsystem, containing α-axis components, are represented by

$$\dot{\mathbf{x}}^{\alpha} = \mathbf{A}\mathbf{x}^{\alpha} + \mathbf{B}\mathbf{u}^{\alpha},\ \mathbf{y}^{\alpha} = \mathbf{C}\mathbf{x}^{\alpha} + \mathbf{D}\mathbf{u}^{\alpha}. \tag{4.1}$$

Therefore, for the imaginary system, which contains β-axis components, the state-space equations would be

$$\dot{\mathbf{x}}^{\beta} = \mathbf{A}\mathbf{x}^{\beta} + \mathbf{B}\mathbf{u}^{\beta},\ \mathbf{y}^{\beta} = \mathbf{C}\mathbf{x}^{\beta} + \mathbf{D}\mathbf{u}^{\beta}. \tag{4.2}$$

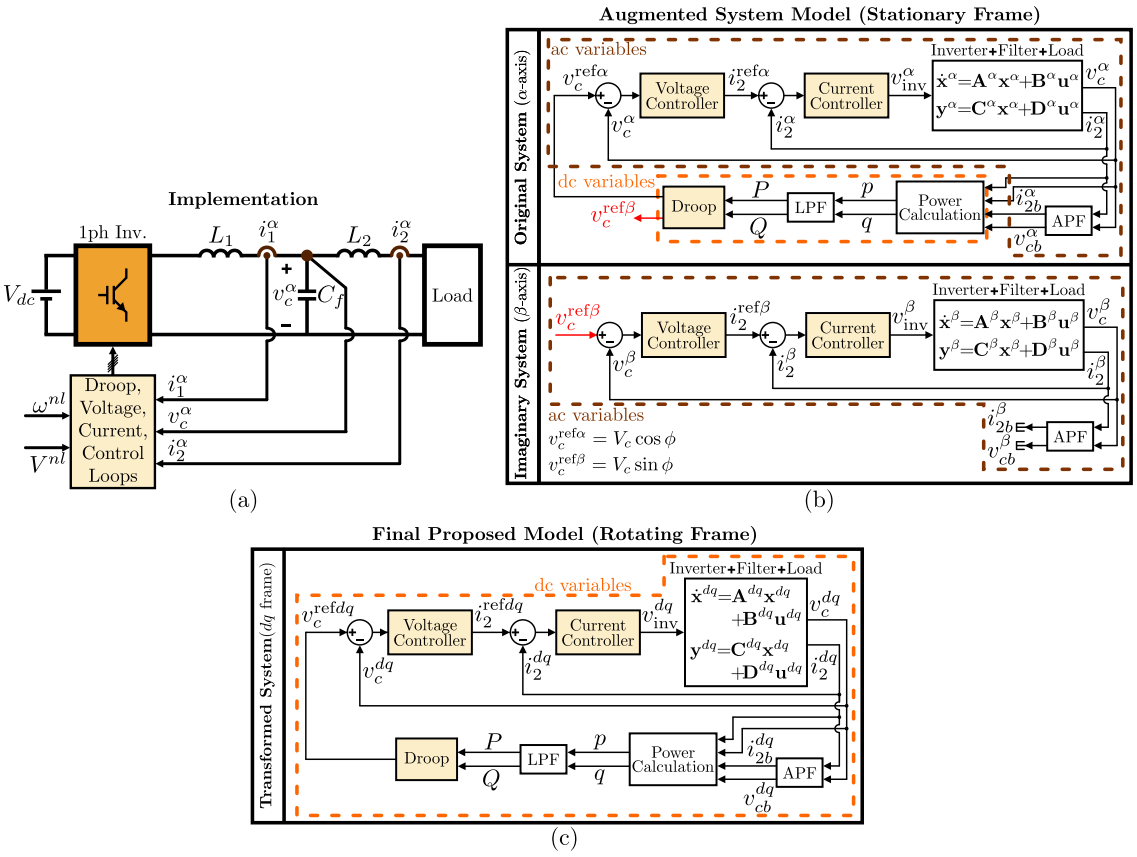

Fig. 4.2: Control system implementation and proposed modeling approach for a single-phase droop-controlled inverter: (a) implementation, (b) model containing the original, imaginary, and augmented systems in stationary frame, and (c) proposed model containing the transformed system in rotating frame.

After defining the imaginary system, the original system and the imaginary system are combined to form the augmented system in the stationary frame. Thus, the state-space equations of the augmented system are

$$\dot{\mathbf{x}}^{\alpha\beta}=\mathbf{A}^{\alpha\beta}\mathbf{x}^{\alpha\beta}+\mathbf{B}^{\alpha\beta}\mathbf{u}^{\alpha\beta},\ \mathbf{y}^{\alpha\beta}=\mathbf{C}^{\alpha\beta}\mathbf{x}^{\alpha\beta}+\mathbf{D}^{\alpha\beta}\mathbf{u}^{\alpha\beta},$$
$$\mathbf{A}^{\alpha\beta}=\begin{bmatrix}\mathbf{A} & \mathbf{0}_{l_1\times l_1}\\ \mathbf{0}_{l_1\times l_1} & \mathbf{A}\end{bmatrix},\mathbf{B}^{\alpha\beta}=\begin{bmatrix}\mathbf{B} & \mathbf{0}_{l_1\times l_2}\\ \mathbf{0}_{l_1\times l_2} & \mathbf{B}\end{bmatrix},\tag{4.3}$$
$$\mathbf{C}^{\alpha\beta}=\begin{bmatrix}\mathbf{C} & \mathbf{0}_{l_3\times l_1}\\ \mathbf{0}_{l_3\times l_1} & \mathbf{C}\end{bmatrix},\mathbf{D}^{\alpha\beta}=\begin{bmatrix}\mathbf{D} & \mathbf{0}_{l_3\times l_2}\\ \mathbf{0}_{l_3\times l_2} & \mathbf{D}\end{bmatrix},$$

where $\mathbf{x}^{\alpha\beta}=\begin{bmatrix}\mathbf{x}^{\alpha} & \mathbf{x}^{\beta}\end{bmatrix}^T$, $\mathbf{y}^{\alpha\beta}=\begin{bmatrix}\mathbf{y}^{\alpha} & \mathbf{y}^{\beta}\end{bmatrix}^T$, and $\mathbf{u}^{\alpha\beta}=\begin{bmatrix}\mathbf{u}^{\alpha} & \mathbf{u}^{\beta}\end{bmatrix}^T$. Also, l_1, l_2, and l_3 denote

the dimensions of the state vectors $\mathbf{x}^{\alpha}, \mathbf{x}^{\beta}$, input vectors $\mathbf{u}^{\alpha}, \mathbf{u}^{\beta}$, and output vectors $\mathbf{y}^{\alpha}, \mathbf{y}^{\beta}$ of the ac subsystem of the original and imaginary systems.

Now, similar to a three-phase system transformation to the rotating frame that is widely discussed in the literature [48, 121, 122], the state-space equations of the augmented system (4.3) are transformed to the rotating frame and represented by

$$\begin{gathered}\dot{\mathbf{x}}^{dq} = \mathbf{A}^{dq}\mathbf{x}^{dq} + \mathbf{B}^{dq}\mathbf{u}^{dq},\ \mathbf{y}^{dq} = \mathbf{C}^{dq}\mathbf{x}^{dq} + \mathbf{D}^{dq}\mathbf{u}^{dq}, \\ \mathbf{A}^{dq}=\begin{bmatrix}\mathbf{A} & \omega\mathbf{I}_{l_1}\\ -\omega\mathbf{I}_{l_1} & \mathbf{A}\end{bmatrix}, \mathbf{B}^{dq}=\mathbf{B}^{\alpha\beta}, \mathbf{C}^{dq}=\mathbf{C}^{\alpha\beta}, \mathbf{D}^{dq}=\mathbf{D}^{\alpha\beta},\end{gathered} \tag{4.4}$$

where $\mathbf{x}^{dq}=\begin{bmatrix}\mathbf{x}^{d} & \mathbf{x}^{q}\end{bmatrix}^{T}$, $\mathbf{y}^{dq}=\begin{bmatrix}\mathbf{y}^{d} & \mathbf{y}^{q}\end{bmatrix}^{T}$, and $\mathbf{u}^{dq}=\begin{bmatrix}\mathbf{u}^{d} & \mathbf{u}^{q}\end{bmatrix}^{T}$. Also, ω refers to the rotating speed of the frame. Observing (4.3) and (4.4), based on elementary rules of linear algebra, it is concluded that $\lambda(\mathbf{A}^{dq}) = \lambda(\mathbf{A}^{\alpha\beta}) \pm j\omega$ and $\lambda(\mathbf{A}^{\alpha\beta}) = \lambda(\mathbf{A})$. Thus, the proposed approach does not alter the stability property, i.e. $\mathrm{Re}\left(\lambda(\mathbf{A}^{dq})\right) = \mathrm{Re}\left(\lambda(\mathbf{A})\right)$.

In summary, in the proposed modeling approach, the imaginary system (4.2) is defined the same as the ac subsystem of the original system (4.1) and excited by the quadrature signal u^{β}. Also, there is no feedback from the imaginary system to the original system. Therefore, the proposed modeling does not alter the stability properties of the original system. Moreover, the control system is designed and implemented in the stationary frame (without OSGs), and the imaginary system is only used for the system modeling and stability analysis. Thus, parameters' mismatch, which is a challenge in FAE method [94] and leads to steady-state errors in the orthogonal signals, does not have such a negative effect on the control system performance. This is further explained in Section 4.4.

The following algorithm summarizes the framework of the proposed approach. Details of how to run the algorithm are discussed subsequently.

Proposed Step-by-step Modeling Algorithm:

Step 1 : Derive state-space equations of the original system.

Step 2 : Consider the *ac subsystem* of the original system as α-axis system, i.e. (4.1).

Step 3 : Define an imaginary system, β-axis system, the same as the system of Step 2 excited by the quadrature signal, i.e. (4.2).

Step 4 : Combine (4.1)-(4.2) to derive the state equations of the augmented system in the stationary frame, i.e. (4.3).

Step 5 : Apply Park's transformation to (4.3) to derive the equations in the rotating frame, i.e. (4.4).

4.2 Microgrid Equations in Stationary Frame

In this section, the entire state-space equations of the microgrid, depicted in Fig. 4.1, including the parallel inverters and microgrid load are derived in the stationary frame. Also, as all inverters are in a parallel connection with each other, the state-space equations for one of the parallel inverters are derived in the following.

4.2.1 Droop-controlled Inverter Equations in Stationary Frame

The control system of a droop-controlled inverter contains three cascade loops which are the current, voltage, and droop control loops as depicted in Fig. 4.3. The two inner current and voltage control loops have only ac state variables such as voltages, currents, and controllers' state variables. The droop control loop introduces dc variables such as the active and reactive powers. The droop control also contains nonlinear and trigonometric functions. Therefore, the entire system mixes both ac and dc variables and linear and nonlinear dynamics.

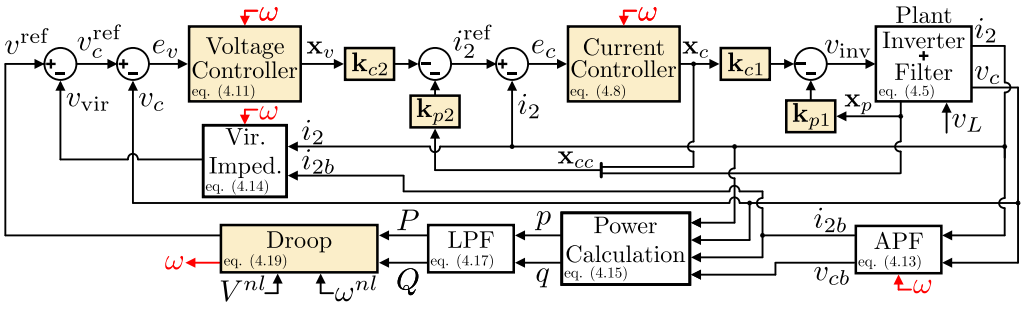

Fig. 4.3: Control loops of a droop-controlled inverter in the stationary frame.

4.2.1.1 Current Control Loop

The structure of the current control loop of an inverter with an LCL filter is shown in Fig. 4.3. The state-space equations of the plant, containing the inverter and its filter, are

$$\dot{\mathbf{x}}_p = \mathbf{A}_p\mathbf{x}_p + \mathbf{B}_p v_{\text{inv}} + \mathbf{B}_{pL} v_L,\ \ \mathbf{y}_p = \mathbf{C}_p\mathbf{x}_p, \tag{4.5}$$

where $\mathbf{x}_p = [i_1\ v_c\ i_2]^T$ and $\mathbf{y}_p = [i_2\ v_c]^T$. Also, i_1, v_c, i_2, v_{inv}, and v_L refer to the current of the inverter-side inductor, the capacitor voltage, the current of the load-side inductor, the inverter voltage, and the load voltage, respectively. Moreover, $\mathbf{A}_p$, $\mathbf{B}_p$, $\mathbf{B}_{pL}$, and $\mathbf{C}_p$ are defined as follows

$$\begin{gathered}\mathbf{A}_p = \begin{bmatrix} 0 & \frac{-1}{L_1} & 0 \\ \frac{1}{C_f} & 0 & \frac{-1}{C_f} \\ 0 & \frac{1}{L_2} & 0 \end{bmatrix}, \mathbf{B}_p = \begin{bmatrix} \frac{1}{L_1} \\ 0 \\ 0 \end{bmatrix}, \mathbf{B}_{pL} = \begin{bmatrix} 0 \\ 0 \\ \frac{-1}{L_2} \end{bmatrix}, \\ \mathbf{C}_p = \begin{bmatrix} \mathbf{C}_{p1} & \mathbf{C}_{p2} \end{bmatrix}^T, \mathbf{C}_{p1} = \begin{bmatrix} 0 & 0 & 1 \end{bmatrix}, \mathbf{C}_{p2} = \begin{bmatrix} 0 & 1 & 0 \end{bmatrix},\end{gathered} \tag{4.6}$$

where L_1, C_f, and L_2 denote the inverter-side inductance, capacitance, and the load-side inductance of the LCL filter.

As one of the control objectives is to regulate the load-side current i_2, the current control loop is closed on that current. In this study, the resonant controller

introduced in Section 3.3 is used, and its transfer function is as follows

$$\frac{U_c}{E_c} = \frac{k_{c12}s + k_{c11}}{s^2 + \omega^2}, \tag{4.7}$$

where u_c is the resonant current controller effort, k_{c11} and k_{c12} are the controller parameters, and $e_c = i_2^{\text{ref}} - i_2$ is the current tracking error. Thus, the State-space equation of the current controller is

$$\begin{gathered} \dot{\mathbf{x}}_c = \mathbf{A}_c\mathbf{x}_c + \mathbf{B}_c e_c, \\ \mathbf{A}_c = \begin{bmatrix} 0 & 1 \\ -\omega^2 & 0 \end{bmatrix}, \ \mathbf{B}_c = \begin{bmatrix} 0 \\ 1 \end{bmatrix}, \end{gathered} \tag{4.8}$$

where $\mathbf{x}_c = [x_{c1} \ x_{c2}]^T$ is the state vector of the current controller, and ω is the operating angular frequency determined by the droop.

Considering $v_{\text{inv}} = -\mathbf{k}_{c1}\mathbf{x}_c - \mathbf{k}_{p1}\mathbf{x}_p$ where $\mathbf{k}_{c1} = [k_{c11} \ k_{c12}]$ and $\mathbf{k}_{p1} = [k_{p11} \ \cdots \ k_{p13}]$, (4.5)-(4.8) form the state-space equations of the current control loop as

$$\begin{gathered} \dot{\mathbf{x}}_{cc} = \mathbf{A}_{cc}\mathbf{x}_{cc} + \mathbf{B}_{cc} i_2^{\text{ref}} + \mathbf{B}_{cL} v_L, \ y_{cc} = \mathbf{C}_{cc}\mathbf{x}_{cc}, \\ \mathbf{A}_{cc} = \begin{bmatrix} \mathbf{A}_c & -\mathbf{B}_c\mathbf{C}_{p1} \\ -\mathbf{B}_p\mathbf{k}_{c1} & \mathbf{A}_p - \mathbf{B}_p\mathbf{k}_{p1} \end{bmatrix}, \\ \mathbf{B}_{cc} = \begin{bmatrix} \mathbf{B}_c \\ \mathbf{0}_{3\times 1} \end{bmatrix}, \mathbf{B}_{cL} = \begin{bmatrix} \mathbf{0}_{2\times 1} \\ \mathbf{B}_{pL} \end{bmatrix}, \mathbf{C}_{cc} = \begin{bmatrix} \mathbf{0}_{1\times 2} & \mathbf{C}_{p2} \end{bmatrix}, \end{gathered} \tag{4.9}$$

where $\mathbf{x}_{cc} = [\mathbf{x}_c \ \mathbf{x}_p]^T$ and $y_{cc} = v_c$. The gain vectors $\mathbf{k}_{c1}$ and $\mathbf{k}_{p1}$ are designed using the LQT method as discussed in Section 3.4.

4.2.1.2 Voltage Control Loop

The voltage control loop is also shown in Fig. 4.3. The voltage controller is also a resonant controller with the following transfer function

$$\frac{U_v}{E_v} = \frac{k_{c22}s + k_{c21}}{s^2 + \omega^2}, \tag{4.10}$$

where u_v is the resonant voltage controller effort, k_{c21} and k_{c22} are the controller parameters, and $e_v = v_c^{\text{ref}} - v_c$ denotes the voltage error. Also, the state-space equation of the voltage controller is

$$\dot{\mathbf{x}}_v = \mathbf{A}_v\mathbf{x}_v + \mathbf{B}_v e_v, \tag{4.11}$$

where $\mathbf{x}_v = [x_{v1}\ x_{v2}]^T$ is the state vector of the voltage controller. Also, $\mathbf{A}_v$ and $\mathbf{B}_v$ are equal to $\mathbf{A}_c$ and $\mathbf{B}_c$ in (4.8), respectively.

Using $i_2^{\text{ref}} = -\mathbf{k}_{c2}\mathbf{x}_v - \mathbf{k}_{p2}\mathbf{x}_{cc}$ where $\mathbf{k}_{c2} = [k_{c21}\ k_{c22}]$ and $\mathbf{k}_{p2} = [k_{p21}\ \cdots\ k_{p25}]$, the state-space equations of the resonant controller (4.11) and the current control loop (4.9) are augmented to derive the voltage control loop equations

$$\begin{gathered}
\dot{\mathbf{x}}_{vc} = \mathbf{A}_{vc}\mathbf{x}_{vc} + \mathbf{B}_{vc}v_c^{\text{ref}} + \mathbf{B}_{vL}v_L,\ \mathbf{y}_{vc} = \mathbf{C}_{vc}\mathbf{x}_{vc}, \\
\mathbf{A}_{vc} = \begin{bmatrix} \mathbf{A}_v & -\mathbf{B}_v\mathbf{C}_{cc} \\ -\mathbf{B}_{cc}\mathbf{k}_{c2} & \mathbf{A}_{cc} - \mathbf{B}_{cc}\mathbf{k}_{p2} \end{bmatrix}, \\
\mathbf{B}_{vc} = \begin{bmatrix} \mathbf{B}_v \\ \mathbf{0}_{5\times 1} \end{bmatrix}, \mathbf{B}_{vL} = \begin{bmatrix} \mathbf{0}_{2\times 1} \\ \mathbf{B}_{cL} \end{bmatrix}, \mathbf{C}_{vc} = \begin{bmatrix} \mathbf{0}_{2\times 4} & \mathbf{C}_p \end{bmatrix},
\end{gathered} \tag{4.12}$$

where $\mathbf{x}_{vc} = [\mathbf{x}_v\ \mathbf{x}_{cc}]^T$ and $\mathbf{y}_{vc} = \mathbf{y}_p$. Moreover, $\mathbf{k}_{c2}$ and $\mathbf{k}_{p2}$ are optimally designed using the LQT method as explained in Section 3.4.

4.2.1.3 Droop Control Loop

The droop control loop consists of the voltage control loop, all-pass filters, virtual impedance, power calculation block, low-pass filters, and droop characteristics

as shown in Fig. 4.3.

All-Pass Filter Block: First-order all-pass filters (APFs) are used to introduce 90° phase-shift. The state-space equations of the APFs are

$$\begin{aligned} \dot{\mathbf{x}}_{ap} &= \mathbf{A}_{ap}\mathbf{x}_{ap} + \mathbf{B}_{ap}\mathbf{u}_{ap},\ \mathbf{y}_{ap} = \mathbf{C}_{ap}\mathbf{x}_{ap} + \mathbf{D}_{ap}\mathbf{u}_{ap}, \\ \mathbf{A}_{ap} &= -\omega\mathbf{I}_2,\ \mathbf{B}_{ap} = \omega\mathbf{I}_2,\ \mathbf{C}_{ap} = 2\mathbf{I}_2, \mathbf{D}_{ap} = -\mathbf{I}_2, \end{aligned} \tag{4.13}$$

where $\mathbf{x}_{ap}$ is the state vector of the APFs, $\mathbf{u}_{ap}$=$[i_2\ v_c]^T$, $\mathbf{y}_{ap}$=$[i_{2b}\ v_{cb}]^T$, and $\mathbf{I}_2$ is the identity matrix of dimension 2.

Virtual Impedance Block: An RL virtual impedance, $G_{\text{vir}} = R_{\text{vir}} + L_{\text{vir}}s$, is used to fix the output impedance of the inverter and to improve the stability of parallel inverters [123, 124]. Considering i_2 and v_{vir} as the input and output of this block, respectively, the voltage drop across the virtual impedance is $v_{\text{vir}} = R_{\text{vir}}i_2 + L_{\text{vir}}\frac{di_2}{dt}$. For a sinusoidal signal with the angular frequency ω, the derivative term can be approximated as $\frac{d(i_2)}{dt} = -\omega i_{2b}$, where i_{2b} is the 90° phase-shifted signal of i_2 and is generated by the APF. Therefore, the virtual impedance equation is rewritten as

$$y_{\text{vir}} = \mathbf{D}_{\text{vir}}\mathbf{u}_{\text{vir}},\ \mathbf{D}_{\text{vir}} = \begin{bmatrix} R_{\text{vir}} & -L_{\text{vir}}\omega \end{bmatrix}, \tag{4.14}$$

where $\mathbf{u}_{\text{vir}}$=$[i_2\ i_{2b}]^T$ and $y_{\text{vir}} = v_{\text{vir}}$.

Power Calculation Block: It calculates the instantaneous active and reactive powers, and its equation is given by

$$\mathbf{y}_{pq} = \mathbf{f}_{pq}(\mathbf{u}_{pq}),\ \mathbf{f}_{pq} = \begin{bmatrix} f_p & f_q \end{bmatrix}^T, \tag{4.15}$$

where $\mathbf{u}_{pq}$=$[i_2\ i_{2b}\ v_c\ v_{cb}]^T$ and $\mathbf{y}_{pq}$=$[p\ q]^T$. Also, power calculation functions f_p and f_q are

$$f_p = 0.5\left(v_c i_2 + v_{cb} i_{2b}\right),\ f_q = 0.5\left(v_{cb} i_2 - v_c i_{2b}\right). \tag{4.16}$$

This block adds nonlinear dynamics to the system.

Low-pass Filter Block: Low-pass filters (LPFs) are used for the power measurement to smooth down active and reactive power characteristics. Also, LPFs give an inertia-type behavior to the inverter [125]. For first-order LPFs with the transfer function $G_{lp}(s)=\frac{1}{\tau_{lp}s+1}$, where τ_{lp} is the time-constant of the LPFs, the state-space equations are

$$\begin{aligned} \dot{\mathbf{x}}_{lp} &= \mathbf{A}_{lp}\mathbf{x}_{lp} + \mathbf{B}_{lp}\mathbf{u}_{lp},\ \mathbf{y}_{lp} = \mathbf{C}_{lp}\mathbf{x}_{lp}, \\ \mathbf{A}_{lp} &= \frac{-1}{\tau_{lp}}\mathbf{I}_2,\ \mathbf{B}_{lp} = \frac{1}{\tau_{lp}}\mathbf{I}_2,\ \mathbf{C}_{lp} = \mathbf{I}_2, \end{aligned} \tag{4.17}$$

where $\mathbf{u}_{lp}=[p\ q]^T$ and $\mathbf{x}_{lp}=\mathbf{y}_{lp}=[P\ Q]^T$.

Droop Block: Droop characteristics are expressed by

$$\begin{aligned} \dot{\phi} &= \omega,\ v^{\text{ref}} = V\cos\phi, \\ \omega &= \omega^{nl} - m_p P,\ V = V^{nl} - m_q Q, \end{aligned} \tag{4.18}$$

where ω, V, and ϕ refer to the angular frequency, amplitude, and angle of the reference voltage v^{ref}. Also, ω^{nl} and V^{nl} denote the no-load angular frequency and amplitude of the no-load voltage, and m_p and m_q are the droop coefficients. These equations can be rewritten in the state-space form as

$$\begin{aligned} \dot{x}_d = \mathbf{B}_d\mathbf{u}_d,\ \mathbf{y}_d = \mathbf{f}_d(x_d,\mathbf{u}_d) = \begin{bmatrix} f_d(x_d,\mathbf{u}_d) & \mathbf{D}_{2d}\mathbf{u}_d \end{bmatrix}^T \\ \mathbf{B}_d = \mathbf{D}_{2d} = \begin{bmatrix} -m_p & 0 & 1 & 0 \end{bmatrix}, \end{aligned} \tag{4.19}$$

where $x_d=\phi$, $\mathbf{u}_d = \begin{bmatrix} P\ Q\ \omega^{nl}\ V^{nl} \end{bmatrix}^T$, $\mathbf{y}_d=\begin{bmatrix} v^{\text{ref}}\ \omega \end{bmatrix}^T$, and $f_d = (V^{nl} - m_q Q)\cos\phi$. The droop loop introduces dc state variables such as the active and reactive powers, and also nonlinear and trigonometric terms.

4.2.2 Microgrid Load Equations in Stationary Frame

It is assumed that the microgrid load is a combination of series resistive R, inductive L, and capacitive C components. Therefore, the load voltage can be calculated as $v_L=Ri_L+L\frac{di_L}{dt}+v_{c_L}$. The capacitive component C introduces a new

state variable as $\dot{v}_{c_L} = \frac{1}{C} i_L$, where v_{c_L} and i_L are the capacitive part of the load voltage and the current, respectively. According to $i_L = \sum_{n=1}^{N} i_{2,n}$ and $\frac{di_{2,n}}{dt} = \frac{v_{c,n} - v_L}{L_{2,n}}$, the load voltage is written as

$$v_L = \frac{R \sum_{n=1}^{N} i_{2,n} + L \sum_{n=1}^{N} \frac{v_{c,n}}{L_{2,n}} + v_{c_L}}{\Lambda}, \tag{4.20}$$

where $\Lambda = 1 + L \sum_{n=1}^{N} \frac{1}{L_{2,n}}$. Hereinafter, the indices "$,n$" and "n" refer to signals, variables, and components of the n^{th} inverter. The state-space equations of the microgrid load are

$$\begin{aligned} \dot{x}_L &= \mathbf{B}_L \mathbf{u}_L, y_L = \mathbf{C}_L x_L + \mathbf{D}_L \mathbf{u}_L, \\ \mathbf{B}_L &= \frac{1}{C} \text{ones}(1, 2N),\ \mathbf{C}_L = \begin{bmatrix} \frac{1}{\Lambda} \end{bmatrix}, \\ \mathbf{D}_L &= \frac{\begin{bmatrix} R \times \text{ones}(1, N) & \frac{L}{L_{2,1}} & \cdots & \frac{L}{L_{2,N}} \end{bmatrix}}{\Lambda}, \end{aligned} \tag{4.21}$$

where $\mathbf{u}_L = [i_{2,1} \ \cdots \ i_{2,N} \ v_{c,1} \ \cdots \ v_{c,N}]^T$, $x_L = v_{c_L}$, $y_L = v_L$.

To sum up, in this section, the state-space equations of the microgrid, depicted in Fig. 4.1, are derived in the stationary frame. Therefore, in the next section, an imaginary-twin system is defined with respect to (4.5)-(4.21) to generate required signals for Park's transformation without adding any OSGs.

4.3 Microgrid Equations in Rotating Frame

4.3.1 Proposed Approach Implementation

According to the proposed modeling algorithm in Section 4.1, first, all state equations of the original system, derived in Section 4.2, are considered to form the α-axis system (*Step 1* and *Step 2*). Then, the imaginary system, β-axis system, is defined accordingly, (*Step 3*). In this case, the state-space equations containing ac variables in Section 4.2, i.e. (4.5)-(4.14) and (4.21), are valid for the imaginary

system as well. Also, as the inputs of the imaginary system $v_n^{\text{ref}\beta}$ and the ac subsystem of the original system $v_n^{\text{ref}\alpha}$ are orthogonal, their variables are orthogonal as well. Now, the original and imaginary systems are combined to form the augmented system in the stationary frame as depicted in Fig. 4.4 (*Step 4*). Finally, the equations of the augmented system are converted to the rotating frame (*Step 5*). In this study, all state-space equations are transformed to the first inverter frame, whose angle is determined by the first inverter droop angle ϕ_1 and rotates with the angular frequency $\omega_1 = \frac{d\phi_1}{dt}$.

4.3.2 Droop-controlled Inverter Equations in Rotating Frame

In the following, the equations of the n^{th} droop-controlled inverter (4.12)-(4.19) are transformed to the rotating frame using the equation derived for the transformation (4.4) [48].

Regarding the voltage and current control loops of the n^{th} inverter, equation (4.12), which contains both loops dynamics, is written in the rotating frame as

$$\begin{gathered}
\dot{\mathbf{x}}_{vc,n}^{dq} = \mathbf{A}_{vc,n}^{dq}\mathbf{x}_{vc,n}^{dq} + \mathbf{B}_{vc,n}^{dq}v_{c,n}^{\text{ref}dq} + \mathbf{B}_{vL,n}^{dq}v_L^{dq}, \\
\mathbf{y}_{vc,n}^{dq} = \mathbf{C}_{vc,n}^{dq}\mathbf{x}_{vc,n}^{dq}, \\
\mathbf{A}_{vc,n}^{dq}=\begin{bmatrix} \mathbf{A}_{vc,n} & \omega_1\mathbf{I}_7 \\ -\omega_1\mathbf{I}_7 & \mathbf{A}_{vc,n} \end{bmatrix}, \mathbf{B}_{vc,n}^{dq}=\begin{bmatrix} \mathbf{B}_{vc,n} & \mathbf{0}_{7\times1} \\ \mathbf{0}_{7\times1} & \mathbf{B}_{vc,n} \end{bmatrix}, \\
\mathbf{B}_{vL,n}^{dq}=\begin{bmatrix} \mathbf{B}_{vL,n} & \mathbf{0}_{7\times1} \\ \mathbf{0}_{7\times1} & \mathbf{B}_{vL,n} \end{bmatrix}, \mathbf{C}_{vc,n}^{dq}=\begin{bmatrix} \mathbf{C}_{vc,n} & \mathbf{0}_{2\times7} \\ \mathbf{0}_{2\times7} & \mathbf{C}_{vc,n} \end{bmatrix},
\end{gathered} \tag{4.22}$$

where $\mathbf{x}_{vc,n}^{dq} = \begin{bmatrix}\mathbf{x}_{v,n}^d & \mathbf{x}_{cc,n}^d & \mathbf{x}_{v,n}^q & \mathbf{x}_{cc,n}^q\end{bmatrix}^T$ and $\mathbf{y}_{vc,n}^{dq} = \begin{bmatrix}i_{2,n}^d & v_{c,n}^d & i_{2,n}^q & v_{c,n}^q\end{bmatrix}^T$. Also, $\mathbf{x}_{cc,n}^{dq} = \begin{bmatrix}\mathbf{x}_{c,n}^d & \mathbf{x}_{p,n}^d & \mathbf{x}_{c,n}^q & \mathbf{x}_{p,n}^q\end{bmatrix}^T$ and $\mathbf{x}_{p,n}^{dq}=\begin{bmatrix}i_{1,n}^d & v_{c,n}^d & i_{2,n}^d & i_{1,n}^q & v_{c,n}^q & i_{2,n}^d\end{bmatrix}^T$.

The next step is to transform the state-space equations of the droop loop to the rotating frame. Considering the state-space equations of APFs (4.13), the

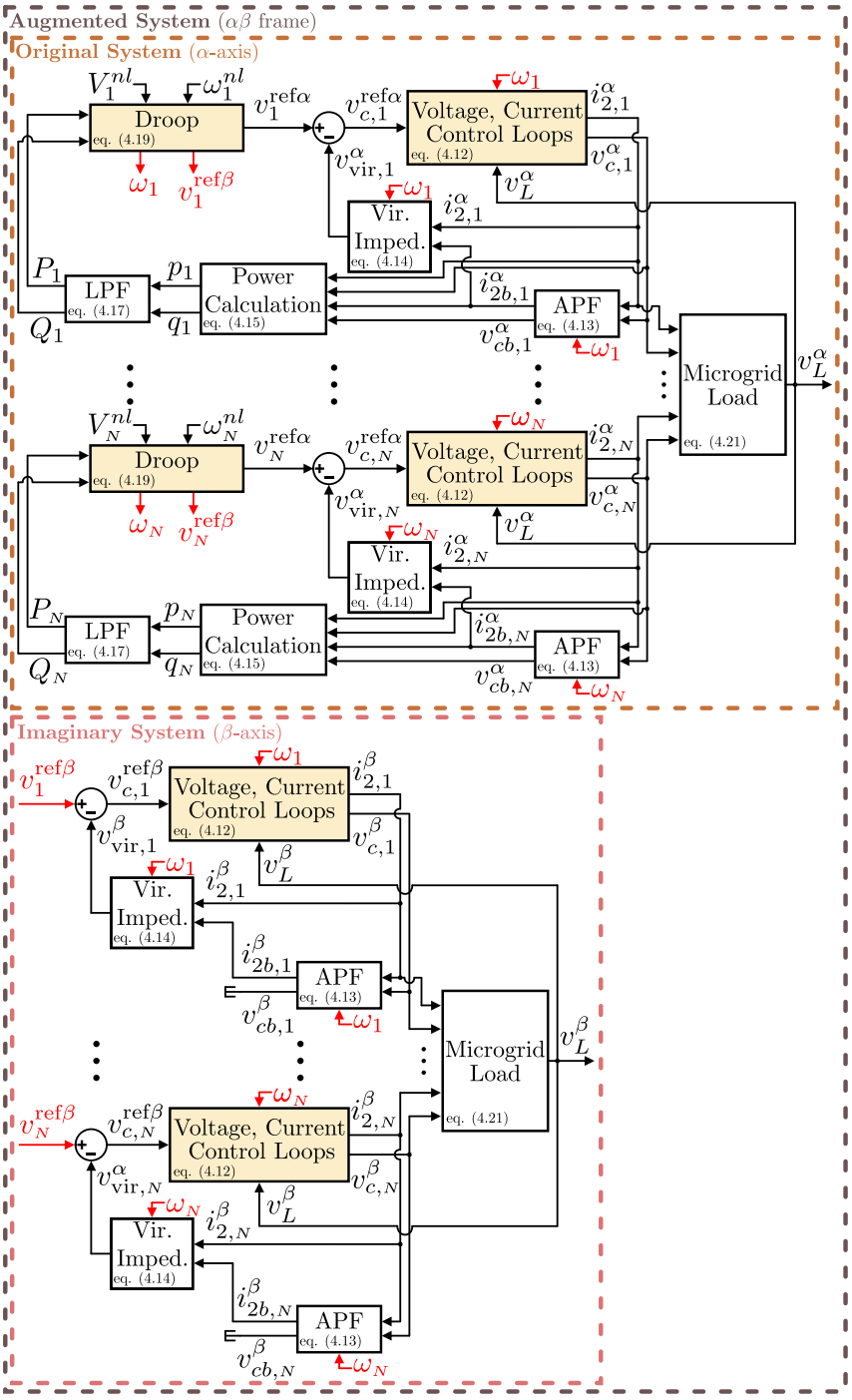

Fig. 4.4: Control block diagrams of the original, imaginary, and augmented systems for N parallel inverters in stationary frame.

transformed equations are

$$\begin{aligned}
\dot{\mathbf{x}}_{ap,n}^{dq} &= \mathbf{A}_{ap,n}^{dq}\mathbf{x}_{ap,n}^{dq} + \mathbf{B}_{ap,n}^{dq}\mathbf{u}_{ap,n}^{dq},\\
\mathbf{y}_{ap,n}^{dq} &= \mathbf{C}_{ap,n}^{dq}\mathbf{x}_{ap,n}^{dq} + \mathbf{D}_{ap,n}^{dq}\mathbf{u}_{ap,n}^{dq},\\
\mathbf{A}_{ap,n}^{dq}&=\begin{bmatrix}\mathbf{A}_{ap,n} & \omega_1\mathbf{I}_2\\ -\omega_1\mathbf{I}_2 & \mathbf{A}_{ap,n}\end{bmatrix}, \mathbf{B}_{ap,n}^{dq}=\begin{bmatrix}\mathbf{B}_{ap,n} & \mathbf{0}_{2\times2}\\ \mathbf{0}_{2\times2} & \mathbf{B}_{ap,n}\end{bmatrix},\\
\mathbf{C}_{ap,n}^{dq}&=\begin{bmatrix}\mathbf{C}_{ap,n} & \mathbf{0}_{2\times2}\\ \mathbf{0}_{2\times2} & \mathbf{C}_{ap,n}\end{bmatrix}, \mathbf{D}_{ap,n}^{dq}=\begin{bmatrix}\mathbf{D}_{ap,n} & \mathbf{0}_{2\times2}\\ \mathbf{0}_{2\times2} & \mathbf{D}_{ap,n}\end{bmatrix},
\end{aligned} \tag{4.23}$$

where $\mathbf{u}_{ap,n}^{dq}=\begin{bmatrix}i_{2,n}^{d} & v_{c,n}^{d} & i_{2,n}^{q} & v_{c,n}^{q}\end{bmatrix}^T$, $\mathbf{y}_{ap,n}^{dq}=\begin{bmatrix}i_{2b,n}^{d} & v_{cb,n}^{d} & i_{2b,n}^{q} & v_{cb,n}^{q}\end{bmatrix}^T$.

Considering (4.14), the transformed equation of the virtual impedance block in the rotating frame is

$$\mathbf{y}_{\mathrm{vir},n}^{dq} = \mathbf{D}_{\mathrm{vir},n}^{dq}\mathbf{u}_{\mathrm{vir},n}^{dq},\ \mathbf{D}_{\mathrm{vir},n}^{dq} = \begin{bmatrix}\mathbf{D}_{\mathrm{vir},n} & \mathbf{0}_{1\times2}\\ \mathbf{0}_{1\times2} & \mathbf{D}_{\mathrm{vir},n}\end{bmatrix}, \tag{4.24}$$

where $\mathbf{u}_{\mathrm{vir},n}^{dq}=\begin{bmatrix}i_{2,n}^{d} & i_{2b,n}^{d} & i_{2,n}^{q} & i_{2b,n}^{q}\end{bmatrix}^T$, $\mathbf{y}_{\mathrm{vir},n}^{dq}=\begin{bmatrix}v_{\mathrm{vir},n}^{d} & v_{\mathrm{vir},n}^{q}\end{bmatrix}^T$.

As for the power calculation block, (4.15) can be rewritten based on the rotating frame variables as

$$\mathbf{y}_{pq,n} = \mathbf{g}_{pq,n}(\mathbf{u}_{pq,n}^{dq}),\ \mathbf{g}_{pq,n} = \begin{bmatrix} g_{p,n} & g_{q,n}\end{bmatrix}^T, \tag{4.25}$$

where $\mathbf{u}_{pq,n}^{dq}=\begin{bmatrix}i_{2,n}^{dq} & i_{2b,n}^{dq} & v_{c,n}^{dq} & v_{cb,n}^{dq}\end{bmatrix}^T$, $\mathbf{y}_{pq,n}=[p_n\ q_n]^T$ and

$$\begin{aligned}
g_{p,n}&=0.25\left(v_{c,n}^{d}i_{2,n}^{d}+v_{c,n}^{q}i_{2,n}^{q}+v_{cb,n}^{d}i_{2b,n}^{d}+v_{cb,n}^{q}i_{2b,n}^{q}\right),\\
g_{q,n}&=0.25\left(v_{cb,n}^{d}i_{2,n}^{d}+v_{cb,n}^{q}i_{2,n}^{q}-v_{c,n}^{d}i_{2b,n}^{d}-v_{c,n}^{q}i_{2b,n}^{q}\right).
\end{aligned} \tag{4.26}$$

For the LPF block of the n^{th} inverter, (4.17) is rewritten as

$$\dot{\mathbf{x}}_{lp,n} = \mathbf{A}_{lp,n}\mathbf{x}_{lp,n} + \mathbf{B}_{lp,n}\mathbf{u}_{lp,n},\ \mathbf{y}_{lp,n} = \mathbf{C}_{lp,n}\mathbf{x}_{lp,n}, \tag{4.27}$$

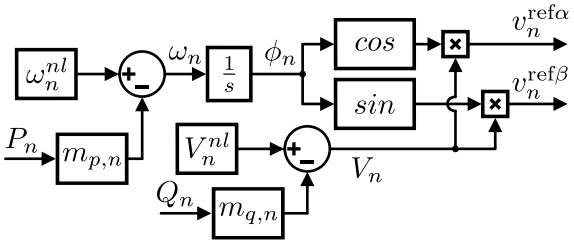

Fig. 4.5: Droop configuration of the n^{th} inverter.

where $\mathbf{u}_{lp,n}$=$[p_n\ q_n]^T$ and $\mathbf{x}_{lp,n}$=$\mathbf{y}_{lp,n}$=$[P_n\ Q_n]^T$.

Fig. 4.5 depicts the droop block diagram that illustrates how the reference signals are generated for the original system $v_n^{\text{ref}\alpha}$ and the imaginary system $v_n^{\text{ref}\beta}$. In this figure, as ϕ_n is a ramp function, it is not proper for the system linearization and finding the operating point. Since all equations are transformed to the first inverter rotating frame, a new state variable $z_{d,n}$ is defined as $z_{d,n} \triangleq \phi_n - \phi_1$. Although both ϕ_n and ϕ_1 are ramp functions, their difference $z_{d,n}$ is a dc variable. According to the new variable definition and (4.18), the droop characteristics of the n^{th} inverter in the rotating frame are

$$\begin{aligned} \dot{z}_{d,n} &= \dot{\phi}_n - \dot{\phi}_1 = \omega_n^{nl} - m_{p,n}P_n - \omega_1, \\ v_n^{\text{ref}d} &= V_n \cos z_{d,n},\ v_n^{\text{ref}q} = V_n \sin z_{d,n}, \\ \omega_n &= \omega_n^{nl} - m_{p,n}P_n,\ V_n = V_n^{nl} - m_{q,n}Q_n. \end{aligned} \tag{4.28}$$

Therefore, according to (4.19) and (4.28), the state-space equations of the droop characteristics in the rotating frame are

$$\begin{aligned} \dot{z}_{d,n} = \mathbf{B}_{d,n}^{dq}\mathbf{u}_{d,n}^{dq}, \mathbf{y}_{d,n}^{dq} &= \begin{bmatrix} \mathbf{g}_d(z_{d,n}, \mathbf{u}_{d,n}^{dq}) & \mathbf{D}_{3d,n}\mathbf{u}_{d,n}^{dq} \end{bmatrix}^T \\ \mathbf{B}_{d,n}^{dq} = \begin{bmatrix} \mathbf{B}_{d,n} & -1 \end{bmatrix},\ \mathbf{D}_{3d,n}^{dq} &= \begin{bmatrix} \mathbf{D}_{2d,n} & 0 \end{bmatrix}, \end{aligned} \tag{4.29}$$

where $\mathbf{u}_{d,n}^{dq} = [\mathbf{u}_{d,n}\ \omega_1]^T$, $\mathbf{y}_{d,n}^{dq}$=$\begin{bmatrix} v_n^{\text{ref}d} & v_n^{\text{ref}q} & \omega_n \end{bmatrix}^T$, and

$$\mathbf{g}_d = \begin{bmatrix} (V_n^{nl} - m_{q,n}Q_n)\cos z_{d,n} & (V_n^{nl} - m_{q,n}Q_n)\sin z_{d,n} \end{bmatrix}^T.$$

It is worth mentioning that because all equations are transformed to the first inverter

rotating frame, the droop state of the first inverter $z_{d,1}$ is automatically removed from the state-space equations of the microgrid in the rotating frame.

4.3.3 Microgrid Load Equations in Rotating Frame

Using the proposed method, the state-space equations of the microgrid load in the rotating frame are

$$\begin{gathered}\dot{\mathbf{x}}_L^{dq} = \mathbf{A}_L^{dq}\mathbf{x}_L^{dq} + \mathbf{B}_L^{dq}\mathbf{u}_L^{dq},\ \mathbf{y}_L^{dq} = \mathbf{C}_L^{dq}\mathbf{x}_L^{dq} + \mathbf{D}_L^{dq}\mathbf{u}_L^{dq},\\ \mathbf{A}_L^{dq}=\begin{bmatrix} 0 & \omega_1 \\ -\omega_1 & 0 \end{bmatrix}, \mathbf{B}_L^{dq}=\begin{bmatrix} \mathbf{B}_L & \mathbf{0}_{1\times 2N} \\ \mathbf{0}_{1\times 2N} & \mathbf{B}_L \end{bmatrix},\\ \mathbf{C}_L^{dq}=\begin{bmatrix} \mathbf{C}_L & 0 \\ 0 & \mathbf{C}_L \end{bmatrix}, \mathbf{D}_L^{dq}=\begin{bmatrix} \mathbf{D}_L & \mathbf{0}_{1\times 2N} \\ \mathbf{0}_{1\times 2N} & \mathbf{D}_L \end{bmatrix},\end{gathered} \tag{4.30}$$

where $\mathbf{x}_L^{dq}=\begin{bmatrix} v_{c_L}^d & v_{c_L}^q \end{bmatrix}^T$, $\mathbf{y}_L^{dq}=\begin{bmatrix} v_L^d & v_L^q \end{bmatrix}^T$, and

$$\mathbf{u}_L^{dq}=\begin{bmatrix} i_{2,1}^d & \cdots & i_{2,N}^d & v_{c,1}^d & \cdots & v_{c,N}^d & i_{2,1}^q & \cdots & i_{2,N}^q & v_{c,1}^q & \cdots & v_{c,N}^q \end{bmatrix}^T.$$

Finally, based on (4.22)-(4.30), Fig. 4.4, which illustrates the microgrid model, including the original, imaginary, and augmented systems in the stationary frame, can be redrawn as depicted in Fig. 4.6. This figure shows the mathematical model of the single-phase microgrid in the rotating frame based on the proposed approach. This model only contains dc variables; thus, the stability analysis of the microgrid and the parameter sensitivity can be studied as explained in Section 4.4.

Furthermore, according to Fig. 4.4 and Fig. 4.6, it is observed that, for N parallel inverters, the total number of state variables of the augmented and transformed systems equals $21N + 1$. On the other hand, the number of state variables of the original system is equal to $12N + 1$. Although the proposed method for modeling a single-phase microgrid, controlled in the stationary frame, increases the order of the entire system, the transformation does not affect dynamics and stability properties of the original system as discussed in Section 4.1.

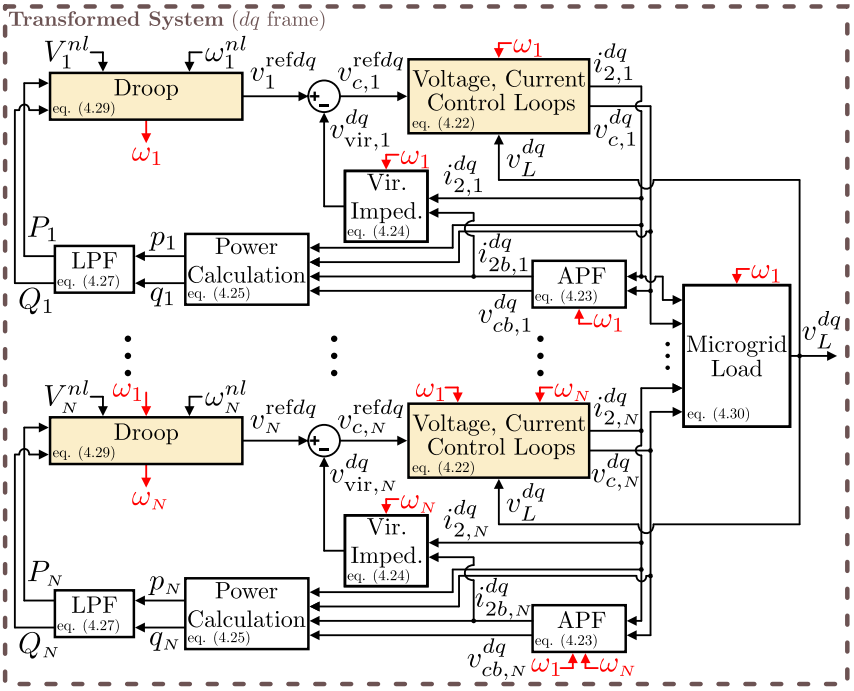

Fig. 4.6: Control block diagrams of the transformed system for N parallel inverters in the rotating frame.

4.4 Stability Analysis and Model Verification

In this section, the microgrid stability analysis is addressed using the proposed model, shown in Fig. 4.6. Then, the accuracy of the proposed modeling approach is verified and compared with existing approaches. For this purpose, linearized small-signal equations are required that are provided in Appendix B.

4.4.1 Stability Analysis of Microgrid

The linearized equations, presented in Appendix B, are used for the small-signal stability analysis of a microgrid consisting of two inverters with numerical parameters represented in Table 4.1 that feed an RL load ($R = 28\ \Omega,\ L = 5$ mH). In this case ($N = 2$), the original system and the proposed model are of order 25 and 43, respectively. Also, Table 4.2 points out the parameters of the voltage and current controllers. Using the proposed model, closed-loop poles of the linearized system are calculated. Fig. 4.7 shows the dominant closed-loop poles for all those

Table 4.1: Nominal system parameters of microgrid

Inverter 1		Inverter 2	
Parameter	Value	Parameter	Value
P_1^{fl}	1 kW	P_2^{fl}	2 kW
$L_{1,1}$	2 mH	$L_{1,2}$	3 mH
$C_{f,1}$	2.2 μF	$C_{f,2}$	1 μF
$L_{2,1}$	2 mH	$L_{2,2}$	2 mH
$L_{\text{vir},1}$	2 mH	$L_{\text{vir},2}$	2 mH
$R_{\text{vir},1}$	0.1Ω	$R_{\text{vir},2}$	0.1Ω
$\tau_{lp,1}$	$\frac{1}{2\pi 10}s$	$\tau_{lp,2}$	$\frac{1}{2\pi 10}s$
ω_1^{nl}	$2\pi 60.5\frac{\text{rad}}{s}$	ω_2^{nl}	$2\pi 60.5\frac{\text{rad}}{s}$
V_1^{nl}	170 V	V_2^{nl}	170 V
$m_{p,1}$	$\frac{2\pi}{1000}$	$m_{p,2}$	$\frac{2\pi}{2000}$
$m_{q,1}$	0.01	$m_{q,2}$	0.005

Table 4.2: Parameters of current and voltage controllers

	Inverter 1		Inverter 2	
	Parameter	Value	Parameter	Value
Current Controller	$k_{c11,1}$	-3.08×10^7	$k_{c11,2}$	-3.03×10^7
	$k_{c12,1}$	-3.89×10^4	$k_{c12,2}$	-4.07×10^4
	$k_{p11,1}$	20.58	$k_{p11,2}$	31.63
	$k_{p12,1}$	0.13	$k_{p12,2}$	0.11
	$k_{p13,1}$	-0.82	$k_{p13,2}$	-8.63
Voltage Controller	$k_{c21,1}$	-6.6×10^4	$k_{c21,2}$	-6.2×10^4
	$k_{c22,1}$	-162	$k_{c22,2}$	-172
	$k_{p21,1}$	-4.36×10^3	$k_{p21,2}$	-3.38×10^3
	$k_{p22,1}$	2.75×10^3	$k_{p22,2}$	2.23×10^3
	$k_{p23,1}$	0.09	$k_{p23,2}$	0.07
	$k_{p24,1}$	6.9×10^{-3}	$k_{p24,2}$	1.9×10^{-3}
	$k_{p25,1}$	-0.22	$k_{p25,2}$	-0.31

whose absolute values of their real parts are under $1000s^{-1}$. All closed-loop poles are on the left side of complex plane, which means that the system is stable. The accuracy of the proposed and existing models and also the impact of parameter variations on the system stability are studied below.

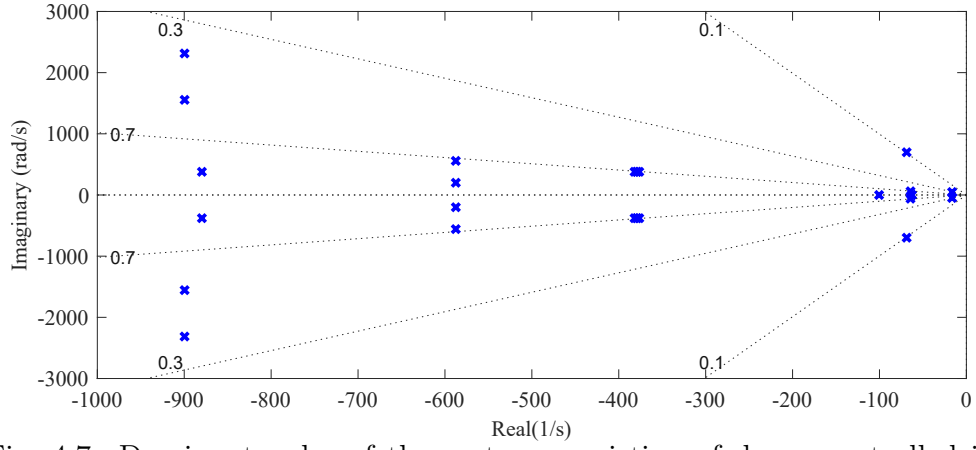

Fig. 4.7: Dominant poles of the system consisting of droop-controlled inverters.

Table 4.3: Transfer functions of conventional OSG methods

Hilbert Transform	SOGI
$G_h(s) = \frac{\omega_b - s}{\omega_b + s}$	$G_\alpha(s) = \frac{k_d \omega_b s}{s^2 + k_d \omega_b s + \omega_b^2}$ $G_\beta(s) = \frac{k_d \omega_b^2}{s^2 + k_d \omega_b s + \omega_b^2}$

ω_b: Angular frequency.
k_d: Damping factor ($k_d = 0.7$).

4.4.2 Model Verification

Scenario-I: In this scenario, first, the models' accuracy is assessed at nominal parameters represented in Table 4.1. Fig. 4.8 shows the difference of active power injection of the first inverter P_1 between the models and actual system responses $e_{P_1} = P_{1\text{model}} - P_{1\text{actual}}$, for four cases: the system controlled in the stationary frame and its proposed model, and systems controlled in the rotating frame using Hilbert transform, SOGI, and FAE for OSG and their models. The transfer functions of the conventional OSG technique are also represented in Table 4.3. As illustrated in Fig. 4.8(a)-4.8(d), at nominal system parameters, all models predict the responses of their actual systems successfully, and error signals, shown in green for nominal system parameters, are damped to zero quickly.

Moreover, Fig. 4.8 compares the dynamic performance of the systems controlled in the stationary or rotating frames and their models accuracy when there is 30% mismatch between the nominal values and actual values of the load-side inductance

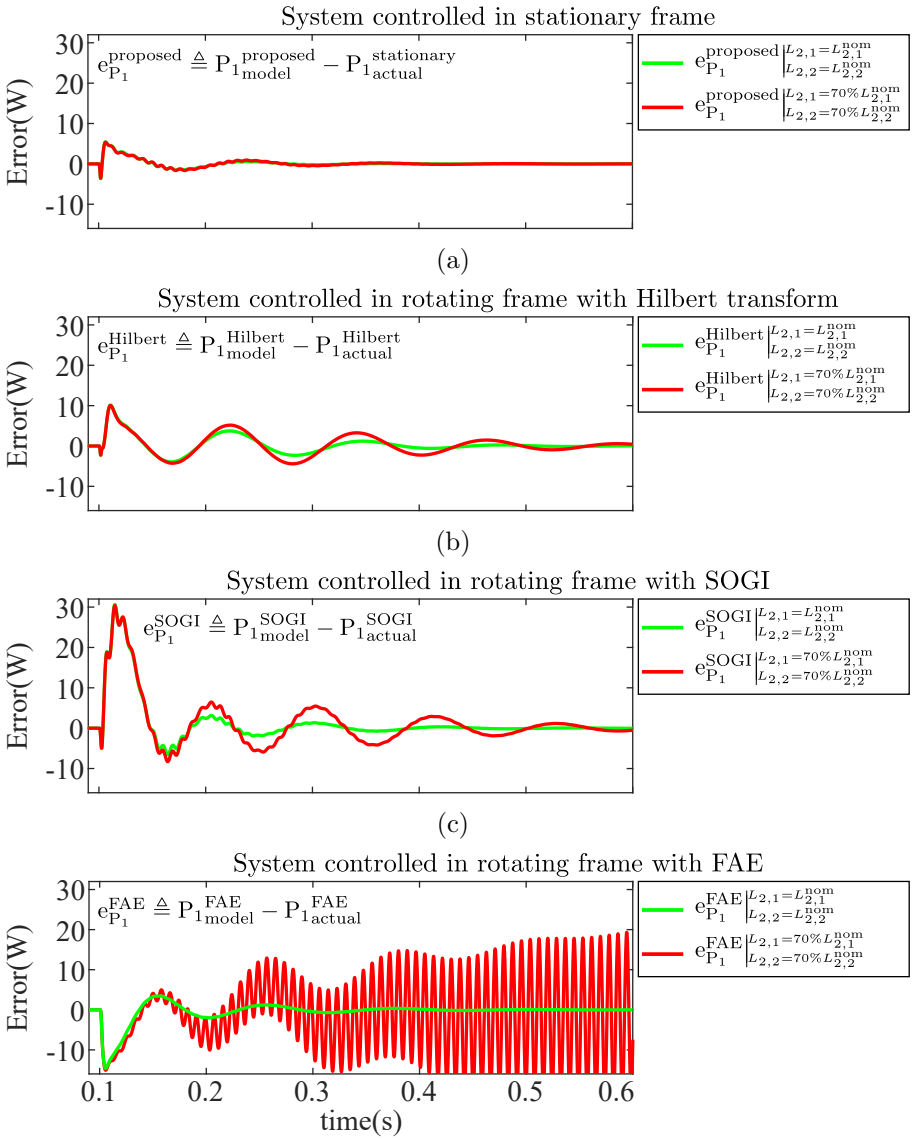

Fig. 4.8: Model prediction errors and robustness against load-side inductance $L_{2,1}, L_{2,2}$ variations.

of inverters, i.e. $L_{2,1} = 70\% L_{2,1}^{\text{nom}}$ and $L_{2,2} = 70\% L_{2,2}^{\text{nom}}$. According to this figure, the proposed model successfully represents the system controlled in the stationary frame in the presence of the inductance value mismatches. However, the system controlled in the rotating frame with FAE is much more sensitive to the parameter mismatches and becomes unstable. The reason is that the FAE is a model-based approach, which makes the FAE sensitive to system uncertainties. In fact, the mismatches between the nominal and actual system parameters lead to steady-state errors in

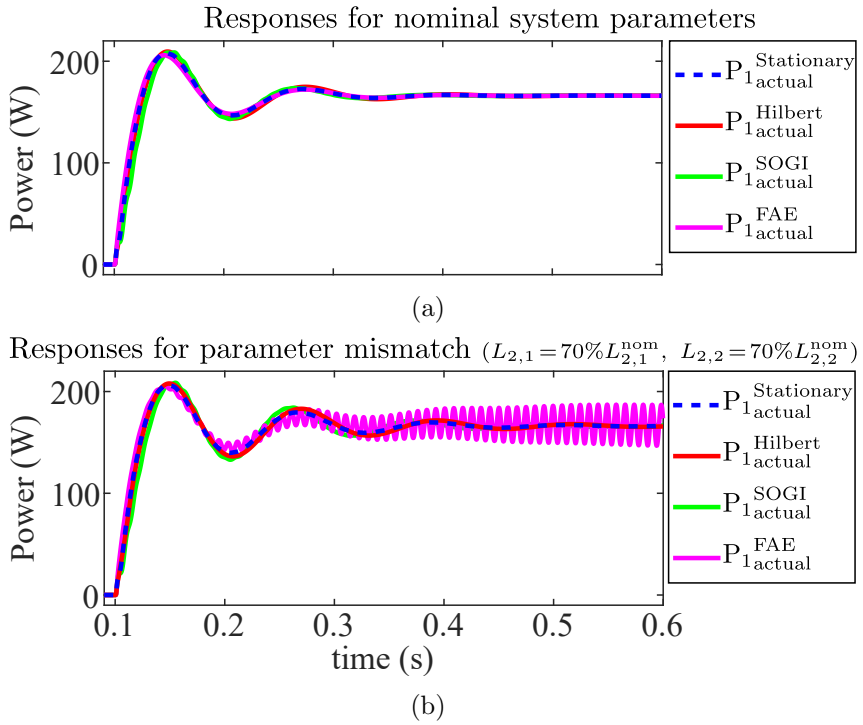

Fig. 4.9: Active power injections of the first inverter controlled either in the stationary or rotating frame (*Scenario-I*).

the orthogonal signal generations, which make the system responses more oscillatory than other OSG methods such as Hilbert transform and SOGI. That is why double-frequency oscillations appear on the active power injection characteristics as shown in Fig. 4.8(d). However, this situation does not happen for the proposed approach because the imaginary system, used for deriving the accurate mathematical model, is not even implemented in the actual controller. Thus, it does not create sensitivity to uncertainties.

In addition, Fig. 4.9 compares active power responses of the first inverter, controlled either in the stationary or rotating frame, at the nominal parameters and when $L_{2,1}=70\%L_{2,1}^{\text{nom}}$ and $L_{2,2}=70\%L_{2,2}^{\text{nom}}$. Although the time responses of the systems are almost similar at the nominal parameters as depicted in Fig. 4.9(a), the system controlled in the rotating frame with FAE becomes unstable as shown in Fig. 4.9(b) due to the model-based nature of the FAE method.

The impact of a parameter mismatch on the stability and performance of the aforementioned systems, controlled in either the stationary frame or the rotating

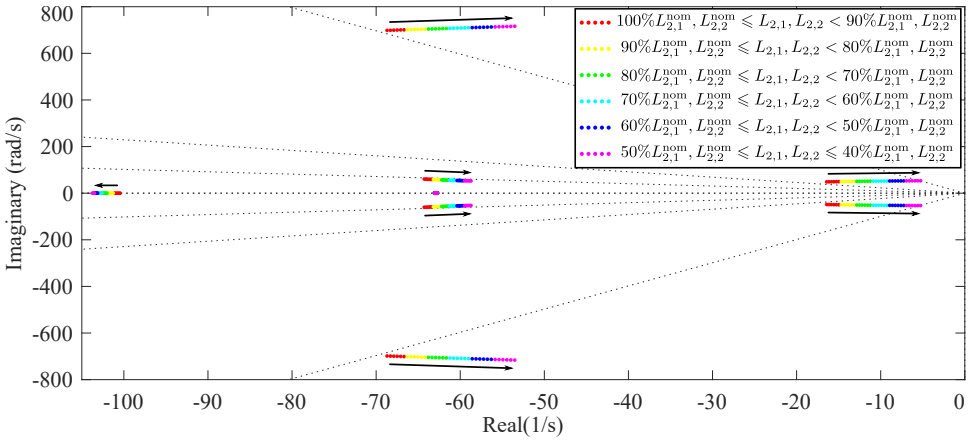

Fig. 4.10: Dominant pole variations due to the drop of $L_{2,1}$ and $L_{2,2}$ to 40% of their nominal values.

frame, is studied in the following. For this purpose, it is assumed that the values of $L_{2,1}$ and $L_{2,2}$ vary from 100% to 40% of their nominal values $L_{2,1}^{\text{nom}}$ and $L_{2,2}^{\text{nom}}$ due to the system uncertainties such as weak microgrid situations, saturation of the inductor cores, and so on. Fig. 4.10 shows how the dominant poles are affected due to the inductance value mismatches. As depicted in this figure, the dominant poles move toward the marginal stability border. Also, the integral of absolute error (IAE) index [126] is used to compare the accuracy of the proposed model for the system controlled in the stationary frame with models for systems controlled in the rotating frame. For this purpose, IAE index is calculated for $\text{e}_{\text{P}_1}^{\text{proposed}}$, $\text{e}_{\text{P}_1}^{\text{Hilbert}}$, $\text{e}_{\text{P}_1}^{\text{SOGI}}$, and $\text{e}_{\text{P}_1}^{\text{FAE}}$ for different inductance value mismatches in a specific time period as displayed in Fig. 4.11. The proposed model has the minimum IAE index among the other existing models, which indicates that the proposed model for single-phase systems controlled in the stationary frame is more reliable than models for systems controlled in the rotating frame for the stability analysis and studying the system behavior in the presence of parameter mismatches.

Scenario-II: In this scenario, the aforementioned systems are pushed close to the border of instability to evaluate the models' accuracy in this operating mode and to highlight how the undesirable dynamics of OSG methods affects the stability of the systems controlled in the rotating frame. For this purpose, the droop slope of the second inverter $m_{p,2}$ is increased to 0.015. Fig. 4.12 depicts how the dominant

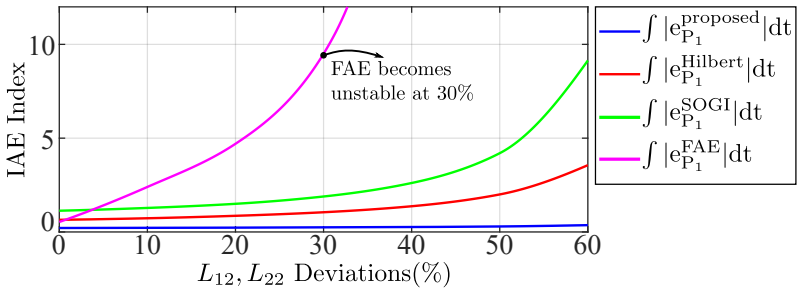

Fig. 4.11: IAE comparison.

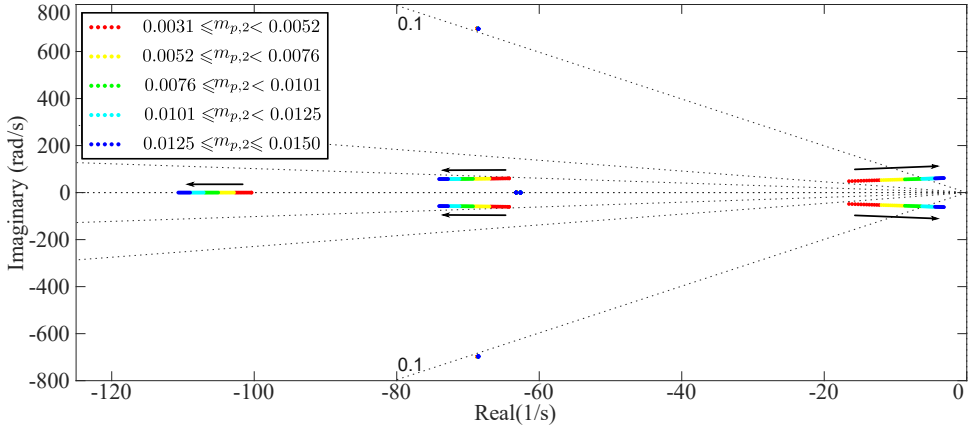

Fig. 4.12: Dominant pole variations due to $m_{p,2}$ changes to have a marginal stability operating mode.

poles change and approach to the instability border. The dominant poles are finally located at $\lambda = -3.197 \pm j61.77$. Fig. 4.13 shows the active power injection of the first and second inverters in the marginal stability operating mode when the actual system is controlled in the stationary frame and modeled using the proposed method, and also for cases that the system is controlled in the rotating frame using Hilbert transform, SOGI, or FAE for OSG and modeled in the rotating frame. The real part of the dominant poles predicts the response time constant of $\tau = \frac{1}{3.197} = 0.31$ s which is confirmed in Fig. 4.13(a) ($\tau = 0.3$ s). Moreover, the imaginary part of the dominant poles indicates an oscillation at a frequency of 9.83 Hz which matches the actual system response modeled by the proposed approach shown in Fig. 4.13(a), where $f_{osc} = 9.8$ Hz.

Furthermore, Fig. 4.14 displays active power injections of the first inverter, controlled either in the stationary or rotating frame, in the marginal stability operating mode. According to Fig. 4.12 and Fig. 4.14, the systems controlled in the

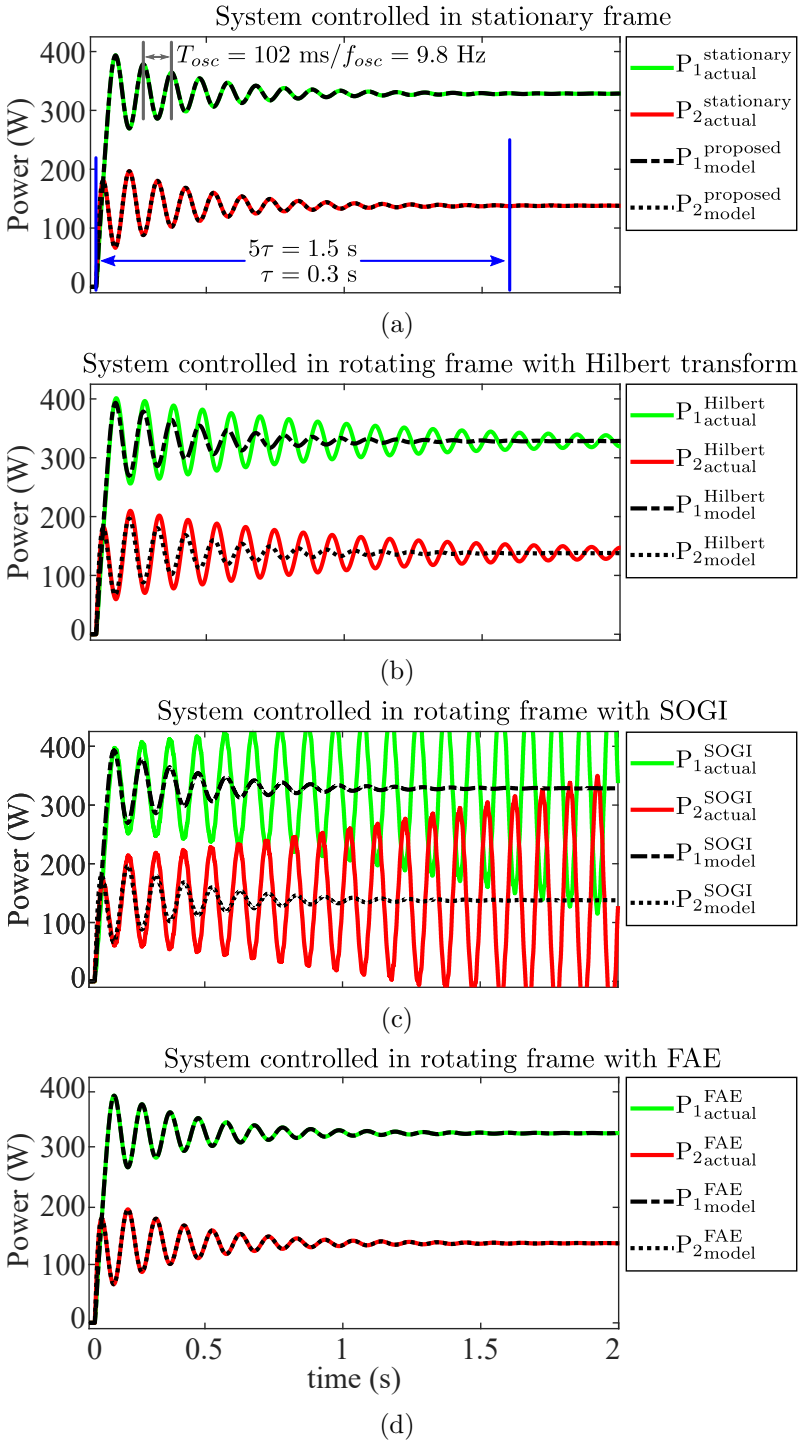

Fig. 4.13: Active power injection responses for actual systems, controlled in either the stationary or rotating frame, and their models predictions.

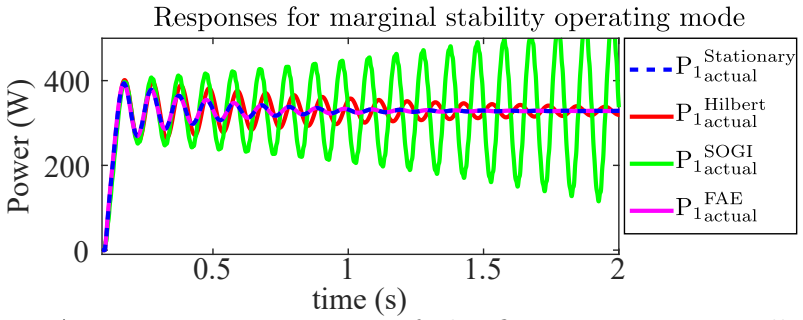

Fig. 4.14: Active power injections of the first inverter controlled in the stationary or rotating frame (*Scenario-II*).

rotating frame, which use Hilbert transform or SOGI, become more oscillatory or unstable, and their responses do not match the dominant poles that their models predict. This is due to the undesirable OSG dynamics, which is overlooked in the design and stability analysis of the systems controlled in the rotating frame.

Scenario-III: In this scenario, the capability of the proposed modeling approach for predicting the internal loops dynamics, i.e. voltage and current loops, is assessed. Fig. 4.15 displays current and voltage waveforms of the actual system controlled in the stationary frame and the proposed model predictions. According to this figure, the parallel inverters start operating at $t = 0.1$ s. Also, the system load varies from 500 W and 33 VAr to 985 W and 65 VAr at $t = 0.4$ s. As shown in this figure, the proposed model can precisely represent the fast dynamic responses of the actual system controlled in the stationary frame as well. Moreover, the figure demonstrates that the parallel inverters are synchronized with each other.

To summarize, considering *Scenario-I* and *Scenario-II*, the system controlled in the stationary frame has wider stability margins than the system controlled in the rotating frame due to the undesired dynamics of OSG blocks, and the proposed model provides an accurate tool to analyze the stability of such system controlled in the stationary frame. Moreover, according to *Scenario-III*, the proposed modeling approach is able to accurately predict and model the internal loops dynamics.

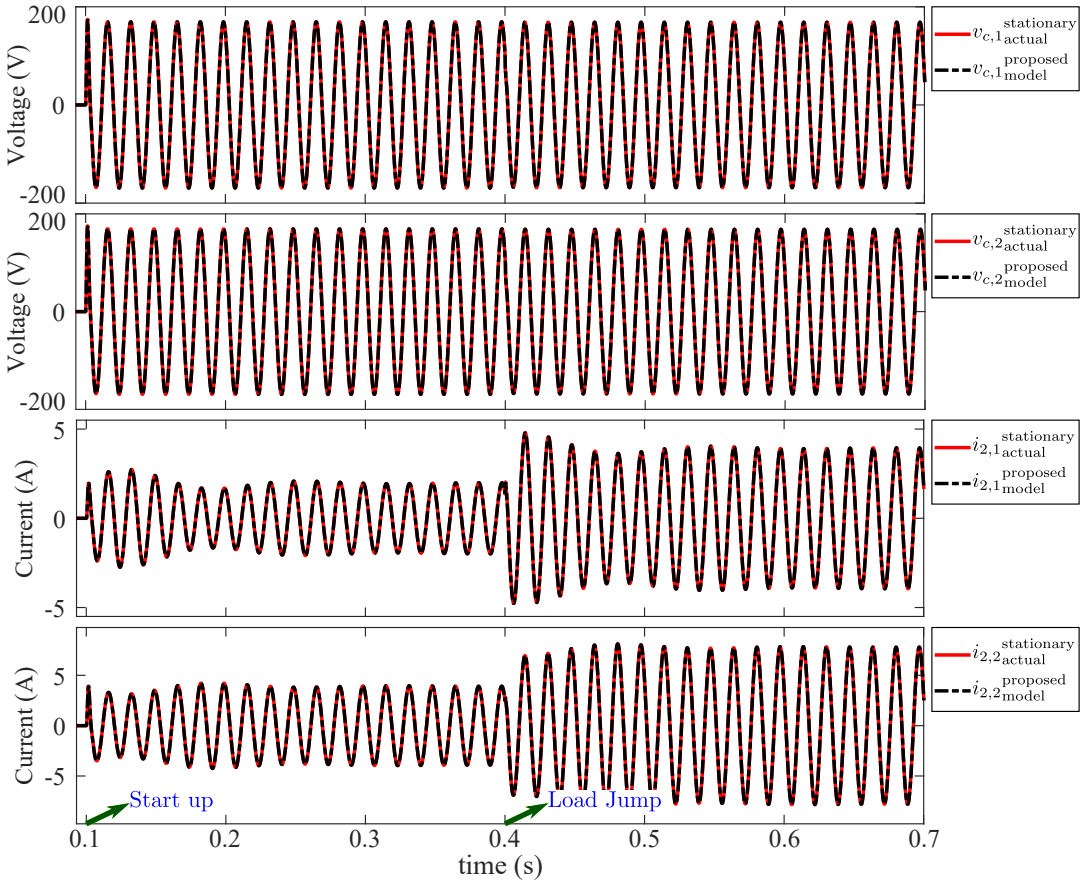

Fig. 4.15: Voltage and current waveforms of the actual system controlled in the stationary frame and the proposed model predictions.

4.5 Interactions Among GFM and GFL Inverters

In the previous section, the interactions among droop-controlled inverters, GFM inverters, are studied, and the accuracy of the proposed modeling approach within different scenarios is verified. In the following, to cover a more general case, it is assumed that the microgrid, shown in Fig. 1.4, contains two droop-controlled inverters in addition to a current-controlled mode (CCM) inverter, GFL inverter.

In this case, the current control loop equations of the CCM inverter can be derived in the stationary and rotating frames using the proposed approach as explained in Sections 4.2, 4.3. The equation derivation process for the CCM inverter is the same as stated in Sections 4.2 and 4.3. Then, the equations of the CCM inverter are combined with the equations of droop-controlled inverters to form the

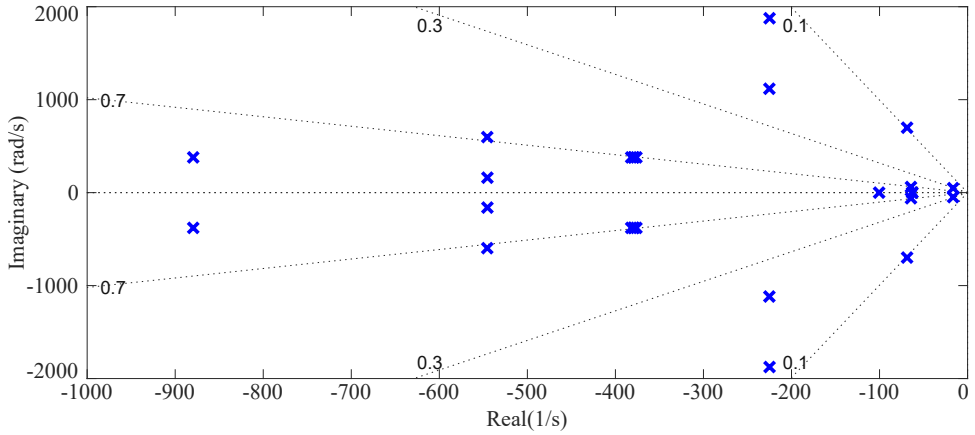

Fig. 4.16: Dominant poles of system containing droop-controlled and CCM inverters.

Table 4.4: Parameters of CCM inverter

	Inverter 3	
	Parameter	Value
	P_3^{nom}	500 W
	$L_{1,3}$	2.8 mH
	$C_{f,3}$	1.5 μF
	$L_{2,3}$	2 mH
Current Controller	$k_{c11,3}$	9×10^4
	$k_{c12,3}$	-4.28×10^4
	$k_{p11,3}$	22.6
	$k_{p12,3}$	0.14
	$k_{p13,3}$	-0.9

microgrid equations in the stationary and rotating frames.

Similar to Section 4.4, the system equations in the rotating frame should be linearized for the small-signal stability analysis of the microgrid, which consists of two droop-controlled inverters and the CCM inverter whose parameters are listed in Table 4.4. In this case, the order of the original system equals 30, and the proposed model is of order 53. Fig. 4.16 shows the dominant closed-loop poles of the linearized system. As depicted in this figure, all poles fall in the left hand plane (LHP), which indicates that the system is stable.

Fig. 4.17(a) shows a sample of the simulation results of the system operating at the nominal parameters and the proposed model predictions. As shown in this

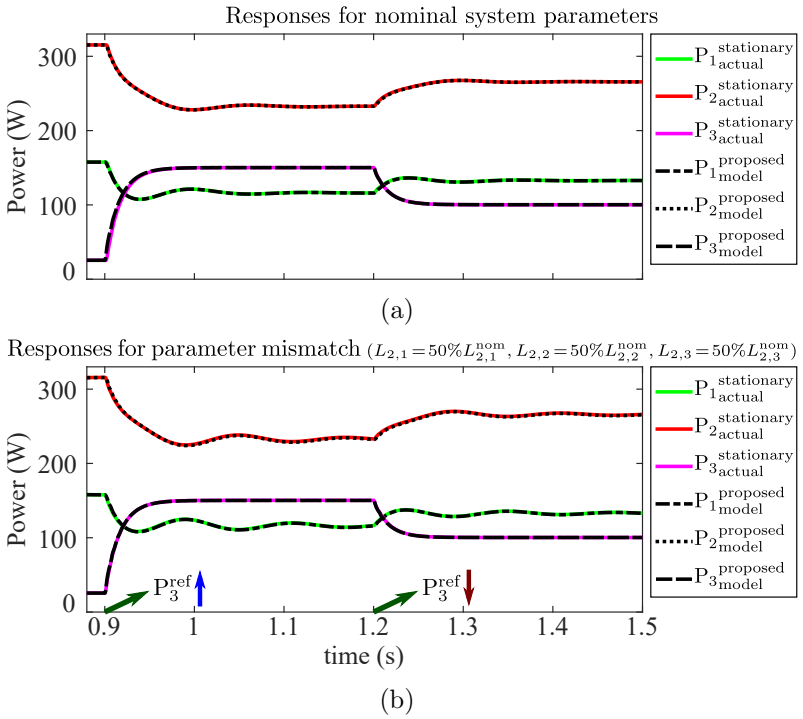

Fig. 4.17: Interactions among the CCM and droop-controlled inverters due to P_3^{ref} jumps and the proposed model predictions (*Scenario-III*).

figure, the reference power of the CCM inverter P_3^{ref} jumps from 25 W to 150 W at $t=0.6$ s. Then, P_3^{ref} decreases to 100 W at $t=0.9$ s. It is observed that the proposed model accurately predicts system responses and the interactions among the different inverters. Moreover, Fig. 4.18 displays the synchronous operations of the CCM and droop-controlled inverters and also accurate predictions of the proposed model for the fast dynamics system responses.

Next, it is assumed that there is 50% mismatch among the nominal and actual values of the load-side inductances, i.e. $L_{2,1} = 50\%L_{2,1}^{\text{nom}}$, $L_{2,2} = 50\%L_{2,2}^{\text{nom}}$, and $L_{2,3}=50\%L_{2,3}^{\text{nom}}$. Time responses of the system are depicted in Fig. 4.17(b) for the same variations of P_3^{ref}. According to this figure, the proposed model successfully represents the system controlled in the stationary frame in the presence of the inductance value mismatches as well.

To sum up, it is shown that not only can the proposed modeling approach be used to analyze the stability and to predict the time responses of the systems controlled in the stationary frame, but also the proposed model is able to accurately

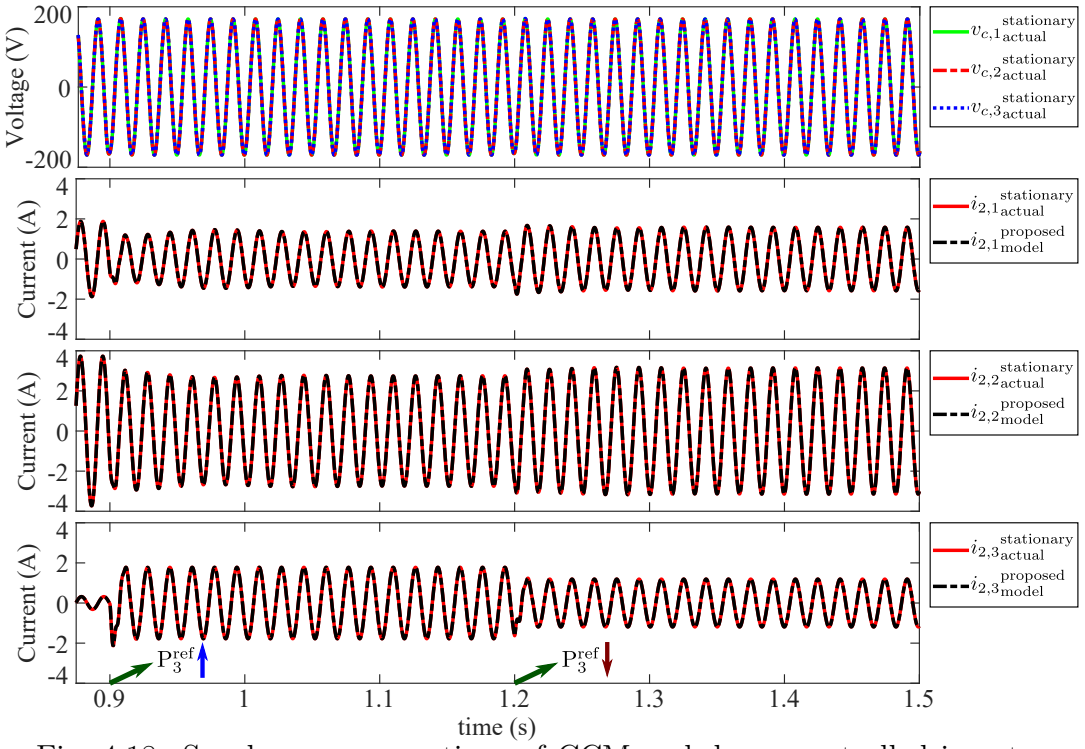

Fig. 4.18: Synchronous operations of CCM and droop-controlled inverters and the proposed model predictions.

predict the interactions among different types of inverters.

4.6 Experimental Results

In the experimental setup, the dc supplies are implemented with Chroma programmable dc power supply 62012P and Sorensen programmable power supply SGX500X10C. The inverter controllers are implemented on dSPACE MicroLabBox (RTI 1202). For the numerical parameters in Table 4.1, Fig. 4.19 illustrates the normal operating of two inverters with cascade control loops (droop, voltage, and current control loops) when the system load jumps from 260 W and 40 VAr to 440 W and 80 VAr, and then, goes back to the previous condition.

In the next scenario, the system is pushed to the instability border by changing the droop slope of the second inverter $m_{p,2}$. Fig. 4.20 depicts current and voltage waveforms, and active power injection of two inverters in the marginal stability operating mode. The oscillation frequency f_{osc} equals 10.09 Hz, and the system

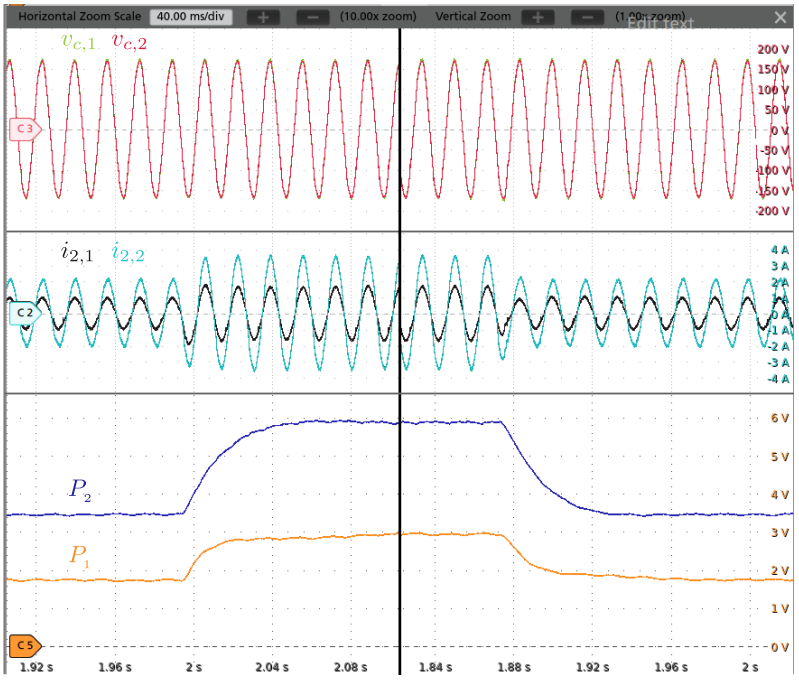

Fig. 4.19: Experimental results for the normal operating of two parallel inverters: load jumps and returns from 260 W and 40 VAr to 440 W and 80 VAr.

time constant τ equals $\frac{1.46}{5} = 0.29$ s. Comparing the experimental results, shown in Fig. 4.20, with the simulation results, depicted in Fig. 4.12, confirms the accuracy of the proposed model.

4.7 Summary

In this chapter, a method is proposed for modeling and stability analysis of a single-phase microgrid including parallel inverters controlled in the stationary frame. The modeling is based on the introduction of an imaginary system to be augmented with the original system and form an equivalent system in the stationary frame based on α-axis and β-axis components. Therefore, using the method, all ac state variables can be converted to dc variables. The proposed model does not alter the eigenvalues, nor does it introduce time-varying terms. The accuracy of the proposed model is verified using simulation and experimental results. It is also shown that a single-phase system controlled in the stationary frame is more stable

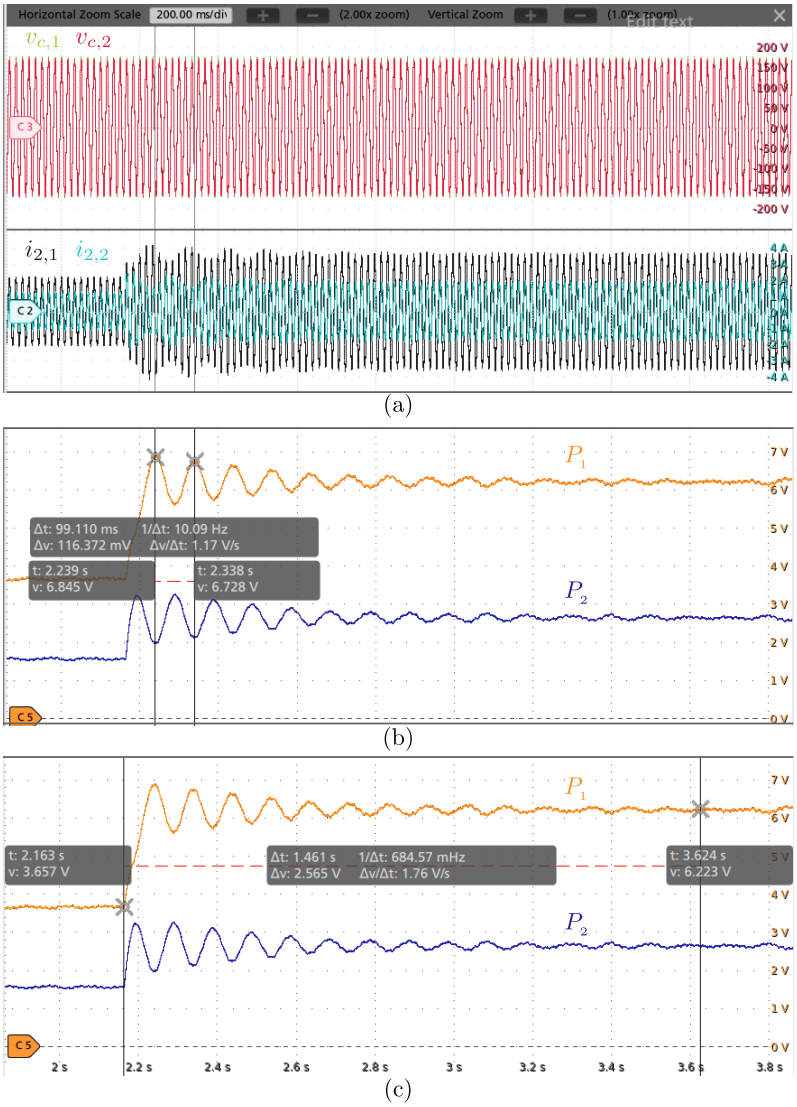

Fig. 4.20: Experimental results for the marginal stability operating mode with a droop coefficient of $m_{p,2} = 0.015$ (a) current and voltage waveforms, (b) oscillation frequency f_{osc} measurement, and (c) time constant τ_{osc} measurement.

and robust than the same system controlled in the rotating frame due to drawbacks of inevitable OSG blocks in control loops.

Chapter 5

Modified Droop Strategy for Wide Load Range Efficiency Improvement of Parallel Inverter Systems

Parallel inverters are increasingly used in many modern power applications, and thus, improving the parallel-inverter system efficiency plays a key role in energy savings. As explained in Section 1.4, the conventional droop strategy, which is commonly used for power sharing among inverters, leads to a low efficiency especially at light loads. The reason is that the low power demand is divided among inverters, which forces them to process a fraction of the low power at a low efficiency according to their efficiency curve depicted in Fig. 5.1(a).

To avoid such operating conditions, a communicationless modified droop strategy is proposed in this chapter to improve the overall system efficiency of parallel inverters. The main idea is to revise the power sharing among parallel inverters such that the output power of each inverter is maintained within a proper range with respect to the inverter efficiency curve. As a result, according to the loads demand, an optimal number of inverters supply the loads, and the unnecessary inverters do not share any power as depicted in Fig. 5.1(b).

On the other hand, in very-light load situations where $P_k < 0.3P_k^{fl}$ and $k = 1, 2, 3$, none of the inverters can operate within the proper power range. In this case, the proposed method uses a communicationless online-inverter detection (OID) approach introduced in [127] so that each inverter detects other available inverters in the system, and the inverter with the lowest rated power supplies the load to achieve a higher system efficiency.

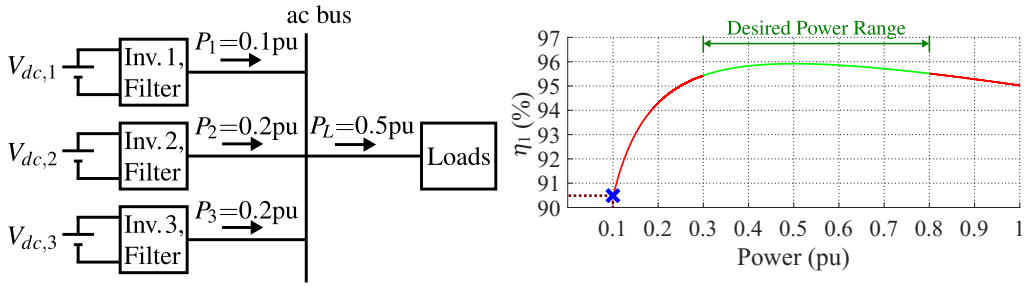

(a) Load power using conventional droop method: $P_L = \sum_{k=1}^{3} P_k = 0.5$ pu.

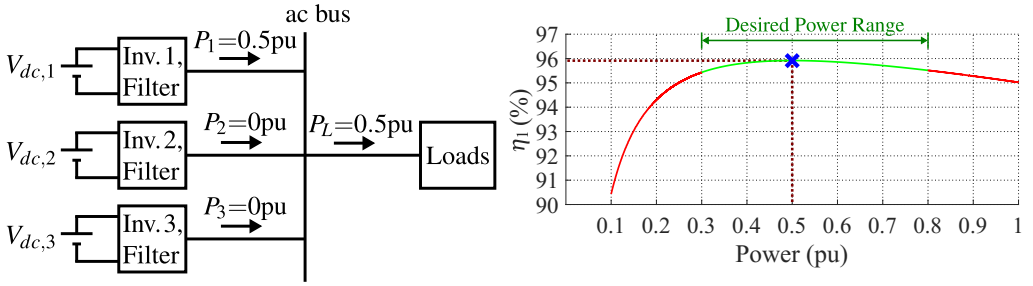

(b) Load power using proposed method: $P_L = P_1 = 0.5$ pu.

Fig. 5.1: Power sharing and inverter efficiency comparison of three parallel inverters in the (a) conventional droop and (b) proposed method.

As the proposed method is decentralized and modular, more inverters can be added to the system without changing the settings of the previously installed inverters. Moreover, the proposed method is still operational even if some inverters become offline due to disconnection or going out of service, which indicates that there is no single point of failure. Ultimately, the lifetimes of inverters with higher rated powers are extended by the proposed method since they operate at a fraction of the time that they would otherwise do in the conventional droop method. Simulation and experimental results at different load levels verify the effectiveness of the proposed method.

5.1 System Configuration and Single Inverter Modeling

The parallel inverter system configuration is illustrated in Fig. 5.2. It consists of three parallel single-phase inverters that are connected to the loads via LCL filters.

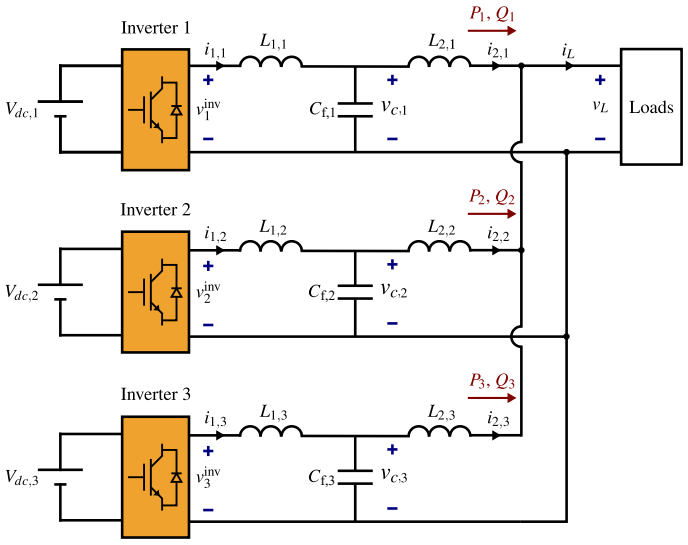

Fig. 5.2: Parallel inverter system configuration.

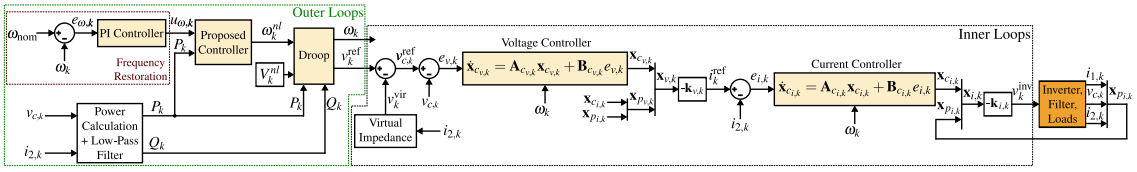

Fig. 5.3: Control system structure of the k^{th} inverter.

To verify the performance of the proposed method in different scenarios where identical or nonidentical inverters are online in the system, the full-load powers of Inverter 2 and Inverter 3 are assumed to be twice the full-load power of Inverter 1, i.e. $P_3^{fl} = P_2^{fl} = 2P_1^{fl} = 2$ kW.

Each inverter has a decentralized cascade control system shown in Fig. 5.3. The inner loops control the voltage and current of the inverter. The outer loops, including the frequency restoration loop, proposed controller, and conventional droop controller generate the reference voltage for the inner loops. As depicted in Fig. 5.3, the proposed controller determines the no-load frequency ω_k^{nl} of the droop controller to modify the contribution of the k^{th} inverter in the power sharing. More details on the principles of operations of the proposed controller and how it interacts with other controllers is provided in Section 5.2. In the following, state-space models of the k^{th} inverter are derived. Hereinafter, the indices "i", "v", "p", "c", "L", and "k" represent the signals and variables of the current control loop, voltage control

loop, plants, controllers, loads, and k^{th} inverter.

The system load is assumed to be a combination of series resistive R_L, inductive L_L, and capacitive C_L components. Therefore, the load voltage is calculated as v_L=$R_L i_L$+$L_L \frac{di_L}{dt} + v_{c_L}$, where v_{c_L} and i_L are the capacitive part of the load voltage and the load current, respectively, given by

$$v_{c_L} = \frac{1}{C_L} \int i_L dt,\ i_L = \sum_{k=1}^{3} i_{2,k}. \tag{5.1}$$

For the current controller, the inverter and LCL filter are considered as the plant. The state-space equation of the current control loop plant is given by

$$\dot{\mathbf{x}}_{p_{i,k}} = \mathbf{A}_{p_{i,k}} \mathbf{x}_{p_{i,k}} + \mathbf{B}_{p_{i,k}} v_k^{\text{inv}} + \mathbf{B}_{p_{L,k}} v_L, \tag{5.2}$$

where $\mathbf{x}_{p_{i,k}} = [i_{1,k}\ v_{c,k}\ i_{2,k}]^T$, and $i_{1,k}$, $v_{c,k}$, $i_{2,k}$, and v_k^{inv} refer to the current of the inverter-side inductor $L_{1,k}$, voltage of the capacitor $C_{f,k}$, current of the load-side inductor $L_{2,k}$, and inverter voltage, respectively. Moreover, $\mathbf{A}_{p_{i,k}}$, $\mathbf{B}_{p_{i,k}}$, and $\mathbf{B}_{p_{L,k}}$ are defined as follows

$$\mathbf{A}_{p_{i,k}} = \begin{bmatrix} 0 & \frac{-1}{L_{1,k}} & 0 \\ \frac{1}{C_{f,k}} & 0 & \frac{-1}{C_{f,k}} \\ 0 & \frac{1}{L_{2,k}} & 0 \end{bmatrix}, \mathbf{B}_{p_{i,k}} = \begin{bmatrix} \frac{1}{L_{1,k}} \\ 0 \\ 0 \end{bmatrix}, \mathbf{B}_{p_{L,k}} = \begin{bmatrix} 0 \\ 0 \\ \frac{-1}{L_{2,k}} \end{bmatrix}. \tag{5.3}$$

The state-space equation of the resonant current controller is

$$\dot{\mathbf{x}}_{c_{i,k}} = \mathbf{A}_{c_{i,k}} \mathbf{x}_{c_{i,k}} + \mathbf{B}_{c_{i,k}} e_{i,k}, \tag{5.4}$$

where $\mathbf{x}_{c_{i,k}}$ is the state vector of the current controller and $e_{i,k} = i_k^{\text{ref}} - i_{2,k}$ is the current tracking error. Moreover, $\mathbf{A}_{c_{i,k}}$ and $\mathbf{B}_{c_{i,k}}$ are

$$\mathbf{A}_{c_{i,k}} = \begin{bmatrix} 0 & 1 \\ -\omega_k^2 & 0 \end{bmatrix},\ \mathbf{B}_{c_{i,k}} = \begin{bmatrix} 0 \\ 1 \end{bmatrix}. \tag{5.5}$$

Assuming $\mathbf{x}_{i,k}=[\mathbf{x}_{c_{i,k}}\ \mathbf{x}_{p_{i,k}}]^T$ and $v_k^{\text{inv}}=-\mathbf{k}_{i,k}\mathbf{x}_{i,k}$, where $\mathbf{k}_{i,k}$ is the current controller gain vector, (5.2)-(5.5) form the state-space equation of the current control loop as

$$\begin{aligned}\dot{\mathbf{x}}_{i,k}&=\left(\mathbf{A}_{i,k}-\mathbf{B}_{i,k}^{v^{\text{inv}}}\mathbf{k}_{i,k}\right)\mathbf{x}_{i,k}+\mathbf{B}_{i,k}i_k^{\text{ref}},\\ \mathbf{A}_{i,k}&=\begin{bmatrix}\mathbf{A}_{c_{i,k}} & -\mathbf{B}_{c_{i,k}}\mathbf{C}_{p_{i,k}}\\ \mathbf{0} & \mathbf{A}_{p_{i,k}}\end{bmatrix},\ \mathbf{C}_{p_{i,k}}=\begin{bmatrix}0 & 0 & 1\end{bmatrix},\\ \mathbf{B}_{i,k}^{v^{\text{inv}}}&=\begin{bmatrix}\mathbf{0}\\ \mathbf{B}_{p_{i,k}}\end{bmatrix},\ \mathbf{B}_{i,k}=\begin{bmatrix}\mathbf{B}_{c_{i,k}}\\ \mathbf{0}\end{bmatrix}.\end{aligned}\tag{5.6}$$

For the voltage control loop, the current loop represented by (5.6) is considered as a new plant with state variables $\mathbf{x}_{p_{v,k}}=[\mathbf{x}_{c_{i,k}}\ \mathbf{x}_{p_{i,k}}]^T$, and state matrices $\mathbf{A}_{p_{v,k}}=\mathbf{A}_{i,k}-\mathbf{B}_{i,k}^{v^{\text{inv}}}\mathbf{k}_{i,k}$, $\mathbf{B}_{p_{v,k}}=\mathbf{B}_{i,k}$. Additionally, the voltage controller is a resonant controller, whose state-space equation is

$$\dot{\mathbf{x}}_{c_{v,k}}=\mathbf{A}_{c_{v,k}}\mathbf{x}_{c_{v,k}}+\mathbf{B}_{c_{v,k}}e_{v,k},\tag{5.7}$$

where $\mathbf{x}_{c_{v,k}}$ is the state vector of the voltage controller, and $e_{v,k}=v_{c,k}^{\text{ref}}-v_{c,k}$ denotes the voltage tracking error. Furthermore, $\mathbf{A}_{c_{v,k}}$ and $\mathbf{B}_{c_{v,k}}$ are equal to $\mathbf{A}_{c_{i,k}}$ and $\mathbf{B}_{c_{i,k}}$ in (5.5), respectively. Then, similar to the current loop, define $\mathbf{x}_{v,k}=[\mathbf{x}_{c_{v,k}}\ \mathbf{x}_{p_{v,k}}]^T$ and $i_k^{\text{ref}}=-\mathbf{k}_{v,k}\mathbf{x}_{v,k}$, where $\mathbf{k}_{v,k}$ is the voltage controller gain vector. Thus, (5.6) and (5.7) are augmented to form the state-space equation of the voltage control loop as

$$\begin{aligned}\dot{\mathbf{x}}_{v,k}&=\left(\mathbf{A}_{v,k}-\mathbf{B}_{v,k}^{i^{\text{ref}}}\mathbf{k}_{v,k}\right)\mathbf{x}_{v,k}+\mathbf{B}_{v,k}v_k^{\text{ref}},\\ \mathbf{A}_{v,k}&=\begin{bmatrix}\mathbf{A}_{c_{v,k}} & -\mathbf{B}_{c_{v,k}}\mathbf{C}_{p_{v,k}}\\ \mathbf{0} & \mathbf{A}_{p_{v,k}}\end{bmatrix},\mathbf{C}_{p_{v,k}}=\begin{bmatrix}0\ 0\ 0\ 1\ 0\end{bmatrix},\\ \mathbf{B}_{v,k}^{i^{\text{ref}}}&=\begin{bmatrix}\mathbf{0}\\ \mathbf{B}_{p_{v,k}}\end{bmatrix},\ \mathbf{B}_{v,k}=\begin{bmatrix}\mathbf{B}_{c_{v,k}}\\ \mathbf{0}\end{bmatrix}.\end{aligned}\tag{5.8}$$

A virtual impedance L_k^{vir} is also used to improve the stability of the system and ensure inductive impedance between the inverter and the loads [47, 123]. Considering $i_{2,k}$ and v_k^{vir} as the input and output of the virtual impedance block, respectively,

the voltage drop across the impedance is $v_k^{\text{vir}} = L_k^{\text{vir}} \frac{di_{2,k}}{dt}$.

Moreover, an LPF is used to provide virtual inertia and improve the stability of the inverter similar to virtual synchronous machines [6, 128, 129]. For a first-order LPF with the transfer function $G_{lp}(s)=\frac{\omega_{cf}}{s+\omega_{cf}}$, where ω_{cf} is the cut-off frequency, the state-space equations are

$$\begin{gathered}\dot{\mathbf{x}}_{lp,k} = \mathbf{A}_{lp,k}\mathbf{x}_{lp,k} + \mathbf{B}_{lp,k}\mathbf{u}_{lp,k},\ \mathbf{y}_{lp,k} = \mathbf{C}_{lp,k}\mathbf{x}_{lp,k}, \\ \mathbf{A}_{lp,k} = -\omega_{cf}\mathbf{I}_2,\ \mathbf{B}_{lp,k} = \omega_{cf}\mathbf{I}_2,\ \mathbf{C}_{lp,k} = \mathbf{I}_2,\end{gathered} \tag{5.9}$$

where $\mathbf{I}_2$ is the identity matrix of dimension 2, $\mathbf{u}_{lp,k}=[p_k\ q_k]^T$, and $\mathbf{x}_{lp,k}=\mathbf{y}_{lp,k}=[P_k\ Q_k]^T$. In addition, p_k, q_k, P_k, and Q_k refer to the instantaneous and filtered active and reactive powers.

The equations of the droop controller that generates the reference voltage is summarized as

$$\begin{gathered}\omega_k = \omega_k^{nl} - m_{p,k}P_k,\ \phi_k = \int \omega_k dt \\ V_k = V_k^{nl} - m_{q,k}Q_k,\ v_k^{\text{ref}} = V_k \cos\phi_k,\end{gathered} \tag{5.10}$$

where ω_k, ω_k^{nl}, $m_{p,k}$, P_k, and ϕ_k denote the reference frequency, no-load frequency, frequency-droop coefficient, filtered active power, and reference voltage phase angle, respectively. Moreover, V_k, V_k^{nl}, $m_{q,k}$, and Q_k refer to the reference voltage amplitude, no-load voltage amplitude, voltage-droop coefficient, and filtered reactive power, respectively. Additionally, v_k^{ref} is the reference voltage.

Ultimately, a PI controller is utilized in the frequency restoration loop as follows

$$u_{\omega,k} = b_k^{\text{prop}} e_{\omega,k} + b_k^{\text{int}} \int e_{\omega,k} dt, \tag{5.11}$$

where $u_{\omega,k}$, $e_{\omega,k}$, b_k^{prop}, and b_k^{int} refer to the controller output, frequency error, proportional gain, and integral gain.

5.2 Proposed Method

The main idea of the proposed method is to maintain the output power of the inverters within a desired range, corresponding to a high efficiency, by reducing the output power of the unnecessary inverters to zero. In addition to efficiency improvement, the inverter lifetimes can be extended by the proposed method as explained in this section.

5.2.1 Efficiency Improvement

The efficiency curve of the ABB 2-kW solar inverter [130] is considered as the typical efficiency curve of the inverters in this study. To derive a mathematical model for the efficiency curve, the quadratic power loss model [131] is used as follows

$$P_k^{\text{loss}} = a_0 + a_1 P_k^{\text{out}} + a_2 P_k^{\text{out}^2}, \tag{5.12}$$

where a_0, a_1, and a_2 are constant parameters that can be obtained via efficiency curve fitting, as depicted in Fig. 5.4 for active powers from 0.1 pu to 1 pu, where 1 pu corresponds to the full-load power, P_k^{fl}. According to the curve, if the output power of each inverter is maintained within $0.3P_k^{fl}$ and $0.8P_k^{fl}$, i.e. the desired power range, the inverter efficiency will be higher than 95.5%. As a result, the overall system efficiency will be improved.

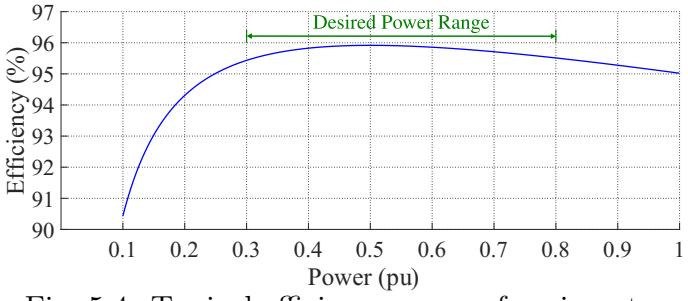

Fig. 5.4: Typical efficiency curve of an inverter.

5.2.2 Implementation of the Proposed Method

Fig. 5.5 presents the details of the proposed control system of the k^{th} inverter, where the no-load frequency ω_k^{nl} of the droop controller is determined through a multiplexer (Mux). If the inverter power is within the desired range, the output of the Mux $\omega_k^{nl,\text{mux}}$ is equal to the output of the frequency controller $u_{\omega,k}$, and the frequency is restored at 60 Hz; otherwise, $\omega_k^{nl,\text{mux}}$ is set to $\omega_{\text{nom}} = 2\pi 60$ $^{\text{rad}}/_{\text{s}}$. In other words

$$\omega_k^{nl,\text{mux}} = \begin{cases} \omega_{\text{nom}} & Sel_k = 1 \\ u_{\omega,k} & Sel_k = 2 \end{cases} \tag{5.13}$$

where Sel_k is the selector signal of the Mux, which is determined as follows

$$Sel_k = Hys_{1,k} + Hys_{2,k} + VLS_k, \tag{5.14}$$

where $Hys_{1,k}$ and $Hys_{2,k}$ are the output of Hysteresis-1_k and Hysteresis-2_k, respectively, and VLS_k is the very-light load correction signal, which will be activated at very-light loads. The objective of Hysteresis-1_k and Hysteresis-2_k is to determine whether the inverter power is below or above $0.3P_k^{fl}$ and $0.8P_k^{fl}$, respectively. Considering P_3^{fl}=P_2^{fl}=$2P_1^{fl}$=2 kW, and taking the possible load levels into account, the

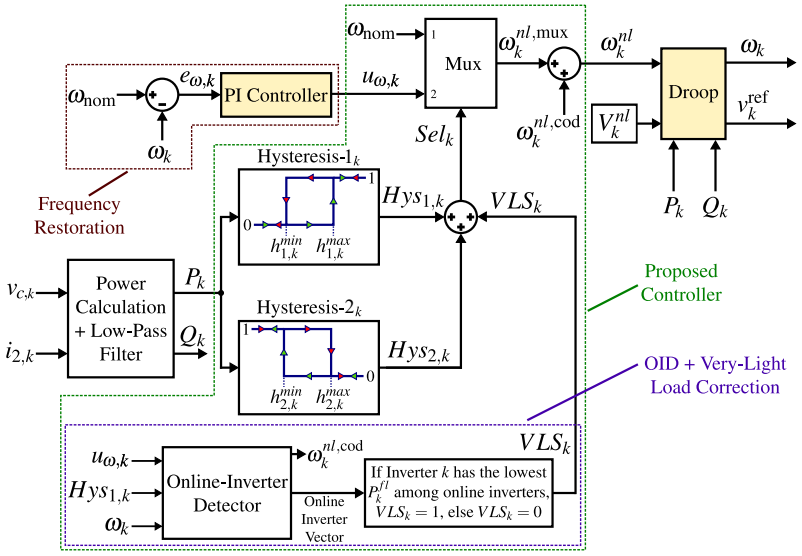

Fig. 5.5: Proposed controller of the k^{th} inverter.

system operates in 3 different modes described in the following.

5.2.2.1 Mode 1 (Normal Operation)

At least one of the inverters operates within the desired power range and restores the system frequency at 60 Hz. In this mode, the injected power by the inverters operating out of the desired power range would be zero since their no-load frequencies ω_k^{nl} are equal to the system frequency at ω_{nom}. Fig. 5.6(a) depicts the droop curves of inverters operating in *Mode 1* when a light load is connected to the system. Since P_{L_1} only lies within the desired power range of Inverter 1, this inverter solely supplies the load. In Fig. 5.6(b), the load increases to an amount more than $0.8P_1^{fl}$. Thus, Inverter 2 starts to supply the load. It is worth noting that in case that two or more inverters have the same rated power, the inverter with the smallest assigned ID "k" supplies the load before the others. Finally, as shown in Fig. 5.6(c), when the load increases to an amount more than $0.8P_1^{fl} + 0.8P_2^{fl}$, all three inverters supply the load, while operating within the desired power range.

5.2.2.2 Mode 2 (Very-Heavy Load)

In this mode, all inverters operate above the desired power range, i.e. $0.8P_k^{fl} < P_k \leqslant P_k^{fl}$ and $k = 1, 2, 3$. Therefore, the no-load frequency of each inverter ω_k^{nl} is set to ω_{nom} to operate similar to the conventional droop, and the loads demand is shared among the inverters proportional to their power ratings. Fig. 5.6(d) illustrates the droop characteristics of the inverters when a very-heavy load is connected to the system, with a power such that $\sum_{k=1}^{3} 0.8P_k^{fl} < P_{L_4} \leqslant \sum_{k=1}^{3} P_k^{fl}$.

5.2.2.3 Mode 3 (Very-Light Load)

This mode happens if all inverters operate below the desired power range, i.e. $P_k < 0.3P_k^{fl}$ and $k = 1, 2, 3$. In this case, all online inverters should be detected by the OID approach proposed in [127]; consequently, the inverter with the lowest

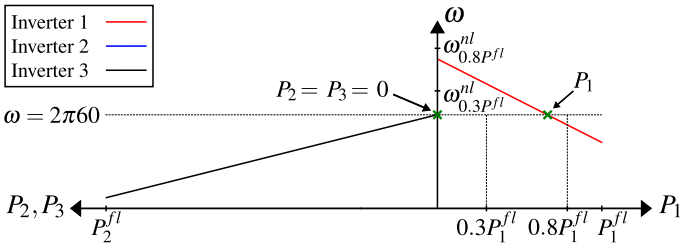

(a) $0.3P_1^{fl} \leqslant P_{L_1} \leqslant 0.8P_1^{fl} \Rightarrow Sel_1 = 2, Sel_2 = Sel_3 = 1 \Rightarrow P_{L_1} = P_1$: *Mode 1.*

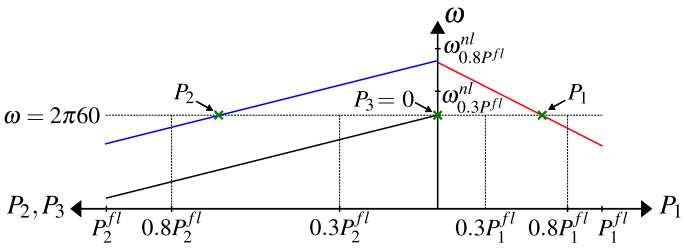

(b) Load increases to $P_{L_2} > 0.8P_1^{fl} \Rightarrow Sel_1 = Sel_2 = 2, Sel_3 = 1 \Rightarrow P_{L_2} = P_1 + P_2$: *Mode 1.*

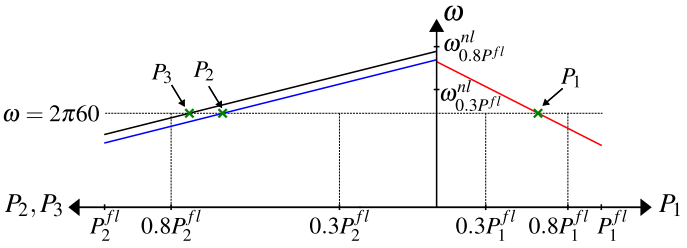

(c) Load increases to $P_{L_3} > 0.8P_1^{fl} + 0.8P_2^{fl} \Rightarrow Sel_1 = Sel_2 = Sel_3 = 2 \Rightarrow P_{L_3} = P_1 + P_2 + P_3$: *Mode 1.*

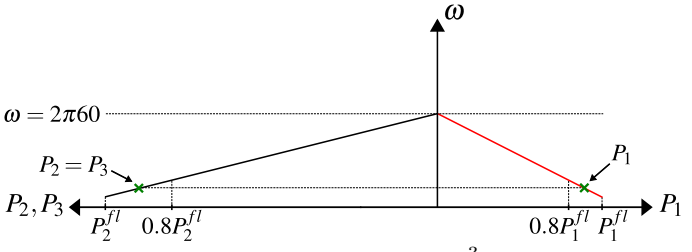

(d) Load increases to very-heavy load $\sum_{k=1}^{3} 0.8P_k^{fl} < P_{L_4} \leqslant \sum_{k=1}^{3} P_k^{fl} \Rightarrow Sel_1 = Sel_2 = Sel_3 = 1 \Rightarrow P_{L_4} = P_1 + P_2 + P_3$: *Mode 2.*

Fig. 5.6: Droop characteristics of the inverters operating in *Mode 1* and *Mode 2* at different load profiles.

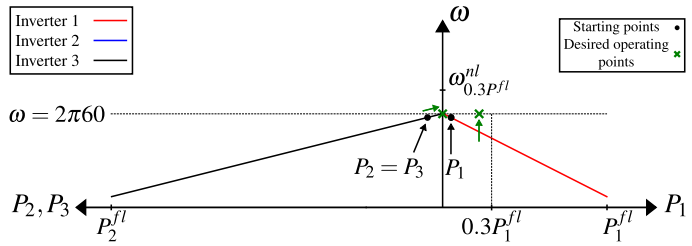

(a) $P_k < 0.3P_k^{fl} \Rightarrow P_L = P_1 + P_2 + P_3$.

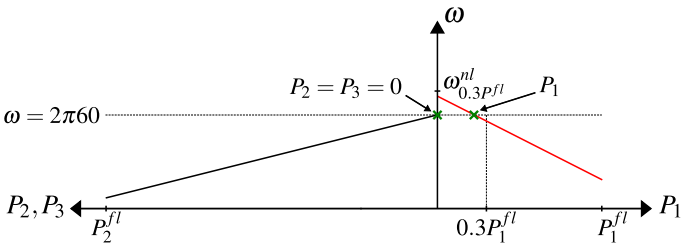

(b) $VLS_1 : 0 \rightarrow 1 \Rightarrow Sel_1 : 1 \rightarrow 2 \Rightarrow P_L = P_1,\ P_2 = P_3 = 0$.

Fig. 5.7: Droop characteristics of the inverters operating in *Mode 3* at (a) the beginning, and (b) the final operating points.

rated power restores the frequency at 60 Hz and supplies the loads, while the other inverters share no power.

Fig. 5.7 illustrates the droop characteristics of the inverters in the very-light load situation, i.e. *Mode 3*. First, the inverters start to share the power proportionally, as depicted in Fig. 5.7(a). Then, the OID is activated, and it is observed that all three inverters are online. Since Inverter 1 has the lowest rated power, only Inverter 1 supplies the load as shown in Fig. 5.7(b).

It is worth mentioning that if there is more than one inverter with the lowest rated power in the system, the OID determines which inverter should supply the load. More details of this operating mode and the OID approach are comprehensively provided in [127].

5.2.3 Inverter Lifetime Extension

There is a correlation between the lifetime consumption of the inverters and how long they contribute to power sharing [132–134]. Therefore, the capability of the proposed method in extending the lifetimes of the inverters should be investigated. According to the proposed method, to improve the system efficiency, the inverters

with smaller power ratings supply the light loads, and the inverters with higher power ratings will be added to the system to supply heavy loads. In light-load cases, the inverters with smaller power ratings can be programmed to automatically reschedule on a regular basis, e.g. every month, such that the inverter IDs are substituted with each other so that different inverters turn on at lighter loads every month, and their lifetimes are extended. Furthermore, the inverters with higher power ratings, which are more expensive, are considered as valuable assets of the system. Such inverters are only added to the system at heavier loads while operating at a high efficiency with a low loss. Hence, their lifetimes are automatically extended by operating in an optimum range instead of sharing power at all times.

5.3 Design of System Parameters

A step-by-step design procedure is described in this section to find the optimal values of the system parameters. First, the voltage and current controllers are tuned to achieve proper voltage and current tracking responses. Subsequently, the droop coefficients are determined such that the frequency and voltage drops caused by the droop strategy lie within an acceptable range. Afterwards, the virtual impedances and the frequency controllers should be designed to improve the system stability and restore the frequency, respectively. Finally, the hysteresis bands are designed according to the desired power ranges of inverters.

5.3.1 Voltage and Current Controllers

Voltage and current controllers are designed using the LQT method introduced in Chapter 3. This method converts the tracking and disturbance rejection problems to a regulation problem that can be solved using the well-known LQR method. The design procedure of the current and voltage controllers for Inverter 1 is provided in detail in Section 3.4.

5.3.2 Droop Coefficients

As the deviations of voltage amplitude and frequency at different load levels are dependent on the droop coefficients, $m_{p,k}$ and $m_{q,k}$ should be designed properly to maintain the deviations within an acceptable range. Considering the system operating modes, the maximum frequency is $f_{\text{nom}} = 60$ Hz. Moreover, when the system is operating in *Mode 2*, the frequency drops to its minimum value at full load, where the no-load frequency and power injection of Inverter k are $\omega_k^{nl} = 2\pi 60$ $^{\text{rad}}/_{\text{s}}$ and $P_k = P_k^{fl}$, respectively. Assuming the minimum allowable frequency, ω_k^{fl}, to be 1% below $2\pi 60$ $^{\text{rad}}/_{\text{s}}$, the frequency-droop coefficient is obtained from (5.10) as follows

$$m_{p,k} = \frac{\omega_k^{nl} - \omega_k^{fl}}{P_k^{fl}}. \tag{5.15}$$

Similarly, the voltage-droop coefficient can be derived by assuming a maximum of 3% voltage deviation around the nominal value, where $V_k^{nl} = 170$ V and $Q_k = Q_k^{fl}$. Therefore, according to (5.10), the voltage-droop coefficient is given by

$$m_{q,k} = \frac{V_k^{nl} - V_k^{fl}}{Q_k^{fl}}. \tag{5.16}$$

5.3.3 Virtual Impedances

The design objective of tuning the virtual impedances is to minimize the active power oscillations caused by load variations. Since the inverters with higher rated powers have higher voltage drops at their output, the virtual impedances are assumed to be related to the rated powers as follows

$$L_1^{\text{vir}} P_1^{fl} = L_2^{\text{vir}} P_2^{fl} = L_3^{\text{vir}} P_3^{fl}. \tag{5.17}$$

The design procedure includes two steps. In the first step, the effect of the virtual impedance variations on the system dominant poles is observed, and a proper parameter range, in which the system is stable, is selected. In the next step, the system is simulated with different values of the virtual impedance to monitor its

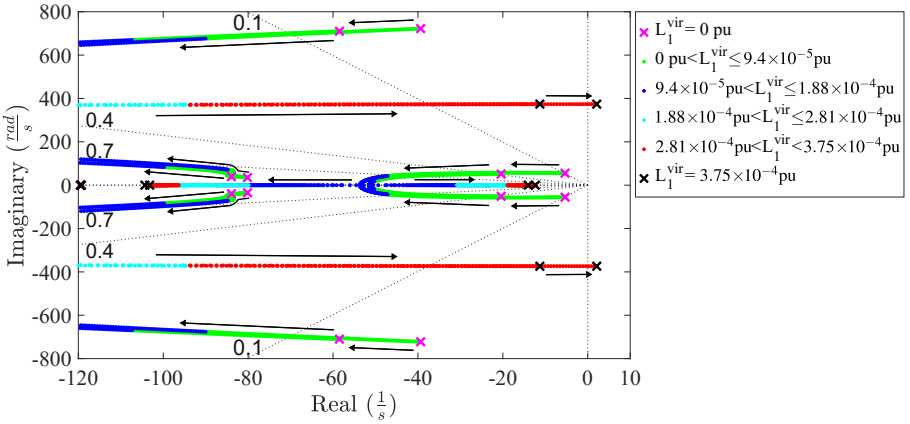

Fig. 5.8: Step 1 of designing L_1^{vir}: selecting the proper range according to the root locus of the system dominant poles by variations in L_1^{vir}.

impact on the active power oscillations in the worst-case scenario, which is a simultaneous change in the loads and no-load frequencies applied at the beginning of the simulation. The power error is defined as $e_{P,k} \triangleq P_{ss,k} - P_k$, where $P_{ss,k}$ is the steady-state value of the active power, and P_k is the value of active power at any point of time. Then, the IAE performance index for the k^{th} inverter, IAE_k, and the entire system, IAE_{total}, are obtained as follows

$$IAE_k = \int_0^{\infty} |e_{P,k}(t)|dt, \;\; IAE_{\text{total}} = \sum_{k=1}^{3} IAE_k. \tag{5.18}$$

The virtual impedance at which IAE_{total} is minimized is selected as the optimum value.

Also, if L_1^{vir} is tuned, L_2^{vir} and L_3^{vir} are obtained accordingly (5.17). Fig. 5.8 illustrates the displacement of the dominant poles of the system with respect to variations in L_1^{vir} from 0 to 3.75×10^{-4} pu. Hence, the proper range for L_1^{vir} is selected from 0.5×10^{-4} pu to 3×10^{-4} pu. As the next step, Fig. 5.9(a) depicts the active power responses of Inverter 1 with respect to changes in L_1^{vir}, and the corresponding power errors are presented in Fig. 5.9(b). The optimum value of L_1^{vir} that minimizes IAE_{total} is found to be 1.75×10^{-4} pu, corresponding to the purple lines in Fig. 5.9.

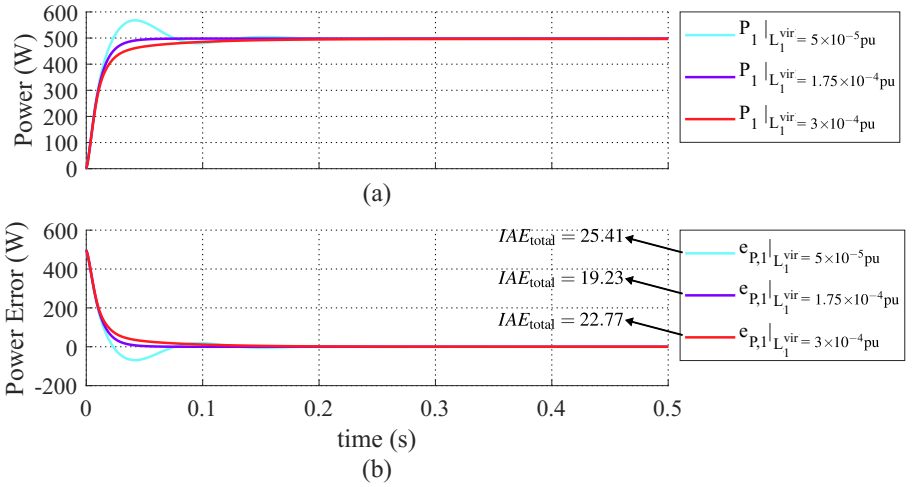

Fig. 5.9: Step 2 of designing L_1^{vir}: obtaining the optimum value of L_1^{vir} by minimizing the IAE index; (a) active power characteristics of Inverter 1 in response to a simultaneous step change in the loads and no-load frequencies of the inverters, and (b) power errors of Inverter 1.

5.3.4 Frequency Controllers

To design the frequency controllers, it is assumed that the system is operating in *Mode 1*, and the controllers should be designed such that the power oscillations are minimized. Since the inverters with the lower rated powers are supposed to supply the lighter loads, their frequency restoration process needs to be faster. Thus, the controller parameters are assumed to be related to the rated powers as follows

$$b_1^{\text{prop}} P_1^{fl} = b_2^{\text{prop}} P_2^{fl} = b_3^{\text{prop}} P_3^{fl}, \tag{5.19}$$

$$b_1^{\text{int}} P_1^{fl} = b_2^{\text{int}} P_2^{fl} = b_3^{\text{int}} P_3^{fl}. \tag{5.20}$$

The design procedure of the frequency controllers is the same as the virtual impedances with the exception that in the second step, the step change is only applied in the load since the no-load frequencies are controlled by the frequency controllers.

Fig. 5.10 shows the displacement of the dominant poles of the system with respect to variations in b_1^{prop} from 0 to 5. The proper range for b_1^{prop} is selected from 0 to 1.25 since this range corresponds to a faster and more stable system according

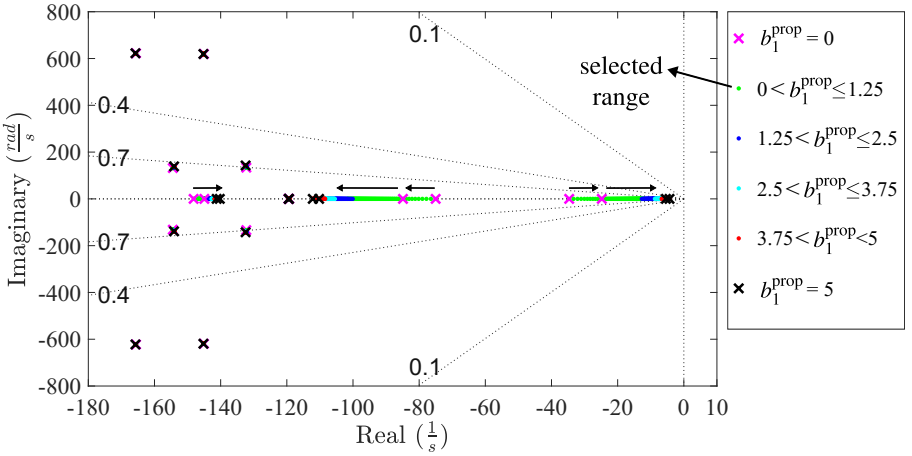

Fig. 5.10: Step 1 of designing b_1^{prop}: selecting the proper range according to the root locus of the system dominant poles by variations in b_1^{prop}.

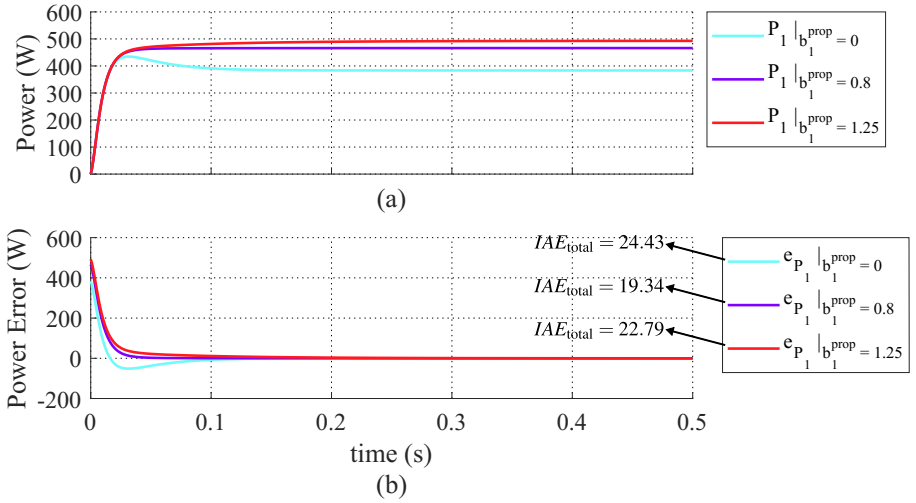

Fig. 5.11: Step 2 of designing b_1^{prop}: obtaining the optimum value of b_1^{prop} by minimizing the IAE index; (a) active power characteristics of Inverter 1 in response to a step change in the load, and (b) power errors of Inverter 1.

to the pole locations. As the second step, Fig. 5.11(a) depicts the active power responses of Inverter 1 with respect to changes in b_1^{prop}, and the corresponding power errors are presented in Fig. 5.11(b). It is worth remarking that since the frequency controllers are changing the droop no-load frequencies, the steady-state powers of the inverters will be different for different values of b_1^{prop}. The optimum value of b_1^{prop} that minimizes IAE_{total} is found to be 0.8, whose response is shown by the purple lines in Fig. 5.11.

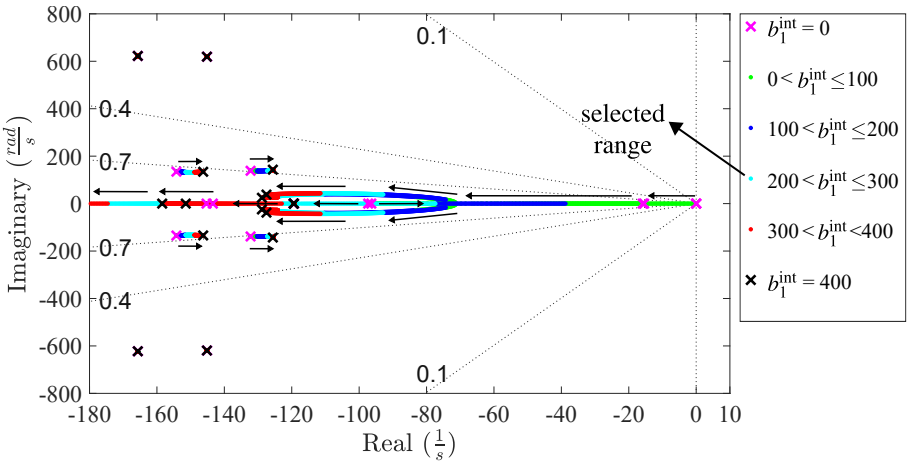

Fig. 5.12: Step 1 of designing b_1^{int}: selecting the proper range according to the root locus of the system dominant poles by variations in b_1^{int}.

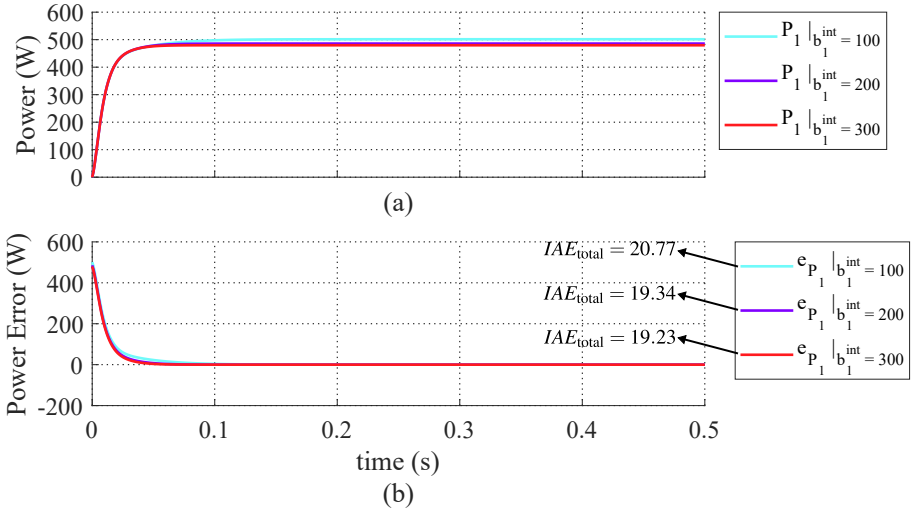

Fig. 5.13: Step 2 of designing b_1^{int}: obtaining the optimum value of b_1^{int} by minimizing the IAE index; (a) active power characteristics of Inverter 1 in response to a step change in the load, and (b) power errors of Inverter 1.

The optimum value of b_1^{int} can be found by the same procedure. Fig. 5.12 shows the displacement of the dominant poles of the system with respect to variations in b_1^{int} from 0 to 400. The proper range for b_1^{int} is selected from 100 to 300. As the second step of design, Fig. 5.13(a) depicts the active power responses of Inverter 1 with respect to changes in b_1^{int}, and the corresponding power errors are presented in Fig. 5.13(b). The optimum value of b_1^{int} that minimizes IAE_{total} is found to be 300, which corresponds to the red lines in Fig. 5.13.

5.3.5 Hysteresis Bands

The hysteresis blocks check whether or not the active powers of inverters lie within the desired power range. Considering (5.14), the hysteresis bands should be selected such that redundant activations and deactivations of the inverters due to changes in the hysteresis outputs are avoided. Thus, supposing a margin of $\pm 10\%$ around $0.3P_k^{fl}$ and $0.8P_k^{fl}$, the upper and lower bands of Hysteresis-1_k and Hysteresis-2_k are given by

$$h_{1,k}^{\min} = 0.9(0.3P_k^{fl}),\ h_{1,k}^{\max} = 1.1(0.3P_k^{fl}), \tag{5.21}$$

$$h_{2,k}^{\min} = 0.9(0.8P_k^{fl}),\ h_{2,k}^{\max} = 1.1(0.8P_k^{fl}). \tag{5.22}$$

5.4 Simulation Results

The parallel inverter system with the parameter values presented in Table 5.1 is simulated to evaluate the performance of the proposed controllers in improving the overall system efficiency. Since Inverter 3 is identical to Inverter 2, its parameters are the same as that of Inverter 2.

As illustrated in Fig. 5.14, first, a very-light load of 0.2 kW is connected to the system at $t = 0.2$ s. Therefore, the OID is enabled during 0.6 s$\leq t \leq$1 s, and it is detected that all three inverters are online. In this case, Inverter 1, which has the lowest rated power, starts to solely supply the load. At $t = 3$ s, the load changes to 1.2 kW, and Inverter 1 increases its power to supply the load; however, since the load is above $0.8P_1^{fl}$, Inverter 2 should turn on to contribute to the load power sharing. Next, the load jumps to 3 kW at $t = 5$ s, where Inverter 3 is also turned on to supply the load. Afterwards, the load increases to 5 kW at $t = 6$ s, where all three inverters operate at almost full-load power. Then, at $t = 7$ s, the load drops to 1.5 kW, where Inverter 2 and Inverter 3 supply the load, and Inverter 1 does not share any power. At $t = 7.5$ s, Inverter 1 is disconnected from the system, and only the identical inverters are online until the end of the simulation. Eventually,

Table 5.1: System parameters

Inverter 1		Inverter 2	
Parameter	Value	Parameter	Value
P_1^{fl}	1 kW	P_2^{fl}	2 kW
$L_{1,1}$	2 mH	$L_{1,2}$	3 mH
$C_{f,1}$	2.2 μF	$C_{f,2}$	1 μF
$L_{2,1}$	2 mH	$L_{2,2}$	2 mH
L_1^{vir}	5.04 mH	L_2^{vir}	2.52 mH
$m_{p,1}$	0.0038	$m_{p,2}$	0.0019
$m_{q,1}$	0.005	$m_{q,2}$	0.0025
V_1^{nl}	170 V	V_2^{nl}	170 V
b_1^{prop}	0.8	b_2^{prop}	0.4
b_1^{int}	300	b_2^{int}	150
$h_{1,1}^{\min}$	270 W	$h_{1,2}^{\min}$	540 W
$h_{1,1}^{\max}$	330 W	$h_{1,2}^{\max}$	660 W
$h_{2,1}^{\min}$	720 W	$h_{2,2}^{\min}$	1440 W
$h_{2,1}^{\max}$	880 W	$h_{2,2}^{\max}$	1760 W

at $t = 8$ s, the load changes to 0.5 kW, which is a very-light load for the identical inverters. Thus, the OID is activated during 8.5 s$\leq t \leq$8.9 s, and it is recognized that only the second and third inverters are available. Hence, only Inverter 2 supplies the load due to having a smaller assigned inverter ID.

Fig. 5.14(a) compares the overall efficiency of the system operating under the proposed and conventional load-sharing methods. It is observed that during the steady-state conditions, the efficiency of the proposed method is higher than or equal to that of the conventional method. In light-load situations, i.e. at 1 s$\leq t \leq$3 s and 9 s$\leq t \leq$11 s, the efficiency improvement can be as much as 14%. Nevertheless, there are two types of transient efficiency drops in the proposed method. The first type is during the OID detection period, which is resolved quickly when the online inverters are detected. The second one, which occurs for a very short period of time, is during the activation/deactivation of the inverters. Furthermore, the inverter active power injections and system operating modes are depicted in Fig. 5.14(b).

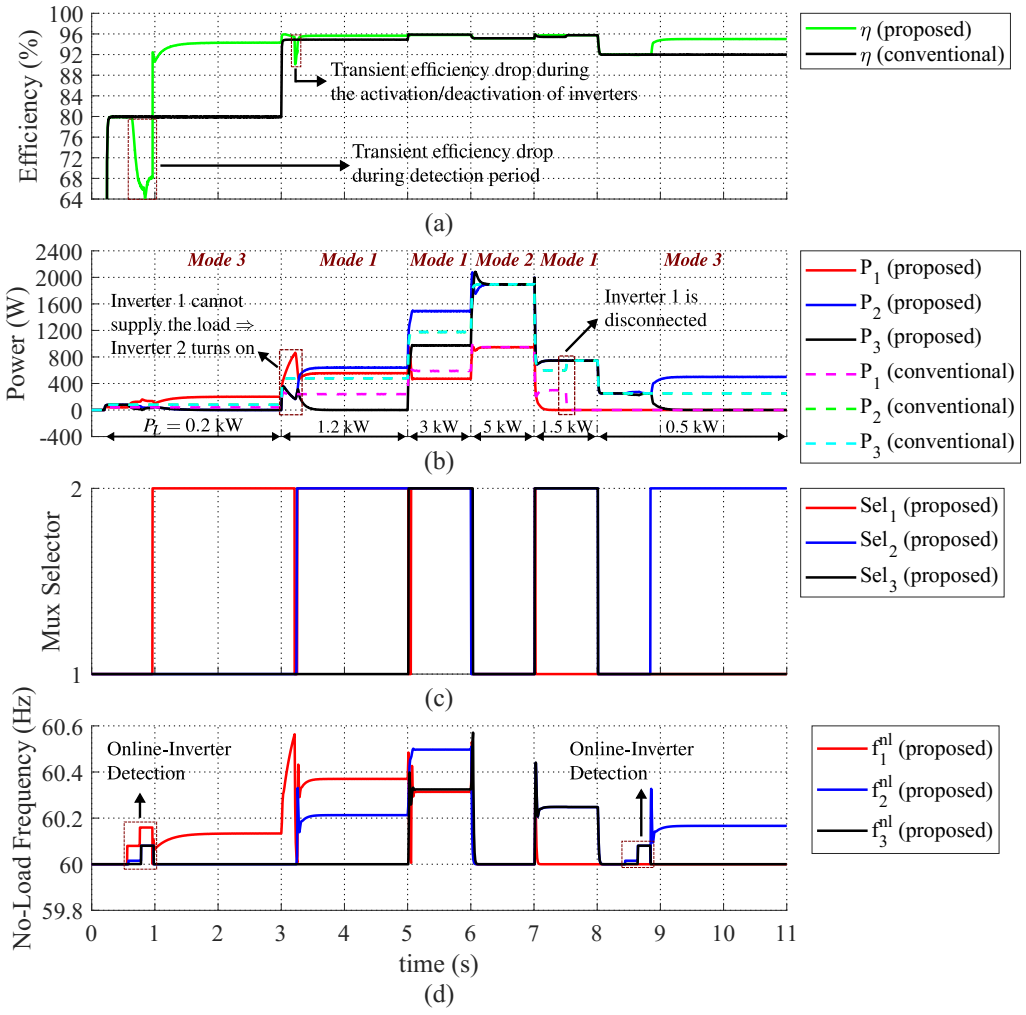

Fig. 5.14: Efficiency comparison between the proposed and conventional methods at different load levels: (a) system efficiencies, (b) inverter active power injections, (c) Mux selector signals, and (d) inverter no-load frequencies.

Additionally, the Mux selector signals and inverter no-load frequencies are shown in Fig. 5.14(c) and Fig. 5.14(d), respectively.

Fig. 5.15 compares the overall system efficiency curves of the proposed and conventional methods within the entire range of loads that the system can support with three online inverters, i.e. 0 W $\leq P_L \leq$ 5 kW. The proposed method significantly increases the overall system efficiency at light loads. As shown in Fig. 5.15, Inverter 1 supplies the load until the inverter power reaches $0.8P_1^{fl}$. Then, Inverter 2 is activated to help Inverter 1 supply the load until its power reaches $0.8P_2^{fl}$, and so on.

5.5 Experimental Results

The experimental results are obtained in two scenarios where two and three inverters are online in the system.

5.5.1 Two Online Inverters

In the first scenario whose experimental setup is depicted in Fig. 5.16, two single-phase parallel inverters with power ratings of $P_1^{fl} = 200$ W and $P_2^{fl} = 400$ W are connected to the loads via LCL filters. The dc supplies are implemented with Chroma programmable dc power supply 62012P and Sorensen programmable power supply SGX500X10C. Furthermore, the inverter controllers are implemented on dSPACE MicroLabBox (RTI 1202). The following experiments are conducted to evaluate the effectiveness of the proposed controllers.

5.5.1.1 Transition between *Mode 1* and *Mode 3*

Fig. 5.17 shows the experimental results when the inverters are operating in *Mode 1* and *Mode 3*. In the beginning, the load is 40 W which is considered as a very-light load. Thus, Inverter 1 solely supplies the load, and the system is in *Mode 3*. Next, the load increases to 240 W. Since 240 W is higher than $0.8P_1^{fl}$, Inverter 1 cannot supply the load individually, and a portion of the demanded power

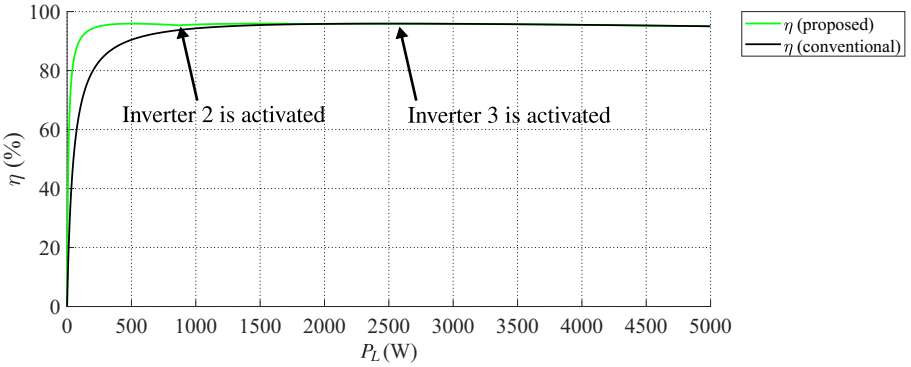

Fig. 5.15: Overall system efficiency comparison between the proposed and conventional methods.

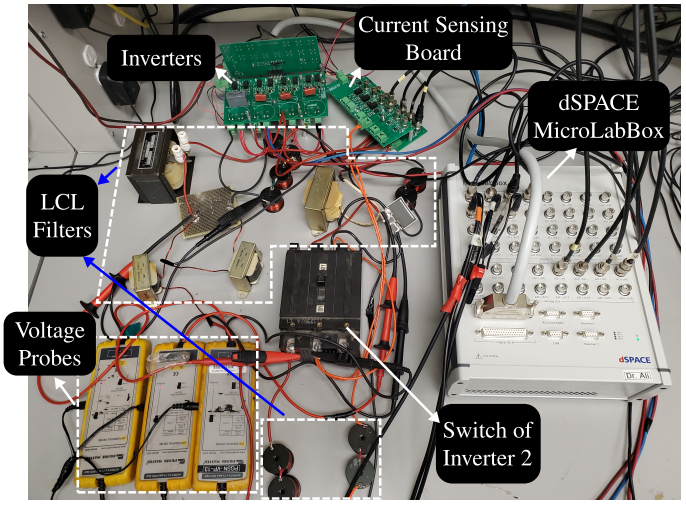

Fig. 5.16: Experimental setup.

is supplied by Inverter 2, which indicates that the system is operating in *Mode 1*. Eventually, the load drops to 40 W. As the mode changes from *Mode 1* to *Mode 3*, the OID is enabled and detects that both inverters are online. Hence, Inverter 1 starts to solely supply the load due to having the lowest rated power. In addition to the active power injections, the load-side inductor currents, capacitor voltages, and no-load frequencies are shown in Fig. 5.17. It should be noted that the active power transients during the turn on process of Inverter 2, i.e. 400 ms $< t <$ 600 ms, are not seen by the load as they are internal transients between the inverters without affecting the sum of all powers provided to the load. Therefore, the load power remains constant during the process of inverters turning on and off since the load is supplied by the sum of P_1 and P_2 by the droop control strategy and the load power reaches its steady-state value much faster than the transient time of turning on Inverter 2.

5.5.1.2 *Operation in Mode 1*

Fig. 5.18 illustrates the experimental results when the inverters are operating in *Mode 1*. Initially, the load is 100 W that lies within the desired power range of Inverter 1. As shown in Fig. 5.18, only Inverter 1 contributes to supplying the load, and the system operates in *Mode 1*. Next, the load changes to 240 W. In this case,

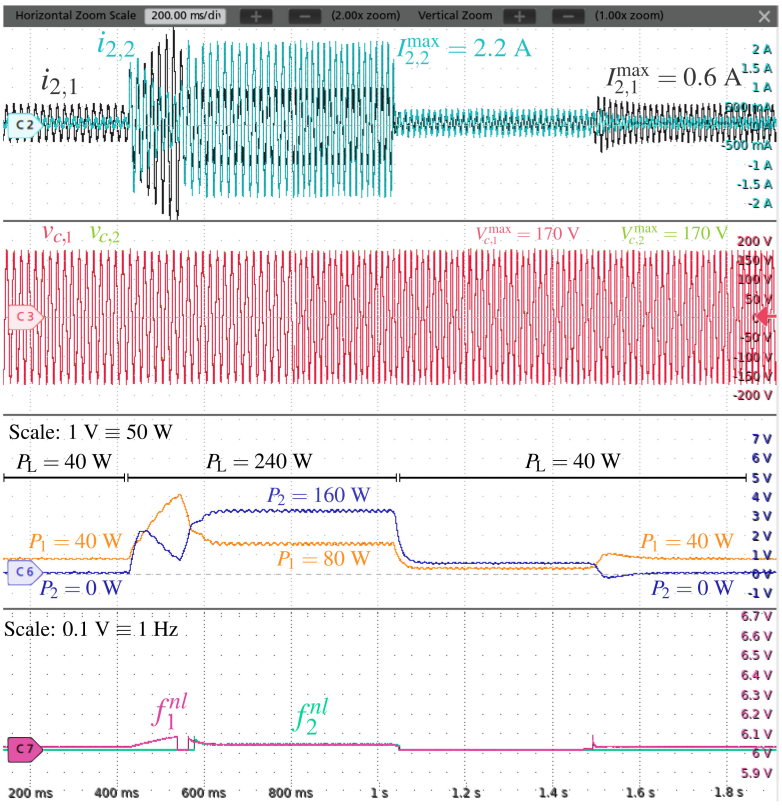

Fig. 5.17: Experimental results with two online inverters: performance of the proposed method in improving the efficiency by deactivating the unnecessary inverter in *Mode 3*.

Inverter 2 cooperates with Inverter 1 in feeding the load. Finally, the load returns to 100 W. Consequently, the proposed controller of Inverter 2 reduces its power injection, and Inverter 1 keeps supplying the load merely. It is worth mentioning that since the inverters proportionally share the power similar to the conventional droop strategy in *Mode 2*, this mode is not included in the experimental results.

5.5.1.3 Discussions

In the experimental results depicted in Fig. 5.17 and Fig. 5.18, it is observed that the power distribution among the inverters is different for the 240 W load. The reason is that the power distribution among the inverters depends on the previous load, system mode, and the changing rate of no-load frequencies. In Fig. 5.17, a very-light load of 40 W is connected at the beginning, and Inverter 1 is solely

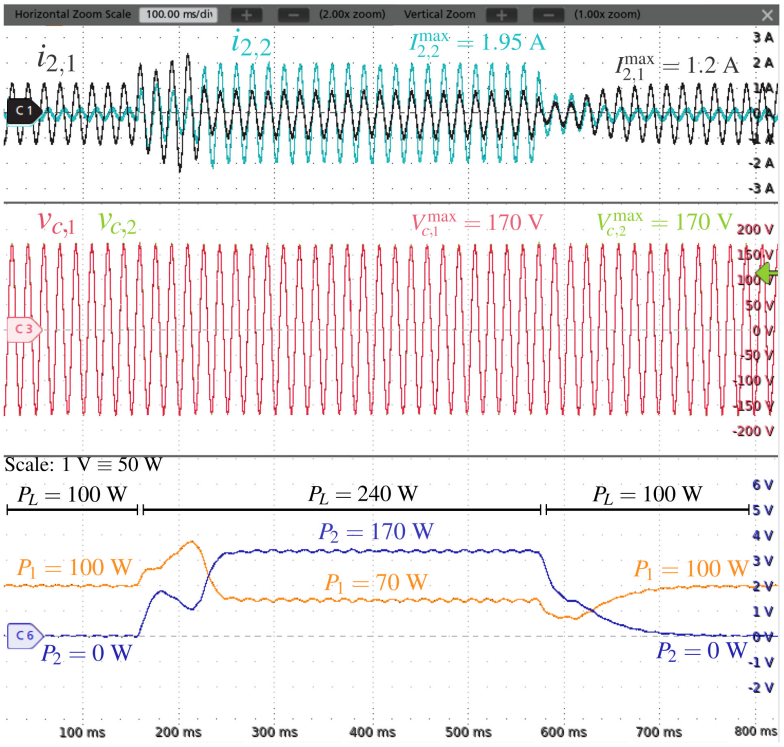

Fig. 5.18: Experimental results with two online inverters: performance of the proposed method in improving the efficiency by deactivating the unnecessary inverter in *Mode 1*.

supplying the load in *Mode 3*. Then, the load changes to 240 W and the system mode changes to *Mode 1*, where Inverter 1 and Inverter 2 inject 80 W and 160 W, respectively. In Fig. 5.18, although Inverter 1 is feeding the load at the beginning of the experiment, its operating mode is *Mode 1*. When the load changes to 240 W, while the system remains in *Mode 1*, Inverter 1 injects 70 W and Inverter 2 supplies 170 W.

Considering the efficiency curve depicted in Fig. 5.4, the experimental system efficiency under the proposed and conventional methods can be compared using Table 5.2. It is observed that the system efficiency is improved at light loads in comparison with the conventional power sharing. Furthermore, according to Fig. 5.17, Fig. 5.18, and Table 5.2, it is concluded that both Inverter 1 and Inverter 2 operate within their desired power ranges at a 240 W load.

Table 5.2: Experimental efficiency comparison between the conventional and proposed methods for two inverters

Efficiency	$P_1 = 40$ W $P_2 = 0$ W	$P_1 = 80$ W $P_2 = 160$ W	$P_1 = 100$ W $P_2 = 0$ W	$P_1 = 70$ W $P_2 = 140$ W
η_1	94.3%	95.8%	96%	95.7%
η_2	-	95.8%	-	95.85%
$\eta_{\text{sys,prop}}$	94.3%	95.8%	96%	95.8%
$\eta_{\text{sys,conv}}$	86.5%	95.8%	93.6%	95.8%

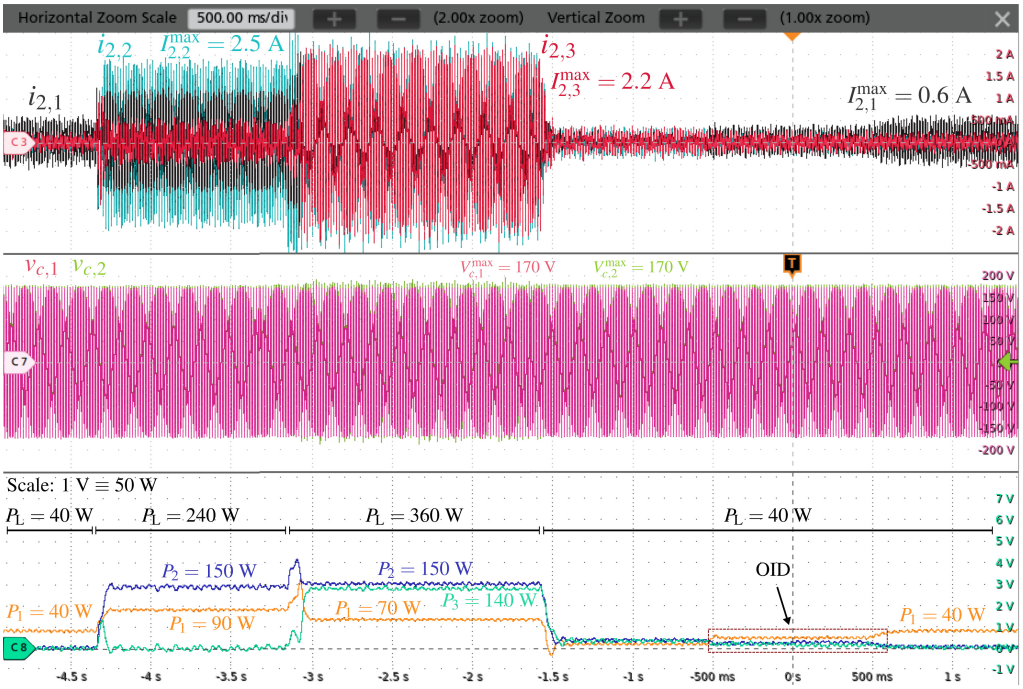

Fig. 5.19: Experimental results with three online inverters: performance of the proposed controller in improving the efficiency by deactivating the unnecessary inverters.

5.5.2 Three Online Inverters

For the second scenario, three single-phase parallel inverters with power ratings of $P_1^{fl} = 200$ W and $P_2^{fl} = P_3^{fl} = 400$ W are connected to the loads via LCL filters. Fig. 5.19 shows the experimental results of the system with three online inverters operating in *Mode 1* and *Mode 3*. First, the load is 40 W which is considered as a very-light load. Hence, Inverter 1 solely supplies the load, and the system operates

Table 5.3: Experimental efficiency comparison between the conventional and proposed methods for three inverters

Efficiency	$P_1 = 40$ W $P_2 = 0$ W $P_3 = 0$ W	$P_1 = 90$ W $P_2 = 150$ W $P_3 = 0$ W	$P_1 = 70$ W $P_2 = 150$ W $P_3 = 140$ W	$P_1 = 40$ W $P_2 = 0$ W $P_2 = 0$ W
η_1	94.3%	95.9%	95.7%	94.3%
η_2	-	95.75%	95.75%	-
η_3	-	-	95.7%	-
$\eta_{\text{sys,prop}}$	94.3%	95.8%	95.72%	94.3%
$\eta_{\text{sys,conv}}$	80%	94.9%	95.7%	80%

in *Mode 3*. Next, the load increases to 240 W. Since Inverter 1 cannot supply the load individually, Inverter 2 starts to supply the load, and the system mode changes to *Mode 1*. Subsequently, the load jumps to 360 W which should be fed by all three inverters. Finally, the load drops to 40 W. As the mode changes from *Mode 1* to *Mode 3*, the OID is activated and detects that all inverters are online. Thus, Inverter 1 starts to supply the load solely due to having the lowest rated power. In addition to the active power injections, the load-side inductor currents and the LCL filter capacitor voltages are shown in Fig. 5.19.

Considering the efficiency curve depicted in Fig. 5.4, the experimental system efficiency under the proposed and conventional methods can be compared using Table 5.3. It is observed that the efficiency improvement is more significant in the second scenario in comparison with the first scenario.

5.6 Summary

A communicationless modified droop strategy is proposed in this chapter to improve the overall system efficiency of parallel inverters. It is observed that the overall system efficiency can be increased by up to 14% at light loads in comparison with the conventional droop strategy. The proposed method maintains the modularity and flexibility in case more inverters will be added to the system. Ultimately,

the proposed method would improve the reliability and system efficiency without any single point of failure. Ultimately, the lifetimes of inverters with higher rated powers are extended by the proposed method.

Chapter 6

Summary and Future Work

6.1 Summary of Contributions

In this thesis, control design, stability analysis, efficiency optimization, and experimental verification for single-phase inverters in microgrid application is presented. The objective of the thesis is to propose systematic, optimal, and robust control methods for inverters operating in a microgrid and to address the stability analysis and efficiency optimization of the overall system while the proposed controllers are deployed. The main contributions and conclusions of this thesis are summarized below.

(i) A robust control system is proposed for a single-phase inverter in a weak grid operation. The proposed control system compensates weak grid uncertainties and practical uncertainties such as computational, and PWM delays. Furthermore, the proposed control system achieves power decoupling between ac and dc sides without any auxiliary circuit.

(ii) An optimal and systematic design approach for a cascade control system is proposed based on the LQT method. This method does consider the interaction among cascaded loops, which leads to relaxing the timescale restriction that the inner loops must be much faster than the outer loops in conventional approaches. Therefore, the speed of the internal loop and the external loop can be similar. Using the proposed method, a cascade control system based on intra-loop state feedback is structured and systematically designed for a single-phase standalone inverter.

(iii) An accurate approach is proposed to derive the mathematical model of a single-phase microgrid containing parallel droop-controlled inverters in details. The proposed model can be used for small-signal stability analysis, tuning the system parameters, and studying the system sensitivity against parameter variations. Moreover, the proposed model is able to represent behaviors of the fast dynamic variables of the internal loops such as currents and voltages.

(iv) A communicationless modified droop strategy is proposed to improve the overall efficiency of a standalone microgrid with parallel inverters. In this strategy, in stead of proportionally sharing the power among all inverters, only a number of inverters contribute to supplying the load such that the output power of each inverter is maintained within a proper range with respect to the inverter efficiency curve. The proposed power-sharing strategy can enhance the overall system efficiency by up to 14% at light loads compared with the conventional droop strategy.

6.2 Future Work

There are a number of directions that this research could proceed in; four of the most promising are outlined below:

(i) Using the proposed systematic design method to design a cascade control system for a grid-connected inverter in weak grid operation, which includes design of current control, dc link control, and PLL loops.

(ii) Using the proposed systematic design method to design a fast control system that limits the short circuit current of GFM inverters in the grid-connected operation mode.

(iii) Using the proposed modeling approach to precisely study the stability of single-phase grid-connected inverters with nonlinear stationary-frame controllers, including the dc link and current controllers.

(iv) Using the proposed unequal power-sharing strategy to improve the overall efficiency in dc microgrids.

Bibliography

[1] S. A. Khajehoddin, M. Karimi-Ghartemani, P. K. Jain, and A. Bakhshai, "DC-bus design and control for a single-phase grid-connected renewable converter with a small energy storage component," *IEEE Transactions on Power Electronics*, vol. 28, no. 7, pp. 3245–3254, 2013.

[2] R. Pradhan and B. Subudhi, "Double integral sliding mode MPPT control of a photovoltaic system," *IEEE Transactions on Control Systems Technology*, vol. 24, no. 1, pp. 285–292, 2016.

[3] M. Trifkovic, M. Sheikhzadeh, K. Nigim, and P. Daoutidis, "Modeling and control of a renewable hybrid energy system with hydrogen storage," *IEEE Transactions on Control Systems Technology*, vol. 22, no. 1, pp. 169–179, 2014.

[4] C. Schmuck, F. Woittennek, A. Gensior, and J. Rudolph, "Feed-forward control of an HVDC power transmission network," *IEEE Transactions on Control Systems Technology*, vol. 22, no. 2, pp. 597–606, 2014.

[5] W. Qi, J. Liu, X. Chen, and P. D. Christofides, "Supervisory predictive control of standalone wind/solar energy generation systems," *IEEE Transactions on Control Systems Technology*, vol. 19, no. 1, pp. 199–207, 2011.

[6] S. A. Khajehoddin, M. K. Ghartemani, and M. Ebrahimi, "Grid-Supporting Inverters with Improved Dynamics Using Enhanced Virtual Synchronous Machine (eVSM)," *IEEE Transactions on Industrial Electronics*, 2018.

[7] Y. Huang, X. Yuan, J. Hu, and P. Zhou, "Modeling of VSC connected to weak grid for stability analysis of DC-link voltage control," *IEEE Journal of Emerging and Selected Topics in Power Electronics*, vol. 3, no. 4, pp. 1193–1204, 2015.

[8] P. Krishayya, R. Adapa, M. Holm, *et al.*, "IEEE guide for planning DC links terminating at AC locations having low short-circuit capacities, part I: AC/DC system interaction phenomena," *CIGRE, France*, 1997.

[9] K. H. Ahmed, A. M. Massoud, S. J. Finney, and B. W. Williams, "A modified stationary reference frame-based predictive current control with zero steady-state error for LCL coupled inverter-based distributed generation systems," *IEEE Transactions on Industrial Electronics*, vol. 58, no. 4, pp. 1359–1370, 2011.

[10] F. Huerta, D. Pizarro, S. Cobreces, F. J. Rodriguez, C. Girón, and A. Rodríguez, "LQG Servo Controller for the Current Control of Grid-Connected Voltage-Source Converters," *IEEE Transactions on Industrial Electronics*, vol. 59, no. 11, pp. 4272–4284, 2012.

[11] T. Hornik and Q.-C. Zhong, "A Current-Control Strategy for Voltage-Source Inverters in Microgrids Based on H_∞ and Repetitive Control," *IEEE Transactions on Power Electronics*, vol. 26, no. 3, pp. 943–952, 2011.

[12] S.-Y. Park, C.-L. Chen, J.-S. Lai, and S.-R. Moon, "Admittance compensation in current loop control for a grid-tie LCL fuel cell inverter," *IEEE Transactions on Power Electronics*, vol. 23, no. 4, pp. 1716–1723, 2008.

[13] G. Shen, D. Xu, L. Cao, and X. Zhu, "An improved control strategy for grid-connected voltage source inverters with an LCL filter," *IEEE Transactions on Power Electronics*, vol. 23, no. 4, pp. 1899–1906, 2008.

[14] S. Yang, Q. Lei, F. Z. Peng, and Z. Qian, "A robust control scheme for grid-connected voltage-source inverters," *IEEE Transactions on Industrial Electronics*, vol. 58, no. 1, pp. 202–212, 2011.

[15] T.-S. Lee, S. Chiang, and J.-M. Chang, "H_∞ loop-shaping controller designs for the single-phase UPS inverters," *IEEE Transactions on Power Electronics*, vol. 16, no. 4, pp. 473–481, 2001.

[16] M. Aten and H. Werner, "Robust multivariable control design for HVDC back to back schemes," *in IEE Proceedings Generation, Transmission and Distribution*, vol. 150, no. 6, pp. 761–767, 2003.

[17] Y. He, K.-w. Wang, and H. S.-h. Chung, "Utilization of proportional filter capacitor voltage feedforward to realize active damping for digitally-controlled grid-tied inverter operating under wide grid impedance variation," *in IEEE Energy Conversion Congress and Exposition (ECCE)*, pp. 4450–4457, 2014.

[18] I. J. Gabe, V. F. Montagner, and H. Pinheiro, "Design and implementation of a robust current controller for VSI connected to the grid through an LCL filter," *IEEE Transactions on Power Electronics*, vol. 24, no. 6, pp. 1444–1452, 2009.

[19] J. C. Peña, G. Melo, C. A. Canesin, and L. P. Sampaio, "Robust control of a single-phase VSI with LCL filter for grid-tie and islanded operation modes applied to PV distributed generation in microgrids environment," *in IEEE Energy Conversion Congress and Exposition (ECCE)*, pp. 785–792, 2014.

[20] N. Amouzegar Ashtiani, S. M. Azizi, and S. A. Khajehoddin, "Control design in μ-synthesis framework for grid-connected inverters with higher order filters," in *2016 IEEE Energy Conversion Congress and Exposition (ECCE)*, pp. 1–6, IEEE, 2016.

[21] Y. Wang, J. Wang, W. Zeng, H. Liu, and Y. Chai, "H_∞ Robust Control of an LCL-Type Grid-Connected Inverter with Large-Scale Grid Impedance Perturbation," *Energies*, vol. 11, no. 1, p. 57, 2018.

[22] T. Yao, I. Leonard, R. Ayyanar, and K. Tsakalis, "μ-synthesized robust controller for multi-SST islanded smart grid," *in IEEE Energy Conversion Congress and Exposition (ECCE)*, pp. 1–8, 2016.

[23] J. R. Massing, M. Stefanello, H. A. Grundling, and H. Pinheiro, "Adaptive current control for grid-connected converters with LCL filter," *IEEE Transactions on Industrial Electronics*, vol. 59, no. 12, pp. 4681–4693, 2012.

[24] S. Buso and P. Mattavelli, "Digital control in power electronics," *Lectures on power electronics*, vol. 1, no. 1, pp. 1–158, 2006.

[25] P. Cortes, J. Rodriguez, C. Silva, and A. Flores, "Delay compensation in model predictive current control of a three-phase inverter," *IEEE Transactions on Industrial Electronics*, vol. 59, no. 2, pp. 1323–1325, 2012.

[26] J. Rodriguez, M. P. Kazmierkowski, J. R. Espinoza, P. Zanchetta, H. Abu-Rub, H. A. Young, and C. A. Rojas, "State of the art of finite control set model predictive control in power electronics," *IEEE Transactions on Industrial Informatics*, vol. 9, no. 2, pp. 1003–1016, 2013.

[27] K. Kim, M. Sung, and H.-W. Jin, "Design and implementation of a delay-guaranteed motor drive for precision motion control," *IEEE Transactions on Industrial Informatics*, vol. 8, no. 2, pp. 351–365, 2012.

[28] J. Wang, J. D. Yan, L. Jiang, and J. Zou, "Delay-dependent stability of single-loop controlled grid-connected inverters with LCL filters," *IEEE Transactions on Power Electronics*, vol. 31, no. 1, pp. 743–757, 2016.

[29] K.-J. Lee, B.-G. Park, R.-Y. Kim, and D.-S. Hyun, "Robust predictive current controller based on a disturbance estimator in a three-phase grid-connected inverter," *IEEE Transactions on Power Electronics*, vol. 27, no. 1, pp. 276–283, 2012.

[30] C. Chen, J. Xiong, Z. Wan, J. Lei, and K. Zhang, "A time delay compensation method based on area equivalence for active damping of an LCL-type converter," *IEEE Transactions on Power Electronics*, vol. 32, no. 1, pp. 762–772, 2017.

[31] Z. Zhou and Y. Liu, "Time delay compensation-based fast current controller for active power filters," *IET Power Electronics*, vol. 5, no. 7, pp. 1164–1174, 2012.

[32] J. R. Fischer, S. A. Gonzalez, M. A. Herran, M. G. Judewicz, and D. O. Carrica, "Calculation-delay tolerant predictive current controller for three-phase inverters," *IEEE Transactions on Industrial Informatics*, vol. 10, no. 1, pp. 233–242, 2014.

[33] M. Karimi-Ghartemani, S. A. Khajehoddin, P. Jain, and A. Bakhshai, "A systematic approach to DC-bus control design in single-phase grid-connected renewable converters," *IEEE Transactions on Power Electronics*, vol. 28, no. 7, pp. 3158–3166, 2013.

[34] N. Amouzegar Ashtiani, S. M. Azizi, and S. A. Khajehoddin, "Robust $H\infty$ DC link control design for high-power density converters with high-order filter in PV systems," in *2017 IEEE Energy Conversion Congress and Exposition (ECCE)*, pp. 58–63, 2017.

[35] H. Li, K. Zhang, H. Zhao, S. Fan, and J. Xiong, "Active power decoupling for high-power single-phase PWM rectifiers," *IEEE Transactions on Power Electronics*, vol. 28, no. 3, pp. 1308–1319, 2012.

[36] R. Wang, F. Wang, D. Boroyevich, R. Burgos, R. Lai, P. Ning, and K. Rajashekara, "A high power density single-phase PWM rectifier with active ripple energy storage," *IEEE Transactions on Power Electronics*, vol. 26, no. 5, pp. 1430–1443, 2010.

[37] T. Hirao, T. Shimizu, M. Ishikawa, and K. Yasui, "A modified modulation control of a single-phase inverter with enhanced power decoupling for a photovoltaic AC module," *in IEEE European Conference on Power Electronics and Applications*, pp. 1–10, 2005.

[38] B. M. Ho, S.-H. Chung, and S. Hui, "An integrated inverter with maximum power tracking for grid-connected PV systems," *in IEEE Applied Power Electronics Conference and Exposition (APEC)*, vol. 3, pp. 1559–1565, 2004.

[39] W. Qi, H. Wang, X. Tan, G. Wang, and K. D. Ngo, "A novel active power decoupling single-phase PWM rectifier topology," in *2014 IEEE Applied Power Electronics Conference and Exposition-APEC 2014*, pp. 89–95, IEEE, 2014.

[40] J. Dai, D. Xu, B. Wu, and N. R. Zargari, "Unified DC-link current control for low-voltage ride-through in current-source-converter-based wind energy conversion systems," *IEEE Transactions on Power Electronics*, vol. 26, no. 1, pp. 288–297, 2011.

[41] J. Yao, H. Li, Y. Liao, and Z. Chen, "An improved control strategy of limiting the DC-link voltage fluctuation for a doubly fed induction wind generator," *IEEE Transactions on Power Electronics*, vol. 23, no. 3, pp. 1205–1213, 2008.

[42] C. Wang, X. Li, L. Guo, and Y. W. Li, "A nonlinear-disturbance-observer-based DC-bus voltage control for a hybrid AC/DC microgrid," *IEEE Transactions on Power Electronics*, vol. 29, no. 11, pp. 6162–6177, 2014.

[43] M. Ciobotaru, R. Teodorescu, and F. Blaabjerg, "Control of single-stage single-phase PV inverter," *EPE Journal*, vol. 16, no. 3, pp. 20–26, 2006.

[44] C. Meza, J. J. Negroni, D. Biel, and F. Guinjoan, "Energy-balance modeling and discrete control for single-phase grid-connected PV central inverters," *IEEE Transactions on Industrial Electronics*, vol. 55, no. 7, pp. 2734–2743, 2008.

[45] J. Alcalá, E. Bárcenas, and V. Cárdenas, "Practical methods for tuning PI controllers in the DC-link voltage loop in Back-to-Back power converters," *in IEEE Power Electronics International Congress (CIEP)*, pp. 46–52, 2010.

[46] J. M. Guerrero, M. Chandorkar, T.-L. Lee, and P. C. Loh, "Advanced control architectures for intelligent microgridsPart I: Decentralized and hierarchical control," *IEEE Transactions on Industrial Electronics*, vol. 60, no. 4, pp. 1254–1262, 2012.

[47] J. M. Guerrero, J. C. Vasquez, J. Matas, L. G. De Vicuña, and M. Castilla, "Hierarchical control of droop-controlled AC and DC microgridsA general approach toward standardization," *IEEE Transactions on industrial electronics*, vol. 58, no. 1, pp. 158–172, 2011.

[48] A. Yazdani and R. Iravani, *Voltage-sourced converters in power systems*, vol. 34. Wiley Online Library, 2010.

[49] J. C. Vasquez, J. M. Guerrero, A. Luna, P. Rodríguez, and R. Teodorescu, "Adaptive droop control applied to voltage-source inverters operating in grid-connected and islanded modes," *IEEE transactions on industrial electronics*, vol. 56, no. 10, pp. 4088–4096, 2009.

[50] F. Chen, R. Burgos, D. Boroyevich, J. Vasquez, and J. M. Guerrero, "Investigation of Nonlinear Droop Control in DC Power Distribution Systems: Load Sharing, Voltage Regulation, Efficiency and Stability," *IEEE Transactions on Power Electronics*, 2019.

[51] F. Gao, D. Li, P. C. Loh, Y. Tang, and P. Wang, "Indirect dc-link voltage control of two-stage single-phase PV inverter," in *Energy Conversion Congress and Exposition, 2009. ECCE 2009. IEEE*, pp. 1166–1172, IEEE, 2009.

[52] E. Villanueva, P. Correa, J. Rodríguez, and M. Pacas, "Control of a single-phase cascaded H-bridge multilevel inverter for grid-connected photovoltaic systems," *IEEE Transactions on Industrial Electronics*, vol. 56, no. 11, pp. 4399–4406, 2009.

[53] N. Amouzegar Ashtiani, S. M. Azizi, and S. A. Khajehoddin, "Robust Control Design for High-Power Density PV Converters in Weak Grids," *IEEE*

Transactions on Control Systems Technology, vol. 27, no. 6, pp. 2361–2373, 2018.

[54] A. Dell'Aquila, M. Liserre, V. G. Monopoli, and P. Rotondo, "Overview of PI-based solutions for the control of DC buses of a single-phase H-bridge multilevel active rectifier," *IEEE Transactions on Industry Applications*, vol. 44, no. 3, pp. 857–866, 2008.

[55] L. Liu, H. Li, and Y. Xue, "A coordinated active and reactive power control strategy for grid-connected cascaded photovoltaic (PV) system in high voltage high power applications," in *Applied Power Electronics Conference and Exposition (APEC), 2013 Twenty-Eighth Annual IEEE*, pp. 1301–1308, IEEE, 2013.

[56] H. Shin and J.-I. Ha, "Individual MPPTs of single-phase three-level split DC-bus inverter," in *Applied Power Electronics Conference and Exposition (APEC), 2014 Twenty-Ninth Annual IEEE*, pp. 669–675, IEEE, 2014.

[57] X. Wu, X. Li, X. Yuan, and Y. Geng, "Grid harmonics suppression scheme for LCL-type grid-connected inverters based on output admittance revision," *IEEE Transactions on Sustainable Energy*, vol. 6, no. 2, pp. 411–421, 2015.

[58] J. Dannehl, F. W. Fuchs, S. Hansen, and P. B. Thogersen, "Investigation of active damping approaches for PI-based current control of grid-connected pulse width modulation converters with LCL filters," *IEEE Transactions on Industry Applications*, vol. 46, no. 4, pp. 1509–1517, 2010.

[59] J. L. Sosa, M. Castilla, J. Miret, J. Matas, and Y. Al-Turki, "Control strategy to maximize the power capability of PV three-phase inverters during voltage sags," *IEEE Transactions on Power Electronics*, vol. 31, no. 4, pp. 3314–3323, 2015.

[60] E. Afshari, G. R. Moradi, R. Rahimi, B. Farhangi, Y. Yang, F. Blaabjerg, and S. Farhangi, "Control strategy for three-phase grid-connected PV inverters

enabling current limitation under unbalanced faults," *IEEE Transactions on Industrial Electronics*, vol. 64, no. 11, pp. 8908–8918, 2017.

[61] M. A. G. López, J. L. G. de Vicuña, J. Miret, M. Castilla, and R. Guzmán, "Control strategy for grid-connected three-phase inverters during voltage sags to meet grid codes and to maximize power delivery capability," *IEEE Transactions on Power Electronics*, vol. 33, no. 11, pp. 9360–9374, 2018.

[62] F. Blaabjerg, R. Teodorescu, M. Liserre, and A. V. Timbus, "Overview of control and grid synchronization for distributed power generation systems," *IEEE Transactions on industrial electronics*, vol. 53, no. 5, pp. 1398–1409, 2006.

[63] M. Zhao, X. Yuan, J. Hu, and Y. Yan, "Voltage dynamics of current control time-scale in a VSC-connected weak grid," *IEEE Transactions on Power Systems*, vol. 31, no. 4, pp. 2925–2937, 2015.

[64] J. Rocabert, A. Luna, F. Blaabjerg, and P. Rodriguez, "Control of power converters in AC microgrids," *IEEE transactions on power electronics*, vol. 27, no. 11, pp. 4734–4749, 2012.

[65] L. Zheng, R. P. Kandula, K. Kandasamy, and D. Divan, "Stacked Low-Inertia Converter or Solid-State Transformer: Modeling and Model Predictive Priority-Shifting Control for Voltage Balance," *IEEE Transactions on Power Electronics*, 2021.

[66] M. Hinkkanen, H. A. A. Awan, Z. Qu, T. Tuovinen, and F. Briz, "Current control for synchronous motor drives: Direct discrete-time pole-placement design," *IEEE Transactions on Industry Applications*, vol. 52, no. 2, pp. 1530–1541, 2016.

[67] K. Cui, C. Wang, L. Gou, and Z. An, "Analysis and Design of Current Regulators for PMSM Drives Based on DRGA," *IEEE Transactions on Transportation Electrification*, vol. 6, no. 2, pp. 659–667, 2020.

[68] H. A. Hussain, "Tuning and Performance Evaluation of 2DOF PI Current Controllers for PMSM Drives," *IEEE Transactions on Transportation Electrification*, 2020.

[69] R. R. Sawant and M. C. Chandorkar, "A multifunctional four-leg grid-connected compensator," *IEEE Transactions on Industry Applications*, vol. 45, no. 1, pp. 249–259, 2009.

[70] R. Teodorescu, M. Liserre, and P. Rodriguez, *Grid converters for photovoltaic and wind power systems*, vol. 29. John Wiley & Sons, 2011.

[71] T. E. Marlin, *Process control: designing processes and control systems for dynamic performance*. McGraw-Hill, 1995.

[72] L. Meng, Z. Shu, Y. Lei, H. Yan, Z. Li, L. Ma, X. Yin, and X. He, "Optimal Input and Output Power Quality Control of Single-Phase AC–DC–DC Converter With Significant DC-Link Voltage Ripple," *IEEE Transactions on Industrial Electronics*, vol. 67, no. 12, pp. 10366–10376, 2020.

[73] N. M. Dehkordi, N. Sadati, and M. Hamzeh, "A robust backstepping high-order sliding mode control strategy for grid-connected DG units with harmonic/interharmonic current compensation capability," *IEEE Transactions on Sustainable Energy*, vol. 8, no. 2, pp. 561–572, 2016.

[74] D. Xu, G. Wang, W. Yan, and X. Yan, "A novel adaptive command-filtered backstepping sliding mode control for PV grid-connected system with energy storage," *Solar Energy*, vol. 178, pp. 222–230, 2019.

[75] B. Fan, S. Guo, Q. Yang, and W. Liu, "Decentralised adaptive control design for single-phase parallel-inverter systems," *IET Renewable Power Generation*, vol. 13, no. 15, pp. 2752–2761, 2019.

[76] T. Roy, M. Mahmud, S. N. Islam, N. Rajasekar, K. M. Muttaqi, and A. M. Oo, "Robust Adaptive Direct Power Control of Grid-Connected Photovoltaic Systems," in *2020 IEEE International Conference on Power Electronics, Smart Grid and Renewable Energy (PESGRE2020)*, pp. 1–6, IEEE, 2020.

[77] R.-J. Wai and Y. Yang, "Design of backstepping direct power control for three-phase PWM rectifier," *IEEE Transactions on Industry Applications*, vol. 55, no. 3, pp. 3160–3173, 2019.

[78] X. Huang, K. Wang, B. Fan, Q. Yang, G. Li, D. Xie, and M. L. Crow, "Robust current control of grid-tied inverters for renewable energy integration under non-ideal grid conditions," *IEEE Transactions on Sustainable Energy*, vol. 11, no. 1, pp. 477–488, 2019.

[79] Y. Han, H. Li, P. Shen, E. A. A. Coelho, and J. M. Guerrero, "Review of active and reactive power sharing strategies in hierarchical controlled microgrids," *IEEE Transactions on Power Electronics*, vol. 32, no. 3, pp. 2427–2451, 2016.

[80] Y. W. Li and C.-N. Kao, "An accurate power control strategy for power-electronics-interfaced distributed generation units operating in a low-voltage multibus microgrid," *IEEE Transactions on Power Electronics*, vol. 24, no. 12, pp. 2977–2988, 2009.

[81] J. M. Carrasco, L. García Franquelo, J. T. Bialasiewicz, E. Galván, R. C. Portillo Guisado, M. d. l. Á. Martín Prats, J. I. León, and N. Moreno-Alfonso, "Power-electronic systems for the grid integration of renewable energy sources: A survey," *IEEE Transactions on Industrial Electronics, 53 (4), 1002-1016.*, 2006.

[82] L. Asiminoaei, E. Aeloiza, P. N. Enjeti, and F. Blaabjerg, "Shunt active-power-filter topology based on parallel interleaved inverters," *IEEE Transactions on Industrial Electronics*, vol. 55, no. 3, pp. 1175–1189, 2008.

[83] R. Li and D. Xu, "Parallel operation of full power converters in permanent-magnet direct-drive wind power generation system," *IEEE Transactions on Industrial Electronics*, vol. 60, no. 4, pp. 1619–1629, 2011.

[84] M. H. Ravanji, N. Amouzegar Ashtiani, M. Parniani, and H. Mokhtari, "Modeling and control of zero-sequence circulating current in parallel converters with space vector modulation," *IEEE Journal of Emerging and Selected Topics in Power Electronics*, vol. 5, no. 1, pp. 363–377, 2016.

[85] K. Tan, X. Peng, P. L. So, Y. C. Chu, and M. Z. Chen, "Centralized control for parallel operation of distributed generation inverters in microgrids," *IEEE Transactions on Smart Grid*, vol. 3, no. 4, pp. 1977–1987, 2012.

[86] P. C. Loh, D. Li, Y. K. Chai, and F. Blaabjerg, "Autonomous control of interlinking converter with energy storage in hybrid AC–DC microgrid," *IEEE Transactions on Industry Applications*, vol. 49, no. 3, pp. 1374–1382, 2013.

[87] F. Katiraei, R. Iravani, N. Hatziargyriou, and A. Dimeas, "Microgrids management," *IEEE power and energy magazine*, vol. 6, no. 3, pp. 54–65, 2008.

[88] R. H. Lasseter, Z. Chen, and D. Pattabiraman, "Grid-forming inverters: A critical asset for the power grid," *IEEE Journal of Emerging and Selected Topics in Power Electronics*, vol. 8, no. 2, pp. 925–935, 2019.

[89] S. Yazdani, M. Ferdowsi, M. Davari, and P. Shamsi, "Advanced current-limiting and power-sharing control in a PV-based grid-forming inverter under unbalanced grid conditions," *IEEE Journal of Emerging and Selected Topics in Power Electronics*, vol. 8, no. 2, pp. 1084–1096, 2019.

[90] W. Duesterhoeft, M. W. Schulz, and E. Clarke, "Determination of instantaneous currents and voltages by means of alpha, beta, and zero components," *Transactions of the American Institute of Electrical Engineers*, vol. 70, no. 2, pp. 1248–1255, 1951.

[91] Y. Sozer and D. A. Torrey, "Modeling and control of utility interactive inverters," *IEEE Transactions on Power Electronics*, vol. 24, no. 11, pp. 2475–2483, 2009.

[92] S. Dasgupta, S. K. Sahoo, and S. K. Panda, "Single-phase inverter control techniques for interfacing renewable energy sources with microgrid Part-I: Parallel-connected inverter topology with active and reactive power flow control along with grid current shaping," *IEEE Transactions on Power Electronics*, vol. 26, no. 3, pp. 717–731, 2010.

[93] R. I. Bojoi, L. R. Limongi, D. Roiu, and A. Tenconi, "Enhanced power quality control strategy for single-phase inverters in distributed generation systems," *IEEE Transactions on Power Electronics*, vol. 26, no. 3, pp. 798–806, 2011.

[94] B. Bahrani, A. Rufer, S. Kenzelmann, and L. A. Lopes, "Vector control of single-phase voltage-source converters based on fictive-axis emulation," *IEEE Transactions on Industry Applications*, vol. 47, no. 2, pp. 831–840, 2010.

[95] M. Ebrahimi, S. A. Khajehoddin, and M. Karimi-Ghartemani, "Fast and robust single-phase *DQ* current controller for smart inverter applications," *IEEE transactions on power electronics*, vol. 31, no. 5, pp. 3968–3976, 2015.

[96] H. Abu-Rub, M. Malinowski, and K. Al-Haddad, *Power electronics for renewable energy systems, transportation and industrial applications*. John Wiley & Sons, 2014.

[97] L. Xinchun, F. Feng, D. Shanxu, K. Yong, and C. Jian, "Modeling and stability analysis for two paralleled UPS with no control interconnection," in *IEEE International Electric Machines and Drives Conference, 2003. IEMDC'03.*, vol. 3, pp. 1772–1776, IEEE, 2003.

[98] M. N. Marwali, J.-W. Jung, and A. Keyhani, "Stability analysis of load sharing control for distributed generation systems," *IEEE Transactions on Energy Conversion*, vol. 22, no. 3, pp. 737–745, 2007.

[99] X. Wang, L. Harnefors, and F. Blaabjerg, "Unified impedance model of grid-connected voltage-source converters," *IEEE Transactions on Power Electronics*, vol. 33, no. 2, pp. 1775–1787, 2017.

[100] X. Yu, A. M. Khambadkone, H. Wang, and S. T. S. Terence, "Control of parallel-connected power converters for low-voltage microgridPart I: A hybrid control architecture," *IEEE Transactions on Power Electronics*, vol. 25, no. 12, pp. 2962–2970, 2010.

[101] G. Chen and X. Cai, "Adaptive control strategy for improving the efficiency and reliability of parallel wind power converters by optimizing power allocation," *IEEE Access*, vol. 6, pp. 6138–6148, 2018.

[102] R. S. Yallamilli, D. M. R. Korada, L. K. Vedulla, and M. K. Mishra, "Effective Current Based Inverter Loss Computation and its Application for Energy Savings in a Microgrid Environment," in *2020 IEEE International Conference on Power Electronics, Smart Grid and Renewable Energy (PESGRE2020)*, pp. 1–6, IEEE, 2020.

[103] J.-H. Teng, S.-H. Liao, W.-H. Huang, and C.-C. Chiang, "Smart control strategy for conversion efficiency enhancement of parallel inverters at light loads," *IEEE Transactions on Industrial Electronics*, vol. 63, no. 12, pp. 7586–7596, 2016.

[104] S. Wang, J. Liu, Z. Liu, T. Wu, and B. Liu, "Efficiency-based optimization of steady-state operating points for parallel source converters in stand-alone power system," in *2016 IEEE 8th International Power Electronics and Motion Control Conference (IPEMC-ECCE Asia)*, pp. 163–170, IEEE, 2016.

[105] S. Wang, J. Liu, Z. Liu, T. Wu, X. Meng, and B. Liu, "A hierarchical operation strategy of parallel inverters for efficiency improvement and voltage stabilization in microgrids," in *2016 IEEE 2nd Annual Southern Power Electronics Conference (SPEC)*, pp. 1–6, IEEE, 2016.

[106] Y. Wang, D. Liu, Z. Chen, and P. Liu, "A hierarchical control strategy of microgrids toward reliability enhancement," in *2018 International Conference on Smart Grid (icSmartGrid)*, pp. 123–128, IEEE, 2018.

[107] Y. Wang, P. Liu, D. Liu, F. Deng, and Z. Chen, "Enhanced Hierarchical Control Framework of Microgrids with Efficiency Improvement and Thermal Management," *IEEE Transactions on Energy Conversion*, 2020.

[108] D. Li and C. N. M. Ho, "A delay-tolerable master–slave current-sharing control scheme for parallel-operated interfacing inverters with low-bandwidth communication," *IEEE Transactions on Industry Applications*, vol. 56, no. 2, pp. 1575–1586, 2019.

[109] Y. Wang, Y. Tan, Z. Chen, X. Wang, and Y. Tian, "A communication-less distributed voltage control strategy for a multi-bus AC islanded microgrid," in *2014 International Power Electronics Conference (IPEC-Hiroshima 2014-ECCE ASIA)*, pp. 3538–3545, IEEE, 2014.

[110] Y. Wang, X. Wang, Z. Chen, and F. Blaabjerg, "Distributed optimal control of reactive power and voltage in islanded microgrids," in *2016 IEEE Applied Power Electronics Conference and Exposition (APEC)*, pp. 3431–3438, IEEE, 2016.

[111] W. Yuan, Y. Wang, X. Ge, X. Hou, and H. Han, "A unified distributed control strategy for hybrid cascaded-parallel microgrid," *IEEE Transactions on Energy Conversion*, vol. 34, no. 4, pp. 2029–2040, 2019.

[112] W. Yuan, Y. Wang, D. Liu, and F. Deng, "Adaptive Droop Control Strategy of Autonomous Microgrid for Efficiency Improvement," in *2019 IEEE 10th International Symposium on Power Electronics for Distributed Generation Systems (PEDG)*, pp. 972–977, IEEE, 2019.

[113] W. Yuan, Y. Wang, D. Liu, F. Deng, and Z. Chen, "Efficiency-prioritized droop control strategy of AC microgrid," *IEEE Journal of Emerging and Selected Topics in Power Electronics*, 2020.

[114] M. Karimi-Ghartemani, S. A. Khajehoddin, P. Jain, and A. Bakhshai, "Comparison of two methods for addressing DC component in phase-locked loop (PLL) systems," *in IEEE Energy Conversion Congress and Exposition (ECCE)*, pp. 3053–3058, 2011.

[115] K. Zhou and J. C. Doyle, "Essentials of robust control," *Prentice hall Upper Saddle River, NJ*, vol. 104, 1998.

[116] M. Karimi-Ghartema, *Enhanced phase-locked loop structures for power and energy applications*. John Wiley & Sons, 2014.

[117] I. S. Board, *IEEE Standard for Interconnecting Distributed Resources with Electric Power Systems: 1547-2003*. IEEE, 2003.

[118] S. A. Khajehoddin, M. Karimi-Ghartemani, and M. Ebrahimi, "Optimal and Systematic Design of Current Controller for Grid-Connected Inverters," *IEEE Journal of Emerging and Selected Topics in Power Electronics*, vol. 6, no. 2, pp. 812–824, 2018.

[119] E. Wu and P. W. Lehn, "Digital current control of a voltage source converter with active damping of LCL resonance," in *Twentieth Annual IEEE Applied Power Electronics Conference and Exposition, 2005. APEC 2005.*, vol. 3, pp. 1642–1649, IEEE, 2005.

[120] A. Shukla, A. Ghosh, and A. Joshi, "State feedback control of multilevel inverters for DSTATCOM applications," *IEEE Transactions on Power Delivery*, vol. 22, no. 4, pp. 2409–2418, 2007.

[121] M. N. Marwali and A. Keyhani, "Control of distributed generation systems-Part I: Voltages and currents control," *IEEE Transactions on power electronics*, vol. 19, no. 6, pp. 1541–1550, 2004.

[122] N. Pogaku, M. Prodanovic, and T. C. Green, "Modeling, analysis and testing of autonomous operation of an inverter-based microgrid," *IEEE Transactions on power electronics*, vol. 22, no. 2, pp. 613–625, 2007.

[123] J. M. Guerrero, J. C. Vasquez, J. Matas, M. Castilla, and L. G. de Vicuna, "Control strategy for flexible microgrid based on parallel line-interactive UPS systems," *IEEE Transactions on industrial Electronics*, vol. 56, no. 3, pp. 726–736, 2009.

[124] J. M. Guerrero, L. G. De Vicuna, J. Matas, M. Castilla, and J. Miret, "Output impedance design of parallel-connected UPS inverters with wireless load-sharing control," *IEEE Transactions on industrial electronics*, vol. 52, no. 4, pp. 1126–1135, 2005.

[125] O. V. Kulkarni, S. Doolla, and B. Fernandes, "Simple Controller Configuration for Decentralized Parallel Operation of Inverters," *IEEE Transactions on Power Electronics*, vol. 34, no. 2, pp. 1356–1369, 2019.

[126] R. C. Dorf and R. H. Bishop, *Modern control systems*. Pearson, 2011.

[127] A. Sheykhi, N. Amouzegar Ashtiani, and S. A. Khajehoddin, "Microgrid Light-Load Efficiency Improvement Based on Online-Inverter Detection," *in IEEE Energy Conversion Congress and Exposition (ECCE)*, pp. 1–6, 2021.

[128] S. D'Arco and J. A. Suul, "Virtual synchronous machinesClassification of implementations and analysis of equivalence to droop controllers for microgrids," in *2013 IEEE Grenoble Conference*, pp. 1–7, IEEE, 2013.

[129] C. Li, R. Burgos, I. Cvetkovic, D. Boroyevich, L. Mili, and P. Rodriguez, "Analysis and design of virtual synchronous machine based STATCOM controller," in *2014 IEEE 15th Workshop on Control and Modeling for Power Electronics (COMPEL)*, pp. 1–6, IEEE, 2014.

[130] ABB, "ABB solar inverters for photovoltaic systems [Datasheets]."

[131] A. E.-M. M. Abd El-Aal, J. Schmid, J. Bard, and P. Caselitz, "Modeling and Optimizing the Size of the Power Conditioning Unit for Photovoltaic Systems," *Journal of Solar Energy Engineering*, vol. 128, pp. 40–44, 03 2005.

[132] Y. Wang, D. Liu, P. Liu, F. Deng, D. Zhou, and Z. Chen, "Lifetime-oriented droop control strategy for AC islanded microgrids," *IEEE Transactions on Industry Applications*, vol. 55, no. 3, pp. 3252–3263, 2019.

[133] S. Peyghami, P. Davari, and F. Blaabjerg, "System-level reliability-oriented power sharing strategy for DC power systems," *IEEE Transactions on Industry Applications*, vol. 55, no. 5, pp. 4865–4875, 2019.

[134] K. Ma, M. Liserre, F. Blaabjerg, and T. Kerekes, "Thermal loading and lifetime estimation for power device considering mission profiles in wind power converter," *IEEE Transactions on Power Electronics*, vol. 30, no. 2, pp. 590–602, 2014.

[135] D. Pan, X. Ruan, C. Bao, W. Li, and X. Wang, "Capacitor-current-feedback active damping with reduced computation delay for improving robustness of LCL-type grid-connected inverter," *IEEE Transactions on Power Electronics*, vol. 29, no. 7, pp. 3414–3427, 2013.

[136] Y. Yang, F. Blaabjerg, and H. Wang, "Low-voltage ride-through of single-phase transformerless photovoltaic inverters," *IEEE Transactions on Industry Applications*, vol. 50, no. 3, pp. 1942–1952, 2013.

[137] Y. Yang, F. Blaabjerg, and Z. Zou, "Benchmarking of grid fault modes in single-phase grid-connected photovoltaic systems," *IEEE Transactions on Industry Applications*, vol. 49, no. 5, pp. 2167–2176, 2013.

[138] P. Piya, M. Ebrahimi, M. Karimi-Ghartemani, and S. A. Khajehoddin, "Fault ride-through capability of voltage-controlled inverters," *IEEE Transactions on Industrial Electronics*, vol. 65, no. 10, pp. 7933–7943, 2018.

[139] D. Energinet, "Technical regulation 3.2. 2 for PV power plants with a power output above 11 kW," *Energinet, Fredericia, Denmark, Tech. Rep*, 2015.

[140] T. Qoria, F. Gruson, F. Colas, G. Denis, T. Prevost, and X. Guillaud, "Critical clearing time determination and enhancement of grid-forming converters embedding virtual impedance as current limitation algorithm," *IEEE Journal of Emerging and Selected Topics in Power Electronics*, vol. 8, no. 2, pp. 1050–1061, 2020.

Appendix A

Derivation of Grid Current Transfer Function with Respect to Uncertainties

Detailed derivation of the equation (2.5) is as follows:

$$\begin{aligned} G_{i_g}(s) = \frac{1}{L_2 s + R_2} \xrightarrow{\Delta} & \frac{1}{\bar{L}_2(1+\mathscr{E}_{L_2}\delta_{L_2})s + \bar{R}_2(1+\mathscr{E}_{R_2}\delta_{R_2})} \\ &= \frac{1}{(\bar{L}_2 s + \bar{R}_2) + \begin{bmatrix} \bar{L}_2\mathscr{E}_{L_2}s & \bar{R}_2\mathscr{E}_{R_2} \end{bmatrix} \begin{bmatrix} \delta_{L_2} \\ \delta_{R_2} \end{bmatrix}} \\ &= \frac{1}{(\bar{L}_2 s + \bar{R}_2)\left(1 + \begin{bmatrix} \dfrac{\bar{L}_2\mathscr{E}_{L_2}s}{\bar{L}_2 s + \bar{R}_2} & \dfrac{\bar{R}_2\mathscr{E}_{R_2}}{\bar{L}_2 s + \bar{R}_2} \end{bmatrix} \begin{bmatrix} \delta_{L_2} \\ \delta_{R_2} \end{bmatrix}\right)} \end{aligned} \tag{A.1}$$

Now, auxiliary matrices K and Δ are defined as follows:

$$K \triangleq \begin{bmatrix} \dfrac{\bar{L}_2\mathscr{E}_{L_2}s}{\bar{L}_2 s + \bar{R}_2} & \dfrac{\bar{R}_2\mathscr{E}_{R_2}}{\bar{L}_2 s + \bar{R}_2} \end{bmatrix}, \quad \Delta \triangleq \begin{bmatrix} \delta_{L_2} \\ \delta_{R_2} \end{bmatrix}. \tag{A.2}$$

Substituting (A.2) into (A.1) results in:

$$\begin{aligned} G_{i_g} &= \frac{1}{\bar{L}_2 s + \bar{R}_2}\left(1 + K\Delta\right)^{-1} \\ &= \frac{1}{\bar{L}_2 s + \bar{R}_2}\left(1 - K\Delta\left(1 + K\Delta\right)^{-1}\right) \end{aligned} \tag{A.3}$$

Based on the upper LFT (2.4) and defining matrices G_{11}, G_{12}, G_{21}, and G_{22} in (2.3) as shown in (A.4), $\bar{G}_{i_g}(s)$ and $G_{i_g}(s)$ in equation (2.5) can be derived as represented in (A.5):

$$\begin{aligned} G_{i_g}(s) &= \mathscr{F}_U\left(\begin{bmatrix} -K & \dfrac{1}{\bar{L}_2 s + \bar{R}_2} \\ -K & \dfrac{1}{\bar{L}_2 s + \bar{R}_2} \end{bmatrix}, \Delta\right) \\ G_{11} = G_{21} = -K &= \begin{bmatrix} \dfrac{-\bar{L}_2 \mathscr{E}_{L_2} s}{\bar{L}_2 s + \bar{R}_2} & \dfrac{-\bar{R}_2 \mathscr{E}_{R_2}}{\bar{L}_2 s + \bar{R}_2} \end{bmatrix}, \\ G_{12} = G_{22} &= \frac{1}{\bar{L}_2 s + \bar{R}_2}, \end{aligned} \tag{A.4}$$

$$\begin{aligned} \bar{G}_{i_g}(s) &= \begin{bmatrix} G_{11} & G_{12} \\ G_{21} & G_{22} \end{bmatrix} \\ &= \frac{1}{\bar{L}_2 s + \bar{R}_2} \begin{bmatrix} -\bar{L}_2 \mathscr{E}_{L_2} s & -\bar{R}_2 \mathscr{E}_{R_2} & 1 \\ -\bar{L}_2 \mathscr{E}_{L_2} s & -\bar{R}_2 \mathscr{E}_{R_2} & 1 \end{bmatrix}, \\ G_{i_g}(s) &= \mathscr{F}_U\left(\bar{G}_{i_g}(s), \begin{bmatrix} \delta_{L_2} \\ \delta_{R_2} \end{bmatrix}\right). \end{aligned} \tag{A.5}$$

Appendix B

Derivation of Linearized Small-signal Equations of Single-phase Standalone Microgrid

In this section, the linearized small-signal equations of the microgrid are derived with respect to the equations provided in Section 4.3 to study the microgrid stability using the Jacobian matrix. Suppose $\mathbf{z}=[z_1 \ \cdots \ z_{l_z}]^T$, and $\mathbf{h}=[h_1 \ \cdots \ h_{l_h}]^T$ is a function on $\mathbf{z}$, where $\mathbf{h}: \mathbb{R}^{l_z} \rightarrow \mathbb{R}^{l_h}$. Thus, the Jacobian matrix of the function $\mathbf{h}$ is

$$\mathbf{J_h}(\mathbf{z}) = \begin{bmatrix} \frac{\partial h_1(\mathbf{z})}{\partial z_1} & \cdots & \frac{\partial h_1(\mathbf{z})}{\partial z_{l_z}} \\ \vdots & \ddots & \vdots \\ \frac{\partial h_{l_h}(\mathbf{z})}{\partial z_1} & \cdots & \frac{\partial h_{l_h}(\mathbf{z})}{\partial z_{l_z}} \end{bmatrix}. \tag{B.1}$$

Now, consider $\mathbf{x}=[x_1 \ \cdots \ x_{l_1}]^T$, $\mathbf{u}=[u_1 \ \cdots \ u_{l_2}]^T$, and $\mathbf{y}=[y_1 \ \cdots \ y_{l_3}]^T$ as the state, input, and output vectors of a system, where $\dot{\mathbf{x}} = \mathbf{f}(\mathbf{x}, \mathbf{u})$ and $\mathbf{y} = \mathbf{g}(\mathbf{x}, \mathbf{u})$. In this case, using the Jacobian matrix (B.1), the linearized small-signal equations of the system are

$$\begin{aligned} &\dot{\widetilde{\mathbf{x}}} = \mathbf{A}^{(\mathrm{op})}\widetilde{\mathbf{x}} + \mathbf{B}^{(\mathrm{op})}\widetilde{\mathbf{u}}, \ \widetilde{\mathbf{y}} = \mathbf{C}^{(\mathrm{op})}\widetilde{\mathbf{x}} + \mathbf{D}^{(\mathrm{op})}\widetilde{\mathbf{u}}, \\ &\mathbf{A}^{(\mathrm{op})} = \mathbf{J_f}(\mathbf{x})\Big|_{\substack{\mathbf{x}=\mathbf{X}^{(\mathrm{op})} \\ \mathbf{u}=\mathbf{U}^{(\mathrm{op})}}}, \mathbf{B}^{(\mathrm{op})} = \mathbf{J_f}(\mathbf{u})\Big|_{\substack{\mathbf{x}=\mathbf{X}^{(\mathrm{op})} \\ \mathbf{u}=\mathbf{U}^{(\mathrm{op})}}}, \\ &\mathbf{C}^{(\mathrm{op})} = \mathbf{J_g}(\mathbf{x})\Big|_{\substack{\mathbf{x}=\mathbf{X}^{(\mathrm{op})} \\ \mathbf{u}=\mathbf{U}^{(\mathrm{op})}}}, \mathbf{D}^{(\mathrm{op})} = \mathbf{J_g}(\mathbf{u})\Big|_{\substack{\mathbf{x}=\mathbf{X}^{(\mathrm{op})} \\ \mathbf{u}=\mathbf{U}^{(\mathrm{op})}}}, \end{aligned} \tag{B.2}$$

The superscript "(op)" refers to the operating point, and the accent "$\sim$" denotes small-signal perturbations around the operating point. Eventually, the operating point can be obtained by numerically solving $\mathbf{f}\left(\mathbf{X}^{(\mathrm{op})}, \mathbf{U}^{(\mathrm{op})}\right) = \mathbf{0}$ and $\mathbf{Y}^{(\mathrm{op})} = \mathbf{g}\left(\mathbf{X}^{(\mathrm{op})}, \mathbf{U}^{(\mathrm{op})}\right)$.

According to the microgrid model in the rotating frame depicted in Fig. 4.6, (4.25)-(4.29), except (4.27), are explicitly nonlinear. Moreover, as ω_n is an output of the droop block, (4.22)-(4.24), and (4.30) are nonlinear as well due to the multiplication of ω_n to other system states or inputs. Therefore, (4.22)-(4.30) should be linearized around an operating point for the small-signal stability analysis by using (B.2).

The equations of the voltage and current loops (4.22) are linearized as

$$\begin{gathered}
\dot{\widetilde{\mathbf{x}}}_{vc,n}^{dq} = \mathbf{A}_{vc,n}^{dq(\mathrm{op})}\widetilde{\mathbf{x}}_{vc,n}^{dq} + \mathbf{B}_{vc,n}^{dq}\widetilde{v}_{c,n}^{\mathrm{ref}dq} + \mathbf{B}_{vL,n}^{dq}\widetilde{v}_{L}^{dq} + \cdots \\
\cdots \mathbf{B}_{vc1,n}^{\omega_1(\mathrm{op})}\widetilde{\omega}_1 + \mathbf{B}_{vc2,n}^{\omega_n(\mathrm{op})}\widetilde{\omega}_n,\ \widetilde{\mathbf{y}}_{vc,n}^{dq} = \mathbf{C}_{vc,n}^{dq}\widetilde{\mathbf{x}}_{vc,n}^{dq}, \\
\mathbf{A}_{vc,n}^{dq(\mathrm{op})} = \mathbf{A}_{vc,n}^{dq}\big|_{\omega_n=\omega_n^{(\mathrm{op})}}, \mathbf{B}_{vc1,n}^{\omega_1(\mathrm{op})} = \frac{\partial \mathbf{A}_{vc,n}^{dq}}{\partial \omega_1}\Big|_{\omega_n=\omega_n^{(\mathrm{op})}}\mathbf{X}_{vc,n}^{dq(\mathrm{op})}, \\
\mathbf{B}_{vc2,n}^{\omega_n(\mathrm{op})} = \begin{cases} \mathbf{0}, & n=1 \\ \frac{\partial \mathbf{A}_{vc,n}^{dq}}{\partial \omega_n}\big|_{\omega_n=\omega_n^{(\mathrm{op})}}\mathbf{X}_{vc,n}^{dq(\mathrm{op})}, & n\neq 1 \end{cases}.
\end{gathered} \tag{B.3}$$

Regarding the APF block, its state-space equations (4.23) are linearized as

$$\begin{gathered}
\dot{\widetilde{\mathbf{x}}}_{ap,n}^{dq} = \mathbf{A}_{ap,n}^{dq(\mathrm{op})}\widetilde{\mathbf{x}}_{ap,n}^{dq} + \mathbf{B}_{ap,n}^{dq(\mathrm{op})}\widetilde{\mathbf{u}}_{ap,n}^{dq} + \mathbf{B}_{ap_1,n}^{\omega_1(\mathrm{op})}\widetilde{\omega}_1 + \mathbf{B}_{ap_2,n}^{\omega_n(\mathrm{op})}\widetilde{\omega}_n, \\
\widetilde{\mathbf{y}}_{ap,n}^{dq} = \mathbf{C}_{ap,n}^{dq}\widetilde{\mathbf{x}}_{ap,n}^{dq} + \mathbf{D}_{ap,n}^{dq}\widetilde{\mathbf{u}}_{ap,n}^{dq}, \\
\mathbf{A}_{ap,n}^{dq(\mathrm{op})} = \mathbf{A}_{ap,n}^{dq}\big|_{\omega_n=\omega_n^{(\mathrm{op})}}, \mathbf{B}_{ap,n}^{dq(\mathrm{op})} = \mathbf{B}_{ap,n}^{dq}\big|_{\omega_n=\omega_n^{(\mathrm{op})}}, \\
\mathbf{B}_{ap_1,n}^{\omega_1(\mathrm{op})} = \frac{\partial \mathbf{A}_{ap,n}^{dq}}{\partial \omega_1}\Big|_{\omega_n=\omega_n^{(\mathrm{op})}}\mathbf{X}_{ap,n}^{dq(\mathrm{op})}, \\
\mathbf{B}_{ap_2,n}^{\omega_n(\mathrm{op})} = \begin{cases} \frac{\partial \mathbf{B}_{ap,1}^{dq}}{\partial \omega_1}\big|_{\omega_1=\omega_1^{(\mathrm{op})}}\mathbf{U}_{ap,1}^{dq(\mathrm{op})}, & n=1 \\ \frac{\partial \mathbf{A}_{ap,n}^{dq}}{\partial \omega_n}\big|_{\omega_n=\omega_n^{(\mathrm{op})}}\mathbf{X}_{ap,n}^{dq(\mathrm{op})} + \frac{\partial \mathbf{B}_{ap,n}^{dq}}{\partial \omega_n}\big|_{\omega_n=\omega_n^{(\mathrm{op})}}\mathbf{U}_{ap,n}^{dq(\mathrm{op})}, & n\neq 1 \end{cases}.
\end{gathered} \tag{B.4}$$

The equation of the virtual impedance block (4.24) is linearized as

$$\begin{gathered}
\widetilde{\mathbf{y}}_{\mathrm{vir},n}^{dq} = \mathbf{D}_{\mathrm{vir},n}^{dq(\mathrm{op})}\widetilde{\mathbf{u}}_{\mathrm{vir},n}^{dq} + \mathbf{D}_{\mathrm{vir},n}^{\omega_n(\mathrm{op})}\widetilde{\omega}_n, \mathbf{D}_{\mathrm{vir},n}^{dq(\mathrm{op})} = \mathbf{D}_{\mathrm{vir},n}^{dq}\big|_{\omega_n=\omega_n^{(\mathrm{op})}}, \\
\mathbf{D}_{\mathrm{vir},n}^{\omega_n(\mathrm{op})} = \frac{\partial \mathbf{D}_{\mathrm{vir},n}^{dq}}{\partial \omega_n}\Big|_{\omega_n=\omega_n^{(\mathrm{op})}}\mathbf{U}_{\mathrm{vir},n}^{dq(\mathrm{op})}.
\end{gathered} \tag{B.5}$$

For the power calculation block (4.25), the linearized equations are as

$$\begin{aligned}
&\widetilde{\mathbf{y}}_{pq,n} = \mathbf{D}_{pq,n}^{(\mathrm{op})}\widetilde{\mathbf{u}}_{pq,n}^{dq},\ \mathbf{D}_{pq,n}^{(\mathrm{op})} = \mathbf{J}_{\mathbf{g}_{pq,n}}(\mathbf{u}_{pq,n}^{dq})\Big|_{\mathbf{u}_{pq,n}^{dq}=\mathbf{U}_{pq,n}^{dq(\mathrm{op})}},\\
&\mathbf{D}_{pq,n}^{(\mathrm{op})}=\left[\begin{matrix}\frac{\partial g_{p,n}}{\partial i_{2,n}^{d}} & \frac{\partial g_{p,n}}{\partial i_{2,n}^{q}} & \cdots & \frac{\partial g_{p,n}}{\partial v_{cb,n}^{d}} & \frac{\partial g_{p,n}}{\partial v_{cb,n}^{q}}\\ \frac{\partial g_{q,n}}{\partial i_{2,n}^{d}} & \frac{\partial g_{q,n}}{\partial i_{2,n}^{q}} & \cdots & \frac{\partial g_{q,n}}{\partial v_{cb,n}^{d}} & \frac{\partial g_{q,n}}{\partial v_{cb,n}^{q}}\end{matrix}\right]\Bigg|_{\mathbf{u}_{pq,n}^{dq}=\mathbf{U}_{pq,n}^{dq(\mathrm{op})}}.
\end{aligned} \tag{B.6}$$

As the equations of the LPF block (4.27) are linear, the small-signal and large-signal equations are the same. Thus, the small-signal equations of the LPF are

$$\dot{\widetilde{\mathbf{x}}}_{lp,n}=\mathbf{A}_{lp,n}\widetilde{\mathbf{x}}_{lp,n}+\mathbf{B}_{lp,n}\widetilde{\mathbf{u}}_{lp,n},\ \widetilde{\mathbf{y}}_{lp,n}=\mathbf{C}_{lp,n}\widetilde{\mathbf{x}}_{lp,n}. \tag{B.7}$$

As for the droop block, equations (4.29) are linearized as

$$\begin{aligned}
\dot{\widetilde{z}}_{d,n}=\mathbf{B}_{d,n}^{dq}\widetilde{\mathbf{u}}_{d,n}^{dq},\ \widetilde{\mathbf{y}}_{d,n}^{dq}=\mathbf{C}_{d,n}^{dq(\mathrm{op})}\widetilde{z}_{d,n}+\mathbf{D}_{d,n}^{dq(\mathrm{op})}\widetilde{\mathbf{u}}_{d,n}^{dq},\\
\mathbf{C}_{d,n}^{dq(\mathrm{op})}=\mathbf{J}_{\mathbf{g}_{d,n}}(z_{d,n})\Big|_{\mathbf{u}_{d,n}^{dq}=\mathbf{U}_{d,n}^{dq(\mathrm{op})}}^{z_{d,n}=Z_{d,n}^{(\mathrm{op})}},\\
\mathbf{D}_{d,n}^{dq(\mathrm{op})}=\left[\mathbf{J}_{\mathbf{g}_{d,n}}(\mathbf{u}_{d,n}^{dq})\Big|_{\mathbf{u}_{d,n}^{dq}=\mathbf{U}_{d,n}^{dq(\mathrm{op})}}^{z_{d,n}=Z_{d,n}^{(\mathrm{op})}}\quad \mathbf{D}_{3d,n}^{dq}\right]^{T}.
\end{aligned} \tag{B.8}$$

Considering the droop block equations (4.28) and (4.29), as ω_n^{nl} and V_n^{nl} are constant values, their small-signal perturbations are equal to zero, i.e. $\widetilde{\omega}_n^{nl}=\widetilde{V}_n^{nl}=0$. In this case, the small-signal input vector of the droop block $\widetilde{\mathbf{u}}_{d,n}^{dq}$ is reduced to $\widetilde{\mathbf{u}}_{r_{d,n}}^{dq}=\left[\widetilde{P}_n\ \widetilde{Q}_n\ \widetilde{\omega}_1\right]^{T}$. Therefore, the linearized small-signal droop equations (B.8) are simplified as

$$\begin{aligned}
\dot{\widetilde{z}}_{d,n} = \mathbf{B}_{r_{d,n}}^{dq}\widetilde{\mathbf{u}}_{r_{d,n}}^{dq},\ \widetilde{\mathbf{y}}_{d,n}^{dq}=\mathbf{C}_{d,n}^{dq(\mathrm{op})}\widetilde{z}_{d,n}+\mathbf{D}_{r_{d,n}}^{dq(\mathrm{op})}\widetilde{\mathbf{u}}_{r_{d,n}}^{dq},\\
\mathbf{B}_{r_{d,n}}^{dq} = \left[-m_{p,n}\quad 0\quad -1\right],\\
\mathbf{C}_{d,n}^{dq(\mathrm{op})} = \left[-V_n^{(\mathrm{op})}\sin Z_{d,n}^{(\mathrm{op})}\qquad V_n^{(\mathrm{op})}\cos Z_{d,n}^{(\mathrm{op})}\qquad 0\right]^{T},\\
\mathbf{D}_{r_{d,n}}^{dq(\mathrm{op})} = \begin{bmatrix}0 & -m_{q,n}\cos Z_{12_n}^{(\mathrm{op})} & 0\\ 0 & -m_{q,n}\sin Z_{d,n}^{(\mathrm{op})} & 0\\ -m_{p,n} & 0 & 0\end{bmatrix},
\end{aligned} \tag{B.9}$$

where $V_n^{(\mathrm{op})} = V_n^{nl} - m_{q,n}Q_n^{(\mathrm{op})}$. Also, $\mathbf{B}_{r_{d,n}}^{dq}$ and $\mathbf{D}_{r_{d,n}}^{dq}$ in (B.9) refer to the reduced forms of $\mathbf{B}_{d,n}^{dq}$ and $\mathbf{D}_{d,n}^{dq}$ in (B.8).

Finally, the microgrid load equations (4.30) are linearized as

$$\begin{aligned} \dot{\widetilde{\mathbf{x}}}_L^{dq} &= \mathbf{A}_L^{dq(\mathrm{op})}\widetilde{\mathbf{x}}_L^{dq} + \mathbf{B}_L^{dq}\widetilde{\mathbf{u}}_L^{dq} + \mathbf{B}_L^{\omega_1(\mathrm{op})}\widetilde{\omega}_1, \\ \widetilde{\mathbf{y}}_L^{dq} &= \mathbf{C}_L^{dq}\widetilde{\mathbf{x}}_L^{dq} + \mathbf{D}_L^{dq}\widetilde{\mathbf{u}}_L^{dq}, \\ \mathbf{A}_L^{dq(\mathrm{op})} = \mathbf{A}_L^{dq}\big|_{\omega_1=\omega_1^{(\mathrm{op})}}, \mathbf{B}_L^{\omega_1(\mathrm{op})} &= \frac{\partial \mathbf{A}_L^{dq}}{\partial \omega_1}\Big|_{\omega_1=\omega_1^{(\mathrm{op})}} \mathbf{X}_L^{dq(\mathrm{op})}. \end{aligned} \tag{B.10}$$

Appendix C

Systematic Design of Enhanced Dynamic Cascade Control for Three-phase PV Systems

C.1 Introduction

In this appendix, a cascade control containing an intra-loop state feedback, introduced in Chapter 3, is designed based on the approach proposed in Section 3.3 for a grid-connected PV system as a practical example. It is shown that the proposed methodology can reduce the size of dc link capacitor up to 7 times without compromising its performance compared with the conventional design approach. Alternatively, the proposed method can improve the performance using the same capacitor size for applications that a large dc capacitance is required. These advantages are achieved because the proposed design approach relaxes the distinct-timescale requirements among cascade loops as discussed in Chapter 3. Also, the low voltage ride through (LVRT) capability of the proposed control system is verified by the simulation and experimental results to demonstrate the proposed control system can tolerate large-signal disturbances. Eventually, the proposed method is also expanded to inverters with high-order LCL filters and weak grid operations.

C.2 Study System

A single-stage grid-connected PV system is considered as the study system, and a cascade control system is designed using both the proposed and conventional

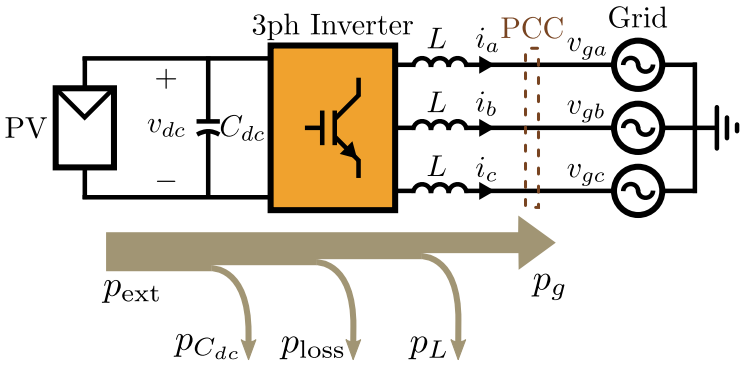

Fig. C.1: Study system configuration and the flow of power.

Table C.1: System parameters

Parameter		Value
PV	V_{oc}	692 V
	I_{sc}	18 A
	V_{MP}	600 V
	P_{nom}	10 kW
Inverter	f_{sw}	10 kHz
	L	5 mH
Grid	f_g	60 Hz
	$V_{g_{L-L}}$	208 V

methods in Section C.3 and Section C.4. Fig. C.1 depicts the study system configuration where the grid is a three-phase 208 V/60 Hz system and the PV includes 500 modules of 20 W (10 series-connected modules per string and 50 parallel strings). This indicates a nominal power of 10 kW at the maximum power voltage of 600 V. The open-circuit voltage of PV is 692 V, and its short-circuit current is 18 A. The inductance $L = 5$ mH is used to filter the switching ripples of the inverter current. Further details of the study system are presented in Table C.1. For the study system shown in Fig. C.1, the control design is challenging because only one converter has to address the PV-side aspects (including input power variations, dc load connection/disconnection, and voltage reference variations to address maximum power point tracking (MPPT)) as well as the grid-side objectives (consisting of current limiting, grid voltage disturbances, and fault ride-through).

C.3 Cascade Control Design for Study System

In this section, a cascade control system, which contains the dc link and current control loops, is designed for the system shown in Fig. C.1. The control system is developed by the proposed and the conventional methods in the synchronous rotating frame (DQ frame) where system variables are dc, and active and reactive powers can be controlled independently by d-axis current i_d and q-axis current i_q, respectively. The performance of both methods is assessed in Section C.4.

C.3.1 Proposed Cascade Control Design

According to Section 3.3, we start from the internal loop, current loop, and design its controller. For this purpose, dynamic equations of the internal loop are firstly derived. The dynamic equation of the current controller is

$$\dot{x}_{c_{1dq}} = A_{c_1} x_{c_{1dq}} + B_{c_1} e_{idq}, \tag{C.1}$$

where $A_{c_1} = 0$ and $B_{c_1} = 1$. Also, $x_{c_{1dq}}$ and $e_{idq} = I_{dq_{\text{ref}}} - i_{dq}$ are the current controller state variables and the error signals of the internal loop, respectively. The dynamic equations of *Plant 1* are

$$\begin{aligned} \dot{i}_d &= \omega i_q + \frac{1}{L}(v_{\text{inv}d} - v_{gd}), \\ \dot{i}_q &= -\omega i_d + \frac{1}{L}(v_{\text{inv}_q} - v_{gq}), \end{aligned} \tag{C.2}$$

where i_{dq}, $v_{\text{inv}dq}$, and v_{gdq} are the injected currents, inverter voltages, and grid voltages, respectively. Also ω is the rotational speed of the rotating frame. Assuming that the coupling terms in (C.2) are compensated to control the current of each axis separately, Fig. C.2 illustrates the proposed current control loop in the rotating frame.

According to the design algorithm described in Section 3.3, *Steps 1-5* are followed to design the internal controller. As the command $I_{dq_{\text{ref}}}$ and the disturbance

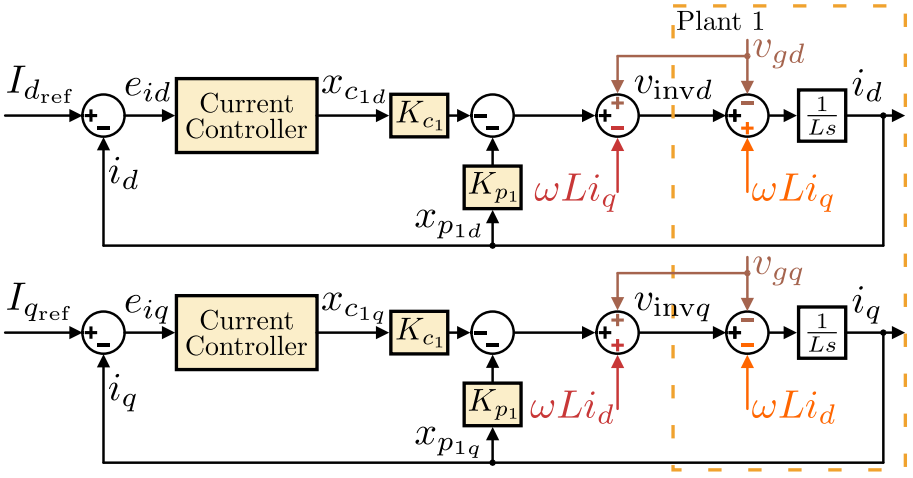

Fig. C.2: Proposed current control loop.

v_{gdq} are dc variables, then $\Delta_1(s) = s$ (*Step 1*). The state-space equation of the current controller (*Step 2*) is represented by (C.1). The state-space equations of *Plant 1*, including the inverter, L filter, and grid, (*Step 3*), are

$$\dot{x}_{p_{1dq}} = A_{p_1} x_{p_{1dq}} + B_{p_1} v_{\text{invdq}} + B_w v_{gdq},\ \ y_{p_{1dq}} = C_{p_1} x_{p_{1dq}}, \tag{C.3}$$

where $x_{p_{1dq}}$, A_{p_1}, B_{p_1}, B_w, and C_{p_1} are defined as $x_{p_{1dq}} = y_{p_{1dq}} = i_{dq}$, $A_{p_1} = 0$, $B_{p_1} = \frac{1}{L}$, $B_w = -\frac{1}{L}$, $C_{p_1} = 1$. Then, the state-space equations of the current controller and *Plant 1* are augmented using (3.15)-(3.17) to form the equation of the internal loop as below (*Step 4*)

$$\dot{x}_{1dq} = A_1 x_{1dq} + B_1^u v_{inv_{dq}} + B_1^{1,\text{ref}} I_{dq_{\text{ref}}} + B_1^w v_{gdq}, \tag{C.4}$$

where x_{1dq} are the state variables of the internal loop $x_{1dq} = \left[x_{c_{1dq}}\ x_{p_{1dq}}\right]^T$, and $I_{dq_{\text{ref}}}$ are determined by the external controllers. Finally, assign an appropriate Q_1, and solve the LQR problem for the internal system to find the optimum values of K_{c_1} and K_{p_1} (*Step 5*). For the numerical parameters of Table C.1, Fig. C.3 shows how the closed-loop poles of the current control loop are placed using the LQT method. Table C.2 represents the values of q_{1i}'s, the controller gains, and the final values of poles locations.

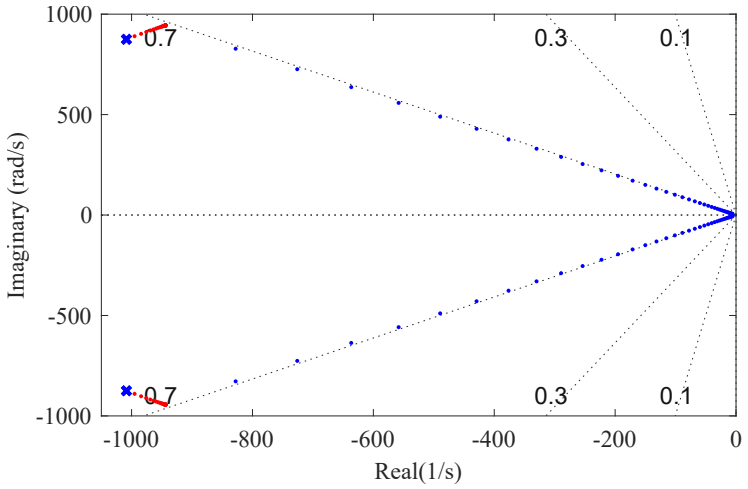

Fig. C.3: Closed-loop poles of the proposed current control loop.

Table C.2: Parameters of proposed current controller for L filter

Parameter		Value
Internal loop state weights	q_{11}	7.94×10^7
	q_{12}	12.59
Current controller gains	K_{c_1}	-8912
	K_{p_1}	10.09
	α_1	0.9
Current controller poles	$\lambda_{1,2}$	$-1008 \pm j875$

The block diagram shown in Fig. C.2 can be modified as shown in Fig. C.4, which has been introduced as two-degrees-of-freedom (2DOF) PI controller in the literature [66–68]. In this figure, α_1 $(-1 \leqslant \alpha_1 \leqslant 1)$ is used to further adjust the rise-time and swiftness of the internal loop. According to Fig. C.4, it is concluded that

$$\frac{I_{dq}(s)}{I_{dq_{\text{ref}}}(s)} = \frac{\alpha_1 K_{p_1} s - K_{c_1}}{L s^2 + K_{p_1} s - K_{c_1}}. \tag{C.5}$$

As shown in (C.5), α_1 only changes the zero of the transfer function and keeps the poles invariant. Thus, the optimum values of K_{c_1} and K_{p_1} are still valid for the modified current loop. Also, according to Fig. C.4 and (C.5), the matrix $B_1^{1,\text{ref}}$ in (3.17) is updated as below

$$B_1^{1,\text{ref}} = \begin{bmatrix} B_{c_1} & \alpha_1 B_{p_1} K_{p_1} \end{bmatrix}^T. \tag{C.6}$$

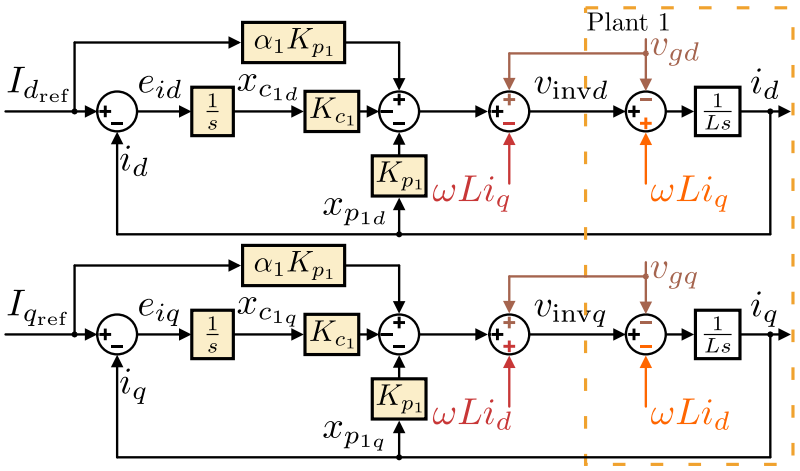

Fig. C.4: Block diagram of the current control loop used in the proposed and conventional methods.

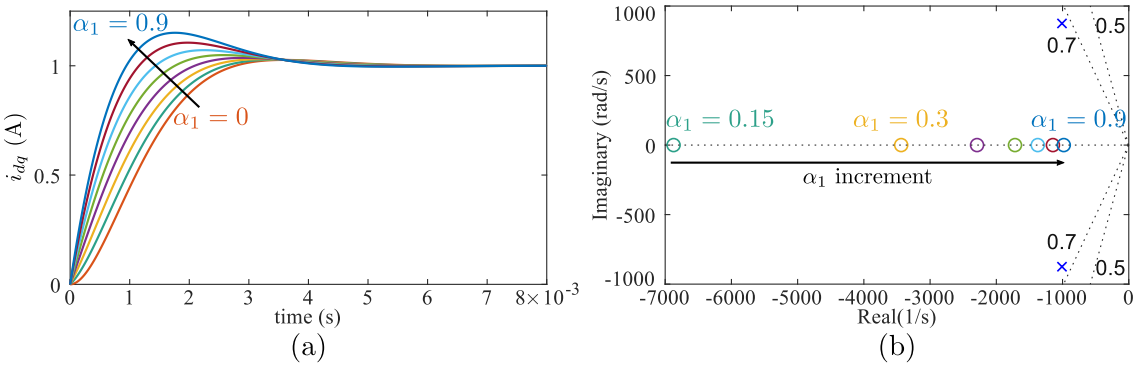

Fig. C.5: Effects of α_1 on the current control loop characteristics: (a) step responses, and (b) system's zero.

Fig. C.5 depicts how the change of α_1 would affect system swiftness, rise-time, and zero of the system. According to this figure, the appropriate swiftness and rise-time of the internal loop are achieved with $\alpha_1 = 0.9$.

After designing the internal loop, we move forward to design the external control loop. To design the dc link controller, the dynamic equations between the dc link voltage and the injected current are used. According to Fig. C.1, p_{ext}, $p_{C_{dc}}$, p_{loss}, p_L, and p_g are the instantaneous extracted power from the PV panel operating at the maximum power point (MPP), stored power in the dc link capacitor, power loss of the inverter, power of the filter, and injected power into the grid, respectively. Thus, the power conservation law results in $p_{C_{dc}} = p_{\text{ext}} - (p_{\text{loss}} + p_L + p_g)$. In

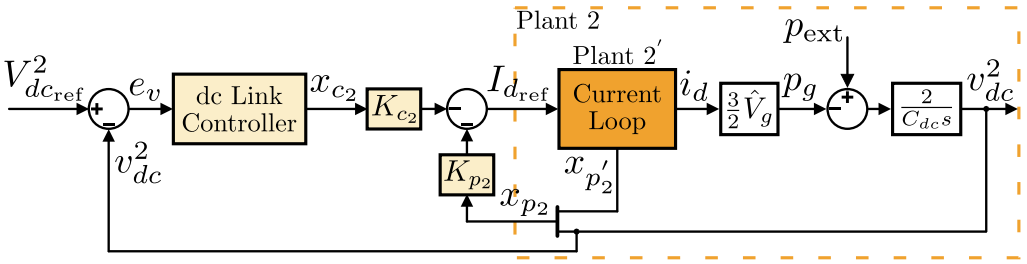

Fig. C.6: Proposed dc link control loop.

this design, p_{loss} and p_L are ignored, which is a common practice for the inverter operating mode. Therefore, $p_{C_{dc}} \approx p_{\text{ext}} - p_g$, where p_g and $p_{C_{dc}}$ can be calculated using $p_g = \frac{3}{2}(v_{gd}i_d + v_{gq}i_q)$ and $p_{C_{dc}} = \frac{C_{dc}}{2}\frac{d(v^2_{dc})}{dt}$. Also, C_{dc} and v_{dc} are the capacitor and the voltage of dc link, respectively. As the PLL finally sets $v_{gq}=0$ and $v_{gd}=\hat{V}_g$, where $\hat{V}_g$ is the grid voltage amplitude, the grid power is simplified as $p_g = \frac{3}{2}v_{gd}i_d$ [48].

The block diagram of the dc link control loop is depicted in Fig. C.6. According to this figure, the dynamic equation of the dc link controller is given by

$$\dot{x}_{c_2} = A_{c_2}x_{c_2} + B_{c_2}e_v, \tag{C.7}$$

where $A_{c_2}=0$ and $B_{c_2}=1$; also, x_{c_2} and $e_v = V^2_{dc_{\text{ref}}} - v^2_{dc}$ are the dc link controller state variable and the error signal of the external loop. In Fig. C.6, *Plant 2′* is the internal loop containing the current controller, inverter, L filter, and grid. It is then modified to form the standard structure of the proposed cascade control system introduced in Section 3.3 (Fig. 3.5). Thus, firstly, dynamic equations for *Plant 2′* are derived as

$$\dot{x}_{p_2'} = A_{p_2'}x_{p_2'} + B_{p_2'}I_{d_{\text{ref}}},\ y_{p_2'} = i_d = C_{p_2'}x_{p_2'}, \tag{C.8}$$

where $x_{p_2'}=x_{1d}$, and matrices $A_{p_2'}$, $B_{p_2'}$, and $C_{p_2'}$ are

$$A_{p_2'} = A_1 - B_1^u K_1,\ B_{p_2'} = B_1^{1,\text{ref}},\ C_{p_2'} = \begin{bmatrix} 0 & 1 \end{bmatrix}. \tag{C.9}$$

According to Fig. C.6, the states of *Plant 2′* should be augmented with the dc link

variable to form the standard structure for *Plant 2* ($x_{p_2} = \begin{bmatrix} x_{p_2'} & v_{dc}^2 \end{bmatrix}^T$). Thus, the state-space equations for *Plant 2* are

$$\dot{x}_{p_2} = A_{p_2} x_{p_2} + B_{p_2} I_{d_{\text{ref}}},\ y_{p_2} = v_{dc}^2 = C_{p_2} x_{p_2}, \tag{C.10}$$

where matrices A_{p_2}, B_{p_2}, and C_{p_2} are defined as

$$A_{p_2} = \begin{bmatrix} A_{p_2'} & 0 \\ -\frac{3}{C_{dc}} \hat{V}_g C_{p_2'} & 0 \end{bmatrix},\ B_{p_2} = \begin{bmatrix} B_{p_2'} \\ 0 \end{bmatrix}, \qquad C_{p_2} = \begin{bmatrix} 0 & 0 & 1 \end{bmatrix}. \tag{C.11}$$

The dc link controller is designed by following *Steps 6-10* of the design algorithm. As the reference $V_{dc_{\text{ref}}}^2$ and the disturbance p_{ext} are dc variables, then $\Delta_2(s) = s$ (*Step 6*). The state-space equation of the voltage controller (*Step 7*) is represented by (C.7). Also, the state-space equations of *Plant 2* (*Step 8*) are given by (C.10) and (C.11). Now, the state-space equations of the voltage controller and *Plant 2* are combined to form the equation of the dc link control loop (*Step 9*) as below

$$\dot{x}_2 = A_2 x_2 + B_2^{1,\text{ref}} I_{d_{\text{ref}}} + B_2^{\text{ref}} V_{dc_{\text{ref}}}^2, \tag{C.12}$$

where the definitions of A_2, $B_2^{1,\text{ref}}$, and B_2^{ref} are provided by (3.28). Finally, assign an appropriate Q_2, and solve the LQR problem for the external system to find the optimum values of K_{c_2} and K_{p_2} (*Step 10*).

Technical Consideration:

In practice, there is an implementation delay T_d due to the inherent features of the PWM and processor calculation. This delay can lead to the system oscillations and instability [53, 135]. The delay can be considered in the design procedure of the proposed control system as explained in [118], where the delay transfer function

$e^{-T_d s}$ may be approximated by

$$e^{-T_d s} \approx \frac{\frac{-T_d}{2}s + 1}{\frac{T_d}{2}s + 1}. \tag{C.13}$$

Then, the state-space equation of the delay approximation is derived as

$$\dot{x}_d = -\frac{2}{T_d}x_d + \frac{2}{T_d}u, \; y_d = 2x_d - u. \tag{C.14}$$

where x_d denotes the state of the delay approximation (C.14). Also, $u(t)$ and $y_d(t)$ refer to the control effort and the approximation of the delayed control effort $u(t - T_d)$, respectively. Next, (C.14) is combined with the state-space equations of *Plant 1* (C.3) to form the augmented plant for the internal loop, i.e. $x_{p_1}^{\text{aug}} = [x_{p_1} \; x_d]^T$. Therefore, the state-space matrices of the augmented plant containing the delay model are derived as

$$\begin{gathered} A_{p_1}^{\text{aug}} = \begin{bmatrix} A_{p_1} & 2B_{p_1} \\ 0 & -\frac{2}{T_d} \end{bmatrix}, \; B_{p_1}^{\text{aug}} = \begin{bmatrix} -B_{p_1} \\ \frac{2}{T_d} \end{bmatrix}, \\ B_w^{\text{aug}} = \begin{bmatrix} B_w \\ 0 \end{bmatrix}, \; C_{p_1}^{\text{aug}} = \begin{bmatrix} C_{p_1} & 0 \end{bmatrix}. \end{gathered} \tag{C.15}$$

Finally, considering (C.15) as the state-space equations of the augmented plant of the internal loop, gains of the proposed control system can be designed by following the same design procedure explained earlier. Also, Fig. C.7 displays the structure of the proposed control system consisting of the delay model [118].

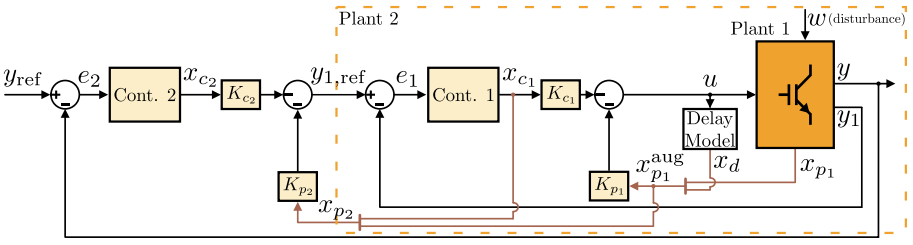

Fig. C.7: Structure of the proposed control system containing the delay model.

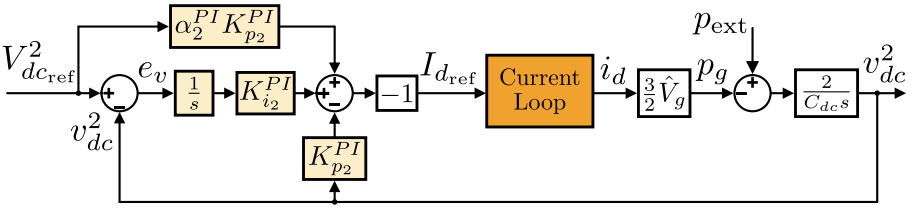

Fig. C.8: Conventional dc link control loop with 2DOF PI controller.

C.3.2 Conventional Cascade Control Design

To have a fair comparison between the proposed and conventional dc link controllers, the same internal current control loop is used for both methods as shown in Fig. C.4.

Similar to the proposed approach, the dynamic equation between the dc link voltage and the injected current is used to control the dc link voltage. The dc link control loop with a 2DOF PI controller is illustrated in Fig. C.8. In the conventional method, the dc link control loop is designed 10-20 times slower than the current control loop. In this example, the control objective is to minimize the dc link capacitor and maintain the fluctuation of dc link less than 10% of the nominal voltage for the full power jump. According to Fig. C.8, the transfer function from p_{ext} to v_{dc}^2 is

$$\frac{v_{dc}^2}{p_{\text{ext}}} = \frac{2}{C_{dc}} \frac{s}{s^2 + 2\zeta_2 \omega_{n_2} s + \omega_{n_2}^2}, \tag{C.16}$$

where ζ_2 and ω_{n_2} can be calculated as

$$2\zeta_2 \omega_{n_2} = \frac{3\hat{V}_g K_{p_2}^{PI}}{C_{dc}}, \ \omega_{n_2}^2 = \frac{3\hat{V}_g K_{i_2}^{PI}}{C_{dc}}. \tag{C.17}$$

(C.16) can be written in time domain as

$$v_{dc}^2(t) = \frac{2p_{\text{ext}}}{C_{dc}\omega_{n_2}\sqrt{1-\zeta_2^2}} e^{-\zeta_2 \omega_{n_2} t} \sin\left(\omega_{n_2}\sqrt{1-\zeta_2^2}t\right). \tag{C.18}$$

To find the peak of v_{dc}^2, the equation $\dot{v}_{dc}^2 = 0$ is solved to find out the peak time $t_p = \frac{1}{\omega_{n_2}\sqrt{1-\zeta_2^2}} \cos^{-1}(\zeta_2)$. Substituting t_p in (C.18), the peak value of v_{dc}^2 is

$$v_{\text{peak}}^2 = \frac{2p_{\text{ext}}}{C_{dc}\omega_{n_2}} e^{\frac{-\zeta_2 \cos^{-1}(\zeta_2)}{\sqrt{1-\zeta_2^2}}}. \tag{C.19}$$

Therefore, as $v_{dc_{\text{peak}}} = \sqrt{v_{\text{peak}}^2 + V_{dc_{\text{ref}}}^2}$, considering r as the maximum acceptable ratio of fluctuation with respect to $V_{dc_{\text{ref}}}$ ($r = \frac{v_{dc_{\text{peak}}} - V_{dc_{\text{ref}}}}{V_{dc_{\text{ref}}}}$), the minimum capacitor that guarantees r percent fluctuation of dc link due to the full power jump can be calculated by substituting r in (C.19) as

$$C_{dc} = \frac{2p_{\text{ext}}}{\left[(1+r)^2 - 1\right] V_{dc_{\text{ref}}}^2 \omega_{n_2}} e^{\frac{-\zeta_2 \cos^{-1}(\zeta_2)}{\sqrt{1-\zeta_2^2}}}. \tag{C.20}$$

According to (C.17), the gains of the dc link controller $K_{p_2}^{PI}$ and $K_{i_2}^{PI}$ can be easily calculated for desirable values of ζ_2 and ω_{n_2}

$$K_{p_2}^{PI} = \frac{2\zeta_2\omega_{n_2}C_{dc}}{3\hat{V}_g},\ K_{i_2}^{PI} = \frac{\omega_{n_2}^2 C_{dc}}{3\hat{V}_g}. \tag{C.21}$$

Since the real part of the poles of the current control loop are around $-1000s^{-1}$ in Fig. C.3, the real part of the poles of the voltage control loop should be around $-100s^{-1}$, i.e. $\zeta_2\omega_{n_2} = 100$ that is 10 times slower. Finally, considering $p_{\text{ext}} = 10\ kW$, $\zeta_2 = 0.7$, $\zeta_2\omega_{n_2} = 100$, and $r = 10\%$, the minimum capacitor is equal to $C_{dc} = 850\ \mu$F using (C.20). Also, Fig. C.9 depicts how these criteria intersect each other. After calculating C_{dc}, $K_{p_2}^{PI}$, and $K_{i_2}^{PI}$ based on the control objective, which is minimizing dc link capacitor and maintaining the dc link fluctuations less than 10%, using (C.20) and (C.21), the other voltage controller variable α_2^{PI} is selected such that it further adjusts the rise-time of the dc link loop and limits the overshoot caused because of $V_{dc_{\text{ref}}}^2$ jump to 10% as displayed in Fig. C.10. Table C.3 shows the current controller parameters ($K_{p_1}^{PI}$, $K_{i_1}^{PI}$, and α_1^{PI}), dc link controller parameters ($K_{p_2}^{PI}$, $K_{i_2}^{PI}$, and α_2^{PI}), and poles of the conventional cascade control system.

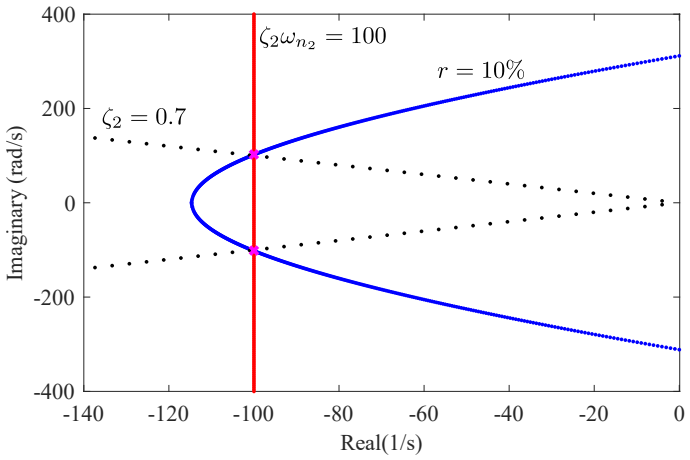

Fig. C.9: Satisfy maximum fluctuation ($r = 10\%$), desirable damping ($\zeta_2 = 0.7$), and appropriate speed of the external loop ($\zeta_2\omega_{n_2} = 100$).

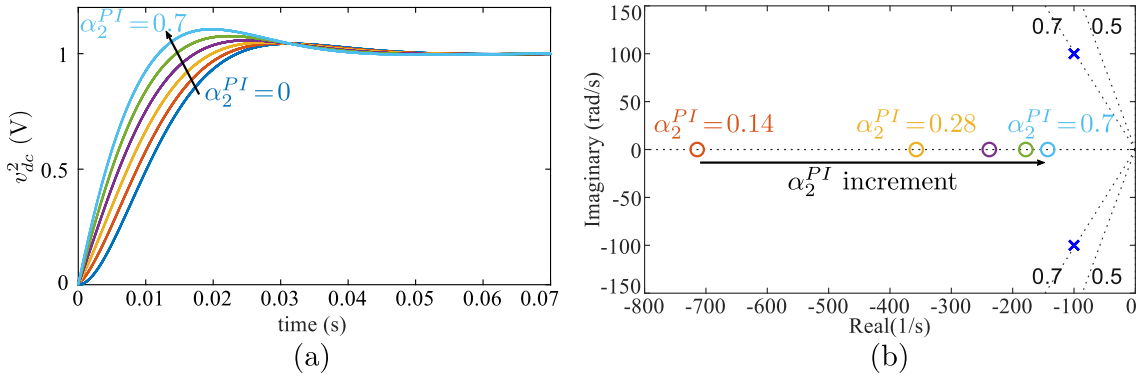

Fig. C.10: Effects of α_2^{PI} on the conventional dc link control loop: (a) step responses, and (b) system's zero.

Table C.3: Parameters of conventional dc link controller for L filter

Parameter		Value
Dc link controller gains	$K_{p_2}^{PI}$	3.3×10^{-4}
	$K_{i_2}^{PI}$	3.4×10^{-2}
	α_2	0.7
Dc link controller poles	$\lambda_{1,2}$	$-100 \pm j100.2$
Current controller poles	$\lambda_{3,4}$	$-1016 \pm j1287$
Resonant poles	$\lambda_{5,6}$	$-1008 \pm j875$

C.4 Performance Comparison

In this section, two designs for the proposed dc link controller, shown in Fig. C.6, are provided and compared with the conventional design for the following cases:

Case 1 : similar overshoots/undershoots at lower dc link capacitance for the proposed method,

Case 2 : transients improvement for the proposed method with similar dc link capacitors for both methods.

As it is explained in the following subsections, it is observed that, for similar overshoots/undershoots, the proposed method requires smaller capacitance, and, for the similar capacitance, the proposed method achieves superior performance.

C.4.1 Similar Overshoots/Undershoots at Lower DC Link Capacitance

The external loop of the proposed method can be designed much faster than the conventional controller, which decreases the size of the required dc link capacitor. The minimum dc link capacitance is designed so that it maintains the dc link voltage fluctuations for a full power jump less than 10% of its nominal voltage. According to Fig. C.6, because the system is of order 4, it should be firstly approximated with a lower order system to find the minimum capacitance maintaining dc link fluctuations within the acceptable level. Accordingly, Fig. C.6 is reconfigured as shown in Fig. C.11.

In this figure, the dashed lines include the current loop and two state feedbacks (x_{c_1}, i_d). The transfer function $\frac{I_d}{I_d^{'}}$ is

$$\frac{I_d}{I_d^{'}} = \frac{\alpha_1 K_{p_1} s - K_{c_1}}{Ls^2 + \Lambda_1 s + \Lambda_2}, \tag{C.22}$$

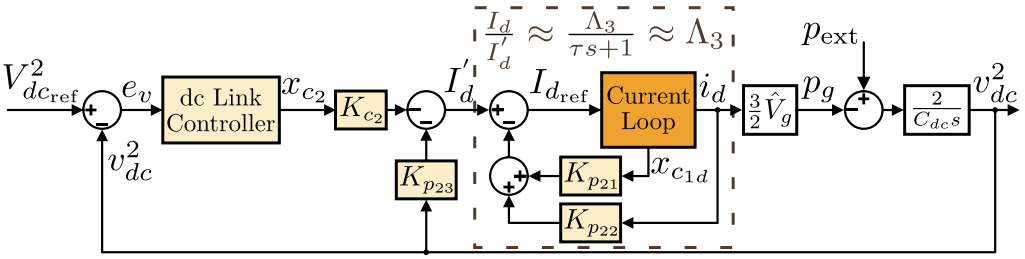

Fig. C.11: Reconfigured dc link control loop.

where $\Lambda_1 = K_{p_1} + K_{p_{21}}L + \alpha_1 K_{p_1} K_{p_{22}}$ and $\Lambda_2 = \alpha_1 K_{p_{21}} K_{p_1} - (1 + K_{p_{22}})\, K_{c_1}$. This transfer function has two poles at $p_1 = -1062$ s^{-1} and $p_2 = -2935$ s^{-1} and a zero at $z_1 = -982$ s^{-1}. Due to the zero-pole cancellation (z_1 and p_1), (C.22) can be approximated with a first-order transfer function $\frac{I_d}{I'_d} \approx \frac{\Lambda_3}{\tau s+1}$, where $\Lambda_3 = \frac{-K_{c_1}}{\Lambda_2}$ and $\tau = \frac{1}{2935}$ s. As the pole of this transfer function is far from the dominant poles of the voltage loop, the transfer function can be approximated with a constant gain within the voltage loop bandwidth as $\frac{I_d}{I'_d} \approx \Lambda_3$. In this case, the dc link control loop illustrated in Fig. C.11 becomes a second-order system. Therefore, similar to the conventional system discussed in Section C.3.2 (C.16)-(C.20), we get

$$\frac{v^2_{dc}}{p_{\text{ext}}} = \frac{2}{C_{dc}} \frac{s}{s^2 + 2\zeta'_2 \omega'_{n_2} s + {\omega'_{n_2}}^2}, \tag{C.23}$$

where ζ'_2 and ω'_{n_2} can be calculated as

$$2\zeta'_2 \omega'_{n_2} = \frac{-3\hat{V}_g K_{p_{23}} \Lambda_3}{C_{dc}},\ {\omega'_{n_2}}^2 = \frac{3\hat{V}_g K_{c_2} \Lambda_3}{C_{dc}}. \tag{C.24}$$

Thus, (C.20) can be used to approximate the minimum capacitance based on the desirable ζ'_2 and ω'_{n_2} to maintain the dc link fluctuations less than 10% of the nominal voltage. The pole of $\frac{I_d}{I'_d}$, that is the loop depicted in the dashed frame in Fig. C.11, is almost three times of the dominant poles of the voltage control loop. In other words, $\frac{I_d}{I'_d}$ is not 10-20 times faster than the voltage loop to completely ignore its dynamics in comparison with the voltage control loop. Therefore, the capacitance is selected almost $20\% - 30\%$ higher than the value calculated in (C.20) to be on

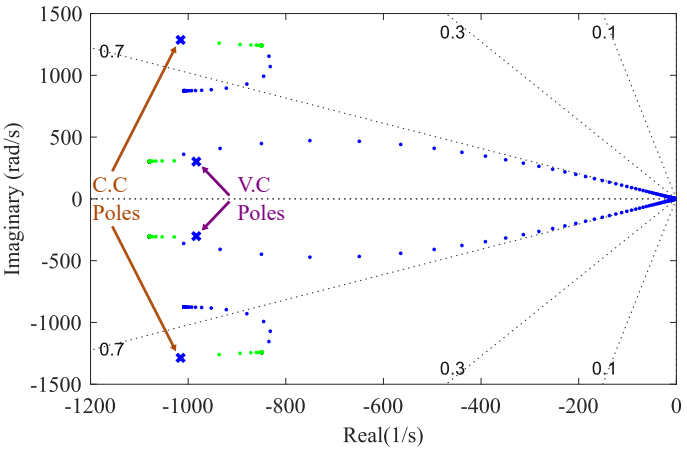

Fig. C.12: Proposed poles of the dc link voltage control loop.

the safe side. It is worth mentioning that the simplification of the current control loop, shown in Fig. C.11, is only used to approximate the capacitance required to maintain the dc link fluctuations less than the acceptable range, and the full model of the current control loop, depicted in Fig. C.4, is used to design the voltage controller as explained in Section 3.3 (*Steps 6-10*).

For the parameters in Table C.1, the minimum capacitor holding the fluctuations less than 10% of the nominal voltage is $C_{dc} = 120$ μF. Fig. C.12 depicts how the closed-loop poles of the whole system are placed properly using the proposed method. In comparison with the conventional method, the required capacitor is 7 times smaller. It is worth mentioning that, in *Case 1*, the dc link capacitance is reduced for applications where there is no overriding requirement on the capacitor size. Table C.4 represents the values of q_{2i}'s selected for the dc link control loop, the controller gains, and the final values of poles locations. Similar to the internal loop, the rise-time and swiftness of the external loop can be modified using α_2. The selection of $\alpha_2 = 0.55$ limits the overshoot caused due to the $V^2_{dc_{\text{ref}}}$ jump to 10% as shown in Fig. C.13. According to this modification, the matrix B_2^{ref} in (3.28) is updated as $B_2^{\text{ref}} = [B_{c_2} \ \alpha_2 B_{p_2} K_{p_{23}}]^T$, where $K_{p_{23}}$ is the feedback gain of the controlled state variable v^2_{dc}.

Fig. C.14(a) shows performances of both systems within different scenarios. The extracted power from PV panel p_{ext} jumps from 0 to 10 kW at $t = 0.1$ s, and

Table C.4: Parameters of proposed dc link controller for L filter

Parameter		Value
External loop state weights	q_{21}	0.141
	q_{22}	0.2
	q_{23}	10^{-4}
	q_{24}	5.01×10^{-8}
Dc link controller gains	K_{c_2}	0.376
	$K_{p_{21}}$	781.4
	$K_{p_{22}}$	0.661
	$K_{p_{23}}$	-6×10^{-4}
	α_2	0.55
Dc link controller poles	$\lambda_{1,2}$	$-983 \pm j302$
Current controller poles	$\lambda_{3,4}$	$-1016 \pm j1287$

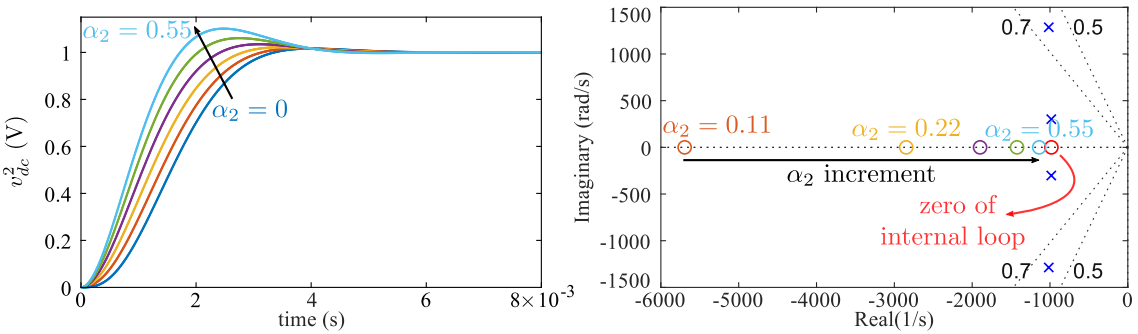

Fig. C.13: Effects of α_2 on the proposed dc link control loop: (a) step responses, and (b) system's zero.

both control systems successfully suppress the dc link fluctuations to less than 10%. A 3 kW dc load is connected to the dc link at $t = 0.2$ s. Then, p_{ext} decreases from 10 kW to 7 kW at $t = 0.3$ s, which leads to the change of $V_{dc_{\text{ref}}}$ to achieve MPPT. After that, the reference of the reactive power jumps to 3 kVAr at $t = 0.4$ s. Finally, the amplitude of the grid voltages $\hat{V}_g$ increase 10% at $t = 0.5$ s. Both systems exhibit almost similar overshoots and undershoots. However, the settling time of responses is much smaller for the proposed method, during different types of practical disturbances while the capacitance of the proposed method is 7 times smaller.

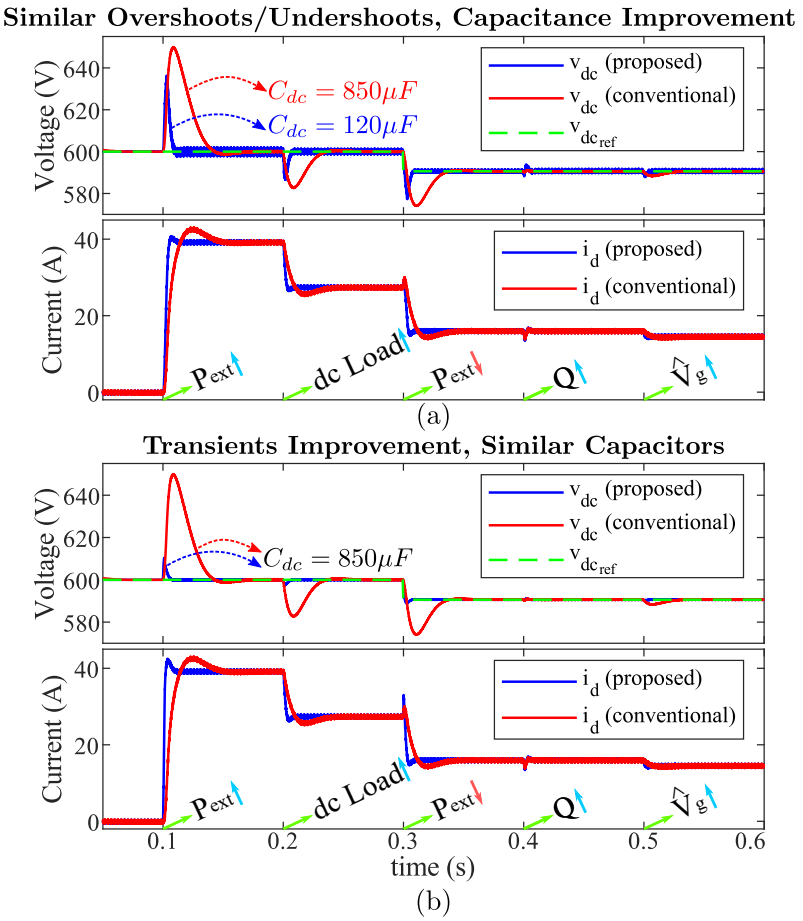

Fig. C.14: Performance comparison of proposed and conventional control systems for PV system with L filter: (a) *Case 1*, and (b) *Case 2* ($C_{dc} = 850\ \mu F$).

C.4.2 Transients Improvement and Similar DC Link Capacitors

In this part, it is shown how the dynamic response of the dc link control loop can be improved by using the proposed control at the same capacitor size of the conventional system. The external loop of the proposed method is designed fast to achieve a better transient response. It is designed as fast as possible while the real parts of the dominant poles of the dc link loop must not exceed the real parts of the dominant poles of the current loop. The closed-loop poles of the dc link control loop are placed properly similar to the last part depicted in Fig. C.12. Eventually,

the swiftness and rise-time of the external loop can be tuned by α_2 as stated before. Fig. C.14(b) illustrates how the proposed control system can improve the dynamic response of the control system as compared to the conventional system when the same capacitor is used in both systems. It is clearly depicted that during the different scenarios, the proposed dc link experiences much smaller fluctuations in comparison with the conventional control system.

C.5 LVRT Capability

Due to the ever increasing penetration of renewable distributed generators (DGs) in power systems, DGs play a significant role in maintaining the system stability during harsh conditions such as short circuit faults. They should ride through the disturbance and contribute to feeding the local loads and compensate for the voltage sag [136, 137]. Detailed desired DG response during a short circuit interval is dictated by various national standards. However, to meet the LVRT standard requirements, a fast control system is essential to follow commands during the voltage sag interval and after that to reduce the post-fault recovery time [95]. In the following, the LVRT capability of the proposed and conventional control systems are compared by the simulation results.

In a rotating frame, active and reactive power can be controlled independently by $I_{d_{\text{ref}}}$ and $I_{q_{\text{ref}}}$, respectively. In normal operation, $I_{d_{\text{ref}}}$ is determined by the dc link controller and $I_{q_{\text{ref}}}$ is set to regulate the desired reactive power. However, depending on depth and duration of the voltage sag, the LVRT standard specifies the amount of the reactive power $I_{q_{\text{ref}}}$ to be injected to the grid [138]. In one approach, namely the constant peak current strategy, the maximum current capacity of the DG is used in LVRT by setting $I_{d_{\text{ref}}}$ as

$$I_{d_{\text{ref}}} = \sqrt{I_{\text{max}}^2 - I_{q_{\text{ref}}}^2}, \tag{C.25}$$

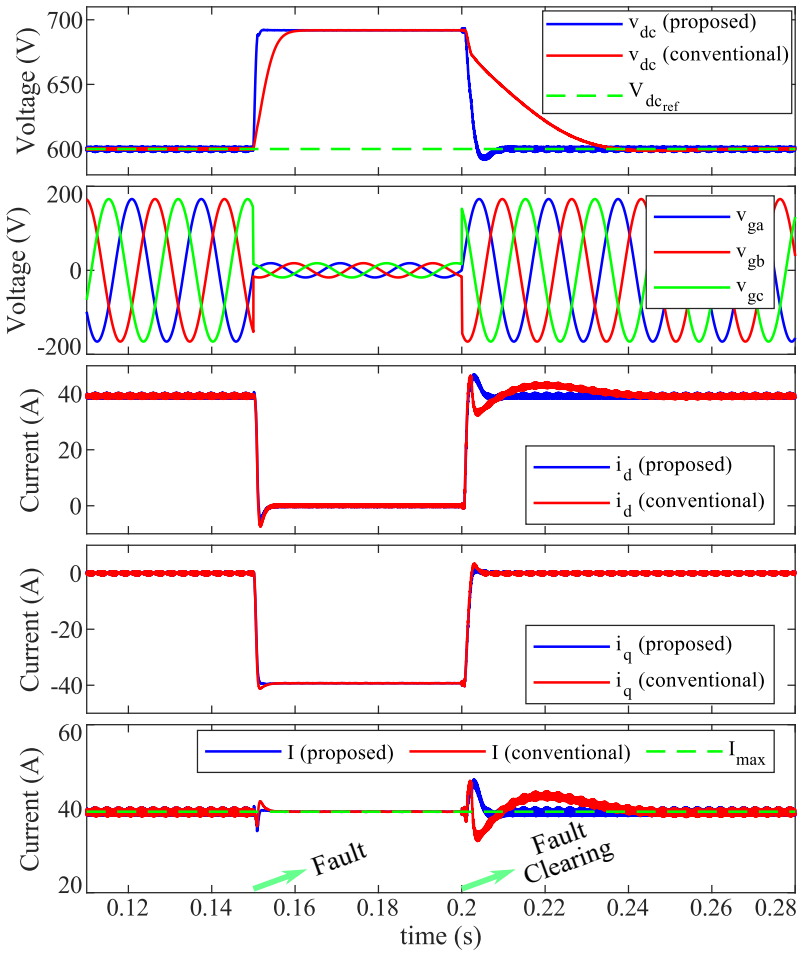

Fig. C.15: LVRT capability of the proposed method and conventional method.

where $I_{\max}$ is the maximum current capacity of the DG without tripping due to the over current. In this study, Danish grid code [139] is used to determine the reactive power requirement for a PV system during a voltage sag interval.

Designing the proposed controller as discussed in section C.4.1 with 7 times smaller dc link capacitance (*Case 1*), its LVRT performance is compared with the conventional method, and results are presented in Fig. C.15. The grid voltage drops to 0.1 pu at $t = 0.15$ s. According to Danish grid code, for this depth of voltage sag, the maximum reactive power must be injected to the grid to compensate the voltage drop, i.e. $I_{d_{\text{ref}}} = 0$, $I_{q_{\text{ref}}} = -I_{\max}$. As depicted in Fig. C.15, both control systems represent an acceptable performance in decreasing the active current i_d to zero

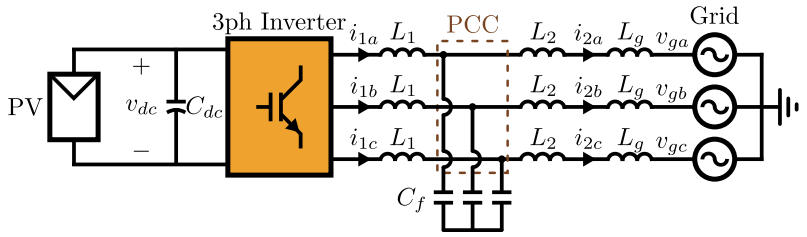

Fig. C.16: Single-stage PV system with an LCL filter connected to a weak grid.

and using the maximum current capacity to inject the maximum reactive current i_q to the grid. However, when the grid voltage is recovered to 1 pu at $t = 0.2$ s, the proposed controller significantly outperforms the conventional method, thanks to much faster dc link control loop. The post-fault recovery time of the proposed control system is around 5.9 ms, less than half a cycle, while the conventional system being around 37.2 ms, more than two cycles. Also, since power converters are able to tolerate $20\% - 40\%$ overcurrents [140], the post-fault overcurrents of the proposed and conventional methods fall within the acceptable overcurrent range as displayed in Fig. C.15.

C.6 High-order Filter in Weak Grid Situation

In this section, to show the flexibility of the proposed approach, it is extended to the design of the cascade control system for an inverter with an LCL filter operating in a weak grid situation. Fig. C.16 depicts the system configuration where $L_1 = 1$ mH, $C_f = 3$ μF, and $L_2 = 0.6$ mH. Also, L_g represents the grid interfacing inductance, which is considered to vary in the range of 0 to 4 mH. Moreover, the capacitor voltage is considered as the PCC.

Similar to Section C.3, assuming the couplings between the quadrature axes are compensated, Fig. C.17 depicts the modified proposed current control loop for the inverter with the LCL filter. Thus, the state-space equations of the current

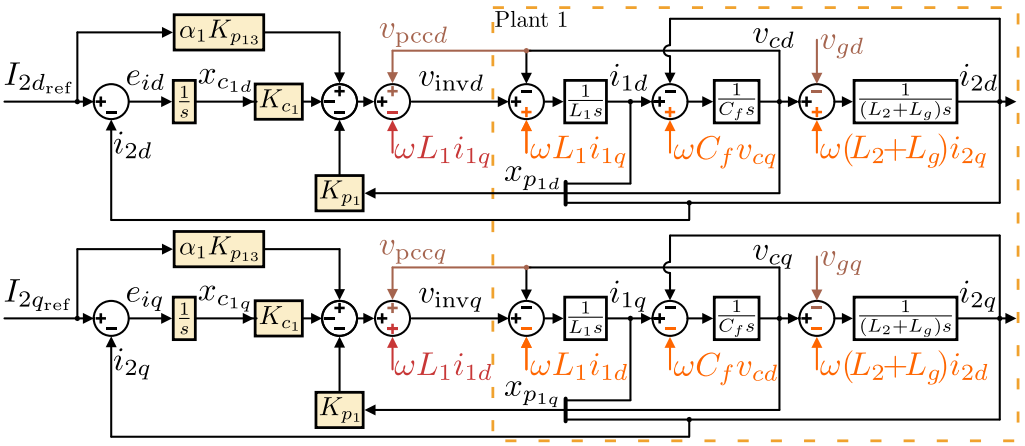

Fig. C.17: Block diagram of the current control loop used in the proposed and conventional methods for the inverter with the LCL filter.

controller and *Plant 1* are

$$\dot{x}_{c_{1dq}} = A_{c_1} x_{c_{1dq}} + B_{c_1} e_{idq}, \tag{C.26}$$

$$\dot{x}_{p_{1dq}} = A_{p_1} x_{p_{1dq}} + B_{p_1} v_{\text{invdq}} + B_w v_{gdq},\ \ y_{p_{1dq}} = C_{p_1} x_{p_{1dq}}, \tag{C.27}$$

where $x_{p_{1dq}} = [i_{1dq}\ v_{cdq}\ i_{2dq}]^T$, $y_{p_{1dq}} = i_{2dq}$, $A_{c_1} = 0$, and $B_{c_1} = 1$. Moreover, A_{p_1}, B_{p_1}, B_w, C_{p_1} are defined as

$$\begin{aligned} A_{p_1} &= \begin{bmatrix} 0 & -\frac{1}{L_1} & 0 \\ \frac{1}{C_f} & 0 & -\frac{1}{C_f} \\ 0 & \frac{1}{L_2+L_g} & 0 \end{bmatrix},\ B_{p_1} = \begin{bmatrix} \frac{1}{L_1} \\ 0 \\ 0 \end{bmatrix}, \\ B_w &= \begin{bmatrix} 0 & 0 & -\frac{1}{L_2+L_g} \end{bmatrix}^T,\ C_{p_1} = \begin{bmatrix} 0 & 0 & 1 \end{bmatrix}. \end{aligned} \tag{C.28}$$

Augmenting (C.26)-(C.28) leads to

$$\dot{x}_{1dq} = A_1 x_{1dq} + B_1^u v_{inv_{dq}} + B_1^{1,\text{ref}} I_{2dq_{\text{ref}}} + B_1^w v_{gdq}, \tag{C.29}$$

where the definition of A_1, B_1^u, and B_1^w are given by (3.17). Also, $B_1^{1,\text{ref}} = [B_{c_1}\ \alpha_1 B_{p_1} K_{p_{13}}]^T$, where $K_{p_{13}}$ is the controller gain applied to the controlled state variable i_{2dq}. Thus, by solving the LQR problem for the internal loop, we find the optimum values of

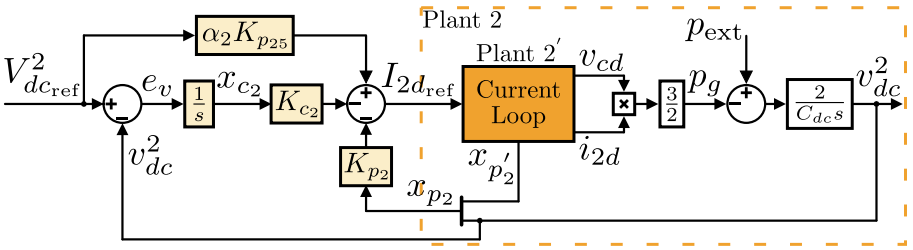

Fig. C.18: Modified proposed dc link loop for the inverter with the LCL filter.

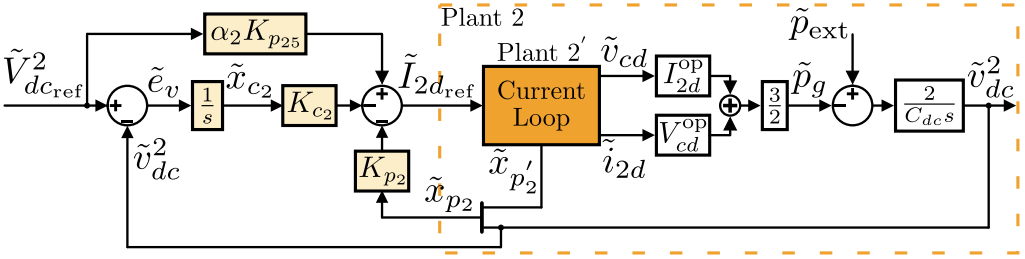

Fig. C.19: Linearized small-signal model of the dc link loop for the inverter with the LCL filter.

K_{c_1} and K_{p_1}. The results are summarized in Table C.5.

Fig. C.18 shows the modified proposed dc link control loop for the inverter with the LCL filter. Since the capacitor voltage is used for the power calculation p_g, *Plant 2* becomes nonlinear. Therefore, the system should be linearized at an operating point by using the small-signal technique. Fig. C.19 illustrates the linearized small-signal model of the dc link control loop where the accent "~" and superscript "op" refer to the small-signal perturbations and operating point values of the system variables, respectively. The state-space equations of the dc link controller and *Plant 2′* are

$$\dot{\tilde{x}}_{c_2} = A_{c_2}\tilde{x}_{c_2} + B_{c_2}\tilde{e}_v, \tag{C.30}$$

$$\dot{\tilde{x}}_{p_2'} = A_{p_2'}\tilde{x}_{p_2'} + B_{p_2'}\tilde{I}_{2d_{\text{ref}}},\ \tilde{y}_{p_2'} = \begin{bmatrix}\tilde{v}_{cd} & \tilde{i}_{2d}\end{bmatrix}^T = C_{p_2'}\tilde{x}_{p_2'}, \tag{C.31}$$

where $A_{c_2}=0$ and $B_{c_2}=1$; also, $A_{p_2'}$, $B_{p_2'}$, and $C_{p_2'}$ are

$$A_{p_2'}=A_1-B_1^u K_1,\ B_{p_2'}=B_1^{1,\text{ref}},\ C_{p_2'}=\begin{bmatrix}0 & 0 & 1 & 0\\ 0 & 0 & 0 & 1\end{bmatrix}. \tag{C.32}$$

Now, with respect to Fig. C.6, the states of *Plant 2'* are augmented with the dc link state variable v_{dc}^2 to derive the state-space equations of *Plant 2* as

$$\dot{\tilde{x}}_{p_2}=A_{p_2}\tilde{x}_{p_2}+B_{p_2}\tilde{I}_{2d_{\text{ref}}},\ \tilde{y}_{p_2}=\tilde{v}_{dc}^2=C_{p_2}\tilde{x}_{p_2}, \tag{C.33}$$

where matrices A_{p_2}, B_{p_2}, and C_{p_2} are defined as

$$\begin{gathered}A_{p_2}=\begin{bmatrix}A_{p_2'} & 0\\ -\frac{3}{C_{dc}}MC_{p_2'} & 0\end{bmatrix},\ B_{p_2}=\begin{bmatrix}B_{p_2'}\\ 0\end{bmatrix},\\ C_{p_2}=\begin{bmatrix}0 & 0 & 0 & 0 & 1\end{bmatrix},\ M=\begin{bmatrix}I_{2d}^{\text{op}} & V_{cd}^{\text{op}}\end{bmatrix}.\end{gathered} \tag{C.34}$$

Assuming $P_g^{\text{op}}=P_{\text{ext}}^{\text{op}}=P_{\text{nom}}$, $V_{cq}^{\text{op}}=0$ V, and $I_{2q}^{\text{op}}=0$ A at the operating point, the values of I_{2d}^{op} and V_{cd}^{op} in (C.34) can be calculated using

$$\frac{3}{2}V_{cd}^{\text{op}}I_{2d}^{\text{op}}=P_{\text{nom}},\ V_{cd}^{\text{op}2}+\left[\omega(L_2+L_g)I_{2d}^{\text{op}}\right]^2=\hat{V}_g^2. \tag{C.35}$$

Augmenting (C.30)-(C.34) forms the state-space equations of the dc link loop as

$$\dot{\tilde{x}}_2=A_2\tilde{x}_2+B_2^{1,\text{ref}}\tilde{I}_{2d_{\text{ref}}}+B_2^{\text{ref}}\tilde{V}_{dc_{\text{ref}}}^2, \tag{C.36}$$

where the definitions of A_2 and $B_2^{1,\text{ref}}$ are given by (3.28). Also, $B_2^{\text{ref}}=[B_{c_2}\ \alpha_2 B_{p_2}K_{p_{25}}]^T$, where $K_{p_{25}}$ is the related feedback gain of the controlled state variable $\tilde{v}_{dc}^2$. Finally, solving the LQR problem for the external loop leads to the optimum values of K_{c_2} and K_{p_2} as noted in Table C.5. For the system configuration depicted in Fig. C.16, the minimum capacitor maintaining the dc link fluctuation less than 10% of the nominal voltage is $C_{dc}=130$ μF.

To study the impact of a parameter mismatch on the proposed control system,

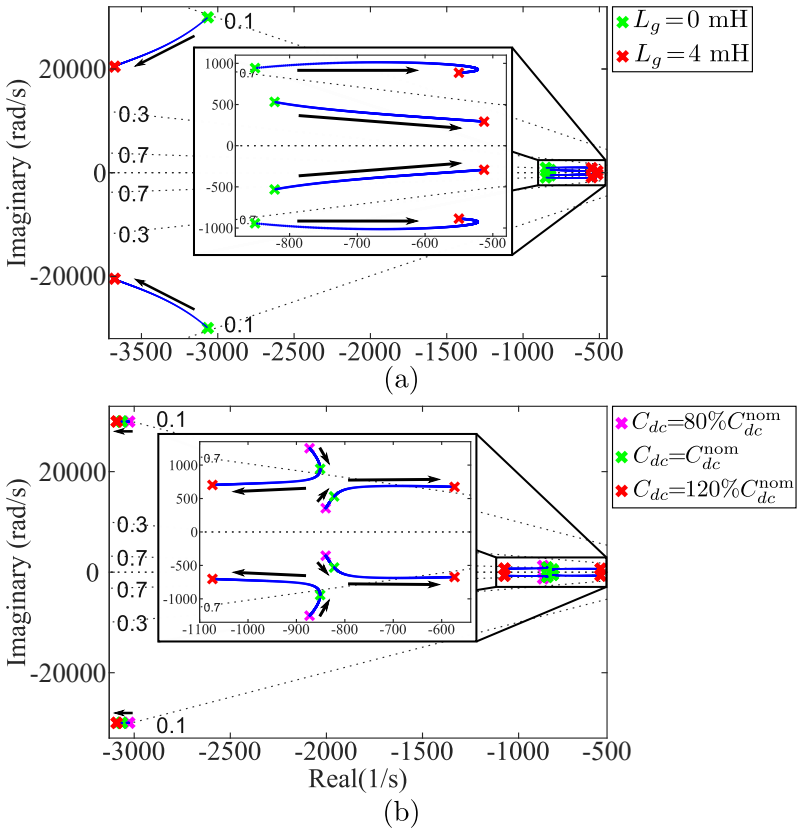

Fig. C.20: Robustness of the proposed cascade control system against parameters mismatches: (a) L_g variations from 0 mH to 4 mH, and (b) C_{dc} deviations from $C_{dc}^{\text{nom}} = 130$ μF.

two scenarios are considered. In the first scenario, the grid inductance L_g is varied from 0 mH to 4 mH. Fig. C.20(a) shows how this affects the closed-loop poles of the system. The poles remain adequately stable, which means that the proposed control system is robust against L_g variations. In the second scenario, the dc link capacitance C_{dc} deviates $\pm 20\%$ of its nominal value C_{dc}^{nom}. Fig. C.20(b) displays the variations of the system poles due to this mismatch where the cascade control system is shown to be robust against C_{dc} variations as well.

Finally, the performances of the proposed and conventional control systems in a weak grid situation (L_g=4 mH) are compared in *Case 1* and *Case 2* for the same scenarios discussed in Section C.4. To have a fair comparison, the current loop of the conventional system is considered the same as the proposed system, illustrated in Fig. C.17. The conventional dc link controller is also designed as stated in

Table C.5: Design parameters of proposed controller for LCL filter

Parameter		Value
Current controller gains	K_{c_1}	-2917.4
	$K_{p_{11}}$	8.13
	$K_{p_{12}}$	0.098
	$K_{p_{13}}$	-4.84
	α_1	-0.5
Dc link controller gains	K_{c_2}	0.22
	$K_{p_{21}}$	764.87
	$K_{p_{22}}$	0.238
	$K_{p_{23}}$	6.07×10^{-3}
	$K_{p_{24}}$	-0.061
	$K_{p_{25}}$	-4×10^{-4}
	α_2	0.53
Dc link controller poles	$\lambda_{1,2}$	$-822 \pm j532$
Current controller poles	$\lambda_{3,4}$	$-851 \pm j943$
Resonant poles	$\lambda_{5,6}$	$-3065 \pm j29966$

Section C.3.2. Fig. C.21(a) shows the simulation results for *Case 1*. According to this figure, both systems exhibit almost similar overshoots/undershoots, however, the settling time of responses is much smaller in the proposed method while using 6.5 times smaller capacitance size. Moreover, Fig. C.21(b) displays how the dynamic response of the dc link control loop can be improved using the proposed control in *Case 2* where the same capacitor ($C_{dc}=850\mu F$) is used for both the proposed and conventional dc link controllers. Also, it is clearly observed that the dc link voltage of the proposed control system experiences much smaller fluctuations in *Case 2*.

C.7 Experimental Results

An experimental verification of the proposed and conventional control systems for the configuration depicted in Fig. C.1 is carried out in this section. The nominal parameters of the system are $S_{\text{nom}}=1$ kVA, $v_{dc}=400$ V, $L=6$ mH, $V_{oc}=450$ V, $I_{sc}=$

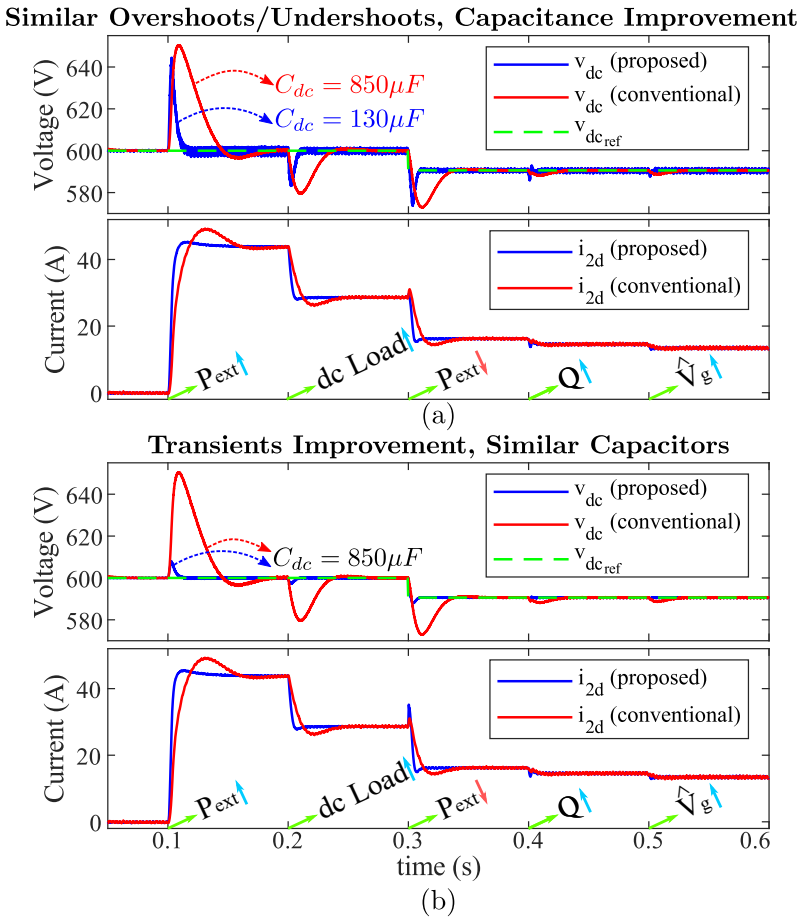

Fig. C.21: Performance comparison of proposed and conventional control systems for PV system with LCL filter in a weak grid situation ($L_g = 4$ mH): (a) *Case 1*, and (b) *Case 2* (C_{dc}=850 μF).

2.75 A, V_{mp}=400 V, and I_{mp}=2.5 A, where V_{oc}, I_{sc}, V_{mp}, and I_{mp} refer to the open-circuit, short-circuit, and maximum power point characteristics of the PV simulator. A view of the experimental setup is shown in Fig. C.22. The PV is emulated with Chroma 62050H-600S and the grid is simulated with a Chroma 3-phase ac source 61703. The controller is implemented on Texas Instrument TMS320F28335 DSP. The minimum capacitors which maintain the dc link fluctuations less than 10% of the nominal voltage due to the full power jump are 35 μF for the proposed system and 191 μF for the conventional system.

Fig. C.23 shows the performance of the proposed and conventional designs when a full power jump (1 kW) occurs. The proposed controller suppresses the dc

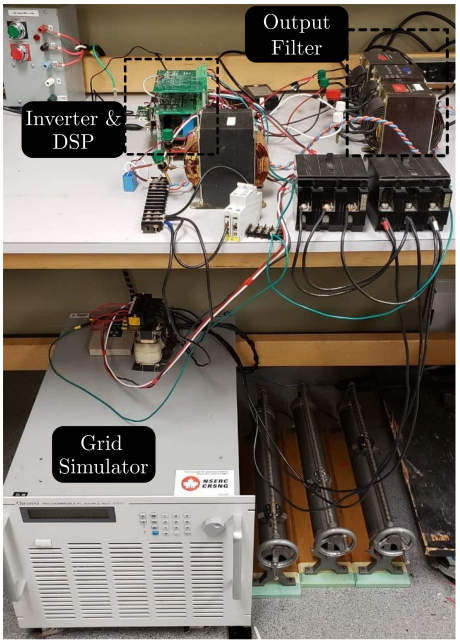

Fig. C.22: Picture of the experimental setup.

link fluctuations much faster. The overshoots/undershoots of the proposed system due to the full power jump are less than half of the conventional one. Different time divisions are selected for the conventional and proposed control systems to display oscillations more clearly.

Fig. C.24 shows the performance when the grid amplitude increases 10% and vice versa while the inverter is injecting 1 kW active power to the grid. The grid amplitude variations causes poorly damped oscillations on the dc link of the conventional system. However, this has negligible effect on the dc link of the proposed system. Although the dc link capacitor of the proposed system is almost 5 times smaller than the conventional system, the proposed control system shows much better performance in all scenarios.

The LVRT performance of the proposed controller is also examined in the experiments, and results are shown in Fig. C.25. The grid voltage in this test drops to 10% of its nominal value. In response, the controller successfully enters the LVRT mode and injects all the inverter capacity as reactive power to the grid according to the Danish grid code. As no active power is injected during the fault, the dc link

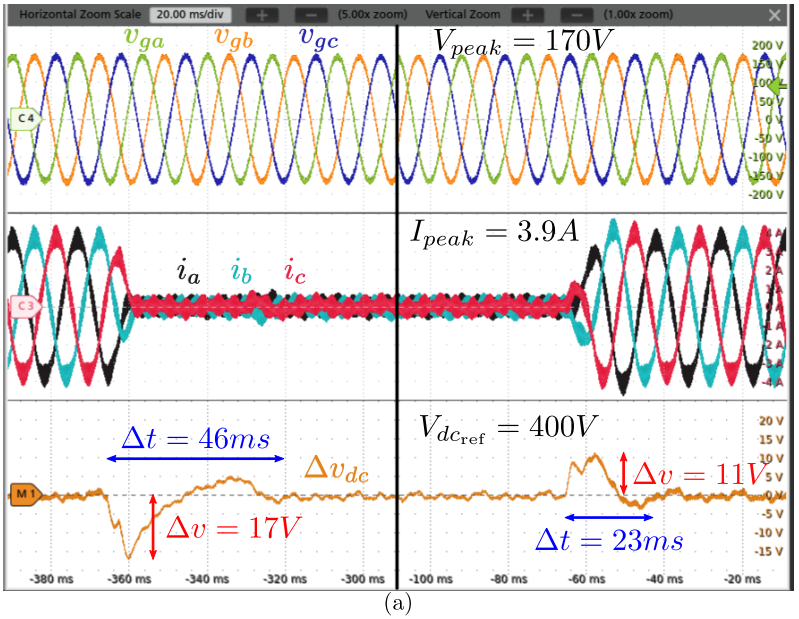

(a)

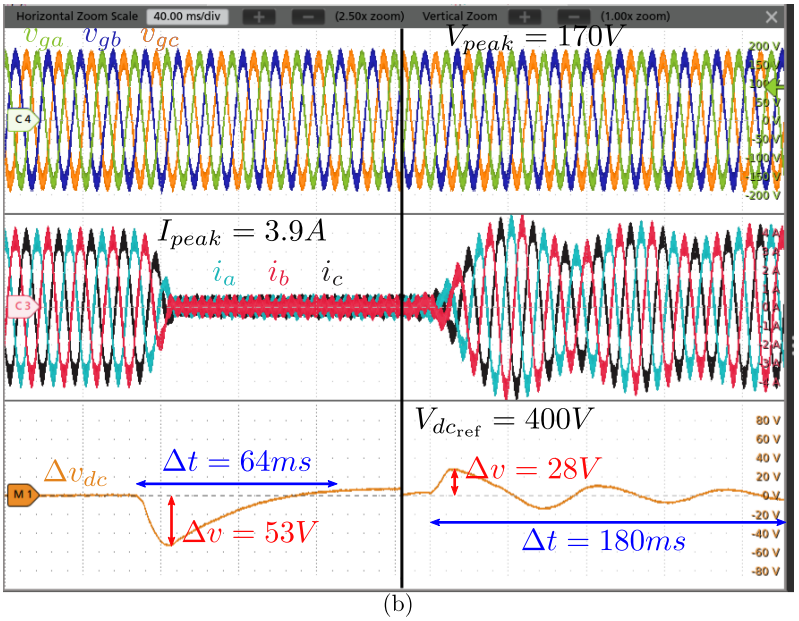

(b)

Fig. C.23: Experimental results for the full power jump (1 kW): (a) proposed control system, and (b) conventional control system.

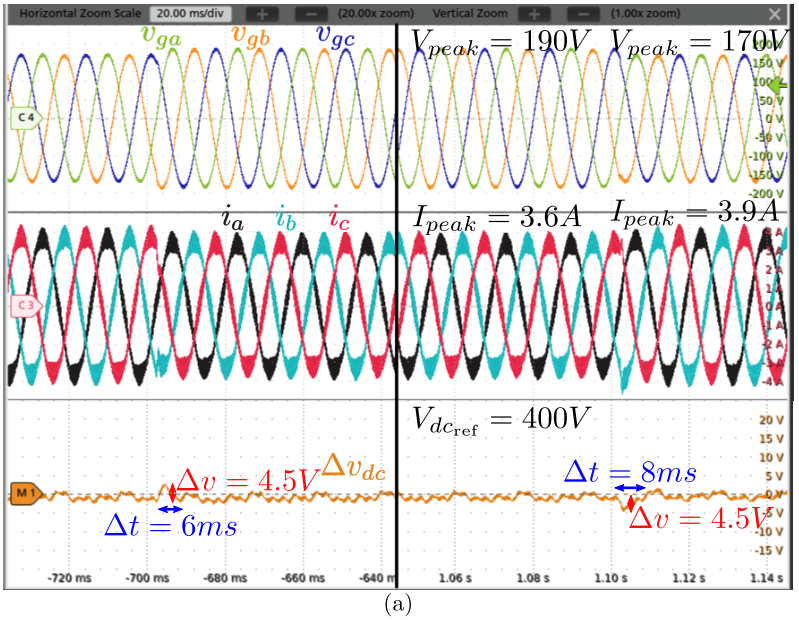

(a)

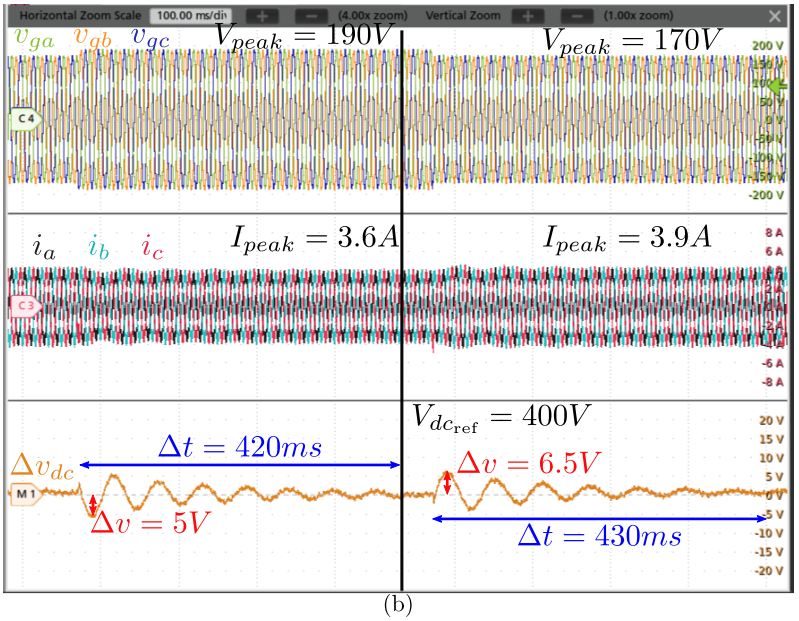

(b)

Fig. C.24: Experimental results for the grid amplitude jump: (a) proposed control system , and (b) conventional control system.

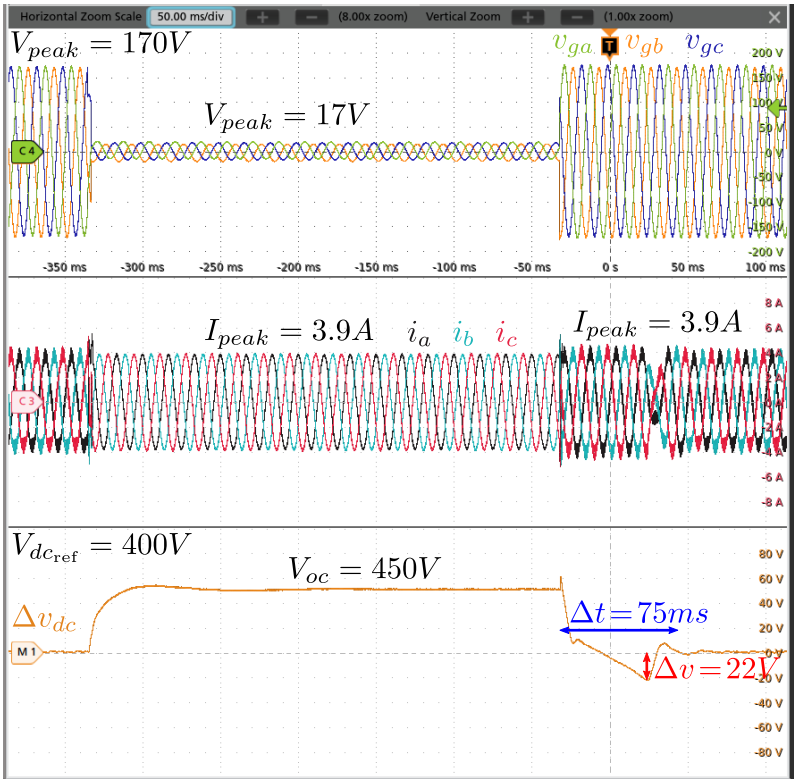

Fig. C.25: Experimental results for LVRT capability of the proposed control system.

voltage rises to V_{oc} according to the V-I characteristics of the PV panel. Inverter current in both pre- and post-fault transitions are shown to be well within the limits of the inverter. The inverter goes back to its normal operation and regulates the dc bus voltage to address MPPT after the post-fault recovery time Δt.